Author:
Lloyd, Ryan

Title:
InSAR Observations of Active Magmatic and Tectonic Processes in the East African Rift

InSAR Observations of Active Magmatic and Tectonic Processes in the East African Rift

Ryan Lloyd

A dissertation submitted to the University of Bristol in accordance with the requirements for award of the degree of Doctor of Philosophy in the Faculty of Science

School of Earth Sciences
University of Bristol

May, 2018

Supervised by Juliet Biggs & Geoff Wadge

Word Count:

36,500

Abstract

Continental rifting is achieved through a combination of magmatic and amagmatic processes. However, these processes can be influenced by heterogeneities at a range of scales, which act as regions of relative strength and weakness in the crust. The subaerial East African Rift, the longest continental rift on Earth, demonstrates the transition between incipient amagmatic and mature magmatic rifting. The rift interacts with geology that spans 3.8 Ga, and thus represents the ideal place to investigate crustal heterogeneities and rifting.

Interferometric Synthetic Aperture Radar (InSAR) has been used to observe the surface deformation caused by transient events associated with rifting throughout the East African Rift System. In this thesis, I explore how heterogeneities influence strain partitioning, magma transportation, and hydrothermal fluid migration, through the combination of InSAR, and other geophysical and geological datasets.

In the southern East African incipient rift environments of Mozambique and Botswana, I provide evidence to indicate pre-rift along rift faults are reactivated in the present-day stress field to influence where and how rifting occurs. By contrast, in the more mature, magmatic, Main Ethiopian Rift, I show pre-rift cross rift faults can influence magma and fluid migration over multiple temporal scales.

Magma plays an important role in accommodating extension in mature rift settings, primarily through dyking. However, the presence of large axial caldera systems suggest that the localisation of magma in reservoirs is also important. Observations of sustained uplift at the Corbetti caldera, in the Main Ethiopian Rift, indicates upper-crustal silicic magma reservoirs at continental rift calderas grow incrementally, through pulses of above-average magma flux.

Author's Declaration

I declare that the work in this dissertation was carried out in accordance with the requirements of the University's *Regulations and Code of Practice for Research Degree Programmes* and that it has not been submitted for any other academic award. Except where indicated by specific reference in the text, the work is the candidate's own work. Work done in collaboration with, or with the assistance of, others, is indicated as such. Any views expressed in the dissertation are those of the author.

.....

Ryan Lloyd

July 26, 2018

Acknowledgments

The last few years have been a fantastic adventure, and I am thankful to so many people for that. The next two hundred or so pages are dedicated to the science, but this is the page about the people, and is thus, to me, the most important. I will always look back fondly on these days. I have been immensely fortunate throughout my PhD, and can only hope to pass on some of the kindness I have experienced.

My NERC studentship was made possible through funding by the LiCS (Looking inside the Continents from Space) consortium, as well as additional support from the Volcano and Magmatic Studies Group (VMSG) and UNAVCO.

First and foremost I wish to thank Juliet Biggs for her tireless supervision, and prompt and thorough feedback that has enabled me to continually grow as a scientist. You have always encouraged me to continue to push myself, and I know you have always had my best interests at heart. There are many lessons I have learnt from you that will stay with me forever. I really have appreciated all of the time and effort you have put in for me.

There have been numerous others who have contributed to my PhD, by kindly providing data, advice, and time. The COMET and RiftVolc groups have provided great opportunities to present and discuss my work, learn more, and interact with peers. For this I am grateful. I also wish to thank the Volcanology and Geophysics research groups here in Bristol, which I have had the pleasure to be part of, and everyone with whom I have shared G10a. I owe a lot to James Hickey and Amy Parker for showing me the ropes in the beginning, David Arnold for sticking by my side throughout, and Yelebe Birhanu for keeping an eye on me in the field.

My acknowledgements certainly would not be complete without thanking those of you who put the tea in team, and made my PhD quite so unforgettable. You have been there throughout the most extraordinary of experiences, and the most ordinary of days. We have seen and done some so many things together that I will never forget, and for that I am hugely grateful. I wish to specifically name Ery, Becky, Nicky, Keri, and Neil. We all know I'm no geologist, but I sure had rocks in the School of Earth Sciences, and you guys were them. This thesis is for you.

My final thanks are for my Vicki, for her continued love, and support throughout.

Contents

List of Figures

List of Tables

Chapter 1

Introduction

1.1. Motivation

Continental rifting occurs over millions of years, prohibiting us from observing the full development in one location. Instead we compare geographically separate areas at different stages of rifting to provide a proxy for the temporal evolution. The East African Rift System (EARS) is a >4,000 km ∼north-south continental rift that runs from Eritrea-Ethiopia in the north, southward through the African continent (Figure 1.1). First identified as a rift in 1891 [*Suess*, 1891], the EARS has since be the subject of numerous geoscientific studies trying to understand how and why rifting occurs.

Fundamentally, rifting occurs via magma intrusion, faulting, and ductile deformation, but these processes are modulated by crustal heterogeneities at a range of scales. The transition between amagmatic and magmatic rifting and how secondary factors, such as crustal heterogeneities, influence these processes is unclear. For example to what degree do crustal heterogeneities guide rifting as it initiates, and over what timescales does this continue? How do different types of crustal heterogeneities (rift-parallel versus rift-oblique faults, relative strong versus relative weak geological bodies) have different controls on rifting?

The earthquakes and volcanic eruptions associated with continental rifting can also pose a significant hazard to life and infrastructure. Understanding these hazards now is especially important in regions such as East Africa, which is rapidly developing socio-economically, but has low levels of awareness and few monitoring resources.

In this thesis I use Interferometric Synthetic Aperture Radar (InSAR) to investigate surface deformation associated with magmatic and amagmatic rifting. InSAR is an ideal tool to study seismic events and to monitor decadal-term processes (e.g., magma reservoir growth). InSAR does not require field campaigns, but observations of surface

deformation can be combined with multiple datasets (e.g., gravity, seismicity, and ground resistivity) to better characterise sources and processes.

The topography, geology, climate, hydrology, and ecosystems produced by rifting in East Africa are thought to have facilitated proto-human evolution [*Hutchison et al.*, 2016; *Maslin et al.*, 2014]. Today, the rift still influences the lives of local populations. For many the rift provides resources for exploitation such as fertile land, hydro- and geothermal energy, tourism, and salt deposits [e.g., *Gíslason et al.*, 2015; *Simiyu*, 2010]. However, the rift also presents hazards associated with earthquakes and volcanoes and, as such, understanding the ongoing volcanic (Chapter 3) and seismic (Chapters 4 and 5) processes is paramount to provide mitigation.

1.2. Continental rifting in East Africa

Continental rifting is the extension and thinning of continental crust towards the formation of ocean basins, achieved through tectonic (faulting), ductile, and magmatic processes [*Buck*, 2006; *Wright et al.*, 2006; *Keir et al.*, 2006; *Ebinger and Casey*, 2001] (Figure 1.2). The relative importance of the forces driving rifting in east Africa have long been debated, with candidates including far-field plate motions, mantle convection, and dynamic topography [e.g., *Kendall and Lithgow-Bertelloni*, 2016; *Buck*, 2006; *Turcotte and Emerman*, 1983; *Dunbar and Sawyer*, 1989]. The magnitudes of the stresses available through these processes are difficult to estimate [e.g., *Bai et al.*, 1992; *Buck*, 2006], but each are thought to be insufficient to rift thick cold continental lithosphere alone. Continental rifting therefore probably requires multiple forces acting together [*Kendall and Lithgow-Bertelloni*, 2016; *Buck*, 2006; *Dunbar and Sawyer*, 1989].

As extension occurs, the ductile lower lithosphere thins, causing vertical migration of decompression derived magma [*Mckenzie and Bickle*, 1988]. This transports heat into the crust, reducing its tensile strength, allowing further ductile deformation [*Daniels et al.*, 2014; *Ebinger*, 2005]. Faulting (amagmatic rifting) occurs in the uppermost brittle portion of the crust, to accommodate extensional stresses. With time, the lithosphere thins and warms sufficiently such that normal faulting is abandoned, magma transportation (magmatic rifting) accommodates extension, and continental rifting transitions into seafloor spreading (Figure 1.2) [*Bialas et al.*, 2010; *Buck*, 2006; *Whitmarsh et al.*, 2001].

Rifting in the EARS initiated following the upwelling of mantle material from the African large low shear velocity province beneath east Africa >40 Ma which caused broad (∼500 km^2) uplift, producing the Ethiopian and Somalian highlands that can be observed today

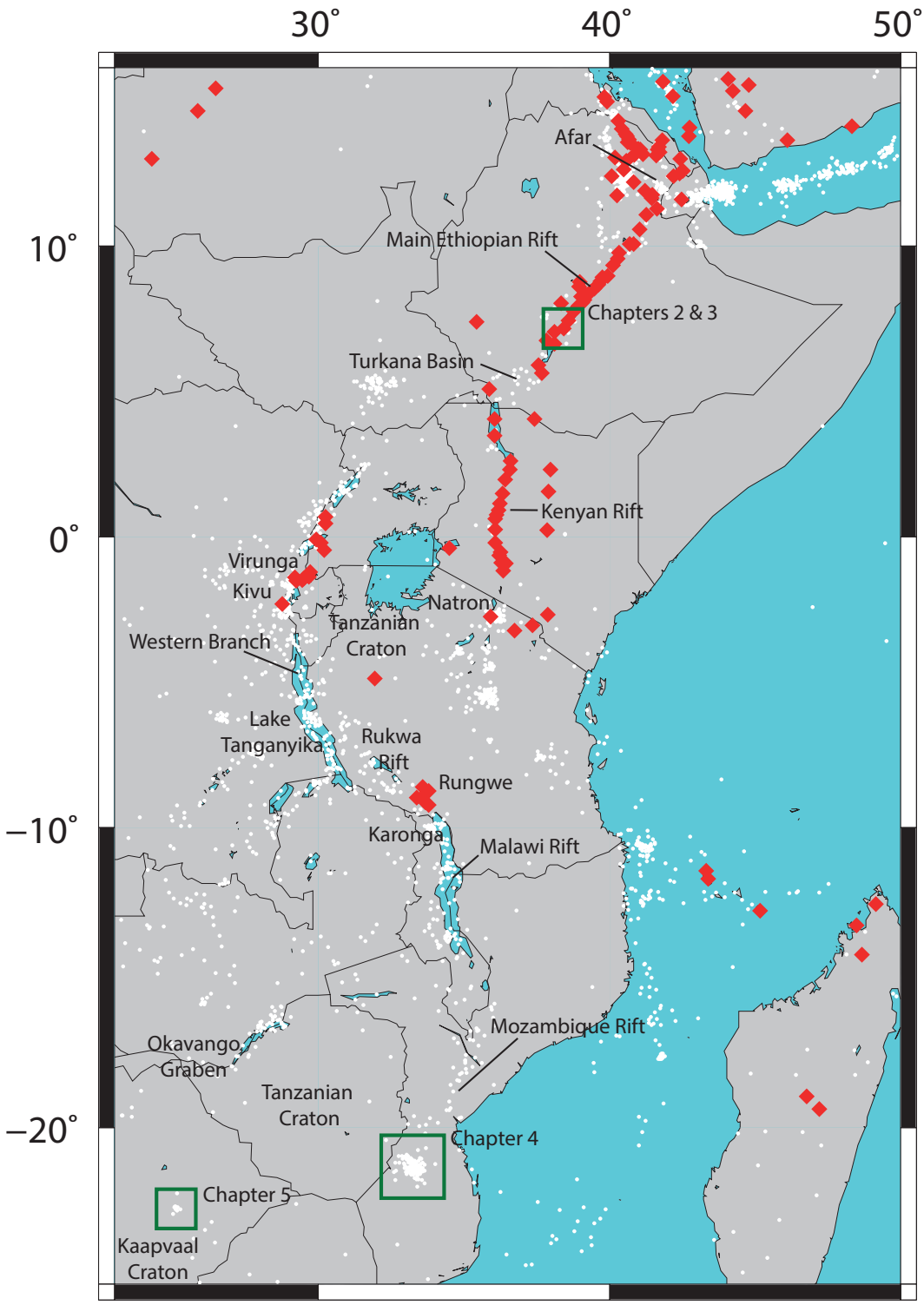

Figure 1.1: The East African Rift. Volcanic centres [*Global Volcanism Program*, 2013] and historical seismicity (USGS catalogue, 2018) are denoted by red diamonds and white circles respectively. The geographical localities of Chapters 2 – 5 are shown by green boxes.

[*Garnero et al.*, 2016; *Garnero and McNamara*, 2008; *Rogers et al.*, 2000; *Ebinger and Sleep*, 1998]. This vertical transport of hot mantle material provided the heat needed to weaken the lithosphere [*Bialas et al.*, 2010; *Buck*, 2006], increased the elevation to provide dynamic topographic forces [*Kendall and Lithgow-Bertelloni*, 2016], and emplaced melt close to the surface [*Ebinger and Sleep*, 1998; *Mckenzie and Bickle*, 1988].

The transport of large volumes of buoyant mantle material towards the surface resulted in pulsed eruptions of voluminous flood basalts (up to 2 km thick) across Kenya, Ethiopia, and the Arabian peninsular ∼45 – 25 Ma [*Rooney*, 2017; *Furman et al.*, 2006; *Baker et al.*, 1996]. Flood basalt volcanism, although a precursor to rifting in the northern EARS, did not preceded extension everywhere along the rift. In the present-day incipient southern EARS, for example, rifting is exclusively accommodated via faulting with no related surface volcanism. Evidence suggests faulting at the surface initiated at ∼25 Ma in the northern present-day EARS [*Bonini et al.*, 2005], via the formation of discrete graben basins, with displacement along high-angle normal border faults [*Hendrie et al.*, 1994; *Morley et al.*, 1992].

The transition from amagmatic incipient rifting to magmatic rifting can be investigated by focussing on either the temporal evolution of a magmatic rift, such as the Main Ethiopian Rift (MER) in the northern EARS, or by comparing localities along the rift at different stages of maturity [*Ebinger*, 2005]. In the next subsections I discuss the amagmatic to magmatic transition by comparing different localities of progressively more developed rifting.

1.2.1. Amagmatic rifting

The least mature sections of the EARS are in southern East Africa. Extension in these regions is inherently small, and thus there is some discussion on the locality of the youngest portions of the EARS. In southern Mozambique, recent normal faulting earthquakes indicate the crust is subject to extension [*Fonseca et al.*, 2014], but the rate is relatively low (<2 mm/yr [*Saria et al.*, 2014]) (Figure 1.1). The M_w 7.0 2006 Machaze earthquake in southern Mozambique was one of the largest earthquake to occur in continental Africa for a century, and was a clear demonstration that incipient rifting continues as far south as -21° N (Chapter 4) [e.g., *Copley et al.*, 2012; *Yang and Chen*, 2008; *Fenton and Bommer*, 2006]. An alternative, or additional, branch of incipient rifting is delineated by seismicity from Malawi, through Zambia and into Botswana (Figure 1.1), where normal faulting suggests some extension has occurred since the Quaternary, and is ongoing today (Chapter 5) [*Modisi*, 2000; *Scholz et al.*, 1976].

North of Mozambique, the Malawi Rift provides a clear example of amagmatic rifting

(Figure 1.1), where extension at rates of ∼2 mm/yr [*Saria et al.*, 2014] is accommodated via faulting along long, steep normal faults that form segmented asymmetric half-graben basins [*Jackson and Blenkinsop*, 1997; *Rosendahl et al.*, 1992; *Ebinger et al.*, 1987]. Border fault formation is thought to, at least in part, locally exploit crustal weak zones where possible [*Ring*, 1994], e.g., the Bilila-Mtakataka fault [*Hodge et al.*, 2018a]. Most of the extension here is accommodated on the high-angle border faults, with relatively little thinning beneath the elevated rift flanks [*Ebinger et al.*, 1987]. Profiles of seismic reflection data across the Malawi Rift show a decrease in intra-basin fault density with time, indicating a changing location of accommodation with increased extension [*Rosendahl et al.*, 1992; *Specht and Rosendahl*, 1989]. At depth, the border faults are thought to be listric, becoming horizontal in the lower crust [*Rosendahl et al.*, 1992; *Specht and Rosendahl*, 1989].

In northern Malawi, a sequence of earthquakes in the Karonga region in 2009 showed segmented fault rupture across ∼40 km in the hanging wall (Figure 1.1). The events were confined to the upper ∼6 km, demonstrating extension is occurring here through sequences of shallow M_w ∼5 – 6 earthquakes [*Fagereng*, 2013; *Biggs et al.*, 2010a].

1.2.2. Transition to magmatic rifting

The transition between amagmatic and magmatic rifting is poorly understood. It is unclear, for example, whether the transition is a function of the magnitude of extension, extension rate, heat flux, lithospheric properties, or a combination of factors. In addition, seismic events occur in rift segments that also have high melt fluxes, demonstrating that the transition is continuous, and that in many locations magmatic and amagmatic processes act together to facilitate rifting [e.g., *Calais et al.*, 2008; *Pizzi et al.*, 2006].

Rungwe, a localised collection of volcanoes in southern Tanzania, is the southernmost expression of magmatism in the EARS (Figure 1.1). The most recent eruption in Rungwe was ∼1 ka, and there is evidence for frequent, and, at times Plinean, eruptions [*Fontijn et al.*, 2012, 2010a]. The eruptive centres of Rungwe are located in the transfer region between the border faults of the Rukwa and Malawi Rifts [*Ebinger et al.*, 1989] (Figure 1.1), and there is evidence of faults controlling the location of the volcanoes and eruptive vents [*Fontijn et al.*, 2010b; *Furman*, 1995].

The EARS bifurcates around the Tanzania Craton into two branches, the Kenyan Rift and Western Rift. In the Western Rift, north-west of Rungwe, rifting is primarily achieved through faulting, with asymmetric basins and steep border faults [*Morley et al.*, 1992; *Ebinger et al.*, 1991; *Ebinger*, 1989] (Figure 1.1). The Western Rift forms a broad north-south arc. The southern section, which underlies Lake Tanganyika is amagmatic

at the surface, with extension of 15 – 20% that is localised to within the basins [*Hodgson et al.*, 2017; *Ebinger*, 1989]. However, an elevated Vp/Vs ratio and deep seismicity suggest magma intrusions may have a role in accommodating extension at depth [*Hodgson et al.*, 2017].

In the northern section of the Western Rift, magmatism is voluminous but localised to the Virunga, South Kivu, and Katwe-Kikorongo regions [*Wood et al.*, 2017; *Pouclet et al.*, 2016; *Ebinger*, 1989] (Figure 1.1). In 2008 the M_w 5.9 Bukavu earthquake occurred beneath Lake Kivu, only 20 km from the nearest surface expressions of volcanism in South Kivu. The event, however, was attributed to slip on a shallow fault (<9 km) unassociated with magma transport [*D'Oreye et al.*, 2011], indicating the Western Rift is transitioning between amagmatic and magmatic extension.

1.2.3. Magmatic rifting

The Kenyan Rift runs between northern Kenya and northern Tanzania to the east of the Tanzania Craton (Figure 1.1). The Kenyan Rift is comprised of ∼60 km wide half-graben basins that formed during the late Oligocene (∼30 Ma) [*Morley et al.*, 1992], with co-eval and subsequent volcanism. A southward propagation of rifting through Kenya is suggested based on increasing crustal thickness and age of volcanism [*Prodehl et al.*, 1997; *KRISP Working Party*, 1991]. In Tanzania rifting is less mature, and extension is accommodated by magma transport in conjunction with faulting. In 2007, near Lake Natron, fault slip was observed to promote magma migration via dyking through stress unclamping [*Biggs et al.*, 2013, 2009a; *Calais et al.*, 2008]. The dyke intrusion was ∼7 km long at ∼4 km depth, with up to 2.4 m of opening, and was accompanied by the deflation of a magma chamber at a depth of 4 – 8 km [*Biggs et al.*, 2009a].

North of the Kenyan Rift is the Main Ethiopian Rift (Figure 1.1), where extension rates are estimated to be 6 – 7 mm/yr, in an east-west direction [*Stamps et al.*, 2018; *Saria et al.*, 2014; *Agostini et al.*, 2009; *Chu and Gordon*, 1999]. The MER today is ∼50 km wide, bounded by border faults with up to ∼3 km offsets [*Ebinger and Casey*, 2001]. Following the initial formation of these graben and half-graben structures at 11 Ma bimodal volcanism began ∼7 – 3 Ma [*Bonini et al.*, 2005; *Woldegabriel et al.*, 1990]. By 1.8 Ma extension became increasingly localised to the rift axis, creating numerous shorter intra-rift faults with ∼1 m offsets, eruptive centres, primarily silicic calderas, and basaltic fissures aligned along the rift axis [*Acocella*, 2014; *Corti*, 2009; *Casey et al.*, 2006; *Pizzi et al.*, 2006; *Acocella et al.*, 2003; *Buck*, 1991; *Woldegabriel et al.*, 1990; *Mohr and Wood*, 1976; *Mohr*, 1967] (Figure 1.2). The intra-rift faults are the surface expression of the rift-axis strain localisation as the ductile transition progressively shallows. Geodetic observations indicate that at present ∼80% of the strain is accommodated within the

rift [*Birhanu et al.*, 2016; *Bilham et al.*, 1999], through faulting on these smaller faults and aseismic deformation.

Seismic observations are able to constrain the distribution of subsurface magma intrusions. In the upper mantle (<100 km) low P- and S-wave velocities show segmented structures across a wide zone beneath the MER, thought to indicate the presence of partial melt [*Gallacher et al.*, 2016; *Bastow et al.*, 2005]. The magnitude and alignment of shear wave splitting measurements with chains of volcanoes and fissures at the surface suggests magma resides within aligned cracks throughout the lithosphere [*Bastow et al.*, 2010; *Kendall et al.*, 2005]. Within the upper 10 – 20 km, velocity variations from seismic refraction surveys and 3-D tomography identify high density, high velocity (Vp 6.5 – 6.8 km/s) elongate bodies (20 by 60 km) beneath the MER axis [*Keranen et al.*, 2004]. These bodies are interpreted to be solidified melt intrusions, and align with the segmented distribution of Quaternary volcanic centres. Magnetotelluric observations of the electrical resistivity of the lithosphere corroborate the seismic interpretations [*Mackenzie et al.*, 2005]. Measurements of geoelectric strike that are parallel to the rift support the hypothesis of melt alignment [*Whaler and Hautot*, 2006], and zones of high conductivity at ∼20 km beneath the Boset magmatic segment are thought to identify mafic intrusions which are possibly partially molten.

Magma plays a fundamental role in weakening the crust, and its petrogenesis can be informative on crustal conditions, specifically rift maturity and local magma supply [*Hutchison et al.*, 2018]. Peralkaline rhyolite fractionation, for example, will occur where magma ascent is inhibited or magma flux is locally reduced, compared to regions which erupt basalt. Melt reaches the surface at distinct volcanic centres within the MER (Figure 1.1). Along the MER axis these centres are mid-Pleistocene calderas (5 – 15 km diameter), with post-caldera eruptions of, typically, peralkaline rhyolite as obsidian flows and domes [*Fontijn et al.*, 2018].

Since 1890 11 of the volcanic centres in the MER and Afar have erupted, in >15 eruptions [*Wadge et al.*, 2016]. In the geological record there is evidence for numerous large magnitude eruptions (up to VEI 3 – 4) over the last 10 – 20 kyr [*Fontijn et al.*, 2018; *Hutchison et al.*, 2016; *Siebert et al.*, 2010]. Over last few decades, geophysical observations have observed unrest at several of these centres, indicating multiple present-day active magmatic systems [*Wilks et al.*, 2017a; *Hutchison et al.*, 2015a; *Biggs et al.*, 2011; *Asfaw*, 1982]. The Corbetti caldera is one such active centre, and the focus of Chapters 2 and 3 (Figure 1.1). Corbetti has evidence for numerous large Holocene eruptions [*Martin - Jones et al.*, 2017; *Rapprich*, 2013], but has no permanent or real-time monitoring.

1.2.4. Transition to seafloor spreading

In Afar, where continental rifting is transiting towards incipient seafloor spreading, geodetic and seismic studies have observed the accommodation of tensile stresses via magmatic rifting in numerous dyke intrusion events [*Pagli et al.*, 2014, 2012; *Nobile et al.*, 2012; *Keir et al.*, 2011; *Wright et al.*, 2006; *Doubre and Peltzer*, 2007; *Amelung et al.*, 2000]. Afar also represents the triple junction between the Nubian, Somalian, and Arabian plates. The full spreading rate between the Nubian and Arabian plates is ∼18 mm/yr, and ∼16 mm/yr between the Somalian and Arabian plates [*Saria et al.*, 2014; *Vigny et al.*, 2006]. Estimates of the crustal thickness in Afar show a transition between ∼28 km near the MER, to ∼10 km in the north [*Craig et al.*, 2011; *Hammond et al.*, 2011; *Dugda et al.*, 2005].

The most dramatic recent example of dyking in Afar is the 2005 Dabbahu dyke intrusion sequence [*Grandin et al.*, 2009; *Hamling et al.*, 2009; *Ebinger et al.*, 2008; *Wright et al.*, 2006]. Within two weeks ∼2.5 km^3 of magma was intruded into the crust between 2 – 9 km deep along an ∼60 km long segment, sourced partly from two nearby shallow (∼6 km) magma reservoirs, and partly from depth. During the dyking event the seismic moment release was more than an order of magnitude less than the geodetic estimate, indicating most of the deformation occurred aseismically. After the initial dyke intrusion there were >13 further discrete intrusions [*Hamling et al.*, 2010]. The sequence provided insights into intrusion mechanisms, magma sources, and stress evolution during dyking in a mature continental rift setting. The Dabbahu dyke intrusion contrasts with the one in northern Tanzania in 2007, most noticeably in its length and volume. The crust in Afar is hotter and thinner than in Tanzania, and as such shallower and larger magma reservoirs can be maintained, resulting in comparatively long, sustained, voluminous dykes (60 km in Afar versus 7 km long in Tanzania [*Biggs et al.*, 2009a; *Wright et al.*, 2006]).

1.3. Inheritance and strain localisation

Throughout the history of the EARS inherited structures have influenced strain localisation. Indeed, several studies conclude that localised weaknesses are required to reduce the tensile strength of the lithosphere enough to allow rifting to occur given the available stresses [*Kendall and Lithgow-Bertelloni*, 2016; *Vauchez et al.*, 1997; *Dunbar and Sawyer*, 1989, 1988]. East African geology can be dated back to the Archean, and numerous processes have introduced crustal heterogeneities. Heterogeneities are able to partition strain and so will inevitably influence rift development across multiple spatial and temporal scales (see *Acocella* [2014]). For example, the MER is oriented

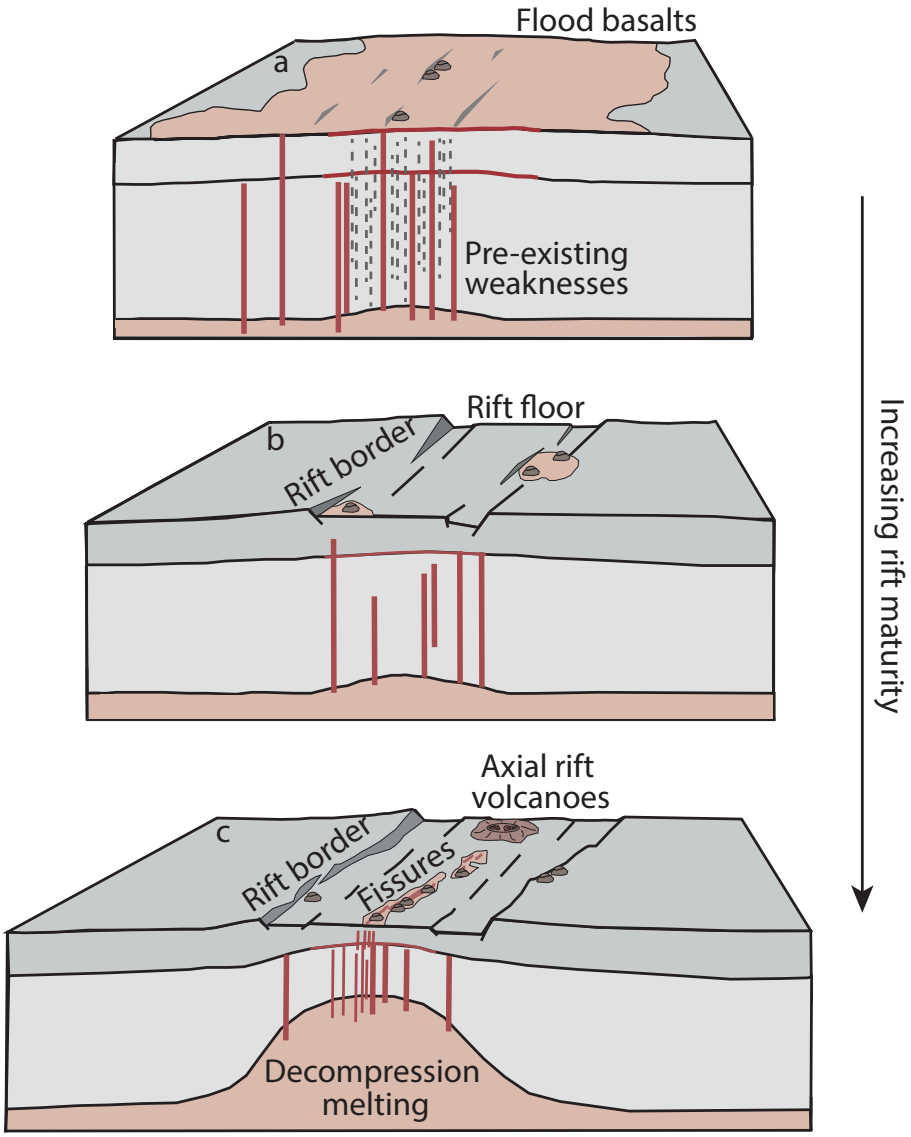

Figure 1.2: Schematic showing increasing rift maturity, from (a) eruption of flood basalts, through the initiation of border faults (b), to the formation of axial volcanic centres and localisation of strain within the rift (c). Modified from *Robertson* [2015] and *Corti* [2009]

approximately NNE-SSW, and it has been hypothesised that this orientation follows a Pan-African suture zone [*Corti*, 2009]. The Ambo shear zone, Ethiopia, is an example of a major oblique structure that has influenced off-rift volcanism and crustal thickness [*Bastow et al.*, 2005]. Crustal heterogeneities can also provide barriers to rifting. This is clearest on the largest scale, where the cold rigid Tanzania Craton forces the rift into two branches [*Koptev et al.*, 2015].

Rifting at the surface is initially facilitated by faulting. Faulting occurs when the shear stress (τ) acting on a material is greater than the effective normal stresses, σ. Figure 1.3 shows a Mohr diagram, of τ as a function of σ acting on an inclined planar surface. On this plot, strength envelopes are shown to represent the point of failure by faulting (rock strength) and frictional (fault strength) processes. Slip will occur as the Mohr circle intersects a strength envelope, e.g., point P. The formation of new faults is shown by Mohr circle A. Mohr circle B represents the conditions for reactivation of a pre-existing fault, dipping at angle θ. Pre-existing faults with a range of dips, β, will be reactivated (intersect the strength envelope) before the formation of new faults, as is seen in nature.

Rock failure can also occur in tensile stress regimes. Within the crust, one way this can be achieved is through magma intrusion, which increases pore pressure. If the pore pressure is greater than the confining pressure, an effective tensile stress field will develop. Mohr circle C is within this tensile regime (Figure 1.3). Failure will occur when the circle intersects point T, which represents the tensile strength of a material.

Pre-existing structures can also guide the transport of fluids within the Earth [e.g., *Lloyd et al.*, 2018; *Robertson et al.*, 2016; *Hutchison et al.*, 2015a; *Le Corvec et al.*, 2013; *Rowland and Sibson*, 2004]. As fluids such as magma rise, their migration will be controlled by the stress field, and be influenced by crustal heterogeneities such as faults [*Wadge et al.*, 2016; *Gaffney et al.*, 2007]. In Kenya and Ethiopia pre-existing cross-rift structures have been hypothesised to control the location and duration of magma ascent, therefore influencing volcano surface geomorphology, and magma petrogenesis [e.g., *Lloyd et al.*, 2018; *Hutchison et al.*, 2018; *Robertson*, 2015; *Acocella et al.*, 2002]. The same is true in the Kivu Basin, where reactivated Precambrian structures are thought to create transfer zones, influencing the stress regime, and thus location of volcanism [e.g., *Smets et al.*, 2016]. Structural controls on the distribution of monogenetic vents and cones has also been observed throughout the rift [e.g., *Muirhead and Kattenhorn*, 2018; *Muirhead et al.*, 2015]. One mechanism for this is differential loading, caused by the topographic scarps of normal faults, deflecting magma into the footwall, rather than the fault acting as a preferential pathway [*Maccaferri et al.*, 2015].

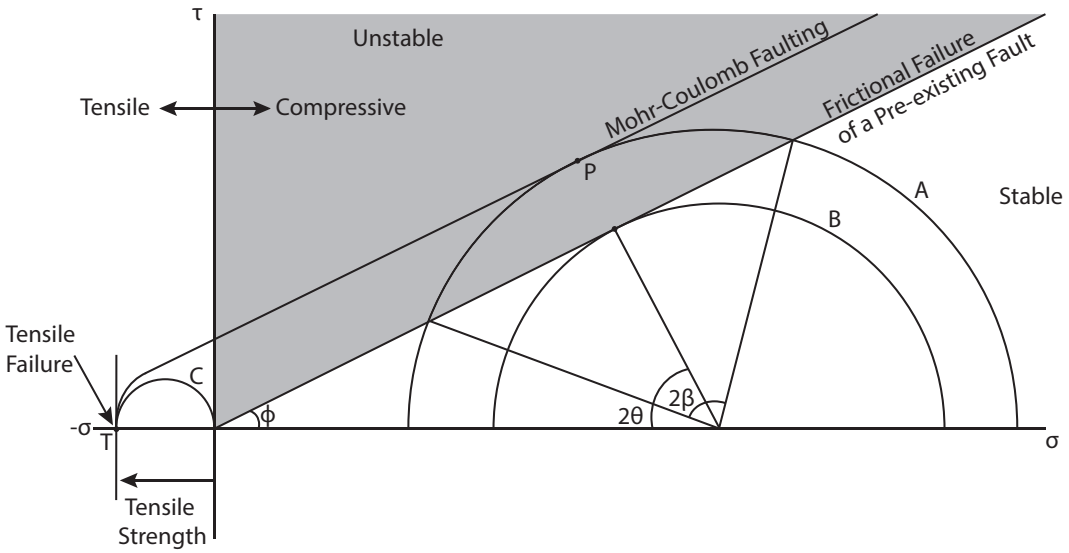

Figure 1.3: Mohr circles showing failure through faulting (circle A), frictional (circle B), and tensile (circle C) processes. The coefficient of friction, μ, is related to the gradient of the strength envelopes through the angle of friction, ϕ, via $\mu = \tan(\phi)$. In the tensile stress regime the failure envelope becomes parabolic.

1.4. Interferometric Synthetic Aperture Radar principles

Interferometric Synthetic Aperture Radar (InSAR) is a satellite-based remote sensing technique that uses active microwaves to measure changes in the satellite-target path length. First employed in the early 1990's to investigate surface displacements during the 1992 Landers earthquake, California [*Massonnet et al.*, 1993], and deformation at Mt Etna, Italy, 1992 – 1993 [*Massonnet et al.*, 1995], InSAR has since been used to investigate natural and anthropogenic signals from across terrestrial and cryosphere environments [e.g., *Walter and Motagh*, 2014; *Park et al.*, 2013; *Ebmeier et al.*, 2012; *Hooper et al.*, 2004]. This has partly been facilitated by the diversity of InSAR capable satellites currently in orbit. The main advantages of InSAR over terrestrial geodetic tools is that InSAR is capable of measuring a continuous displacement field in high spatial resolution. The spatial and temporal resolution that can be achieved using publicly available SAR vary by sensor, as summarised in Table 1.1, but is typically 3 – 30 m spatially, and 1 – 24 days temporally.

Satellite geodesy is an ideal tool to study the processes associated with active rifting. The diversity of satellites currently operational, allowing us to study multi-temporal and -spatial scale deformation processes, makes this is especially true today. Some regions in the rift are inaccessible due to geopolitical, safely, or access reasons that prohibit or complicate fieldwork. InSAR, however, does not require field access. In addition, the low cost and ease of access to regularly acquired SAR data facilitates researchers to use the technique for responsive [e.g., *Hamling et al.*, 2017; *Wright et al.*, 2006] and hypothesis

driven research [e.g., *Pagli et al.*, 2014; *Walters et al.*, 2011]. Figure 1.4 summaries the InSAR observations that have been made in the EARS at the time of writing.

In this thesis I utilise SAR imagery from the European Space Agency (ESA) ENVISAT and Sentinel-1 satellites, the Italian Space Agency (ASI) Cosmo-SkyMed satellite constellation, and the Japanese Aerospace eXploration Authority (JAXA) ALOS-1, and ALOS-2 satellites. Details on how interferograms within this thesis were processed are discussed in each chapter.

1.4.1. Synthetic Aperture Radar

Synthetic Aperture Radar (SAR) capable satellites actively illuminate the Earth's surface with electromagnetic pulses of microwave frequency, facilitating acquisitions in all weather conditions, day and night. SAR satellites operate on a polar orbit and travel in either an ascending (roughly south-north) or descending (roughly north-south) direction. The emitted radiation is back-scattered from the Earth's surface to the sensor, where the amplitude and phase component are recorded as a complex number.

The amplitude component of the radar return is a measure of the amplitude of the signal, and is a function of the backscattering properties of the surface. Amplitude measurements can be used to investigate processes that influence surface backscattering properties, such as the deposition of lava [e.g., *Arnold et al.*, 2017; *Dietterich et al.*, 2012; *Wadge et al.*, 2011]. The phase component is a measure of the fractional cycle of the returned radiation. Its value is psuedo-random, with contributions from the different scatterers within each resolution element and delays along the radar path.

The SAR imagery in this thesis was acquired in a range of acquisition modes, each of which with relative advantages and disadvantages (Table 1.1). Here, I detail the acquisition modes of the Cosmo-SkyMed and Sentinel-1 satellites to provide a comparison. Cosmo-SkyMed (CSK) stripmap images have a high spatial resolution (3 – 5 m), but a narrow swath width (40 km). The Cosmo-SkyMed satellites are part of a constellation, and as interferograms can be created from SAR acquired by any satellite, the repeat time for a given location can be between 16 days with one satellite, to 1 day using multiple satellites. SAR images can be acquired in one of five modes, including stripmap, which I use here. Stripmap mode uses continuous radar pulses made as the satellite orbits with a fixed antenna azimuth angle (Figure 1.5a).

Sentinel-1 is also a constellation, of two satellites. In this thesis I use Interferometric Wide TOPS (Terrain Observation with Progressive Scan) mode data, which produces 250 km wide swaths with 5 x 20 m pixel resolution, and up to a 6 day repeat time (12 days for

Table 1.1: Summary of SAR satellites used in this thesis. Cosmo-SkyMed and Sentinel-1 are constellations and operational times relate to initial launch.

Instrument	Time of satellite operation	Acquisition mode	Wavelength (cm)	Swath width (km)	Pixel resolution (m) Range x Azimuth	Repeat time (days)
Envisat	2002 – 2012	Image Mode	5.6	100	30 x 30	35
Envisat	2002 – 2012	Wide Swath	5.6	400	150 x 150	35
ALOS-1	2006 – 2011	Fine Beam	23.5	70	10 x 10	46
ALOS-2	2014 –	ScanSAR	23.5	490	60 x 60	14
Sentinel-1	2014 –	TOPS	5.6	250	5 x 20	12 (6 with 1a and 1b)
Cosmo-SkyMed	2007 –	Stripmap	3.1	40	3 – 5 x 3 – 5	16 ($\geq$1 for full constellation)

each satellite individually) [*De Zan and Guarnieri*, 2006]. TOPS mode images are made up of three sub-swaths, each with nine bursts (Figure 1.5a). Each burst is imaged by electronically steering the antenna from backwards to forwards in the azimuth direction (Figure 1.5b), before switching sub-swath to image the first burst in the adjacent sub-swath (1 – 3 in Figure 1.5a). The sensor then returns to the first sub-swath to acquire a second burst, and so on. Steering the antenna in the azimuth direction results in varying squint angles (ψ) throughout the burst, with a small portion of the sub-swath (the burst overlap region, ∼10 km long), having forwards and backwards looking squint angles that vary by ∼1° (Figure 1.5b).

1.4.2. SAR interferometry

The phase component of a single SAR image is uninformative on its own. However, with co-registered master (initial acquisition) and slave (repeat acquisition) images an interferogram can be made by multiplying the master image by the complex conjugate of the slave image to determine the difference in phase between the two. For interferograms where scatterers remain stable between SAR acquisitions, the result will be a coherent phase map, within which changes can be interpreted as the satellite-ground range change between the two acquisitions, plus a noise contribution. Details in the InSAR processing methodology are established, and not discussed here. The reader is instead referred to *Rosen et al.* [2012, 2004]; *Bürgmann et al.* [2000]; *Werner et al.* [2000] and *Massonnet and Feigl* [1998].

For most geophysical applications of InSAR the signal of interest is the relative ground displacement, $\Delta\phi_{displacement}$, however there are several other contributions to the recorded phase change, $\Delta\phi_{LOS}$, which need to be considered (Equation 1.1).

$$\Delta\phi_{LOS} = \Delta\phi_{displacement} + \Delta\phi_{topographic} + \Delta\phi_{geometric} + \Delta\phi_{atmospheric} + \Delta\phi_{noise} \tag{1.1}$$

Some sources of noise can be mitigated effectively through corrections. $\Delta\phi_{geometric}$ is a function of differences in the satellite viewing geometry. SAR satellites will rarely return to the same position in space for each acquisition. The difference in location is termed the baseline separation, and results in a phase change between acquisitions. Precise measurements of the satellites orbit are used to correct for this difference in the interferograms, but these measurements have uncertainties that must also be accounted for, usually through the removal of a phase gradient.

The Earth's topography has a control on the radar path length, which varies with satellite position. Therefore, for interferograms with a non-zero perpendicular baseline, there will

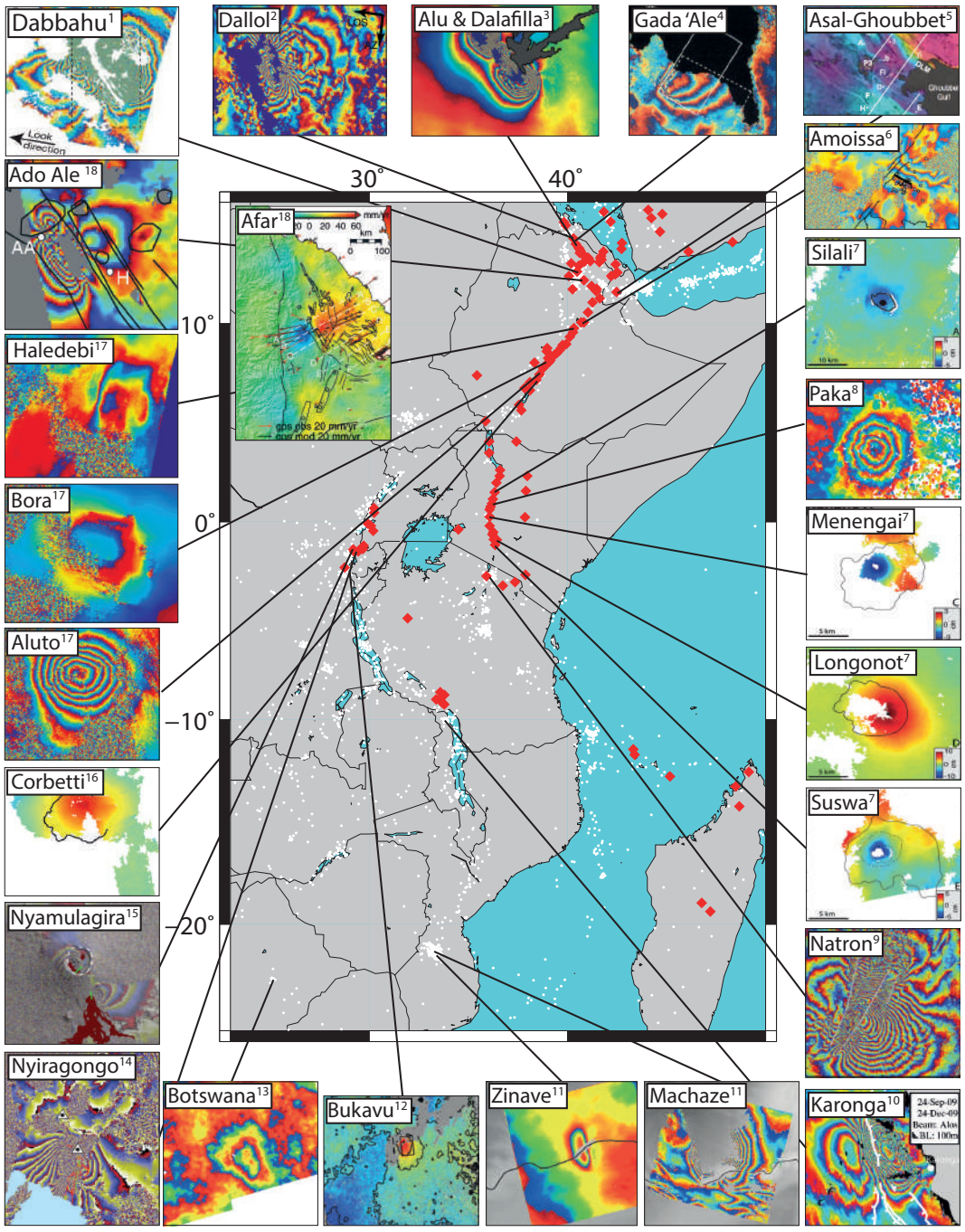

Figure 1.4: Synthesis of InSAR studies in the East African Rift, demonstrating volcanic uplift and subsidence, dyke intrusions and faulting. 1. *Wright et al.* [2006], 2. *Nobile et al.* [2012], 3. *Pagli et al.* [2012], 4. *Amelung et al.* [2000], 5. *Doubre and Peltzer* [2007], 6. *Keir et al.* [2011], 7. *Robertson* [2015], 8. *Biggs et al.* [2009b], 9. *Biggs et al.* [2009a], 10. *Biggs et al.* [2010a], 11. Chapter 4, 12. *D'Oreye et al.* [2011], 13. Chapter 5, 14. *Wauthier et al.* [2012], 15. *Wauthier et al.* [2013], 16. Chapter 3, 17. *Biggs et al.* [2011], 18. *Pagli et al.* [2014].

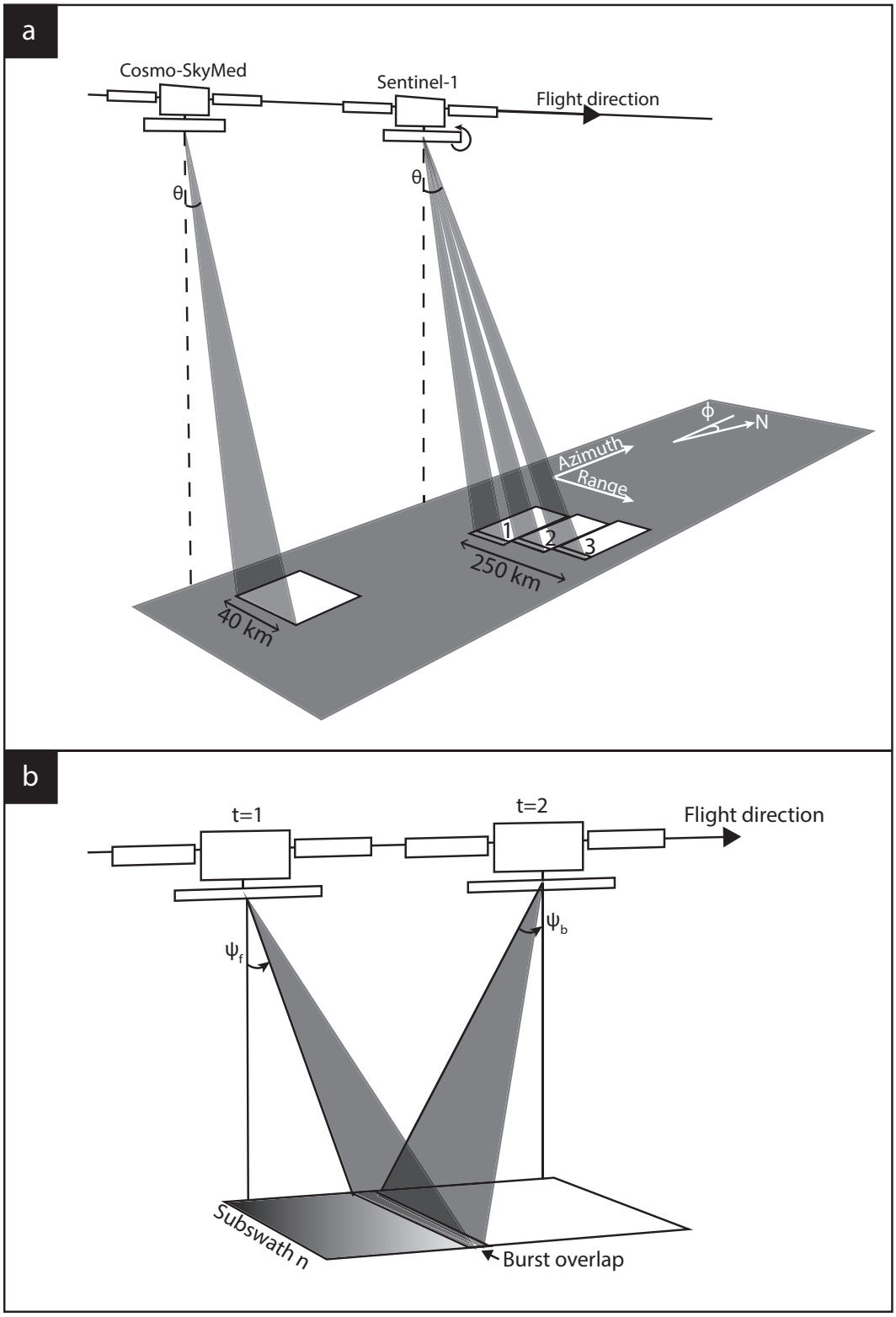

Figure 1.5: a) Schematic of ascending Stripmap and TOPS SAR acquisition modes. ϕ is the satellite heading, relative to north, and θ is the satellite look angle, relative to zenith. b) Illustration of antenna steering in the azimuth direction to produce the bursts in each sub-swath. Antenna is forward looking at time t=1, and backwards at t=2.

be a phase change that results from the difference in path length for a given pixel at a given elevation as seen from different locations. The phase change, which will follow the topography ($\Delta\phi_{topographic}$), can be accounted for by using a digital elevation model (DEM). The resolution of the DEM is often the limiting factor in the spatial resolution of InSAR.

Water vapour will change the refractive index of the atmosphere, increasing the radar path length, causing phase delays. These delays can be highly variable in space and time, and often have the same magnitude as the signal of interest [*Elliott et al.*, 2008; *Wadge et al.*, 2002; *Zebker et al.*, 1997]. Atmospheric delays can be particularly large in tropical regions (<10 cm), and problematic where they correlate with topography: time-varying atmospheric delays centred on a volcano can look like deformation [e.g., *Ebmeier et al.*, 2013; *Parker et al.*, 2015]. $\Delta\phi_{atmospheric}$ is a difficult source of noise to mitigate, although there are several approaches [e.g., *Yu et al.*, 2017a; *Bekaert et al.*, 2015; *Doin et al.*, 2009; *Elliott et al.*, 2008]. We explore methods to correct for or mitigate atmospheric delays using models in Chapter 4, and increasing signal-to-noise ratios through stacking in Chapters 4 and 5.

$\Delta\phi_{noise}$ describes the additional sources of noise, including random and instrument thermal noise. These contributions are usually much smaller in magnitude that the signal, and are thus ignored.

In addition to noise, loss of signal is a primary limitation of InSAR. Coherence, γ, is used as a measure of the correlation between the phase values of neighbouring pixels. Coherence is usually measured in 3 x 3 pixel windows, and where phase values are perfectly correlated the central pixel is said to have a coherence of 1. Incoherence describes the lack of relationship between the phase values of neighbouring pixels. The temporal and line-of-sight perpendicular spatial separation of the satellite between SAR acquisitions are described as the temporal and perpendicular baselines respectively. Large temporal and perpendicular baselines can result in a reduction in interferogram coherence as scatterers will scatter radiation differently from different incidence angles, and through time (e.g., vegetation growth, seasonal snow) [e.g., *Ebmeier et al.*, 2013; *Biggs et al.*, 2007; *Lu et al.*, 2002]. The radar wavelength will have a significant impact on coherence. Scattering will occur off objects whose size is comparable to the radar wavelength. As such, for short-wavelength radiation (e.g., X-band, 3.1 cm) foliage will be effective scatterers, and as foliage can vary greatly with time, X-band radar interferometry can have poor coherence (see Chapter 3). In contrast, L-band radar (23.5 cm wavelength, e.g., as acquired by ALOS-1 and ALOS-2) will scatter off larger objects, which tend to be more stable. The wavelength of a particular sensor will have a considerable influence over its suitability for a particular target.

1.5. Volcano and earthquake geodesy

1.5.1. Volcano geodesy

Volcanoes are the surface expression of the transition of heat from within the Earth to its surface, accompanied by the physical transport of material. Although a 'volcano' may describe the physical structure at the surface, volcanic, magmatic, and related processes occur throughout the subsurface, and all may be sources of deformation observable to InSAR.

Biggs et al. [2014] showed that there is a statistically significant relationship between volcano deformation and eruption. There are ∼1500 subaeariel Holocene volcanoes [*Siebert et al.*, 2010], of which InSAR has identified >200 with deformation [*Biggs and Pritchard*, 2017]. Cumulatively, from these studies we have observed and begun to understand magmatic storage and transportation processes on a range of spatial and temporal scales, across all tectonic environments. In the EARS alone, observations have been made of magma intrusion [*Toombs and Wadge*, 2012; *Biggs et al.*, 2009a; *Wright et al.*, 2006; *Amelung et al.*, 2000] and storage [*Biggs et al.*, 2009b, 2016], volcanic eruptions [*Xu et al.*, 2017; *Pagli et al.*, 2012; *Wauthier et al.*, 2012; *D'Oreye et al.*, 2008], subsidence from cooling, crystallisation and degassing [*Biggs et al.*, 2016], and hydrothermal processes [*Lloyd et al.*, 2018; *Hutchison et al.*, 2016]. In Chapter 3 I investigate prolonged magma reservoir growth at a caldera in the Main Ethiopian Rift, a process that has been observed elsewhere [*Le Mével et al.*, 2015; *Dzurisin et al.*, 2009], but is a first within the EARS.

1.5.2. Earthquake geodesy

InSAR has been utilised throughout the worlds highly straining regions to investigate faulting and the earthquake cycle [*Ingleby and Wright*, 2017; *Elliott et al.*, 2016; *Walters et al.*, 2011; *Reid*, 1910]. The tool has been used to respond to seismic events, by mapping surface ruptures and slip distributions [e.g., *Hamling et al.*, 2017; *Funning et al.*, 2005], as well as to build a picture of the crustal stress fields [e.g., *Walters et al.*, 2011; *Fialko*, 2006].

Rifting is partially achieved through faulting, and InSAR has provided valuable insights into amagmatic rifting within the EARS (Figure 1.4). InSAR is an ideal tool for investigating earthquakes as it can accurately determine the earthquake location [*Funning and Garcia*, 2017; *Weston et al.*, 2011], and, together with seismology, is an ideal dataset to determine the fault properties (e.g., length, strike, dip).

1.5.3. Modelling of geodetic data

InSAR provides a means to observe volcanic and tectonic signals, but it is only through models that we are able to relate observations to processes and gain understanding of causative mechanisms. Modelling involves two important considerations: the first is whether a model is suitable, and the second is how one determines the parameters of the model.

Modelling approaches can broadly be categorised as analytical or numerical. Analytical models are usually simple mathematical approximations [e.g., *Yang et al.*, 1988; *McTigue*, 1987; *Okada*, 1985; *Mogi*, 1958], and have been highly successful at reproducing observations [e.g., *Segall*, 2005; *Biggs et al.*, 2010b, 2009a; *Funning et al.*, 2005]. The difficulty in these models is how they should be interpreted in relation to reality, and their inability to fully explain complex systems. Numerical models, on the other hand, are able to introduce complexity when details on the subsurface are known [e.g., *Hickey et al.*, 2013], but with this there is an increase in non-uniqueness.

Commonly used analytical models include the Okada rectangular dislocation [*Okada*, 1985], and Mogi point source models [*Mogi*, 1958] (Figure 1.6). Embedded in a homogeneous, isotropic, elastic half-space they are used as mathematical descriptions of a sill, dyke, or fault, and magma chamber respectively. A Mogi model represents volume or pressure changes in the subsurface, and Figure 1.6a shows the model geometry, and relation between a source at $(0,0,-d)$ and observations at $(x,y,0)$. As a point source, Mogi models are only valid where the source radius (a) is much smaller than its depth (d). Okada models approximate sills, dykes, and faults as planes since their lengths and widths are orders of magnitude greater than their thicknesses. Figure 1.6b shows the key parameters of an Okada model. The displacement field of an Okada model is a function of tensile (op) and shear (down dip and along strike, ds and ss respectively) dislocations.

The parameters that describe a model can be found through either forward, or inverse modelling [*Tarantola*, 2005]. Forward modelling involves generating the response of pre-determined model parameters to compare to observations. Alternatively, inverse modelling uses the data to solve for the parameters of a model. Throughout this thesis I utilise an inverse approach to solve for the model parameters of the Okada and Mogi models, given their superiority over forward models in exploring the parameter space, providing estimates of model uncertainty, and considering model non-uniqueness [*González et al.*, 2015; *Hooper et al.*, 2013; *Mosegaard and Tarantola*, 1995].

Inverse problems can be linear or non-linear, and discrete or continuous. Linear discrete inverse problems are those that can be described through a linear system of equations

(Equation 1.2), where $\mathbf{d}$ is a matrix of observations, $\mathbf{m}$ is a matrix of unknown model parameters, and $\mathbf{G}$ is the design matrix that maps the data to the model.

$$\mathbf{d} = \mathbf{G}\mathbf{m} \tag{1.2}$$

Linear discrete inverse problems, in the absence of measurement error, where $\mathbf{G}$ is square and invertible, can be solved easily by rearranging for the unknown model parameters $\mathbf{m}$ (Equation 1.3), to give a unique solution.

$$\mathbf{m} = (\mathbf{G}^T\mathbf{G})^{-1}\mathbf{G}^T\mathbf{d} \tag{1.3}$$

Non-linear inverse problems are those where $\mathbf{G}$ is a function of $\mathbf{m}$ such that it cannot be formulated to linearly map $\mathbf{m}$ to $\mathbf{d}$. Continuous inverse problems describe the situation where $\mathbf{m}$ is a function of another variable. Many inverse problems, however, are non-unique, and there will be multiple sets of model parameters that describe the data equally well. Non-uniqueness arises from insufficient sampling of the model space, an infinite number of model parameters, or measurement errors. Non-unique inverse problems can be solved through an optimisation approach.

When interpreting the results of non-unique or poorly constrained inverse problems, it is useful to have confidence intervals for the values of the model parameters. This can be achieved through a Bayesian approach. Bayes' theorem relates what is known before the inversion, *a priori* probabilities of the model parameters, and the fit of the model to the data (the model likelihood), to a posterior probability for a set of model parameters. The goal of an inverse problem formulated in this way is to find the model parameters that maximise the likelihood function.

For a Bayesian inverse problem the initial set of model parameters and associated *a priori* probabilities are pre-defined. These are then used to generate a likelihood for that model. The product of the *a priori* probabilities and model likelihood is proportional to the parameters posterior probability, which becomes the new prior probability density function. The subsequent prior probability distributions can be iteratively sampled to draw the next estimate of the model parameters through the use of an appropriate approach, such as a Markov chain Monte Carlo algorithm, which takes a random walk though the model space. For each iteratively drawn set of model parameters an acceptance/rejection criteria is set based on the model likelihood such that the inversion will begin to converge on the most likely solution. The final posterior probability density function gives the full joint posterior probabilities for all model parameters. The marginal posterior probability density function for each parameter then provides confidence bounds, taking into account likely variations in the other model parameters.

For a more detailed description of inverse problems the reader is referred to *Backus and Gilbert* [1970] and *Tarantola* [2005].

1.6. Thesis structure

This thesis investigates magmatic and amagmatic rifting, primarily using observations of surface deformation measured using InSAR. Where possible, I combine InSAR observations with other datasets to better constrain or confirm signals. We focus on three locations: the Corbetti caldera (Ethiopia), southern Mozambique, and central Botswana. In Ethiopia magma has a significant role in rifting, whereas, in contrast, rifting in Mozambique is accommodated exclusively via faulting. The earthquake in Botswana represents faulting in an extensional stress regime, but in an apparent intra-plate setting. Comparing and contrasting observations from these locations, therefore, allows me to draw comparisons between incipient and mature continental rifting, particularly focussing on the role of crustal heterogeneities.

In **Chapter 2** I investigate the role of crustal heterogeneities on shallow crustal processes at the Corbetti caldera. I use geomorphological observations (caldera geometry and vent locations), the distribution of seismicity, shear-wave splitting measurements, and surface deformation (2007 – 2009) to show that a large pre-rift cross-rift fault structure has influenced crustal magma transport and storage, and shallow hydrothermal circulation. This chapter has previously been published in *Earth and Planetary Science Letters*.

Chapter 3 builds on this work at Corbetti, providing the first observations of a prolonged magma reservoir growth episode in the East African Rift. We document inflation at the caldera, that began mid-2009 and is ongoing at the time of writing, at a vertical rate of 7 cm/yr. Through a joint inversion of InSAR and GPS data we test different analytical model source geometries, and find a point source with a volume change of 1.0 x 10^7 m^3/yr at ~6.6 km depth provides the most statistically justified fit. This source is spatially co-incident with a conductive anomaly, derived from magnetotelluric observations, and lies along the cross-caldera structure we discuss in Chapter 2. We ascertain the source is likely magmatic, and comment on the reservoir architecture, magma flux, and eruption potential of Corbetti. This chapter is published in *Journal of Geophysical Research: Solid Earth*, and has contributed towards a further submission that is currently under review with *Nature Geoscience*.

Chapter 4 investigates the role of pre-existing structures in an incipient rift environment. I analyse the surface deformation caused by the 2016 M_w 5.6 Mozambique earthquake, in comparison to a reanalysis of the nearby 2006 M_w 7.0 high angle normal faulting Machaze earthquake. I invert for uniform and distributed slip models of the earthquake, relating the two events through static stress transfer. We determine that the

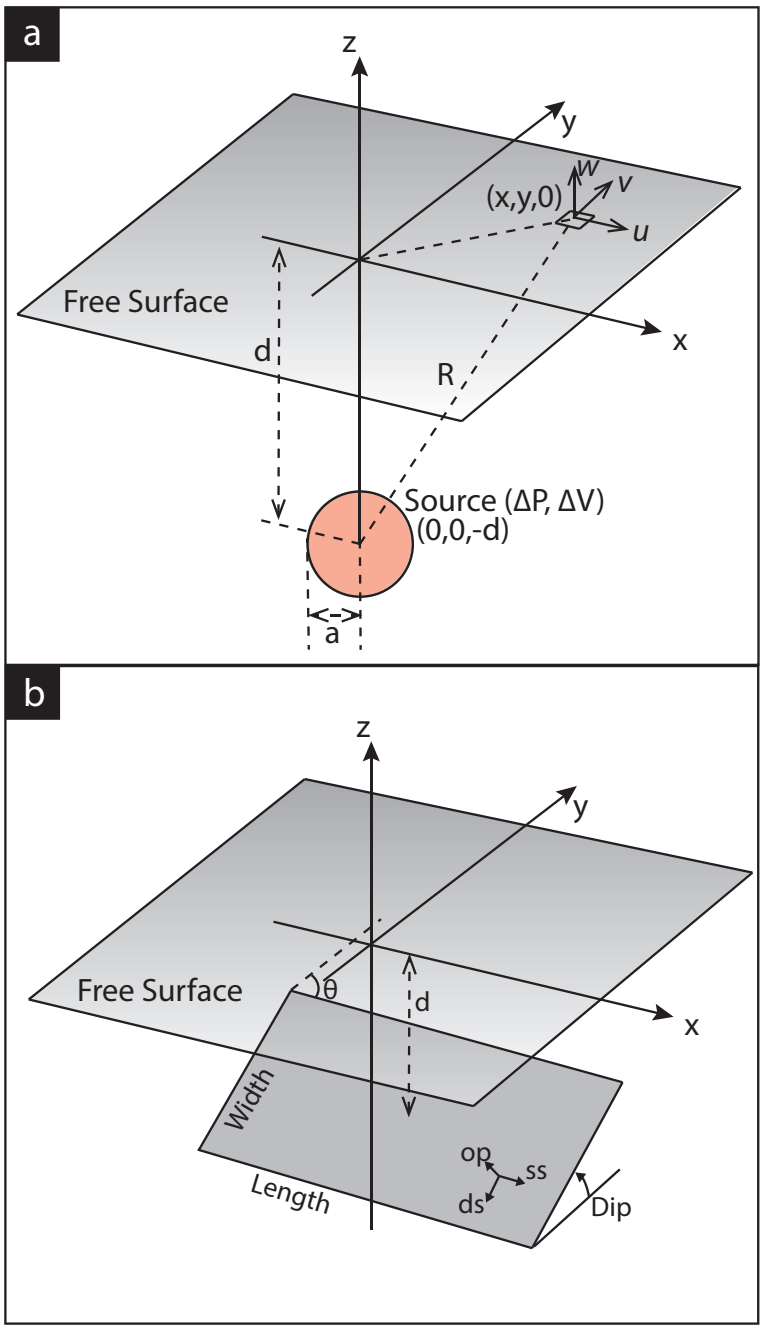

Figure 1.6: a) Geometry and physical parameters of the Mogi model beneath a free surface [*Mogi*, 1958]. Where d is the source depth, a is the source radius, and R the radial distance between the source and surface observations at $(x, y, 0)$. A pressure (ΔP) or volume change (ΔV) of the source results in surface displacements (u, v, w). b) Okada rectangular dislocation model, with a given length, width, dip, and strike (θ), at a depth d [*Okada*, 1985]. *Op*, *ss*, and *ds* correspond to tensile, strike slip, and dip slip components respectively. Modified from *Segall* [2005].

2016 earthquake is an aftershock of the 2006 event, indicating that in low strain regions elevated seismic hazard continues after the main shock for potentially decades. This chapter is currently under review for publication in *Geophysical Journal International*.

Chapter 5 is a study of the co-seismic displacements of the M_w 6.5 April 2017 Moiyabana earthquake (Botswana). This earthquake occurred hundreds of kilometres from the nearest clear expression of extension at the surface, and thus represents a rare opportunity to investigate the local stress regime, and intra-plate earthquakes. The earthquake occurred >20 km deep, providing a normal faulting example of the ambiguity in determining the focal plane from surface observations. Using ascending and descending interferograms, a Bayesian inversion methodology, and typical fault scaling relationships I determine the earthquake likely occurred on a north-east dipping pre-existing structure, in response to far-field stresses that are likely influenced by crustal heterogeneities.

Chapter 2

Evidence for cross rift structural controls on deformation and seismicity at a continental rift caldera

Lloyd, R., J. Biggs, M. Wilks, A. Nowacki, J. Michael Kendall, A. Ayele, E. Lewi, and H. Eysteinsson (2018), Evidence for cross rift structural controls on deformation and seismicity at a continental rift caldera, *Earth and Planetary Science Letters*, *487*, 190 – 200.

Author contributions and declaration:

Supervision was provided by J. Biggs. M. Wilks processed the seismic data, supervised by J.-M. Kendall, and helped write the seismic processing methods. A. Nowacki processed and interpreted the seismic anisotropy data, and wrote the section describing the seismic anisotropy methods. A. Ayele helped facilitate the seismology fieldwork. H. Eysteinsson acquired and processed the magnetotelluric data. ENVISAT data are available from the European Space Agency (ESA). ALOS data were provided through an ESA third party mission. Seismic data were acquired as part of the Aluto Research and Geophysical Observations (ARGOS) project, and are available from the Incorporated Research Institutions for Seismology (http://iris.edu) under the temporary network code XM.

Abstract

In continental rifts structural heterogeneities, such as pre-existing faults and foliations, are thought to influence shallow crustal processes, particularly the formation of rift faults, magma reservoirs, and surface volcanism. We focus on the Corbetti caldera, in the southern central Main Ethiopian Rift. We measure the surface deformation between 22^{nd} June 2007 and 25^{th} March 2009 using ALOS and ENVISAT SAR interferograms and observe a semi-circular pattern of deformation bounded by a sharp linear feature cross-cutting the caldera, coincident with the caldera long axis. The signal reverses in sign but is not seasonal: from June to December 2007 the region south of this structure moves upwards 3 cm relative to the north, while from December 2007 until November 2008 it subsides by 2 cm. Comparison of data taken from two different satellite look directions show that the displacement is primarily vertical. We discuss potential mechanisms and conclude that this deformation is associated with pressure changes within a shallow (<1 km) fault-bounded hydrothermal reservoir prior to the onset of a phase of caldera-wide uplift.

Analysis of the distribution of post-caldera vents and cones inside the caldera shows their locations are statistically consistent with this fault structure, indicating that the fault has also controlled the migration of magma from a reservoir to the surface over tens of thousands of years. Spatial patterns of seismicity are consistent with a cross rift structure that extends outside the caldera and to a depth of ∼30 km, and patterns of seismic anisotropy suggests stress partitioning occurs across the structure. We discuss the possible nature of this structure, and conclude that it is most likely associated with the Goba-Bonga lineament, which cross-cuts and pre-dates the current rift. Our observations show that pre-rift structures play an important role in magma transport and shallow hydrothermal processes, and therefore they should not be neglected when discussing these processes.

2.1. Introduction

The pathway taken by rising magma is influenced by local and regional stresses [e.g., *Maccaferri et al.*, 2014] and lithological and/or rheological boundaries [e.g., *Taisne and Tait*, 2011]. In old continental crust in particular, heterogeneities and structures, such as faults and lithological contrasts, are widespread, and they can strongly influence the location and geometry of magma reservoirs [e.g., *Le Corvec et al.*, 2013]. The roles of these competing factors have been demonstrated at many volcanoes. For example, calderas in the Kenyan Rift align with inherited structures [*Robertson et al.*, 2016], while at Fernandina volcano in the Galápagos, the eruption patterns are controlled by active stress fields [*Bagnardi et al.*, 2013]. In other cases, however, the relative importance of stress versus heterogeneities remains poorly understood [e.g., *Saxby et al.*, 2016; *Marti and Gudmundsson*, 2000].

Here we investigate the structural controls on magmatism and hydrothermal processes at one of the Main Ethiopian Rift calderas, Corbetti. Insights come from geodetic (e.g., Interferometric Synthetic Aperture Radar) data, from which we identify a well defined region of deformation within the caldera, which appears to be structurally bounded by a cross-cutting structure. We perform an analysis of the caldera geometry and the distribution of post-caldera volcanism, which indicate a coincidence between this structure, the caldera long axis, and the alignment of volcanic vents. Our observations are further supported by magnetotelluric interpretations of a large structure that cross-cuts the caldera and seismic data which identifies the structure to the east, where it extends down to ∼30 km through the crust. Seismic anisotropy measurements also indicate a concentration of stress along the structure cross-cutting the caldera, and show that stress perturbations are largest where the greatest surface deformation is observed. We discuss the potential sources which may have caused the deformation (magma, hydrothermal fluids, or meteoric water), and possible interpretations for this structure, including a pre-rift fault system, the edge of older solidified intrusions, or the rim of a Pleistocene caldera.

2.2. Background

2.2.1. The East African Rift

The East African Rift system (EARS) is a ∼4,000 km long continental rift which defines the boundary between the Somalian and Nubian tectonic plates. Rifting occurs through a combination of magmatic and tectonic processes, and inherited structures and fabrics influence where and how this extension is accommodated [e.g., *McConnell*, 1972].

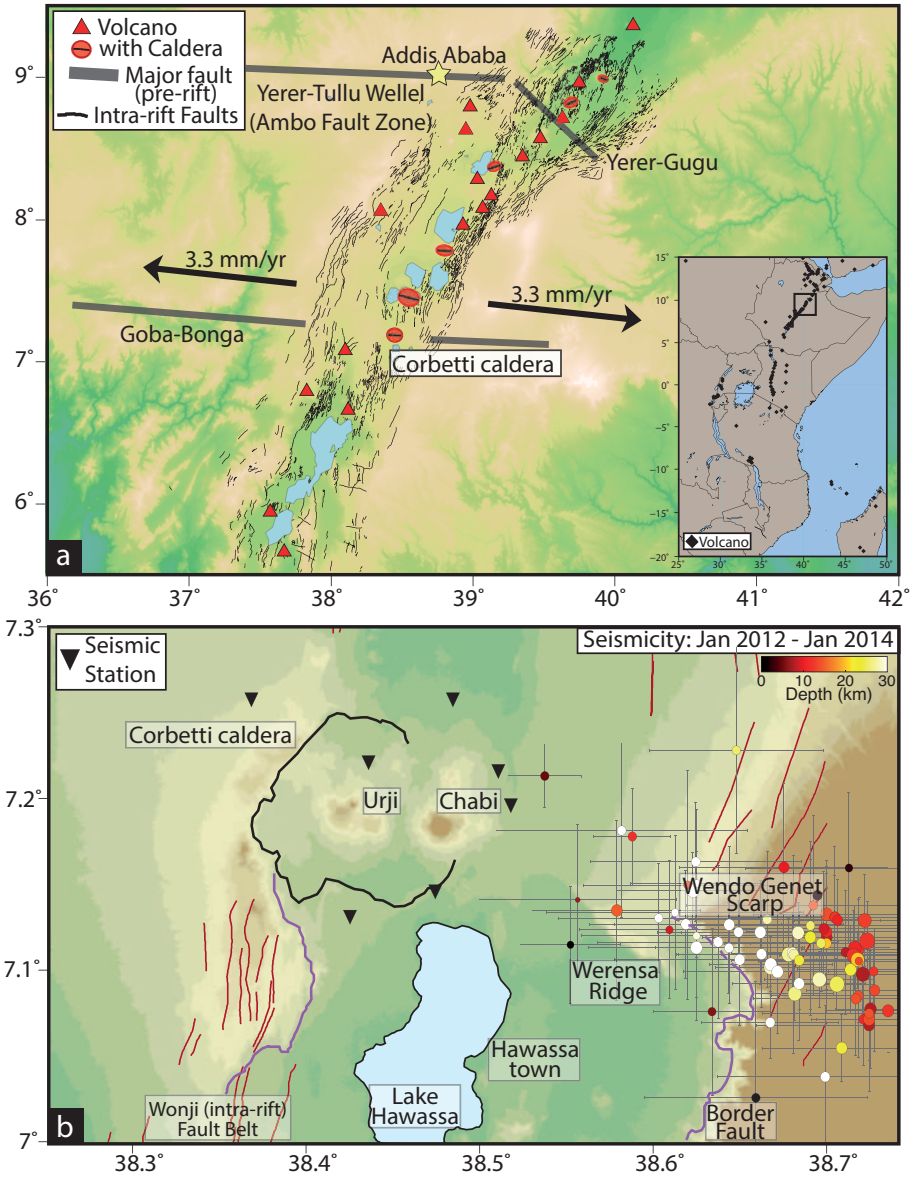

Figure 2.1: a) The Main Ethiopian Rift, with East Africa as inset. Red ellipses: rift calderas, scaled according to size and orientation of caldera rim fault after *Wadge et al.* [2016]. Red triangles: non-caldera volcanoes. Black lines: intra-rift faults [*Agostini et al.*, 2011]. Spreading direction from *Stamps et al.* [2008]. Yellow star: Addis Ababa. b) Corbetti caldera and surrounding region, showing the Wonji faults (red), Wendo Genet Scarp, Werensa Ridge and hypothesised Hawassa caldera (purple line). The seismicity associated with the Wendo Genet Scarp is also shown (71 events with lateral uncertainty <10 km, recorded between January 2012 and January 2014) [*Wilks*, 2016].

The Main Ethiopian Rift (MER) is the northernmost part of the EARS, and is an example of mature continental rifting [*Chorowicz*, 2005]. There are several Quaternary major silicic volcanic system in the MER, some of which have been observed deforming in recent decades: Corbetti, Bora, Haledebi, and Aluto [*Hutchison et al.*, 2016; *Biggs et al.*, 2009b]. The most recent MER eruptions were at Tullu Moje (syn. Bora) in 1900, at Kone (syn. Gariboldi) in ∼1820, and in ∼1810 at Fantale (*Wadge et al.* [2016] and references therein). It has been suggested that the large silicic centres lie at the termini of magmatic segments [*Keranen et al.*, 2004; *Ebinger and Casey*, 2001], where reduced extensional stresses facilitate longer residence times, favouring the development of silicic bodies through fractional crystallisation [*Hutchison et al.*, 2015b; *Peccerillo*, 2003]. However, several centres lie along pre-rift rift oblique faults, for example the elliptical calderas Kone, Gedemsa, and Fentale [*Acocella et al.*, 2002]. An alternative mechanism for the formation of silicic centres is that reactivation of transtensional faults create regions of localised extension, focussing rising magma, and promoting magma reservoir formation [*Holohan et al.*, 2005; *Acocella et al.*, 2002]. Near the Aluto caldera rhombic faulting of the border faults is associated with a pre-existing rift-oblique lithospheric weakness and sinistral oblique crustal shear [*Corti*, 2009; *Boccaletti et al.*, 1998].

2.2.2. Corbetti caldera

The Corbetti caldera, in the southern MER, is the southernmost silicic centre along the MER (Figure 2.1); further south the rift transitions to diffuse faulting and magmatism [*Philippon et al.*, 2014; *Corti*, 2009]. The caldera formed at 182 ± 18 ka, and is one of the largest in the EARS, measuring ∼10 by 15 km [*Hutchison et al.*, 2015b]. The caldera scarp height is greatest to the west (∼200 m), and diminishes in height to the east, where it is unidentifiable. Corbetti is surrounded by agricultural land and is located within 15 km of two major population centres: Hawassa and Shashemene (∼400,000 people within 25 km^2).

There are two major centres of resurgent volcanism within the caldera: Urji (syn. Wendo Koshe) and Chabi, which have both erupted aphyric pantellerites. Urji, the western peak, has fall and flow pumice deposits, illustrative of high explosivity. Chabi, by contrast, is composed of obsidian flows, indicative of more effusive eruptions [*Rapprich et al.*, 2016]. Numerous thick fall deposits and obsidian flows indicate several eruptions have occurred at Corbetti since caldera formation. Tephra from the most recent Plinian eruption at Urji has been dated at 396 ± 38 BC [*Rapprich et al.*, 2016], and at least four obsidian flows post-date this.

Magnetotelluric (MT) measurements and transient electromagnetic method soundings show a sharp resistivity gradient along the caldera long axis [*Gíslason et al.*, 2015]; the

north being more resistive than the south. This resistivity contrast is present in the upper 2 km, and >8 km below sea level. The shallow component of the feature is interpreted to reflect the vertical migration of hydrothermal fluids from depth, which then become entrained in the northward local groundwater gradient. The deeper feature is attributed to a magma body [*Gíslason et al.*, 2015].

2.3. Surface deformation

2.3.1. Interferogram processing

Interferometric Synthetic Aperture Radar (InSAR) is a space-based remote sensing technique, used to measure deformation of the Earth's surface [*Massonnet and Feigl*, 1998]. InSAR uses the difference in the phase component of two radar images, acquired from approximately the same location but at different times, to produce an interferogram. We use SAR data from two satellites, ENVISAT (Image and Wide Swath modes) and ALOS, from between 2007 and 2009 to produce 75 interferograms (Table 2.1).

ENVISAT Wide Swath (WS) interferograms were processed using the GAMMA software package [*Werner et al.*, 2000]. We used 19 scenes from ascending track 386 between October 2006 and August 2008. Interferogram selection was based on image pairs with perpendicular baselines less than 150 m and temporal baselines less than 200 days (Figure A.1). Interferograms with insufficient coherence and those unconnected to the network were then removed, leaving 20 interferograms (Table A.1). We removed topographic phase contributions using a 30 m DEM [*Farr and Kobrick*, 2000], and filtered the interferograms using a non-linear spectral filter [*Goldstein and Werner*, 1998], once with strength 0.8, and again with strength 0.6. Unwrapping was then done using the SNAPHU Minimum Cost Flow (MCF) algorithm with pixels with coherence less than 0.6 masked out [*Chen and Zebker*, 2001].

We processed data from ALOS, an L-band (23.6 cm wavelength) JAXA (Japanese Aerospace Exploration Agency) SAR satellite, using ISCE (InSAR Scientific Computing Environment) [*Rosen et al.*, 2012]. We used 5 acquisitions between June 2007 and December 2008 from ascending Fine Beam track 605 to produce 10 interferograms. Interferogram selection was made based on perpendicular baselines less than 500 m and temporal baselines less than 730 days (Figure A.1). Topographic phase contributions were removed using a 30 m DEM, and interferograms were resampled to 90 m. Each interferogram was then filtered twice (strength 0.4), before being unwrapped using the SNAPHU MCF algorithm, with unwrapping threshold of 0.1 [*Chen and Zebker*, 2001].

ENVISAT Image Mode (IM) data were processed using ISCE [*Rosen et al.*, 2012]. We used 10 Image Mode acquisitions from descending track 321 between October 2007 and March 2009 to produce 45 interferograms. Interferogram selection was based on image pairs with perpendicular baselines less than 800 m and temporal baselines less than 600 days (Figure A.1). Interferograms whose coherence does not extend across the caldera were excluded, to leave 28 (Table A.1). Topographic phase contributions were removed using a 30 m DEM [*Farr and Kobrick*, 2000], after which pixels were multilooked to 120 m to increase coherence and reduce noise. We filter the interferograms using a non-linear spectral filter with strength 0.8 [*Goldstein and Werner*, 1998]. Interferograms were then unwrapped using the SNAPHU MCF algorithm with an unwrapping threshold of 0.1 [*Chen and Zebker*, 2001]. Interferograms from all sensors were de-ramped where necessary.

We choose not to apply atmospheric corrections to our dataset as Corbetti has gentle, low topography (∼200 m), there are very few input data for weather models for East Africa, and the available atmospheric corrections are unable to match any turbulent signals in the data [*Doin et al.*, 2009].

2.3.2. Surface deformation results

The ENVISAT IM data provides the clearest measure of the extent of the signal in the southern portion of Corbetti; it clearly shows a circular minor segment shape, with a sharp northern boundary (Figure 2.2g–l). The ENVISAT IM interferograms start in October 2007, and measure ∼1 cm of range increase between December 2007 and August 2008. The coherence was limited to the Chabi obsidian flows and an area west of the caldera that is not farmed.

The ALOS interferograms from June 2007 to December 2008 confirm the observation from the Envisat IM data, but span a longer time period, showing two distinct periods of deformation (Figure 2.2c–f). The first, from June 2007 to December 2007, is a period of range decrease of ∼2.5 cm in the southern portion of the caldera, with the same spatial pattern as in the ENVISAT WS data (Figure 2.2b–f). Interferograms post-December 2007 show range increase in the same region, totalling ∼1.5 cm by December 2008 (Figure 2.2e–l). The ALOS interferograms are the most coherent, illustrating the value of L-band InSAR for investigating ground deformation of arable land. However, ALOS interferograms with acquisitions on certain dates were affected by strong phase ramps, possibly due to orbital errors or, ionospheric or atmospheric delays, but de-ramping was able to account for this well on a local scale (Figure A.2).

The ENVISAT WS interferograms represent the earliest measures of ground deformation

Table 2.1: Summary of the sensors and associated parameters used in Chapter 2.

Satellite	Mode	Observation period	Wavelength (cm)	Orbit	Number of scenes	Heading angle (°)	Look angle (°)
ENVISAT	Wide Swath (WS)	Oct 2006 – April 2008	5.6 (C-band)	Ascending	19	-12	21
ALOS	Fine Beam	June 2007 – Dec 2008	23.6 (L-band)	Ascending	5	-12	40
ENVISAT	Image Mode (IM)	Oct 2007 – March 2009	5.6 (C-band)	Descending	10	-167	22

in our analysis and show that prior to July 2007 there was no significant deformation at Corbetti (Figure 2.2a). After July 2007, a north-south range change gradient of ∼2 cm over 2 km can be seen across the caldera, consistent with other observations (Figure 2.2b). However, for the C-band WS data, coherence is limited to the Chabi obsidian flows in most interferograms.

2.3.3. Displacement direction

Using interferograms from ascending and descending tracks, which have different LOS vectors but measure the same signal, the vertical (U_u) and east-west (U_e) components of deformation can be estimated. The sensitivity to deformation N-S is poor however [e.g., *Wright et al.*, 2004]. We therefore formulate our equations making the assumption that this component of range change is zero. Mathematically, the range change observed by a satellite can be described by $\mathbf{r} = \hat{\mathbf{p}}.\mathbf{u}$, where $\hat{\mathbf{p}}$ is the unit vector (p_e, p_n, p_u), pointing from the satellite to the ground in the local east, north and up directions, and $\mathbf{u}$ is the column vector of the components of displacement in the same reference frame, (u_e, u_n, u_u)^T.

This approach relies on the assumption that the ascending and descending images measure the same signal, which in the case of time-varying signals require them to have been acquired contemporaneously. To reflect this we selected interferograms with acquisitions close in time; the 26/12/2007 – 10/12/2008 descending ENVISAT and 23/12/2007 – 25/12/2008 ascending ALOS interferograms.

Decomposition of ascending and descending InSAR images into vertical and east-west components indicates the deformation in the south of the caldera between December 2007 and December 2008 is roughly vertical and ∼2 cm in magnitude (Figure 2.3). The east-west component of this deformation shows some features of a similar magnitude, but their spatial extent is inconsistent with the signal seen elsewhere, and so are likely to be atmospheric artefacts. The deforming area in this ALOS interferogram includes a region of atmospheric delay, and contains some short wavelength features north of the caldera. Since the area that deforms in this period is the same as during June 2007 to December 2007, we assume that the uplift is also vertical.

2.3.4. Displacement time series

An individual interferogram records the satellite-ground range change between two acquisitions which are separated in time. To construct a time series of deformation

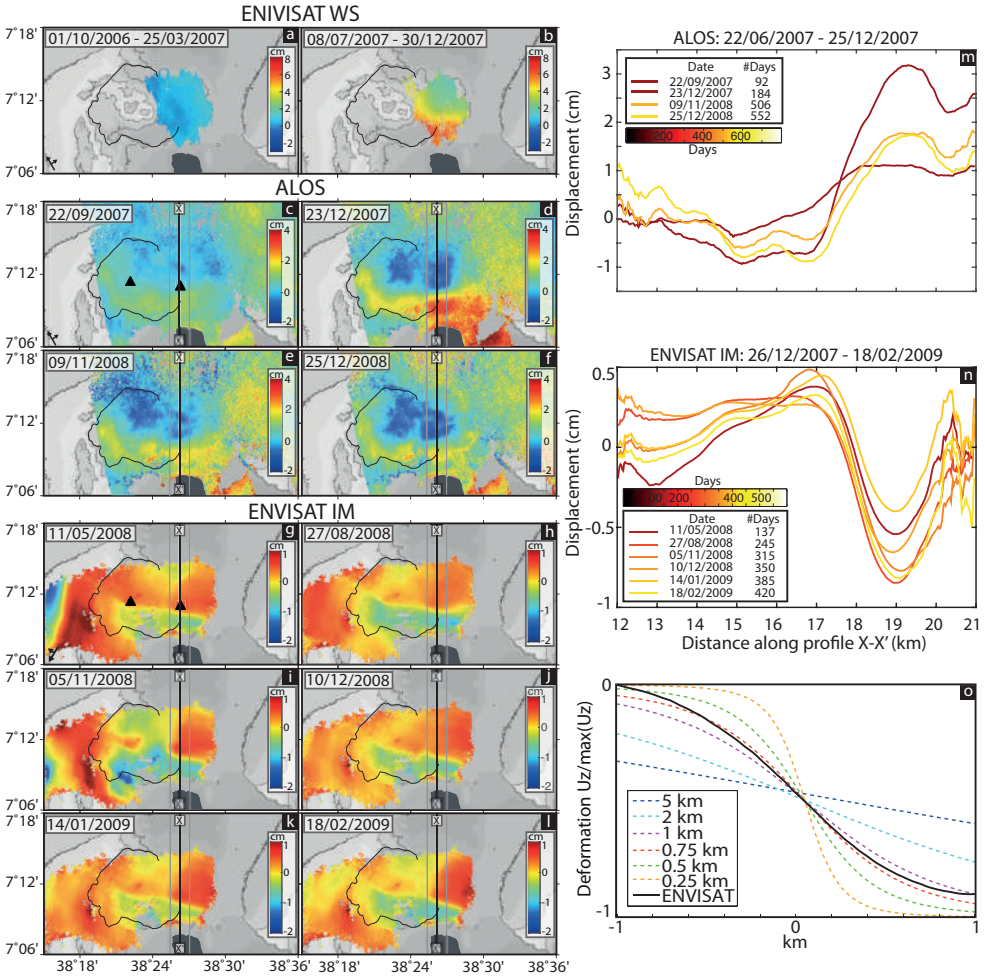

Figure 2.2: a) ENVISAT Wide Swath interferograms showing no deformation between 01/10/2006 – 25/03/2007. b) North-south deformation gradient across the caldera 08/07/2007 – 30/12/2007. c–f) Cumulative displacement between 22/06/2007 – 25/12/2008, derived from ALOS interferograms showing the initial phase of uplift, and subsequent subsidence. g–l) Cumulative displacement between 26/12/2007 – 18/02/2009, as derived from descending ENVISAT IM interferograms. These ENVISAT interferograms capture the subsidence and subsequent uplift. m) Profiles show the deformation along the line X-X' for the ALOS data. Each line is coloured by date, as labelled. Typical mean standard error calculated from across 600 m either side of the line X-X' is 0.2 mm. n) Same as (m), for ENVISAT IM data. o) 2 km Profiles of deformation across the edge of a sill for different sill depths. The solid black line is a profile through the cumulative displacement of ENVISAT IM data between 26/12/2007 – 27/08/2008, reproduced from (n).

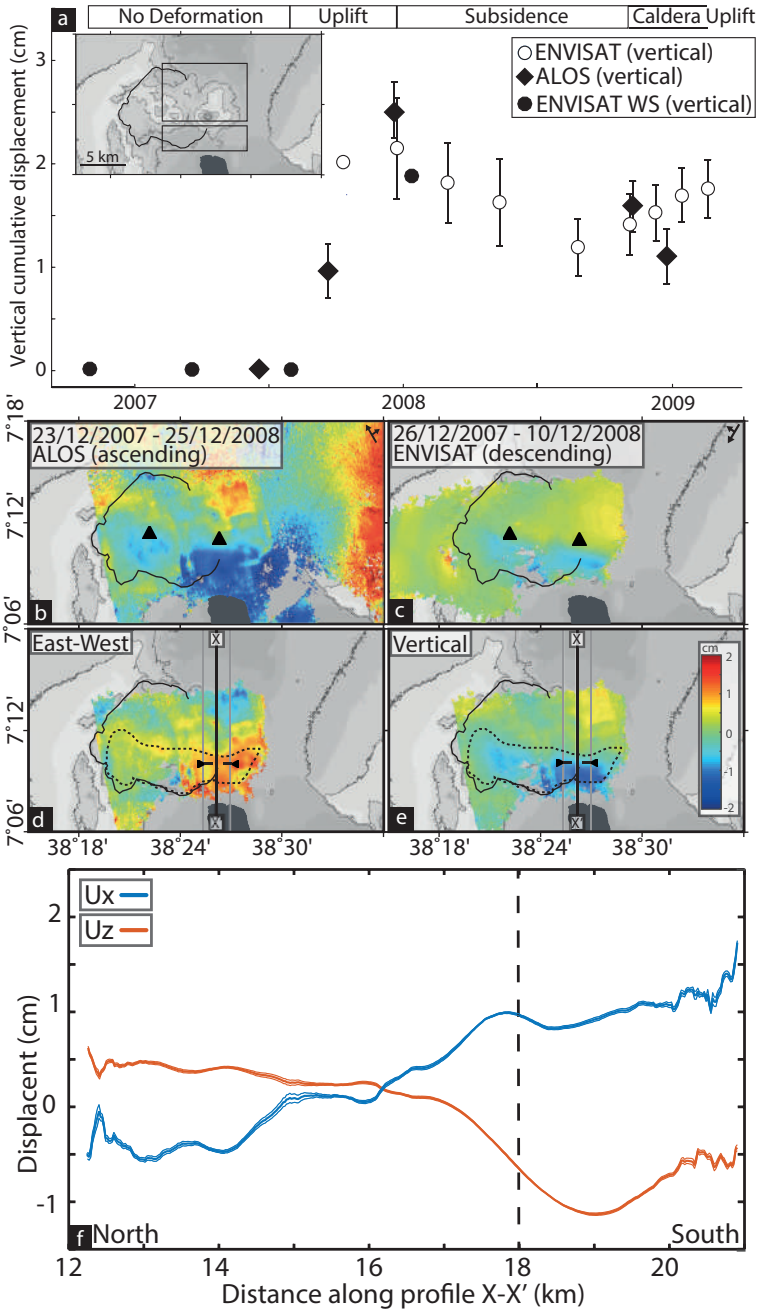

Figure 2.3: a) Time series of deformation from ENVISAT Image Mode, ENVISAT Wide Swath Mode and ALOS data. A map of Corbetti is included as an inset to show the regions between which this relative motion is calculated (southern relative to northern rectangle). b–c) ALOS and ENVISAT interferograms, between December 2007 and December 2008, used to determine the east-west (positive east) and vertical (positive up) components of deformation. d–e) east-west and vertical components of deformation. The dashed line shows the extent of the signal, identified in Figure 2.2h. f) Profile along X-X' through east-west and vertical deformation. Dashed line corresponds to location between triangle markers on X-X', indicating the deformation gradient.

we used the SBAS (short baseline subset) method of *Berardino et al.* [2002]. The displacement during incremental time steps is found from the vector of line-of-sight (LOS) displacements for each given pixel through a design matrix constructed to take into account the timespan of each interferogram. The cumulative displacement between any two dates can then be found by summing the relevant incremental displacements. This linear discrete inverse problem is under-constrained, and following *Berardino et al.* [2002] we use singular value decomposition, normalised using the L2 norm constraint. We applied a bootstrapping test and found our signal is not dependant on any particular satellite image, and therefore robust [e.g., *Ebmeier et al.*, 2013].

Each interferogram provides relative phase changes, and for our time series analysis we considered the relative displacement between a northern (fixed) and southern portion of the caldera, averaged over ∼125 km^2 and 38 km^2 respectively. The uncertainty in our time series analysis is based on the mean variance in each dataset within 10 km^2 away from the caldera, where possible (∼0.79 – 0.84 cm). This is comparable to theoretical estimates of the variance of atmospheric noise over short length scales (∼10 km) from *Emardson et al.* [2003], which is 0.8 cm for any individual acquisition.

Figure 2.3 shows the result of time series analysis from all three InSAR datasets. Following our component analysis, we projected the LOS displacement into the vertical to better compare datasets with different LOS vectors. Individual WS interferograms indicate the absence of signal at Corbetti between October 2006 and July 2007 (Figure 2.2a). The cumulative range change derived from the ALOS data (Figures 2.2 and 2.3) shows 2.5 ± 0.3 cm of range decrease of the southern portion of the caldera at this time, consistent with individual WS interferograms (Figure 2.2a–l). The time series analysis shows that in December 2007 the range change reverses in sign. ENVISAT IM and ALOS data (Figure 2.2c–l) show 1.0 ± 0.3 cm and 1.4 ± 0.3 cm of range increase over ∼8 and 12 months respectively.

The spatial extent of the deformation can be seen in Figure 2.2b–l. Profiles though the region indicate that the northern edge of the signal is sharp; occurring over ∼2 km, and is co-incident with the caldera long axis (Figure 2.2m–n). Figure 2.2g–l shows that the signal is contained within the caldera to the west, but extends outside to the east. For some time-steps (e.g., ENVISAT IM displacement 27/08/2008 – 05/11/2008) the signal appears to extend into the northern portion of the caldera, but we attribute this to atmospheric artefacts based on pair-wise analysis.

2.3.5. Source modelling

To estimate the depth of a source that could cause a signal with such a sharp northern boundary, we forward model the deformation using a horizontal Okada rectangular dislocation model [*Okada*, 1985]. The gradient of the deformation is a first-order indication of source depth, as shallow sources produce sharp edges, while deformation from deeper sources is smoothed by the elastic crust. We do not attempt to eliminate the possibility of an additional deeper source, but use the rectangular dislocation to produce a step-function at depth and hence estimate the maximum depth to the shallowest part of the deformation source. We plot profiles of deformation caused by a sill at depths of 5, 2, 1, 0.75, 0.5 and 0.25 km, normalised based on peak deformation. The modelled sill has a length (100 km), much greater than the kilometre length scale we are interested in, to ensure the shape of the deformation we observe is a result of a single sill edge only. We find that for peak-to-peak deformation to be contained within 2 km, a rectangular dislocation must be less than 0.75 km below the surface (Figure 2.2o). For a 1 km depth, 90% of the deformation is contained within 2 km. A source with a tapered slip distribution would need to be shallower to produce the same deformation gradient. In this experiment we do not consider the interaction between the source and the fault, but we may expect source-fault interaction to amplify the deformation gradient, resulting in an underestimation of the source depth [e.g., *Folch and Gottsmann*, 2006].

2.3.6. Deformation mechanisms

Surface deformation occurs as a result of changes in volume or pressure in the subsurface. There are three possible sources that may have caused the deformation at Corbetti: magma, hydrothermal fluids, or meteoric water.

The sharpness of the northern boundary of the deformation implies that the source is shallow ($\sim$1 km) (see Section 2.3.5) [*Finnegan et al.*, 2008]. The presence of magma at such shallow depths would result in surface manifestations, such as changes in fumarolic behaviour, possible phreatic or phreatomagmatic eruptions from interaction with meteoric water, changes in groundwater chemistry, or felt seismicity, which have not been reported [e.g., *Jay et al.*, 2013; *Wicks*, 2002].

Perturbations in pore fluid pressure associated with hydrothermal circulation can also result in surface deformation [e.g., *Chaussard and Amelung*, 2014; *Finnegan et al.*, 2008], thus it is important to consider coupled hydrothermal and magmatic systems when interpreting deformation at volcanoes with well developed hydrothermal systems. Pore fluid pressure changes can be driven by increased heat or fluid entering the system, or changes to fracture networks in response to subsurface stress changes [e.g., *Rowland*

and Sibson, 2004; *Bonafede*, 1991]. The response to these pressure changes can be either elastic, caused by seasonal rainfall variability, or inelastic, such as non-recoverable aquifer compaction [e.g., *Lanari et al.*, 2004].

The MER and adjacent highlands have highly variable rainfall, which could cause seasonal deformation of shallow aquifers [*Birhanu and Bendick*, 2015]. However, the ENVISAT Wide Swath data shows no deformation between October 2006 and March 2007, indicating that the signal is not part of ongoing seasonal variations, and so is unlikely to be hydrological in nature as this time period covers the April-May rainy season.

We therefore propose that the deformation is related to perturbations in the hydrothermal system, caused by an increased flux of water or heat in response to deeper magmatic processes. An increased flux would result in a pressure and/or temperature increase in the hydrothermal reservoir, causing a volume increase and therefore uplift (Figure 2.4a) [e.g., *Miller et al.*, 2017]. The overpressure then diffused away, possibly by the breaching of a barrier that previously confined the water, such as flow through newly formed cracks, causing subsidence (Figure 2.4b) [*Ali et al.*, 2015]. This process has been observed at Campi Flegrei in the 1980s, and there are similarities between the temporal evolution of the deformation there and our observations at Corbetti [e.g., *Battaglia et al.*, 2006; *Bonafede*, 1991]. Surface deformation caused by coupled magmatic-hydrothermal systems has also been observed elsewhere in the East African Rift: at Aluto, MER [*Hutchison et al.*, 2016], and Longonot, in the Kenyan Rift [*Biggs et al.*, 2016].

The deformation is contained within the Corbetti caldera to the west and south, but extends outside the caldera to the east. At calderas which collapse via piecemeal or piston style mechanisms, sharp offsets occur around the caldera rim, and the caldera floor can become highly fractured [*Holohan et al.*, 2005; *Walter and Troll*, 2001; *Lipman*, 1997]. The variation in caldera scarp height at Corbetti suggests possible asymmetric collapse, and the continuity of the deformation outside the caldera could indicate an absence of a bounding caldera ring fault to the east. These observations are consistent with the collapse of Corbetti caldera via a trapdoor mechanism, where most of the collapse is in the west and the eastern rim acts as the hinge [*Acocella*, 2007; *Girard and Vries*, 2005]. Alternatively, if slip occurred on the entire circumferential caldera fault during collapse, any structures that crossed this fault would be offset.

2.4. Seismicity

The seismicity in the Corbetti region has been studied using an array of broadband seismometers. These seismometers were operational for 2 years (2012 – 2014) at 7 stations, with a maximum of 5 stations working at any given time (Figure 2.1b), described

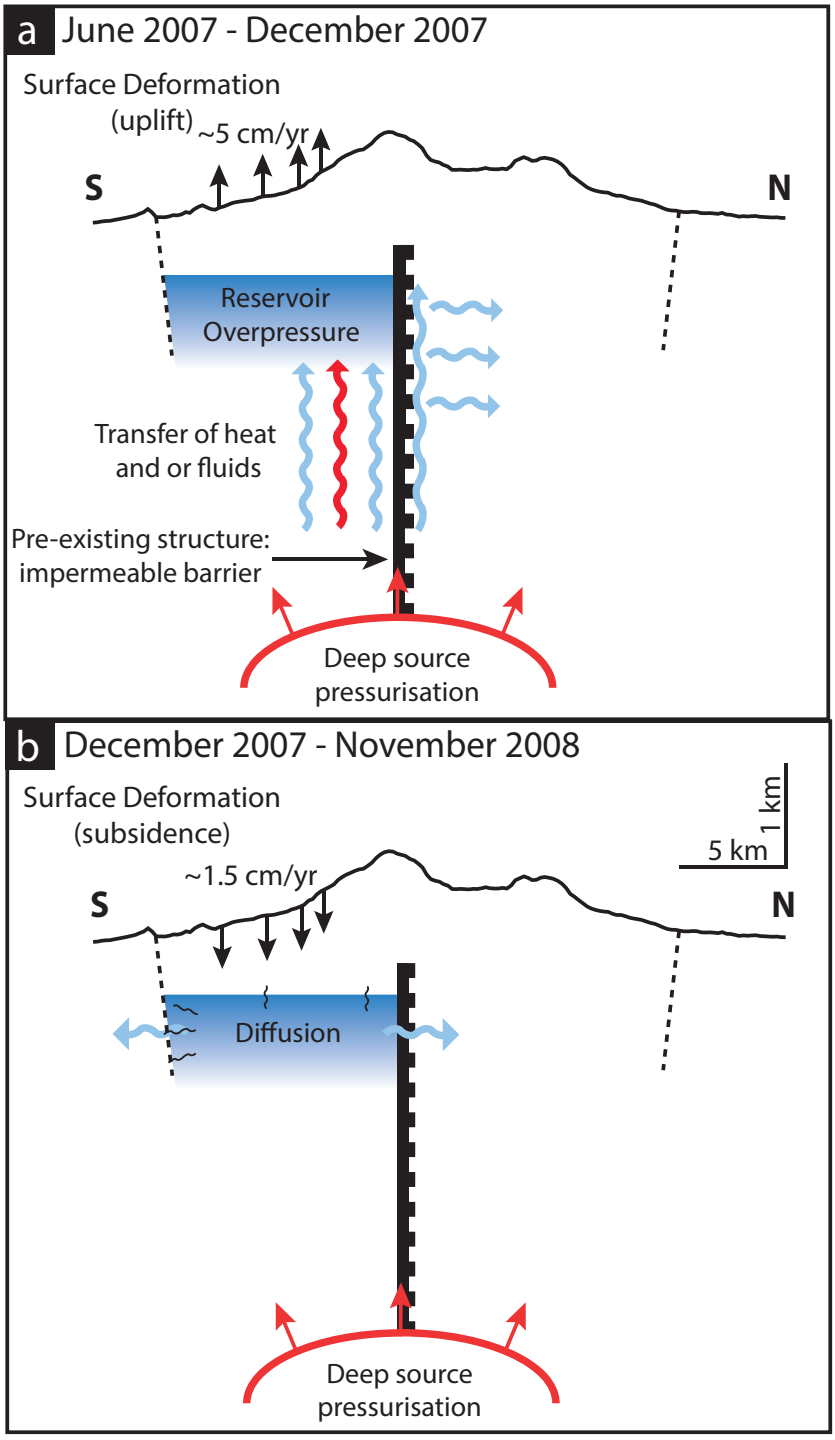

Figure 2.4: Schematic along a north-south profile showing processes involved in reservoir deformation at Corbetti. a) June 2007 – December 2007: pressurisation of a deep source causes heat and or fluids to migrate upwards, into the shallow hydrothermal reservoir. This causes overpressure in the reservoir, which is bounded in the north by an impermeable fault, resulting in uplift at the surface. b) In December 2007 subsidence of the reservoir indicates a decrease in overpressure. Diffusion or transfer of fluids through newly formed cracks may facilitate this depressurisation.

in more detail in *Wilks* [2016]. P- and S-wave first-breaks were manually picked, where coherent at three or more stations, and attributed weightings based on their quality. The software package NONLINLOC [*Lomax et al.*, 2000] was used to locate earthquakes, using P- and S-wave arrival times and a one dimensional velocity model from *Daly et al.* [2008]. Where possible, additional constraints on seismicity in the region came from stations deployed at the nearby Aluto volcano [*Wilks et al.*, 2017a].

2.4.1. Earthquake locations

Over the 2-year deployment period 780 earthquakes were located, 224 of which were within 15 km of Corbetti caldera centre. In contrast, the Aluto volcano, which lies roughly 75 km north of Corbetti, experienced over 2000 similar sized earthquakes in the same time period [*Wilks et al.*, 2017a]. At Corbetti, most of these events were located between Urji and Chabi down to a depth of 9 km. These earthquakes are associated with volcanic deformation that occurs after our InSAR observations, and so do not give any further information on the subsurface structure.

However, during the period January 2012 to January 2014, 71 earthquakes were recorded associated with the ∼E-W trending Wendo Genet Scarp and Werensa Ridge, ∼650 and ∼350 m high respectively and located ∼10 km to the east of Corbetti (Figure 2.1). The presence of slickensides on these features suggests there has been strike slip motion on these faults, although no offsets have been reported [*Rapprich*, 2013; *Korme et al.*, 2004; *Mohr*, 1968]. Left-lateral strike slip displacement here is consistent with models of MER kinematics, derived from structural data, focal mechanisms and GPS velocities [e.g., *Muluneh et al.*, 2014].

Most of the seismicity occurred between 7 and 15 km, with the shallow subsurface comparatively aseismic (9 events <7 km). Between 15 and 20 km no events occur, but between 20 and 32 km, there are 25 earthquakes (with maximum lateral uncertainty <10 km). These deepest events depict a linear structure that dips towards the southwest and are unlikely to be associated with transient volcanic processes at Corbetti given their distance from the caldera. The depth and distribution of the seismicity, on a linear plane down to 30 km, indicates that this structure extends down throughout the crust. The occurrence of seismicity here, along-strike of the deformation we identify within the caldera, suggests that the structure which cross-cuts Corbetti continues outside the caldera, and intersects the border faults.

2.4.2. Seismic anisotropy

We use shear-wave splitting analysis to evaluate seismic anisotropy in the upper crust in the Corbetti region. The vertical alignment of sub-seismic length-scale cracks and fractures in the crust leads to variations in seismic velocities with direction and polarisation. The propagation of two independent shear waves with orthogonal polarisations is perhaps the most unambiguous indicator of seismic anisotropy. The alignment of fracture reveals the orientation and the anisotropy of the stress field [e.g., *Verdon et al.*, 2008]. Fractures will align in the direction of maximum horizontal compressive stress, which is revealed by the polarisation of the fast shear-wave (ϕ). The delay time (δt) between the fast and slow shear-waves is proportional to the fracture density or difference in maximum and minimum horizontal stress. It is also sensitive to the compliance of the fractures, which is related to properties such as permeability and fluid content. For the purposes of this work, we neglect the influence of any intrinsic horizontal crystal alignment in the rocks of the shallow crust or any fine scale horizontal layering, as vertically propagating shear waves will be less sensitive to such anisotropy (see *Verdon et al.* [2009] for more discussion of this).

Shear-wave splitting analysis is performed on ∼1200 source-receiver paths to the Corbetti seismic stations. For details of the methodology, the reader is referred to *Wuestefeld et al.* [2010]. Twenty-eight measurements produce acceptable splitting results. We neglect measurements with errors >20° in ϕ and 0.02 s in δt, and any source-receiver paths inclined >45°. The range of δt is up to 0.31 s, which corresponds to a shear wave anisotropy of up to 9.2%. Shear wave splitting is accrued along the waves' travel path, so in subsequent figures we plot it at the event–station midpoint.

Figure 2.5a shows polar histograms of orientations of the fast shear waves at each station, as well as the overall trend of ϕ. It is apparent that most measurements show a fast shear-wave polarisation that is parallel to the Werensa Ridge, and is consistent with the orientations expected for the principle stresses on an east-west striking strike slip fault. The orientation of the fast shear-wave polarisation is not the same as current plate motion or extension direction implied by the Wonji Fault Belt. However, there is a secondary cluster of rift parallel orientations, which occur in paths outside the caldera to CO3E and CO7E, the stations which also lie furthest from the centre. The magnitude of the splitting is highest in the southern half of the caldera. These observations suggest that the most intense fracturing is in the deforming region, as might be expected, and that the regional stress field is most strongly perturbed within the caldera. Outside the edifice the regional stress field appears to dominate.

Observations of splitting from deep events (down to ∼35 km) below the Wendo Genet Scarp and Werensa Ridge further support the hypothesis that the cross-rift structure

plays a role in modifying the stress field. Figure 2.5b shows the dichotomy in ϕ between splitting in ray-paths travelling north of this zone to station C03E, and those within in it (to C02E). Splitting is cross-rift-parallel for the southern paths and rift-parallel for the northern ones, which also show more anisotropy, though both are relatively weak compared to paths within the caldera.

2.5. Caldera geometry and locations of post-caldera volcanism

We hypothesise the subsurface structure that limits the extent of the deformation also influenced the magma plumbing system at Corbetti, specifically the formation of the pre-caldera magma reservoir and the location of post-caldera volcanism. We test this hypothesis by considering the geometry of the surface features [e.g., *Le Corvec et al.*, 2013; *Acocella et al.*, 2002]. Pre-existing structures can influence the geometry of magma reservoirs, causing them to be elongate in the orientation of the structure [*Robertson et al.*, 2016; *Holohan et al.*, 2005]. The shape of a caldera at the surface is thought to reflect the shape of the pre-caldera magma reservoir and we therefore test whether the caldera rim is elliptical in shape, and whether the long axis of this ellipse is consistent with the deformation boundary. Secondly, since faults can act as a pathway for magma migration, we considered whether there is a preferential alignment of post-caldera vents [*Muirhead et al.*, 2015; *Mazzarini et al.*, 2013].

2.5.1. Caldera rim geometry

We digitised 80 points that describe the location of the exposed caldera rim, identified using high resolution optical imagery (Google Earth, 2016) and published maps, using QGIS [*Gíslason et al.*, 2015; *Rapprich*, 2013]. We then inverted for the long and short axis lengths, caldera orientation, and centre point from these points using the method of *Szpak et al.* [2014]. This method uses an approximate maximum likelihood approach which combines the accuracy of orthogonal methods and the speed of algebraic methods to find the solution to the equation of a conic that is non-degenerate.

The method seeks to minimise the Sampson distance, an algebraic approximation of the orthogonal distance between points and a candidate ellipse [*Szpak et al.*, 2014]. The use of the algebraic Sampson distance allows the mathematical equation of the conic to be expressed in terms of geometric parameters of an ellipse (orientation, length of long and short axes and centre point location), and give a quantitative measure of the

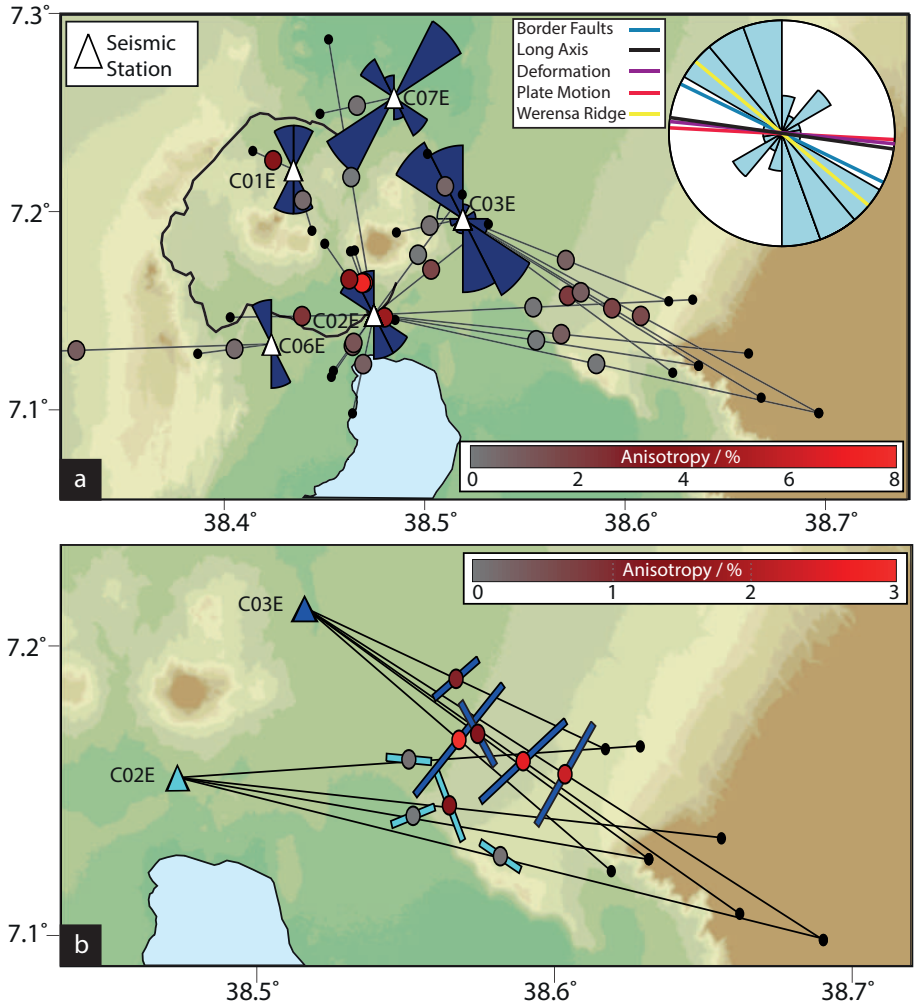

Figure 2.5: a) Shear wave splitting observations made at seismic stations within the Corbetti caldera from local earthquakes located by *Wilks et al.* [2017a]. Polar histograms (dark blue) are shown at each station which recorded at least three observations. The inset (light blue) histogram shows fast orientations for the whole data set. Blue, black, red and purple lines are the same as Figure 2.6, which show the orientation perpendicular to border faults, of the caldera long axis, plate motion, and deformation boundary, respectively. Circles show earthquake locations giving shear wave splitting observations, with colour indicating the strength of shear wave anisotropy. Lines connect events (black dots) with stations (white triangles). Note that anisotropy is largest for paths closest to the centre of the caldera, and that the dominant trend is sub-parallel to the trend of the Wendo Genet Scarp and Werensa Ridge. b) Variation of shear wave splitting with path from events near the Wendo Genet Scarp and Werensa Ridge. Coloured bars show the orientation of the fast shear wave measured at stations C02E (cyan) and C03E (blue), respectively, with the length of the bar proportional to the shear wave anisotropy, with a minimum bar length of 2% anisotropy. Coloured circles also show anisotropy as per the scale shown (note the scale is different between subplots). Circles and bars are plotted at the event–station midpoint. Black dots show earthquake locations and lines connect events and stations. Paths which spend longer to the north of the scarp show a rift-parallel ϕ trend, whilst those to the south have ϕ closer to the scarp strike.

uncertainties in the form of a covariance matrix. This method makes the assumption that the noise associated with the location of each point on the caldera is independent and Gaussian.

The ellipse that best describes the surface expression of the Corbetti caldera rim is centred at 38.381° E 7.192° N, and has a 13.8 ± 0.4 km long axis orientated 097 ± 3°, and a 11.3 ± 0.2 km short axis (Figure 2.6). The ratio of long axis to short axis length defines the caldera ellipticity, which at Corbetti is 0.82 ± 0.03: we therefore consider the caldera to be elliptical. The caldera long axis is co-incident with the boundary of the deformation region (Figure 2.6). Since the shape of the caldera rim is taken to reflect the geometry of the pre-collapse magma storage region, it implies that the structure influenced magma migration prior to the caldera collapse at 182 ± 18 ka.

2.5.2. Post-caldera volcanism

Crustal structures can also act as pathways for migrating magma, influencing the location of small vents [e.g., *Le Corvec et al.*, 2013; *Korme et al.*, 2004, 1997]. To test whether the structure influenced magma migration since the caldera collapse at Corbetti, we quantify the locations of post-caldera volcanism in relation to the caldera geometry. We digitised the location of the 16 post-caldera vents greater than 10 m in diameter, identified using high resolution optical imagery (Google Earth, 2016) and published maps [*Rapprich et al.*, 2016; *Gíslason et al.*, 2015; *Rapprich*, 2013], using QGIS (Figure 2.6).

Our hypothesis is that post-caldera volcanism is influenced by a subsurface structure, taken to be coincident with the caldera long axis. This predicts that vent locations will be closer to the caldera long axis than a random distribution of vents within the caldera and can be statistically tested by comparing the mean distance between the mapped vents and the caldera long axis, and the same measurement for a synthetic, random dataset of vent locations. We only used vents within the caldera, which we defined as the area inside the caldera rim, where exposed, and within the best fitting ellipse that describes the caldera where there is no clear rim. To find the probability that the vent locations inside Corbetti are closer to the caldera long axis than if generated at random, we simulated 10,000 other 16 vent locations and found the mean distance for each simulation. The proportion of simulated mean distances less than the observed mean distance gives the probability that randomly formed vents would be located closer to the caldera long axis than the observed vents.

Figure 2.6 shows the distribution of random mean vent-long axis distances for 10,000 simulations. The proportion of simulations with mean distances less than the measured mean distance, 1390 m, defines the probability that the actual distribution of vents are

located at random. For a structure aligned with the caldera long axis, this proportion is 3.0%, which demonstrates statistical significance. Furthermore the major centres of resurgent volcanism, Urji and Chabi, both lie along the ellipse long axis.

However, clustering of vents in the centre of the caldera would also produce a small mean vent-structure distance, but the vents will lie equally close to a line of any orientation through the caldera. As such, we find the probability that the observed vents are distributed closer to 'structures' orientated N-S, NE-SW, and NW-SE. These probabilities are 0.46, 0.24, and 0.25 respectively, much higher than for the hypothesised E-W structure (0.03). However, even in a homogeneous medium, vent locations are unlikely to be random because established magma pathways are often reused and surface topography exerts stresses that may influence magma migration [e.g., *Roman and Jaupart*, 2014; *Xu and Jónsson*, 2014; *Pinel and Jaupart*, 2003].

Nonetheless, we conclude the post-caldera volcanism is located closer to a subsurface planar structure than randomly distributed vents would be. This suggests that such a structure influenced magma migration over the timescales of post-caldera vent formation, which is on the order of tens of thousands of years [*Hutchison et al.*, 2015b; *Rapprich*, 2013].

2.6. Nature of subsurface structure

In this section we discuss the candidates for the subsurface structure, of which several are plausible in rift settings: for instance the stock of an earlier volcano, the rim of a preceding caldera, or a pre-caldera fault. The candidate must be able to explain the orientation and ellipticity of the caldera, the distribution of post-caldera vents, and the horizontal and vertical extents inferred from seismic and InSAR observations.

Beneath the caldera complexes in the MER solidified magmatic intrusions have been identified with gravity and seismic surveys [*Cornwell et al.*, 2006; *Maguire et al.*, 2006]. An intrusion beneath the northern half of the Corbetti caldera, with its edge along the caldera long axis, would enhance deformation in the southern portion of the caldera relative to the north, as observed. This is because crystallised silicic material has different material properties (e.g., rigidity and permeability) to partially molten intrusions [e.g. *Hickey et al.*, 2013]. Material properties that are spatially variable in this way would also explain the shear wave splitting measurements that suggest differences in fracture density between the north and the south. While we cannot discount this explanation, it is unable to explain the caldera orientation or the location of post-caldera vents, which occur in both the northern and southern parts of the caldera.

An alternative explanation is that the cross-cutting structure is related to the ring fault of the Hawassa Pleistocene collapse caldera [*Rapprich*, 2013; *Woldegabriel et al.*, 1990]. There is a change in strike from east-west within the caldera, to north-west – south-east at the Werensa Ridge and Wendo Genet Scarp, which would be consistent with a caldera ring fault. However, caldera faults typically extend to depths of less than 10 km [see *Cole et al.*, 2005; *Holohan et al.*, 2005; *Saunders*, 2001], and magnetotelluric data within the caldera shows the structure extends to at least 10 km [*Gíslason et al.*, 2015] (Figure 2.6), while outside the caldera, seismicity on the Wendo Genet Scarp and Werensa Ridge indicate the structure extends to 30 km depth [*Wilks*, 2016] (Figure 2.1).

Our preferred candidate for the structure that cross-cuts Corbetti is a pre-existing fault. Pre-rift faults cross-cut the Precambrian basement throughout Ethiopia, and many have been reactivated by the current phase of rifting [*Corti*, 2009; *Chorowicz*, 2005; *Korme et al.*, 2004]. For example, the pre-Jurassic Ambo Fault Zone (AFZ) and the Yerer-Gugu lineament controlled the Pleistocene development of the transfer zone between the northern and central MER around 8° N [*Bonini et al.*, 2005] (Figure 2.1). The AFZ can be identified perpendicular to the rift as an off-rift low velocity structure [*Bastow et al.*, 2005]. Another pre-rift structure, the Goba-Bonga lineament, is thought to have impeded the northwards propagation of the Kenyan Rift at ∼11 Ma and stalled MER rifting during the Miocene [*Bonini et al.*, 2005]. Oligio-miocene (20 – 30 Ma) volcanism is aligned along the AFZ and the Goba-Bonga lineament on the western rift flank [*Corti et al.*, 2018; *Corti*, 2009; *Korme et al.*, 2004], suggesting such structures remain important magma pathways for tens of millions of years.

Corbetti caldera lies on the cross-rift projection of the Goba-Bonga lineament. The Werensa Ridge and Wendo Genet Scarp are thought to be the surface expression of the Goba-Bonga lineament, where it obliquely intersects the rift border fault [*Žáček et al.*, 2014]. The structures do have a different strike to the structure identified within the Corbetti caldera, but a curvature of the shallow resistive anomaly (Figure 2.6) can be seen connecting the two: from east-west inside the caldera to north-west – south-east to the east. Furthermore, it is not uncommon for fault systems to change strike along their lengths [e.g., *Sengör et al.*, 2005]. At the Werensa Ridge and Wendo Genet Scarp there is seismicity (71 earthquakes, magnitudes between 0.65 and 4.10, January 2012 – January 2014) down to ∼30 km (Figure 2.1) [*Wilks*, 2016]. The Moho here is ∼38 km deep [*Keranen and Klemperer*, 2008] and so the depth extent of the seismicity is evidence that this fault cross-cuts almost the entire crust and has the potential to influence magma storage and transportation on a crustal scale. The occurrence of earthquakes at lower crustal depths is not atypical in the MER, seismicity has been observed ∼35 km deep at similar crustal-scale pre-rift structures such as the Yerer-Tullu Wellel (Figure 2.1) [*Keir et al.*, 2009].

This interpretation of the structure provides an explanation for all of the observations, including the pre-caldera elliptical magma body, post-caldera magmatism, deformation, resistivity and seismicity. This major crustal structure acts to guide the vertical transport of hydrothermal fluids into the shallow subsurface, and as a barrier to horizontal fluid flow, defining the lateral extent of the hydrothermal reservoir. The presence and location of the structure is also consistent with the hypothesis that some MER silicic centres formed where transtensional faults cross-cut the rift, creating regions of localised extension or weaker material that promotes magma reservoir formation [*Acocella et al.*, 2002].

2.7. Conclusions and comparisons

We show that pre-rift structures influence magmatic and hydrothermal processes over a range of timescales at the Corbetti caldera, Ethiopia. A rift-oblique structure influenced (1) surface deformation associated with a fault bounded reservoir, which shows the influence of faults on hydrothermal circulation over annual timescales; (2) the location of post-caldera volcanism, which highlights the influence on shallow magma transportation pathways over tens of thousands of years; and (3) the caldera geometry, indicative of a control on crustal magma storage over hundreds of thousands of years.

This work raises questions regarding the influence of pre-rift oblique structures in continental rifting, both in terms of their influence on magmatic processes but also their role in strain accommodation. A comparison can be drawn to the Taupo Rift System, New Zealand, where pre-existing oblique structures align with volcanic domes [e.g., the Tarawera Dome Complex, *Cole et al.*, 2010] and control hydrothermal circulation [*Rowland and Sibson*, 2004]. In contrast, where rifting occurs in Icelandic, there is no basement continental crust, and to date there appears to be little evidence of oblique structures influencing volcanism.

This study demonstrates the importance of combining different techniques and datasets that give observations of multiple processes over multiple timescales to understand magmatic-hydrothermal systems. Our observations have implications in understanding the relative importance of heterogeneities that affect the development of magmatic systems, especially in active tectonic regimes such as continental rifts. It provides insight into how these same processes influence hydrothermal reservoir formation, and also how they respond to external influences.

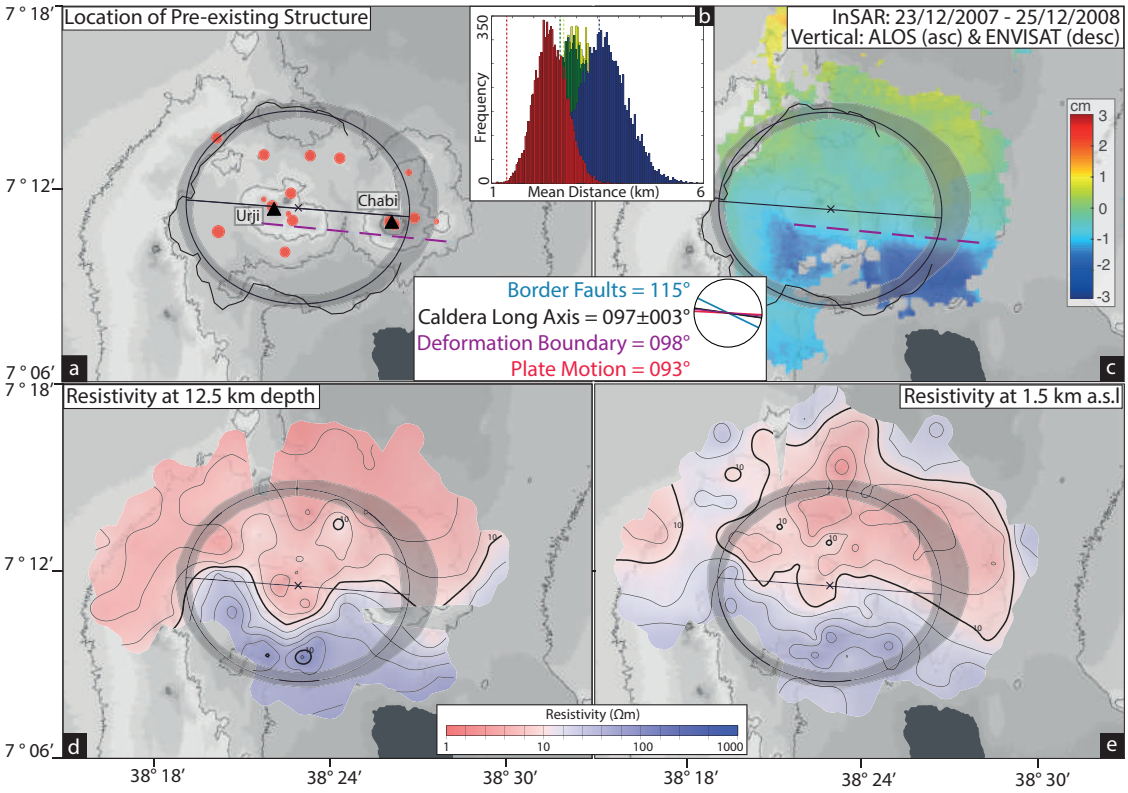

Figure 2.6: Geophysical and structural data indicating there is a pre-existing fault trending ∼097° through Corbetti. a) The straight black line shows the caldera long axis, black cross the caldera centre and black line the exposed caldera rim. Red circles identify vents or craters decametre in scale or larger, as identified by satellite optical imagery. Black triangles demarcate the apexes of Urji (west) and Chabi (east). The purple dashed line shows the location of the pre-existing fault as observed using InSAR (c). b) The histogram shows the mean vent-structure distances for 10,000 simulations of 16 vent locations inside the caldera for E-W (red), N-S (blue), NW-SE (green) and NE-SW (yellow) orientated structures. Dashed vertical lines indicate the mean vent-structure distance for each orientation of the corresponding colour. c) InSAR data from 23/12/2007 – 25/12/2008 showing the deforming region. d–e) Magnetotelluric data after *Gislason et al.* [2012]. Inset shows the orientations of the caldera long axis, deformation boundary, current plate motion direction [*Stamps et al.*, 2008], and the perpendicular direction to the border faults.

Chapter 3

Sustained uplift at a continental rift caldera

Lloyd, R., J. Biggs, Y. Birhanu, M. Wilks, J. Gottsmann, J.-M. Kendall, A. Ayele, E. Lewi, H. Eysteinsson (2018), Sustained Uplift at a Continental Rift Caldera, *Journal of Geophysical Research: Solid Earth*, *123*, 1-18.

Author contributions and declaration:
J. Biggs provided supervision throughout. J. Biggs, Y. Birhanu, M. Wilks, J. Gottsmann, and J.-M. Kendall assisted with fieldwork, facilitated in part by A. Ayele and E. Lewi. Y. Birhanu processed the GPS data, and helped write the GPS processing methods. M. Wilks processed the seismic data, supervised by J.-M. Kendall, and helped write the seismic processing methods. J. Gottsmann provided useful discussions throughout. H. Eysteinsson acquired and processed the magnetotelluric data.

ENVISAT and Sentinel-1 data are available from the European Space Agency (ESA). ALOS data were provided through an ESA third party mission. Cosmo-SkyMed data were made available through an Italian Space Agency (ASI) open call. The loan of GPS equipment was provided by the NERC Geophysical Equipment Facility.

Abstract

Caldera systems are often restless and experience pulses of uplift and subsidence, with a weak, but significant link to eruption. Characterising the spatial and temporal patterns of deformation episodes provides insight into the processes responsible for unrest and the architecture of magmatic and hydrothermal systems. Here we combine Interferometric Synthetic Aperture Radar images with data from the Global Positioning System and a network of seismometers at a continental rift caldera Corbetti, Ethiopia. We document inflation that started mid-2009 and is ongoing as of 2017, with associated seismicity. We investigate the temporal evolution of the deformation source using a Hastings-Metropolis algorithm to estimate posterior probability density functions for source model parameters, and use the Akaike Information Criterion to inform model selection. Testing rectangular dislocation and point sources, we find a point source at a depth of 6.6 km (95% confidence: 6.3 – 6.8 km) provides the statistically justified fit. The location of this source is coincident with a conductive anomaly derived from magnetotelluric measurements. We use a joint inversion of two geodetic datasets to produce a time series which shows a volume input of 1.0 x 10^7 m^3/yr. This is the first observation of a prolonged period of magma reservoir growth in the Main Ethiopian Rift and has implications for hazard assessment and monitoring. Corbetti is <20 km from two major population centres, and has estimated return periods of ∼500 and ∼900 years for lava flows and Plinian eruptions respectively. Our results highlight the need for long-term geodetic monitoring, and the application of statistically robust methods to characterise deformation sources.

3.1. Introduction

3.1.1. Crustal magma and continental rifts

Magma reservoirs in the Earth's crust are currently thought to be interconnected crystal-melt mush regions [*Cashman and Sparks*, 2013], and understanding the architecture and evolution of magmatic systems is a fundamental goal in volcanology. Observations or inferences of the depth, size or temporal evolution of a magma reservoir can put constraints on, for example, how large magma reservoirs form, the temporal and spatial characteristics of magma recharge [*Gudmundsson*, 1990], and the size, style and duration of potential eruptions [*Becerril et al.*, 2013; *Bower and Woods*, 1998].

In continental rift systems four major styles of volcanism are observed: large silicic centres along the rift axis [*Abebe et al.*, 2007], spatially distributed fields of basaltic monogenetic volcanism [*Mazzarini et al.*, 2004], fissure eruptions [*Pagli et al.*, 2012], and off-rift volcanism [*Maccaferri et al.*, 2014]. Each of these styles are a product of different magma reservoir architectures and storage conditions. In continental rifts, faulting and magma throughout the crust is necessary to reduce the crustal tensile strength enough to facilitate rifting [*Buck*, 2006], and transport via dyking has a distinctively different influence on the rifting process than storage of silicic magma at calderas. Rifting initially begins as a zone of diffuse faulting, which transitions into being driven through repeated magmatic intrusions in a narrow region along the rift axis [*Ebinger et al.*, 2017; *Beutel et al.*, 2010]. These repeated intrusions are thought to build up along the rift-axis to form crustal magma reservoirs, which then fractionate, forming the centres observed beneath the axial silicic volcanoes [*Gudmundsson*, 2011]. Seismic evidence for aligned melt in the crust suggests that the orientation of the melt is an important factor in facilitating rifting [*Kendall et al.*, 2006; *Keir et al.*, 2005].

InSAR (Interferometric Synthetic Aperture Radar) and GPS (Global Positioning System) are complementary techniques that are ideally suited for observing surface deformation associated with magmatic processes. InSAR observations have a high spatial resolution (typically 30 m), and GPS data can have high temporal resolution (typically up to days). However, there are limitations: GPS stations only provide a measure of the surface deformation at their location, and are vulnerable to damage. InSAR, on the other hand, can lose coherence if the ground scattering properties change too much, and the temporal resolution is dependent on satellite data acquisition dates, which can be variable. In addition, geophysical signals can last longer than the observation period of some sensors or deployments, and so data from multiple sensors may need to be combined. The differing spatial and temporal resolutions of GPS and InSAR can also lead to complications in combining observations for modelling. Since the purpose of making these observations is to comment on the subsurface, we combine our data to

look at the temporal evolution of the signal through the use of a source model [*Biggs et al.*, 2010b].

In this paper we focus on the surface deformation of a Main Ethiopian Rift (MER) silicic caldera, Corbetti, to investigate the magmatic storage conditions and temporal evolution, e.g., pulsed versus continuous supply. We perform inversions of surface deformation, observed with InSAR and GPS, for analytical source model parameters using a Bayesian approach [e.g., *Bagnardi and Hooper*, 2018; *González et al.*, 2015]. This approach allows us to report our optimal model parameters with posterior probability density functions, and specifically comment on poorly constrained parameters, and parameters trade-offs. To quantitatively compare our models we use the Akaike Information Criterion, which allows us to consider their complexity and likelihood. To investigate the temporal evolution of the source we combine our data through the use of a source model to jointly invert for the cumulative volume change.

3.2. Background

3.2.1. The East African Rift

The East African Rift System (EARS) is a major continental rift separating the Nubian and Somalian tectonic plates (Figure 3.1). It extends from Ethiopia and Eritrea in the north, southwards to Mozambique. Along the EARS spreading rates vary from ∼6.6 mm/yr in the Main Ethiopian Rift (MER), to less than 3 mm/yr in Mozambique [*Stamps et al.*, 2008]. The presence or absence of magma within the rift is key to the distribution of hazards and strain. Since 1890 there have been 11 eruptions, from 7 volcanoes, in Ethiopia alone [*Wadge et al.*, 2016].

The causes of deformation within the EARS spans a range of processes: eruptions [*Pagli et al.*, 2012], magmatic intrusions [*Biggs et al.*, 2016, 2009b], hydrothermal activity [*Hutchison et al.*, 2016], earthquakes [*Biggs et al.*, 2010a], slow-slip faulting events [*Calais et al.*, 2008], and subsidence from cooling, crystallisation and degassing [*Biggs et al.*, 2016]. It is notable that periods of prolonged magma reservoir growth have not yet been described in this setting, but are common elsewhere [e.g., *Le Mével et al.*, 2015; *Dzurisin et al.*, 2009].

Corbetti caldera, in the southern MER, formed in a >10 km^3 volume eruption at 182 ± 28 ka [*Hutchison et al.*, 2015a]. Within the caldera are two major centres of resurgent volcanism, Urji (syn. Wendo Koshe) and Chabi, and several smaller vents and cones (Figure 3.1). The post-caldera volcanism is exclusively characterised by the eruption

of peralkaline rhyolites in both pyroclastic sequences and aphyric obsidian flows dated between ∼20 ka and ∼0.5 ka [*Fontijn et al.*, 2018; *Martin - Jones et al.*, 2017; *Rapprich et al.*, 2016; *Hutchison et al.*, 2015a]. *Martin - Jones et al.* [2017] identify and analyse ∼12 ash layers deposited in a lake over the last 10 kyr ∼30 km away from Corbetti to derive a return period of explosive eruptions of 900 ± 220 years [*Connor et al.*, 2003]. Based on the four most recent lava flows, *Rapprich et al.* [2016] propose an effusive eruption return period of 500 – 550 years.

Corbetti has been observed recently deforming: 1994 – 1996 there was >1.4 cm of uplift, and 1997 – 2000 <14 cm of subsidence, as measured by InSAR [*Biggs et al.*, 2011]. This subsidence was modelled as a point source at a depth of 5.8 – 7.8 km. No deformation was observed between 2003 and mid-2007. Between June 2007 and November 2008 a localised region of uplift followed by subsidence was observed in the south of the caldera, the source of which is interpreted to be a shallow hydrothermal or ground water system [*Lloyd et al.*, 2018]. A large rift oblique fault structure also crosses through the caldera [*Lloyd et al.*, 2018]. This structure is thought to have influenced initial magma reservoir formation, and hydrothermal fluid and magma migration within the caldera.

Magnetotelluric (MT) observations, which are sensitive to the ground resistivity [e.g., *Samrock et al.*, 2015; *Didana et al.*, 2014; *Whaler and Hautot*, 2006], have been used to image the subsurface beneath Corbetti [*Gíslason et al.*, 2015]. *Gíslason et al.* [2015] find a conductive anomaly <2 km thick layer in the upper 2 km, beneath the northern half of the caldera, which is interpreted to be a layer of hydrothermally altered clays. Beneath Urji and the centre of the caldera there is another conductive anomaly. The 10 Ωm contour up-domes to a depth of 3 km below sea level (b.s.l). Down to 7 km b.s.l this anomaly is ∼2 km wide (north-south), below which it broadens by ∼2 km to the north. This deeper anomaly is interpreted by *Gíslason et al.* [2015] as a region of partial melt. Fumerole geochemistry analysis in 2011 identified high geothermal temperatures (>300°C), suggesting a heat source at depth [*Gíslason et al.*, 2015].

More than 500,000 people live in and around the Corbetti region, primarily in the major population centres of Hawassa and Shashemene, but also on the surrounding agricultural land. The caldera is a potential geothermal resource [*Gíslason et al.*, 2015], and within 10 km of a national airport. Lake Hawassa, which supports a fishing economy, is also within 10 km. The RiftVolc and ARGOS projects have carried out temporary deployments of seismic and geodetic equipment at Corbetti, but there is no permanent or real-time monitoring network [*Birhanu et al.*, 2018; *Wilks et al.*, 2017a].

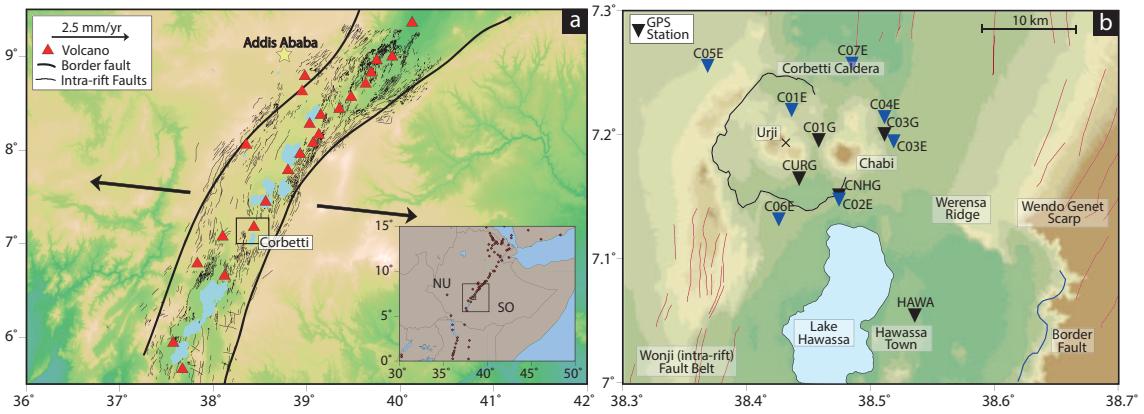

Figure 3.1: a) The Main Ethiopian Rift, with northern East Africa inset (NU: Nubian plate, SO: Somalian plate). The main volcanic centres are shown by red triangles, faults by black lines [*Agostini et al.*, 2011]. b) The Corbetti caldera. GPS stations used in this study are shown by inverted black triangles. The stations HAWA, CURG, C01G, and C03G were set up in March 2013. C01G and C03G became inoperable following vandalism (C01G: 15/04/2015, C03G: 05/09/2014). Station CNHG was installed in October 2015 as a replacement (Figure B.1). Seismic stations locations are shown by blue triangles. C01E, C02E, and C03E were deployed in January 2012, C05E and C06E in January 2013. C03E was relocated to C04E in May 2014. In October 2013 C07E was deployed. The black cross shows the centre of the caldera [*Lloyd et al.*, 2018].

3.3. Surface deformation

3.3.1. Interferogram processing

InSAR uses the phase component of two Synthetic Aperture Radar images of the Earth's surface to determine the change in path length that has occurred in the satellite's line-of-sight (LOS). We produced ~420 interferograms, using SAR data from four different satellites or satellite constellations, over Corbetti caldera from between October 2007 and January 2017 (Table B.1). ALOS, ENVISAT, and Cosmo-SkyMed (CSK) interferograms were processed using the ISCE software package [*Rosen et al.*, 2012]. Sentinel-1 interferograms were processed using the GAMMA software [*Werner et al.*, 2000], within the LiCSAR facility [*González et al.*, 2016]. The topographic contribution in all interferograms were removed using the 30 m SRTM DEM [*Farr and Kobrick*, 2000]. Table B.2 shows the parameters selected for each sensor made during processing. To maximise coherence in CSK data, interferograms were resampled to 60 m pixels before the removal of topographic phase contributions. Interferograms were then filtered (strength 0.6), resampled (120 m pixels) and then filtered again (strength 0.6) before unwrapping [*Chen and Zebker*, 2001; *Goldstein and Werner*, 1998]. Atmospheric artefacts were investigated using ascending and descending acquisitions covering the same time period, and pair-wise logic using networks of interferograms [e.g., *Ebmeier et al.*, 2013; *Pritchard and Simons*, 2004]. We tested using weather models [e.g., *Yu et al.*, 2017a,b] to correct

atmospheric delays, but as the climate is generally dry and the relief low, they showed little correspondence with the interferograms. A linear ramp was removed from each interferogram to correct for long wavelength atmospheric or orbital delays [*Biggs et al.*, 2007]. The temporal coverage of all interferograms can be seen in Figure B.1.

This InSAR dataset contains interferograms produced using radar data with a range of wavelengths: 3.1 cm (X-band), 5.6 cm (C-band) and 23.1 cm (L-band) (CSK, Sentinel-1 and ENVISAT, and ALOS respectively). The MER is densely vegetated, with primarily agricultural land in the Corbetti region. As is commonly seen in InSAR data, we found this repeated resurfacing of the ground surface resulted in a loss of coherence, especially so for our X-band and long temporal baseline C-band interferograms. All coherent interferograms with temporal baselines greater than ∼1 month and after March 2009 showed concentric fringes of a decrease in range change, consistent with uplift. Due to a loss of coherence in agricultural areas, the extent of the deformation is unconstrained in several C- and X-band interferograms. For coherent interferograms longer than ∼1 year, however, low rates of deformation can be seen to extend <4 km outside the caldera.

3.3.2. Global Positioning System processing and methods

Five continuous GPS stations were operational during the observation period, four on the volcano (CURG, C01G, C03G, and CNHG) and one in Hawassa (HAWA) (see Figure 3.1b for locations and Figure B.1 for temporal coverage). Station positions, delays and ambiguities were solved for using the GAMIT/GLOBK software package [*Herring et al.*, 2010]. International Global Navigation Satellite System reference sites were used to constrain the solution in the International Terrestrial Reference Frame 2014 [*Altamimi et al.*, 2016]. The station location and time series for the volcano GPS sites are calculated relative to HAWA. Daily GPS solutions were resampled to weekly solutions for analysis and modelling.

The GPS station C01G is the closest to the centre of the caldera. The maximum vertical deformation at C01G was 6.5 ± 1.3 cm between 22/03/2013 and 15/04/2015, whereas there was only 0.6 ± 0.6 cm of northwards, and 2.3 ± 0.7 cm eastwards motion during the same period (Figure 3.2). CURG is the longest running GPS station: 31/03/2013 – 31/12/2016. This station was moving 2.9 ± 0.3 cm/yr SWW (azimuth of 206 ± 005°) and up at 3.9 ± 0.7 cm/yr (Figure 3.2). C03G, east of the caldera, was moving 1.9 ± 0.6 cm/yr E (108 ± 014°), and up at 1.8 ± 1.7 cm/yr (22/03/2013 – 05/09/2014). CNHG, located at the southern caldera rim, was moving 1.5 ± 0.3 cm/yr SE (156 ± 023°) and up at 2.2 ± 2.1 cm/yr (07/10/2015 – 31/12/2016).

3.4. Time series analysis

We produce time series of the LOS range change using ALOS and Sentinel-1 data independently, using the SBAS (short baseline subset approach) methodology [*Berardino et al.*, 2002]. The uncertainty in the InSAR time series is determined by the mean standard deviation of the range change for each dataset, calculated for the region outside of 10 km from the centre of the caldera. Seasonal hydrological contributions to deformation in this area have been shown to be more than an order of magnitude smaller (<2 mm) than the uplift at Corbetti [*Birhanu et al.*, 2018], demonstrating no seasonal corrections need to be applied to the GPS time series.

Time series analysis using ENVISAT and ALOS interferograms indicates that there is no edifice centric deformation at Corbetti between October 2007 and March 2009 (Figure 3.3a and d). Uplift followed by subsidence localised to the southern half of the caldera is observed however, previously described and interpreted by *Lloyd et al.* [2018] to be associated with a hydrothermal system. Between March 2009 and September 2009 deformation begins, at a peak rate of 4.0 ± 1.2 cm/yr (maximum ascending LOS) until September 2010 (Figure 3.3a and d). Any displacement during the time period September 2010 to March 2012 is unconstrained by our dataset (Figure B.1). After March 2012 individual CSK interferograms show that uplift occurred at a rate of 7.5 – 14.8 cm/yr relative to HAWA, but the InSAR coherence is too poor to produce a displacement time series between HAWA and CURG. Individual interferograms are included on Figure 3.3. The consistent location and spatial extent of the signal before and after our data gap suggests that the displacement is continuous. The GPS data at CURG shows a variation in vertical rate from 2.2 ± 3.6 cm/yr between March 2013 and November 2013, to 4.3 ± 0.9 cm/yr from November 2013 to December 2016 (Figure 3.2). Between August 2015 and December 2016 the ascending and descending Sentinel-1 time series' show continuous linear uplift at 5.5 ± 1.0 cm/yr and 5.0 ± 0.7 cm/yr, respectively (maximum LOS).

We compare the InSAR time series to the 3-component monthly GPS time series projected into the satellite LOS. The location of CURG does not correspond to the maximum deformation, but was selected as it is the longest running GPS station, and to facilitate a comparison between the GPS and InSAR data. The ascending and descending Sentinel-1 data agree within error with the GPS displacement measurements projected into LOS at CURG between August 2015 and October 2016 (Figure 3.2). A comparison between the InSAR and GPS values for CURG and C01G can be found in Table B.3.

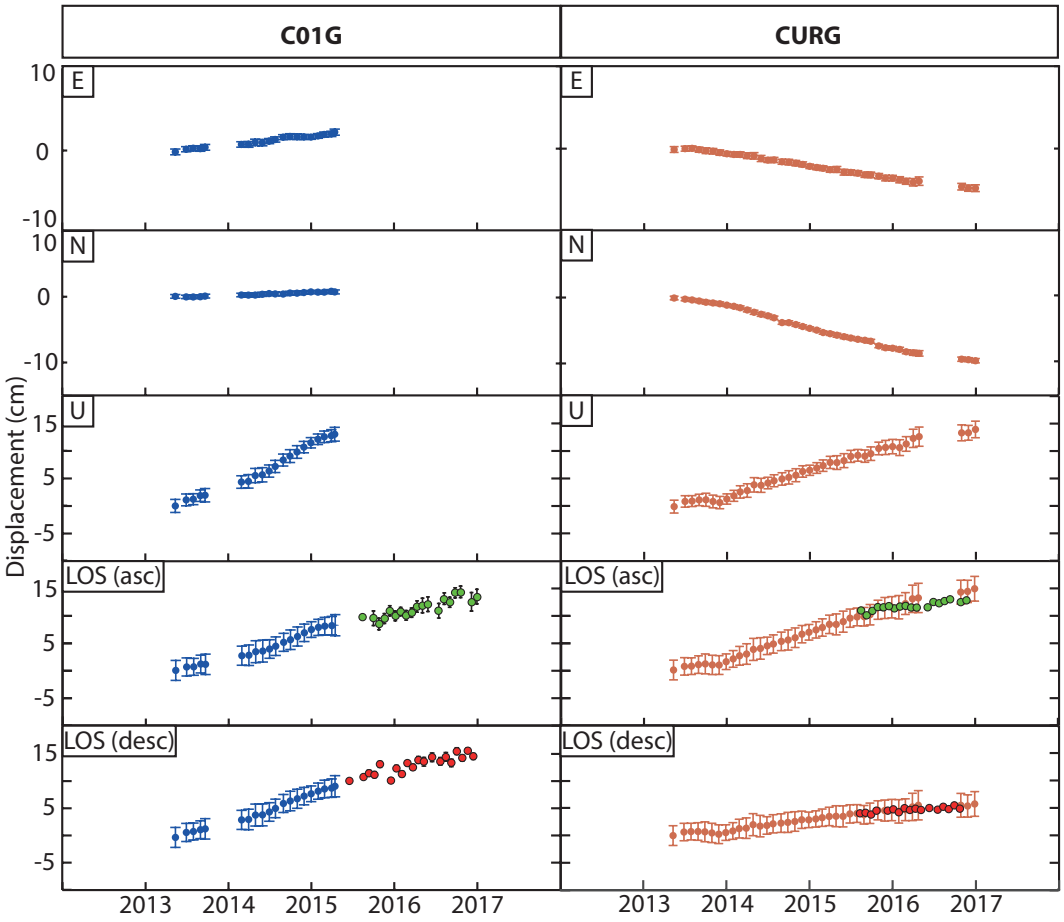

Figure 3.2: East (E), North (N), up (U), ascending (asc LOS), and descending (desc LOS) displacements for C01G (left) and CURG (right). A time series of ascending (green) and descending (red) Sentinel-1 displacements for the location of CURG is presented with the CURG GPS data projected into the respective LOS.

3.5. Inverse modelling

3.5.1. Bayesian inversion for analytical source models

Pre-eruptive surface deformation in volcanic settings can be caused by a volume or pressure change in the subsurface. In volcanic settings, the source of this change could be magmatic, hydrothermal, or a combination. We choose to explore two analytical source models embedded in a homogeneous elastic half space to describe the deformation: a point source [*Mogi*, 1958] (hereafter named 'Mogi source'), and a rectangular dislocation [*Okada*, 1985] (hereafter named 'Okada source'). We discount a possible dyke intrusion as the deformation at Corbetti is radially symmetric, rather than the three lobed pattern characteristic of dyking observed using InSAR [e.g., *Keir et al.*, 2011].

For all our models we selected a Poisson's ratio of 0.25, and a shear modulus of 16.5 GPa, which are typical values for similar caldera systems [e.g., *Coco et al.*, 2016; *Masterlark*,

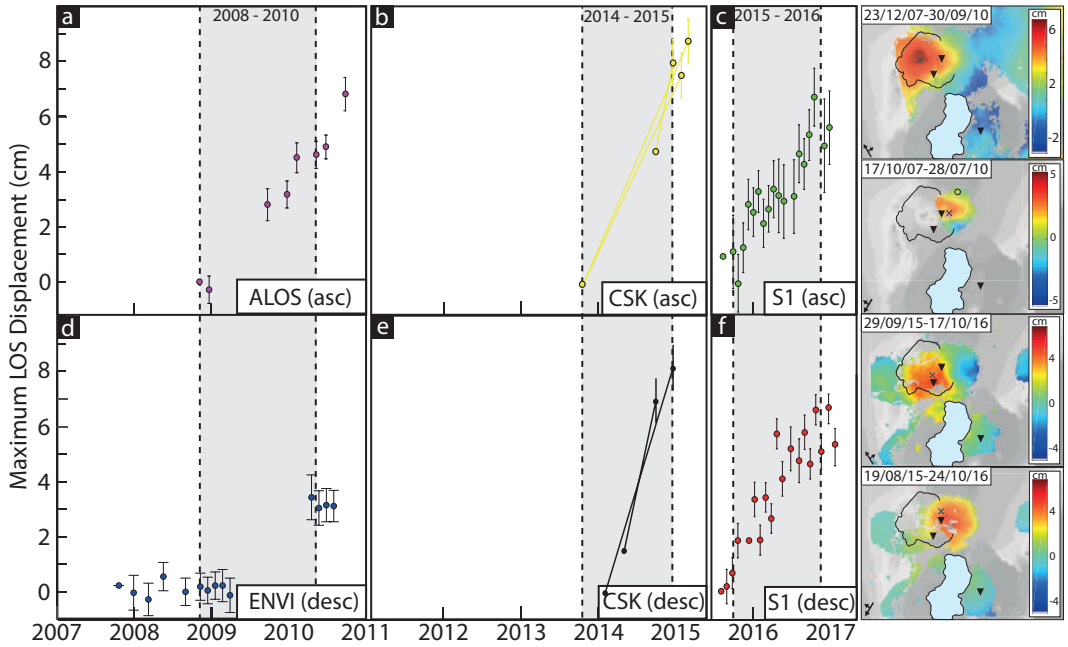

Figure 3.3: Left: Maximum LOS displacement (locations shown by an X on the right hand panels) from ALOS ascending (a), Cosmo-SkyMed ascending (b), Sentinel-1 ascending (c), ENVISAT descending (d), Cosmo-SkyMed descending (e), and Sentinel-1 descending time series analysis, or interferograms (connecting lines on b and e). The time series are relative to GPS station HAWA, or the open circle if HAWA is incoherent (d). The grey regions correspond to the time periods used in the source inversion in Section 3.5.1. Right: Cumulative displacement during the observation period of each satellite (top to bottom: ALOS: 23/12/2007 – 30/09/2010, ENVISAT: 17/10/2007 – 28/07/2010, Sentinel-1 ascending: 29/09/2015 – 17/10/2016, Sentinel-1 descending: 19/08/2015 – 24/10/2016), shown relative to the same locations as the time series.

2007]. Corbetti has low relief; the elevation of the caldera rim and resurgent volcanism is <400 m higher than the rift valley floor. As such, we consider the effects of topography in our modelling, or associated atmospheric artefacts to be negligible [*Parker et al.*, 2015; *Masterlark*, 2007].

The time series analysis indicates a negative range change, consistent with uplift, from between March and September 2009 until the end of our observations in January 2017, where constrained by InSAR data (Figure 3.3). To investigate any changes through time, such as variations in the driving behaviour (e.g., injection rate [*Hickey et al.*, 2016; *Parks et al.*, 2015]) or source location [*Biggs et al.*, 2016; *Bignami et al.*, 2014], we model the rate of range change from the InSAR and GPS data for three ∼1 year-long time periods: the onset of the signal (November 2008 – June 2010), after ∼5 years (January 2014 – January 2015), and after ∼6 years (October 2015 – October 2016) (Table B.4). We also perform a combined inversion, using all of the data together. For the years where GPS stations did not run continuously, we use the available data within that year to calculate the rate of deformation, which we assume is constant for that time period. The three periods were selected because: 1) ∼1 year of observations provides a high signal to noise ratio, 2) over ∼1 year C-band interferograms do not de-correlate significantly, and 3) during these time periods there are observations of the signal from ascending and descending satellite viewing geometries.

We search for the best model of the deformation using a Bayesian inverse modelling approach, incorporating Monte Carlo algorithms [*Mosegaard and Tarantola*, 1995; *Hastings*, 1970], that estimates the posterior probability density function for the best fitting parameters of each analytical source model, using the open source software GBIS (Geodetic Bayesian Inversion Software) [*Bagnardi and Hooper*, 2018; *González et al.*, 2015; *Hooper et al.*, 2013]. We assume that all measurement errors are Gaussian. For each interferogram we calculate the 1-D exponential covariance function, and subsample using the quadtree method, based on the data variance away from the signal [*Jonsson et al.*, 2002]. Iterative sensitivity tests are conducted throughout the Bayesian inversion to ensure fast convergence, and that all parameters contribute equally to changes in likelihood. We also solve for a constant offset in each interferogram.

To qualitatively compare Bayesian models one would use the Bayes Factor [*Brunetti et al.*, 2017; *Jeffreys*, 1935]. However, the model marginal likelihood, which is the likelihood function integrated over the model parameters, is challenging to calculate analytically [*Kass and Raftery*, 2008], and the results of approximation methods are generally unstable (see *Raftery et al.* [2007]). As such, we use the Akaike Information Criterion (AIC) [*Akaike*, 1974]. AIC considers the trade-off between goodness of fit (represented by the model likelihood) and model complexity, and is described by Equation 3.1, where k is the number of model parameters, and l is the maximum value

of the likelihood function. AIC's applicability in comparing non-nested models also supports its suitability over other methods (e.g., the F-test).

$$AIC = 2k - 2\ln(l). \tag{3.1}$$

Two AIC values can be compared to determine a model's relative likelihood, L. The relative likelihood is how likely one model is, compared to a reference model with a smaller AIC value, to minimise the information loss [*Burnham and Anderson*, 2003]. The relative likelihood is calculated using Equation 3.2, where AIC_{min} is the minimum AIC value, and AIC_i is the model for comparison.

$$ln(L) = (AIC_{min} - AIC_i)/2 \tag{3.2}$$

The model inputs are detailed in Table B.4, initial conditions and range in Table B.5, model results are summarised in Table B.6, and root-mean-square (rms) and AIC values in Table B.7. The location (0,0) in our models is the centre of the caldera: 38.381° E 7.192° N [*Lloyd et al.*, 2018] (see Figure 3.1b).

In our inversion we allowed the parameters to explore the full parameter space, for example for a strike between 0 – 360°. The table of results are presented in this way (Table B.6), but in the interest of visual comparisons we re-frame some of the model parameters, i.e., a 10 x 10 km Okada model with strike 90° would plot in the same place as a 10 x 10 km Okada model with a strike of 180° in Figure 3.4c.

Model results

For the Mogi model the joint posterior probability density functions for the 2008 – 2010, 2015 – 2016, and combined (which uses all of the data) inversions, overlap near 0 km north and 2.0 km east of the centre of the caldera (Figure 3.4a), between Urji and Chabi (Figure 3.4f). Their marginal probability density functions for the depth also overlap between ∼6.4 km and 6.6 km (Figure 3.4b). This qualitatively suggests that the source is similar during these time periods. In contrast, the 2014 – 2015 source sits away from the other models in both the X – Y and depth – volume change parameter spaces (Figure 3.4a and b). The optimal rates of volume change are 0.5 x 10^7 to 1.2 x 10^7 m^3/yr for 2008 – 2010 and 2015 – 2016 respectively, and 0.9 x 10^7 m^3/yr (combined) (Figures 3.4b and B.2). The 2014 – 2015 Mogi model inversion produces a clearly different solution: a source that sits 0.9 km further to the north (0.6 – 1.1 km, 95% confidence), deeper (7.2 – 8.2 km, 95% confidence) and with a significantly greater rate of volume change (2.4 x 10^7 m^3/yr, 95% confidence: 2.1 – 2.8 x 10^7 m^3/yr).

However, although a Mogi source is able to model each time period relatively well and the inferred locations are consistent within error, a joint inversion using a single Mogi source for all the time periods combined fits the data less well. A source at 6.6 km with a rate of volume change of 0.9 x 10^7 m^3/yr over-predicts the uplift between 2008 – 2010, but under-predicts the uplift between 2014 – 2015 and 2015 – 2016 (Figure 3.5). The 2008 – 2010 and 2015 – 2016 time periods are more similar, and a single Mogi source fits the combined data from these time periods well (Figure 3.5). This location is able to explain the 2014 – 2015 signal in most of the caldera, but there are residuals in the north (Figure 3.5).

The inversion for an Okada model yields similar ranges of estimated model parameters (Figures 3.4c–e and B.3). Figure 3.4c shows the X and Y locations for the centre of the Okada model. Depth against opening per year shows a trade-off that is the same shape for the 2008 – 2010, 2015 – 2016, and combined models, suggesting the source is between 6 and 8 km deep, with an opening between 0.07 and 0.19 m/yr (Figure 3.4d). The 2014 – 2015 trade-off has the same trend, but greater opening per year. Figure 3.4e shows the optimal Okada models are ∼7 x 11 km in size, (aspect ratios of 1.47 (2008 – 2010), 1.57 (2014 – 2015), 1.1 (2015 – 2016) and 1.53 (combined)) indicating a slight elongation. The Okada models are all orientated with long axis ∼097° – 112° (Table B.6), and coincide with the surface expressions of Urji and Chabi. We find the rate of volume change of the combined Okada model (Figure B.3) is comparable to the volume change of the combined Mogi model, but lower by ∼10%.

The residuals to the GPS data used in the combined inversion also reflect the pattern seen in the InSAR. For both the Mogi and Okada models, deformation at station CO1G, 1.4 km away from the source, is under-predicted (Figure B.5). At distal stations, the vertical component of the deformation is consistent with the observations, but the amplitude and orientation of the horizontal components are not. This suggests that our models do not completely capture the source geometry, which in reality may be more vertically ellipsoidal, which would produce a higher vertical to horizontal deformation ratio.

Statistical model selection

For the 2008 – 2010, 2014 – 2015, and combined inversions the Okada source fits the data better than the Mogi source (Table B.7). However, in all cases the AIC values indicate that the increase in fit cannot be statistically justified given the increase in the number of model parameters, and therefore there is a preference for the more simple Mogi model (Table B.7). For the combined inversion, the Okada model is 0.7 times as probable to minimise the information loss (fit the data) as well as the Mogi model.

The offset in the joint posterior probability density functions for both the Mogi and Okada models suggests qualitatively that the source during 2014 – 2015 is different to during 2008 – 2010 and 2015 – 2016. To test this, we compared three Mogi model situations using AIC: one where a single set of parameters describes all of the data (the combined model), one where the parameters in each time step are independent, and one where the parameters during 2014 – 2015 are independent of 2008 – 2011 and 2015 – 2016, which are the same. In the former case l in Equation 3.1 is the product of the maximum likelihood function values of the three models, and k is the sum of the number of parameters in each model. The AIC value for the independent parameters model is -12.7, for the constant parameters model AIC = 2.5, and for the independent 2014 – 2015 model AIC = -5.4. These AIC values indicate that the data are best modelled using separate model parameters through time.

We also test whether the residuals to the models can be explained by the inclusion of a second, shallower source [e.g., *Lloyd et al.*, 2018], but find that it cannot be justified over the 2014 – 2015 time interval (Appendix B).

3.5.2. Volume change time series

Since the individual models suggest that the source varies throughout 2008 – 2017 (Figures 3.5 and B.4), we investigate whether the temporal evolution can be explained by a varying volume change of a fixed source through time using the methodology of *Biggs et al.* [2010b], [*Hutchison et al.*, 2016; *Parks et al.*, 2015]. The inversion is based on the small baseline subset (SBAS) time series approach to produce a time series of deformation for each data point independently, and can combine networks of unconnected interferograms through singular value decomposition [*Berardino et al.*, 2002] with campaign and continuous GPS. The use of a simple analytical source model allows us to combine datasets with different 3-component observation vectors, since the observed surface displacement can be predicted through the scalar product of the 3-component observation vectors and the predicted deformation caused by the source. Furthermore, the use of a fixed source does not require data points to be present in all time periods, allowing the incorporation of interferometric datasets with spatially variable coherence. A full explanation of the method can be found in *Biggs et al.* [2010b].

We use a Mogi source as the AIC values are lower than those for the Okada model. The exact nature of the source is unimportant, since it acts as a Green's function to represent the shape of the surface deformation, and the goal here is to investigate temporal changes in the location or volume change of the source.

We invert for the location and volume change of the Mogi source at a fixed depth, using the same material properties for the subsurface as before. We use the latitude,

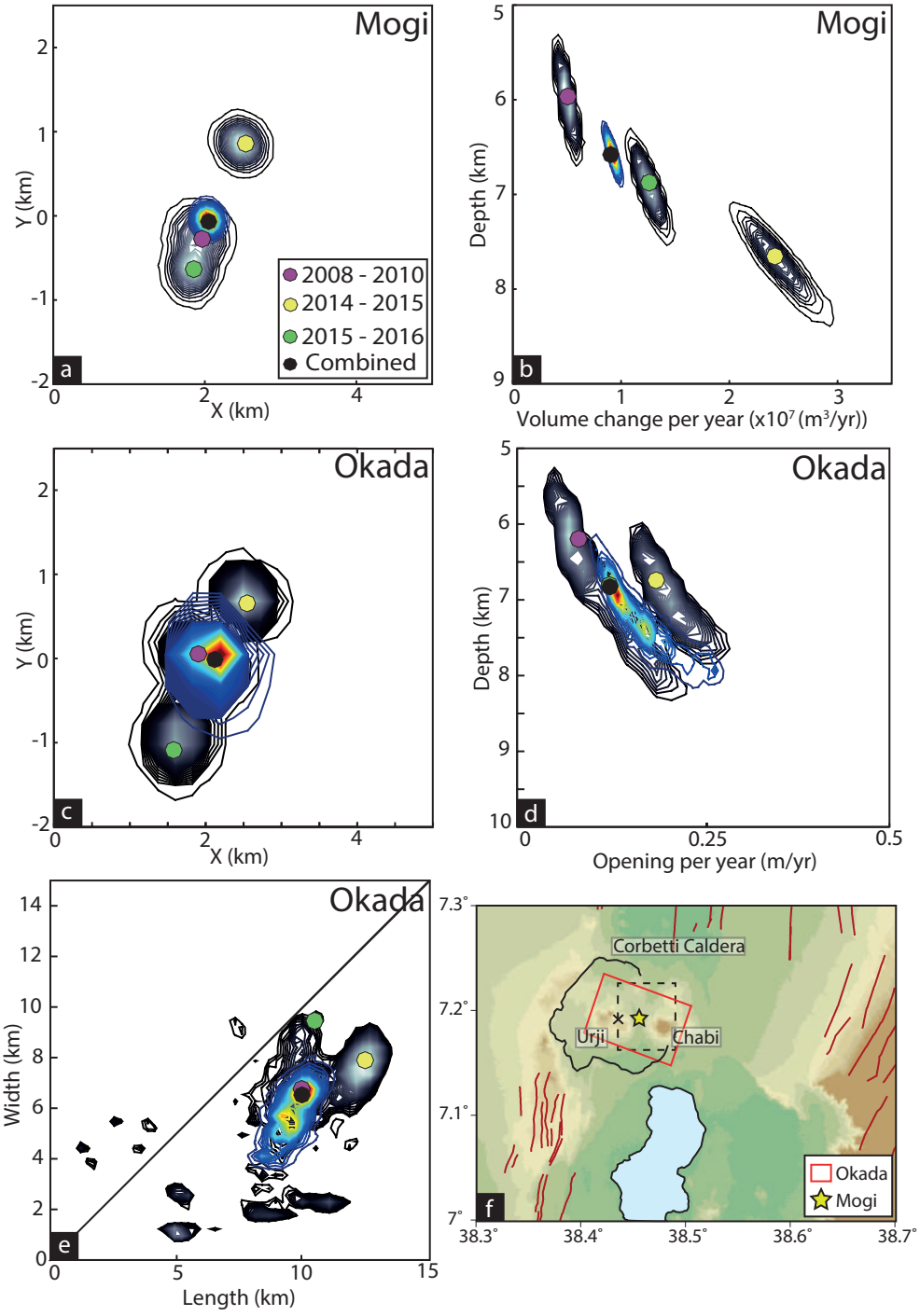

Figure 3.4: Joint probability density functions for key model parameters for the Mogi and Okada models using the combined, 2008 – 2010, 2014 – 2015, and 2015 – 2016 datasets, plotted together. In all subplots greyscale contours correspond to individual time period inversions, coloured contours represent the combined inversion. Coloured circles denote the optimal values. a) Mogi X against Y position, b) Mogi volume change per year against depth, c) Okada X against Y position, d) Okada opening per year against depth, e) Okada length against width. Subplot (f) shows the location of the combined inversion Mogi (yellow star) and Okada (red rectangle) sources with the caldera outline. The dashed region represents the extent shown by (a) and (b).

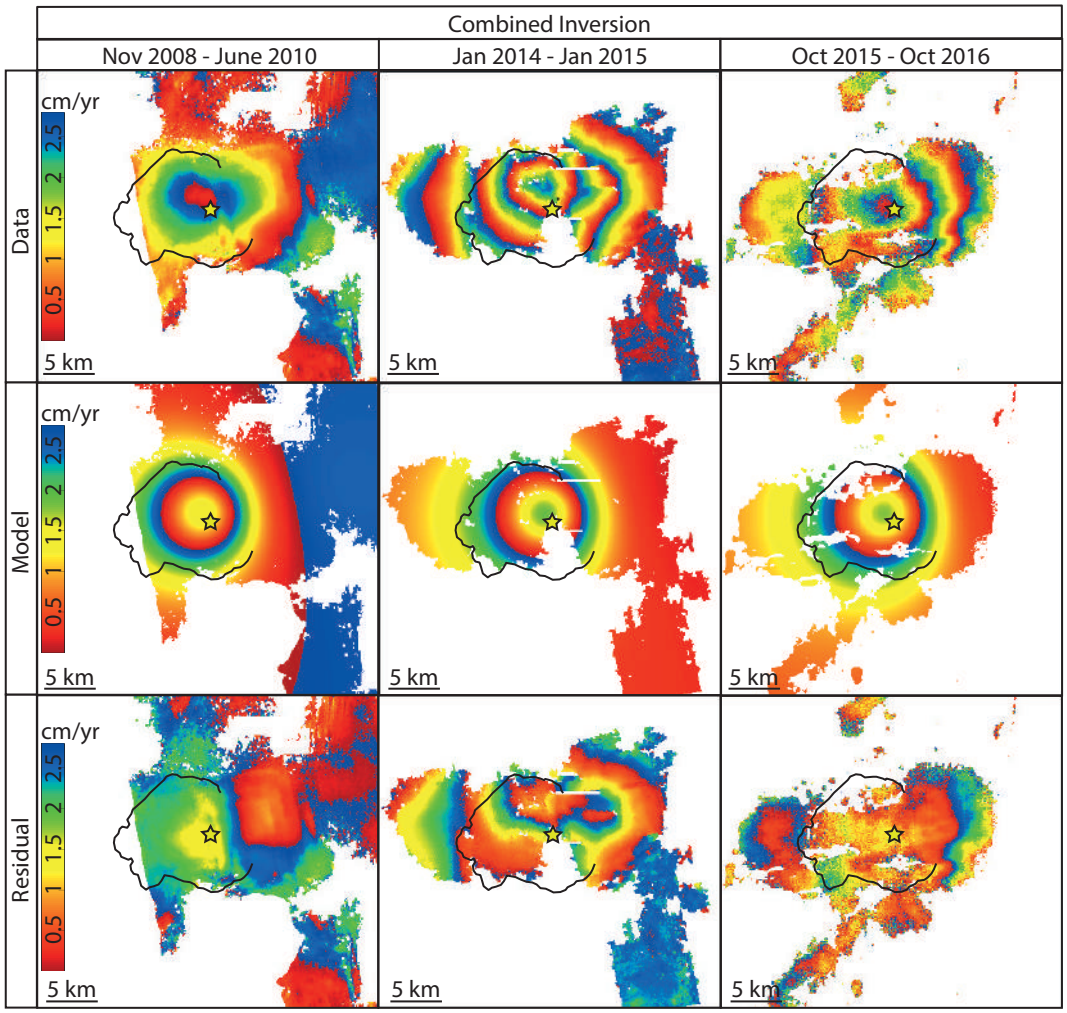

Figure 3.5: Mogi model data-model-residual plots (wrapped) for an interferogram from each time period used in the combined inversion. The caldera outline is shown on each subplot, which corresponds to that in Figure 3.1. The yellow star denotes the location of the Mogi source.

longitude and depth from the optimal combined source inversion to act as a guide for a grid search to find the best fitting location within a 0.1° x 0.1° region at depth slices between 4.6 – 8.6 km (Figures 3.6b, d–f, and B.6). Each interferogram is down-sampled by a factor of 2 within 8 km of the surface projection of the source, and a factor of 8 outside of 8 km. The error in each interferogram is based on the standard deviation outside of this 8 km radius, and is propagated through the inversion.

We perform an inversion for the cumulative volume change between 09/11/2008 and 30/09/2010 (ALOS data, 13 interferograms), and 03/03/2012 and 28/01/2017 (CSK: 42 ascending and 38 descending interferograms, Sentinel-1: 32 ascending and 34 descending interferograms, and the 3-component GPS from all 4 stations within the caldera). We chose to exclude the ENVISAT data from this inversion as most interferograms were either too incoherent, too noisy, or covered the period with no deformation. For the 2012 – 2017 period we repeat the inversion using GPS data only, InSAR data only, and GPS and InSAR data together (Figure 3.6). In all inversions we use the weekly 3-component GPS solutions at each station.

Volume change time series results: 2012 – 2017

The total volume change using the InSAR and GPS data between 03/03/2012 and 28/01/2017 is 4.2 ± 0.5 x 10^7 m^3 (Figure 3.6c). From 22/03/2013, when the GPS data become available, the rate of volume change is 1.1 ± 0.1 x 10^7 m^3/yr. Between 03/03/2012 and 14/04/2013 this rate is low: 0.9 ± 1.0 x 10^6 m^3/yr. This result is likely to be because any displacement during this period is only observed in the CSK interferograms, which at this time have poor coherence and are thus unable to constrain the full spatial extent and temporal evolution of any displacement. The low volume change estimates before April 2013 are therefore probably related to the data availability. This result is included for completeness, but we do not discuss it further.

According to the grid search the best fitting location of the Mogi source for 03/05/2012 – 28/01/2017 is situated ∼1.5 km NE of the centre of the caldera (Figure 3.6f). For the GPS data alone (Figure 3.6d) there is a corridor of preferred locations which traverses NW-SE through the caldera, between the GPS stations. The InSAR only inversion is able to constrain that the source is not east of the caldera, as many of the interferograms used in the inversion are only coherent in this region, over the Chabi basalts (Figure 3.6e). By combining the datasets though, the inversion is able to constrain the source location well, to near the centre of the caldera (Figure 3.6f), consistent with the Bayesian inversion result. For this inversion we selected to use the model depth result from Section 3.5.1, as the methodology and more coherent data used in that inversion have greater sensitivity to source depth.

Next, we perform a curve fitting analysis to investigate temporal changes in the rate of volume change after April 2013. This volume change can be described well by a linear function with time, with gradient of 1.12 x 10^7 m^3/yr (95% confidence bounds: 1.09 – 1.15 x 10^7 m^3/yr) (solid blue line, Figure 3.6c). The coefficient of determination (r^2) of this fit is 0.96, and the mean rms to the data is 1.9 x 10^6 m^3, smaller than the mean uncertainty (3.5 x 10^6 m^3). The dashed line on Figure 3.6c shows the optimal rate from the previous inversion for the 2015 – 2016 time period for comparison (Table B.6). This rate agrees well with the linear function calculated here.

Although the volume change for a single model is, within error, constant with time during 2013 – 2017, the model residuals (Section 3.5.1) suggest source variation during 2014 – 2015. To test this we investigate temporal variations in the model residuals using the rms to each interferogram in the time series analysis, and find they do increase 2014 – 2015, compared to outside this time period (see Appendix B, Figure B.7a). The increase is small however, and not discussed further.

Volume change time series results: 2008 – 2010

We apply the same method to the inversion of ALOS data and find a 14 ± 0.08 x 10^6 m^3 volume increase from the start of the data, 09/11/2008, to 30/09/2010. However, the data are unable to explicitly constrain the deformation onset (Figure 3.3d), so we calculate a rate of volume change from when individual interferograms show deformation: 26/09/2009 to 30/09/2010. The best fitting rate is 1.0 x 10^7 m^3/yr (95% confidence intervals 0.6 – 1.4 x 10^7 m^3/yr) (solid line, Figure 3.6a), which is consistent with the rate of volume change derived from the non-linear source inversion for individual interferograms. By assuming that the volume change began and continued to behave linearly before 29/09/2009 we can extrapolate back to find the date at which the volume change began. This date is the 19/05/2009. The 95% confidence range of this date: 13/04/2009 and 18/07/2009, is consistent with the independent constraints on the onset of the surface deformation using ENVISAT data (after 05/03/2009).

The best fitting source location is in the north-east of the caldera, away from the main resurgent centres of volcanism (Chabi: ∼4 km, Urji: ∼7 km) and ∼3 km NE of the optimal location from the combined source inversion (Figure 3.6b, yellow star). The depth with minimum rms is 6.6 km (Figure B.6a), coincident with the combined source inversion.

All of the previous inversions agree on a source with a rate of volume change of ∼1.0 x 10^7 m^3/yr, and a depth of ∼6.6 km. However, residuals to the inversions for a source

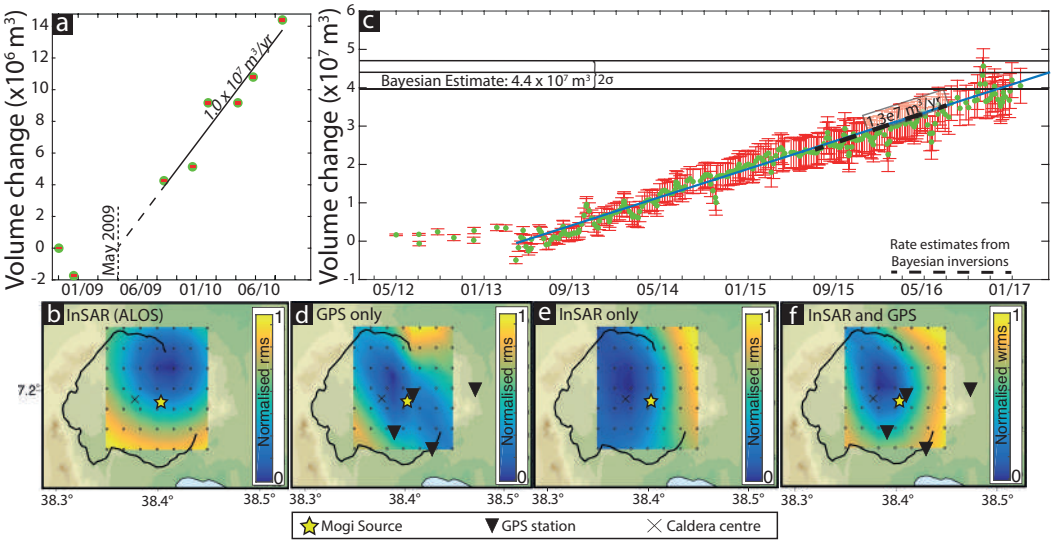

Figure 3.6: a) Cumulative volume change at Corbetti 09/11/2008 – 30/09/2010. b) Minimum root-mean-square (rms) source locations from grid search (0.015° spacings) for optimal source location. Source is fixed at 6.6 km depth. The black cross denotes the centre of the caldera [*Lloyd et al.*, 2018], and yellow star shows the best fitting source location from the combined Bayesian inversion. c) Cumulative volume change at Corbetti 03/05/2012 – 28/01/2017. The black dashed line shows the volume change estimates from the Bayesian inversion for the 2015 – 2016 time period. The blue line represents the best linear fit to the data 13/04/2013 – 27/01/2017. d–f) Interpolated minimum root-mean-square source locations from grid search (0.015° spacings) for optimal source location using GPS (d), InSAR (e) and InSAR and GPS (f), for a source fixed at 6.6 km depth. The black cross denotes the centre of the caldera [*Lloyd et al.*, 2018]. The yellow star shows the best fitting source location from the combined Bayesian inversion.

model suggest that there is a variation in the rate of volume change, depth, or both, specifically during 2014 – 2015 (Figures 3.5, B.4, and B.7). The inversion for the time series of volume change allows us to test whether variations in rate of volume change are able to describe the data, by fixing the depth. The time series using a fixed depth shows a strikingly linear increase in volume change between 2013 and 2017, and the total volume of 4.2 ± 0.5 x 10^7 m^3 (Figure 3.6c) is within error of the total volume change estimated using the rate from the source model inversion (Section 3.5.1) over the same duration of time (4.9 years): 4.4 ± 0.4 x 10^7 m^3. This therefore suggests that either the source depth, or depth and volume change may vary during 2014 – 2015. The location of the model residuals indicates a preference for this deeper source to be in the north, or, more likely, a northwards deeper continuation of the primary source.

3.6. New and existing subsurface geophysics

Volcanic-tectonic seismicity is an indicator of brittle rock failure, caused by subsurface stress changes in a volcanic setting. Between January 2012 – January 2014 an array of seven seismic stations were deployed at Corbetti (Figure 3.1b, Table B.8), with up to five working at any given time. C01E, C02E, and C03E were deployed in January 2012, C05E and C06E in January 2013. C03E was relocated to C04E in May 2014. C07E was deployed in October 2013 [*Wilks*, 2016]. P- and S-wave first-breaks were picked manually, with weightings based on their quality. These weightings (given values of 0 to 3) are related to P-wave arrival time uncertainties of 0.05, 0.1, 0.2, and 0.5 s, and S-wave uncertainties of 0.1, 0.2, 0.3, and 0.5 s [*Wilks*, 2016]. We use the probabilistic, non-linear earthquake location software NONLINLOC to locate the seismicity [*Lomax et al.*, 2000], using seismic arrival times and a 1-D velocity model from *Daly et al.* [2008], derived from seismic tomography in the northern MER. For the larger events, additional constraints on the seismicity at Corbetti were made, where possible, from a nearby seismic deployment at Aluto [*Wilks et al.*, 2017a].

The network detected 224 earthquakes within 15 km of the caldera centre, between local magnitudes 0.22 and 2.77. Of the events with <2 km uncertainty there is a cluster of seismicity located between Chabi and Urji (Figure 3.7a). Peaks in the number of events at Corbetti occur primarily in the shallow subsurface (above sea level) and at depths between 3 and 5 km (Figure 3.7b). Some seismicity also extends down to ∼9 km. The shallow seismicity is likely within a hydrothermal system [*Wilks et al.*, 2017a], but earthquakes with depths 3 – 5 km are consistent with brittle fracture above a source ∼6.5 km below the surface. Figure 3.7b shows these earthquakes projected onto an MT profile [*Gíslason et al.*, 2015], where it can be seen they occur around the conductive anomaly in regions of higher resistivity. This location is also along the large fault structure that cross-cuts the caldera [*Lloyd et al.*, 2018] (Figure 3.7).

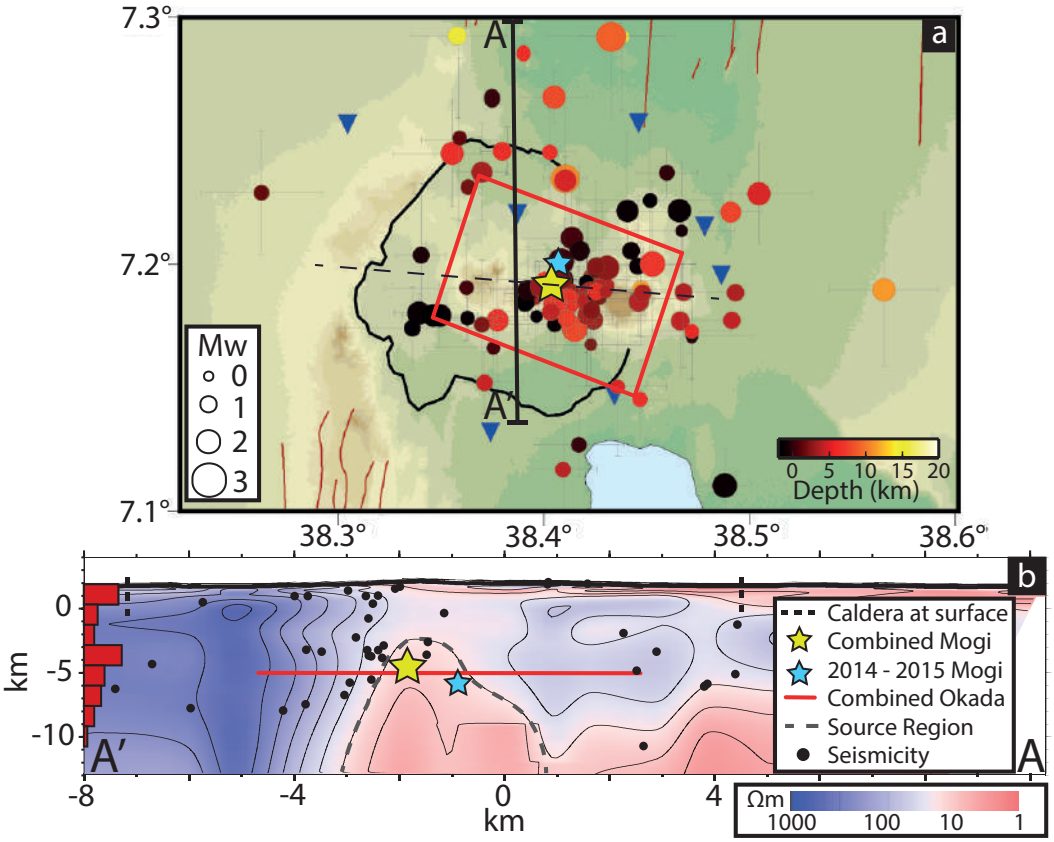

Figure 3.7: a) Seismicity at Corbetti January 2012 to January 2014, coloured by depth and sized by magnitude [*Wilks*, 2016]. Blue triangles are seismic stations. The yellow star is the optimal Mogi source location from the combined Bayesian inversion, the red rectangle is the optimal Okada model using the same data. The blue star is the optimal Mogi location from the 2014 – 2015 Bayesian inversion. Profile A-A' is a profile through the magnetotelluric data, shown in subplot (b). Dashed line shows orientation of cross-rift structure that intersects Corbetti [*Lloyd et al.*, 2018]. b) Ground resistivity at Corbetti along the north-south profile A-A' on subplot (a) [*Gíslason et al.*, 2015], with optimal sources the Mogi models overlain. Black dots represent earthquakes that occurred within 5 km of the profiles, with <2 km X, Y, and Z uncertainty. Histogram on the left of the profile shows the relative number of earthquakes with depth.

3.7. Discussion

We have modelled the uplift at Corbetti by mathematically approximating the source as a point source and the subsurface as an elastic half-space. Simple analytical approaches are important to understand systems where subsurface conditions are poorly constrained, but the inherent assumptions usually oversimplify natural systems. In this section we discuss what our model might physically represent, and the implications for reservoir architecture, magma flux, and eruption potential. We also discuss the limitations that simplified assumptions of the subsurface physical properties, such as magma compressibility and viscoelastic behaviour, may have on our interpretations.

3.7.1. Reservoir architecture

The best-fitting source model is a point source at a depth of ∼6 – 7 km beneath Corbetti, which has been inflating for over 8 years. The source is located between the two major centres of resurgent volcanism (Chabi and Urji) which are considered to be geochemically homogeneous but exhibit contrasting styles of volcanism [*Rapprich et al.*, 2016]. The chemical homogeneity suggests that the eruptive products from both volcanoes have a common long-lasting (10^3 – 10^4 years) source. The Mogi source from the combined inversion (yellow star, Figure 3.7b) is co-located with a region of elevated conductivity. The depth and duration of the deformation, in addition to the coincident elevated conductivities, and occurrence of seismicity, suggest that the source is magmatic [*Cardona et al.*, 2018; *Lu et al.*, 2010; *Heise et al.*, 2010].

In Figure 3.7a we also show the location of the optimal Mogi model from the 2014 – 2015 source inversion (blue star), which is located 7.6 km deep and ∼1 km north of the combined Mogi source. This hints at a deeper source, or deeper northward extension of the source, that is consistent with the shape of the conductive anomaly. Our observations, and comparisons to other systems suggest the geophysical data likely image a large interconnected storage network [e.g., *Biggs et al.*, 2016; *Greenfield and White*, 2015; *Tarasewicz et al.*, 2012], such as a series of vertically stacked sills [e.g., *Field et al.*, 2012].

The analytical model solutions assume an elastic half-space rheology for the crust such that volume changes within the source produce an instantaneous response at the surface. Hot or fractured rocks may behave viscoelastically, however. At long-lived volcanic systems like Corbetti, where the crust has likely been repeatedly thermally primed by numerous earlier intrusions [*Rapprich et al.*, 2016], the viscoelastic response may have a significant influence on the location, amplitude, and temporal evolution of the observed surface deformation [e.g., *Masterlark*, 2007; *Hickey et al.*, 2016]. At the Aira

and Santorini calderas sustained uplift is thought to be driven by pulses of magma injection accompanied by seismicity, that is separated by aseismic gaps where uplift is sustained by the viscoelastic response [*Hickey et al.*, 2016; *Parks et al.*, 2015].

At Corbetti the rate of volume change is constant through time for the two studied time intervals (Figure 3.6). For a source in a viscoelastic medium, this could be explained in one of three ways: 1) through continuous magma injection, 2) a single magma injection pulse followed by viscoelastic relaxation over a time period much greater than the continuously observed time period (>5 years), or 3) pulsed magma injections, where the time between pulses is much shorter than the relaxation time. The single injection case requires a relaxation time of greater than 5 years, which is more than an order of magnitude greater than Campi Flegrei, for example (∼months, [*Bonafede and Ferrari*, 2009]). Campi Flegrei has been modelled previously as a source embedded in a viscoelastic shell [*Dragoni and Magnanensi*, 1989]. Corbetti would therefore require a relatively thicker shell or higher viscosity in comparison [*Newman et al.*, 2001; *Dragoni and Magnanensi*, 1989]. On the other hand, regular pulsed injections are not supported by the observed seismicity. Therefore, we conclude that the system is likely being fed by a continuous phase of magma injection.

3.7.2. Magma flux

In the period 2009 – 2017, the inversion of the observed surface deformation indicates a volume addition of 0.9 – 1.1 x 10^7 m^3/yr. Geological observations show that post-caldera eruptive products are dominantly peralkaline rhyolites [*Fontijn et al.*, 2018; *Rapprich et al.*, 2016; *Di Paola*, 1971] which are produced following extreme fractional crystallisation of mafic material [*Rapprich et al.*, 2016; *Peccerillo et al.*, 2007]. Analysis using trace elements from Pantelleria and Aluto suggests 90 – 96% fractional crystallisation of the parental alkali basalts is required to fractionate pantellerite melts [*Gleeson et al.*, 2017; *Neave et al.*, 2012]. At Corbetti magmas of intermediate chemical composition are absent in the post-caldera eruptive record and the pantellerites have low crystallinity [*Rapprich et al.*, 2016]. This implies that a high proportion of the mafic input material is still within a subsurface reservoir, and that much of the long-term intruded volume is not erupted.

Observations of erupted volcanic products at Corbetti suggest that 'typical' eruptions have a volume of up to ∼5 x 10^8 m^3 (dense rock equivalent) [*Rapprich et al.*, 2016]. Taking an ∼900 year recurrence interval (over the last 10 k.y., [*Martin - Jones et al.*, 2017]), and assuming ∼5 x 10^8 m^3 per eruption, gives a long-term eruption rate of ∼6 x 10^5 m^3/yr. Fractionation of 90 – 96% implies that the peralkaline eruption rate should be ∼4 – 10% of the basaltic magma supply rate. Assuming all of the fractionated,

peralkaline material is erupted this would give an estimated supply rate of 0.5 – 1.4 x 10^7 m^3/yr.

We discuss two plausible end-member scenarios to explain the inflation episode we observe at Corbetti: 1) the input of parental alkali basalts, or 2) the transportation of fractionated peralkaline rhyolite. In the following calculations for both scenarios we assume that all of the fractionated material is eruptible. In the first scenario, at the observed rate of volume addition (10^7 m^3/yr) of parental basalt it would take 500 – 1500 years to accumulate enough material to fractionate ∼5 x 10^8 m^3 of peralkaline magma (from ∼1.25 x 10^{10} m^3 of intruded basalt) (see Figure B.2 for the distribution of peralkaline volumes and timescales given 90% and 96% fractionation, and the volume change confidence thresholds). This time period encompasses the recurrence interval estimated by *Martin - Jones et al.* [2017]. However, this implies the current rate of volume change is continuous, which contrasts with previously observed periods of no deformation or subsidence [*Lloyd et al.*, 2018; *Biggs et al.*, 2011].

Alternatively, the observed deformation may represent the transport of peralkaline rhyolites. The reservoir is likely to be a laterally- and vertically-extensive mush zone, with multiple melt-rich lenses. A broad zone of subsidence has been observed around uplift caused by vertical magma migration [*Henderson and Pritchard*, 2017], but these observations are rare, and coherence outside the volcanic centre at Corbetti is likely too poor for any such signal to be detected. A volume addition of 10^7 m^3/yr would take ∼50 years to produce 5 x 10^8 m^3 of peralkaline magma. The flux period is much shorter than the recurrence interval, and may suggest that eruptible magma reservoirs form through pulsed magma fluxes, a conclusion supported by thermal models [e.g., *Menand et al.*, 2015]. This volume of fractionated material (10^7 m^3/yr), assuming it is 4 – 10% of the parental basalt supply rate, implies a large long-term basaltic supply rate of ∼10^8 m^3/yr (Figure B.2). This rate is larger than our estimate from erupted products, but this discrepancy may come from eruptions missing in the geological record (*Martin - Jones et al.* [2017] only consider the largest events), or a non-continuous basalt supply rate.

Based on our discussion above, the magma flux beneath Corbetti is between 10^7 m^3/yr (assuming direct observation of parental basaltic magma input) and 10^8 m^3/yr (derived basaltic flux, assuming we are observing the vertical movement of the evolved component). Estimates of the flux required for magma to remain unfrozen in the crust vary depending on magma composition, the state of the intruded crust, and tectonic environment, but relevant estimates are between 10^5 – 10^7 m^3/yr [e.g., *Karakas and Dufek*, 2015; *Menand et al.*, 2015; *Annen*, 2009]. At Corbetti our estimated flux is greater than this limit and so, if continuous, would be more than sufficient to sustain a long-lived reservoir. The flux is also in line with estimates from other caldera systems [e.g., *Jellinek and DePaolo*, 2003].

3.7.3. Eruption potential

One purpose of observing volcano deformation is to understand the current volcanic system, and/or the societal impact activity may have. Numerous factors influence the hazard potential of a volcano, but quantification of where, how much, and how quickly magma is stored is critical to understanding the magnitude of a possible eruption. This is especially true at volcanoes with no previously observed eruptions close to large population centres, like Corbetti.

A magmatic reservoir will fail when a critical overpressure is reached, resulting in either eruption, or lateral magma movement over a variety of scales [e.g., *Gudmundsson*, 2012; *Gudmundsson and Nilsen*, 2006]. Reservoir failure can be triggered internally or externally, e.g., via roof failure or sector collapse [e.g., *Biggs et al.*, 2016; *Gregg et al.*, 2012; *Voight et al.*, 2006; *Lipman et al.*, 1981]. External triggers represent a source of unpredictability of potential eruptions, and are not considered here. At Corbetti, there is no evidence of an eruption in recent decades, or major form of reservoir failure, meaning the reservoir must be large and/or compressible enough to accommodate the strain associated with the intruding magma [*Degruyter et al.*, 2016; *Gottsmann and Odbert*, 2014]. External evidence for a large ($\sim 10^2$ km^3) magma reservoir comes from the MT observations and the high degree of fractionation required to produce the peralkaline, aphyric erupted products. Whether the reservoir at Corbetti will fail following this deformation event will depend on many currently unconstrained factors, including the magma compressibility, and the thermal maturity of the system [*Karakas et al.*, 2017; *Schöpa and Annen*, 2013].

Although there is a statistically significant link between volcano deformation and eruption, this link is weaker in rift settings, and calderas [*Biggs et al.*, 2014]. At many volcanoes, periods of deformation associated with magma occur in the absence of eruptions [e.g., *Ebmeier et al.*, 2018; *Le Mével et al.*, 2015; *Biggs et al.*, 2009b; *Pedersen and Sigmundsson*, 2004; *Amelung et al.*, 2000]. These episodes are usually attributed to magma reservoir growth or re-organisation, and could represent the processes currently ongoing at Corbetti should no eruption occur.

3.8. Conclusions

From a combination of data from four SAR satellites/constellations and a network of continuous GPS sites we observe 7 cm/yr of uplift at Corbetti directly above the source,

which has been ongoing since 2009, in response to a subsurface volume change of $\sim 10^7$ m^3/yr. Evidence from the depth, duration, rate, and modelling of this deformation, as well as seismic and magnetotelluric data, strongly suggest that the origin of this source is a pulse of magma intruding into a pre-existing reservoir.

From an analysis of Bayesian posterior probably density functions as well as the temporal and spatial analysis of model residuals, we identify that the primary magmatic reservoir is at ∼6.6 km depth, with perhaps a deeper northward protrusion (∼7.6 km deep). This is supported by the magnetotelluric observations, and presumably represents a large interconnected magma network. The deformation could be precursory to a reservoir failure and potential subsequent eruption, or represent a period of non-eruptive reservoir growth beneath the volcano.

This work highlights the importance of a framework within which one can combine different geodetic datasets to investigate long-term deformation signals, and a statistically robust method to compare source models.

Chapter 4

The ongoing decade-long Machaze-Zinave aftershock sequence in the slowly straining Mozambique Rift

Lloyd, R., J. Biggs, A. Copley, (2018), *Geophysical Journal International*, *In Prep*

Author contributions and declaration:

J. Biggs supervised the work. A. Copley provided the ENVISAT SAR and processed SPOT5 data, performed the body wave inversion, wrote the body wave methods, and provided advice throughout. The Sentinel-1 data used in this study is available from the European Space Agency (ESA). A. Fagereng, M. Werner, and J. Elliott also provided useful discussions.

Abstract

Southern Mozambique is considered the southernmost expression of the continental East African Rift. Here, extensional rates are low and rifting is achieved through normal faulting. Incipient rift environments provide an ideal location to investigate the role of reactivated pre-existing structures, aftershock sequences, and fault interactions in rift development.

In 2016 a M_w 5.6 earthquake occurred in the Zinave region of southern Mozambique, ∼10 km south-east of the M_w 7.0 2006 Machaze earthquake. We reanalyse ENVISAT InSAR observations of the Machaze earthquake, together with new Sentinel-1 Interferometric Synthetic Aperture Radar (InSAR) observations of the Zinave earthquake, and solve for uniform and distributed slip models for both events. We find the Machaze earthquake occurred on a steeply dipping (∼75°) fault, in agreement with other studies, but that the Zinave earthquake occurred on an ∼60° dipping fault. The Machaze earthquake caused a Coulomb stress increase of ∼0.2 MPa on the Zinave fault. The full >10 year record of seismicity following the Machaze event can be fit by the Omori law, showing that the Zinave earthquake is part of a decade-long aftershock sequence, consistent with long-duration aftershock sequences in other slowly straining regions. Aftershocks represent a major hazard that needs to be considered if a large earthquake were to occur in the southern East African Rift system today.

4.1. Introduction and background

The continental East African Rift System (EARS) is the surface expression of the separation of the Nubian and Somalian tectonic plates. It can be followed southward from Ethiopia to Malawi, south of which extension rates are low (<2 mm/yr) [*Saria et al.*, 2014; *Stamps et al.*, 2008], and the focus of extension is less distinct [*Bird et al.*, 2006; *Chorowicz*, 2005]. South of Malawi two branches of the EARS have been hypothesised based on the distribution of seismicity and faulting. These branches are a) the Luangwa Rift, trending northeast-southwest through Zimbabwe and Botswana [e.g., *Kinabo et al.*, 2007; *Modisi*, 2000; *Scholz et al.*, 1976], and b) the Mozambique Rift, which continues southwards [e.g., *Stamps et al.*, 2018; *Fonseca et al.*, 2014; *Fairhead and Henderson*, 1977] (Figure 4.1a). Faulting in the Mozambique Rift may therefore represent the southernmost and least mature portion of the continental EARS. A band of seismicity can be seen along the Mozambique Rift, from the Urema Graben in the north to the Machaze region of southern Mozambique [*Fonseca et al.*, 2014] (Figure 4.1a). South of Machaze there appears to be little seismicity, possibly suggesting a change in strain rate or crustal rheology. Understanding how and where the EARS extends through this region is important for understanding the development of continental rifts.

In rift environments, pre-existing structures exhibit a control on the distribution of faulting [e.g., *Muirhead and Kattenhorn*, 2018; *Kinabo et al.*, 2008; *Versfelt and Rosendahl*, 1989; *Milani and Davison*, 1988]. This is because the frictional strength of faults, i.e., the stress required for slip on pre-existing faults, can be lower than the stress required for fault formation [*Scholz*, 2002]. Faults therefore represent planes of weakness, and may be reactivated in stress conditions that are not orientated optimally for failure. This has implications for incipient rifting, as large pre-existing structures can control the stress distribution and geometry of a rift [e.g., *Kinabo et al.*, 2008; *Versfelt and Rosendahl*, 1989]. In some regions, however, pre-existing structures are absent, or not suitably orientated for reactivation. In these cases, extension will not be fully accommodated through fault reactivation, and new structures may form.

Co-seismic slip induces stresses on the surrounding rock [*Stein et al.*, 1994; *King et al.*, 1994], which can promote or inhibit failure, either immediately or after a period of time [*Nostro et al.*, 2005; *Tuttle et al.*, 2002]. Indeed, fault interaction plays an important role in influencing earthquake recurrence and fault growth in extensional settings [e.g., *Hodge et al.*, 2018b; *Nicol et al.*, 2010]. In the 2009 Karonga earthquake sequence, Malawi, each new earthquake occurred within a region of positive static stress change from the previous event. This process of segmented fault rupture allowed for the lateral transition of slip on faults over ∼40 km, whilst being confined to the upper ∼10 km [*Fagereng*, 2013; *Biggs et al.*, 2010a].

By studying incipient rifts we can observe rift development processes in action, and we aim to understand the growth and interaction of faults [*Hodge et al.*, 2018b; *Walsh et al.*, 2002; *Scholz et al.*, 1993]. Understanding how faults within a system interact is important in determining the induced or reduced hazard an earthquake might represent for its vicinity [e.g., *Wedmore et al.*, 2017; *Lin and Stein*, 2004]. This is especially true in regions with low strain rates, which can produce long aftershock sequences [*Stein and Liu*, 2009], elevating the hazard for up to hundreds of years after the main shock.

4.1.1. The Mozambique Rift

On 22^{nd} February 2006, a M_w 7.0 normal faulting earthquake occurred in the Machaze region of Mozambique, in the southern East African Rift [*Copley et al.*, 2012; *Yang and Chen*, 2008; *Fenton and Bommer*, 2006]. This normal-faulting earthquake was one of the largest earthquakes in continental Africa for a century, and demonstrates that the region is subject to extensional stresses. On 22^{nd} September 2016, 10.5 years after and <10 km from the Machaze earthquake, a M_w 5.6 normal faulting earthquake occurred in the Zinave National Park (USGS; http://earthquake.usgs.gov). Plate motion models using GPS data, earthquake slip vectors, and geological indicators infer a microplate, the Rovuma, in southern Mozambique. The Machaze-Zinave region sits near the boundary between the Nubian and Rovuma plates [*Saria et al.*, 2014]. This region is also the intersection of a three major inherited structures which obliquely intersect (Figure 4.1a): 1) the ∼E-W Limpopo Belt, hosting the Okavango and Limpopo Dyke Swarms (∼180 Ma and 728 ± 3 – 1683 ± 18 Ma [*Jourdan et al.*, 2006; *Le Gall et al.*, 2002]), 2) the ∼NE-SW tending Urema Graben and other unnamed fault structures north of Machaze [*Steinbruch*, 2010], 3) and the ∼NNW-SSE Mazenga Graben to the south (Figure 4.1a). The Kaapvaal and Zimbabwe Cratons are south-west and north-west of the Machaze region respectively. This region of the Mozambique coastal planes is thought to have a 5 – 10 km thick sedimentary sequence of post-Jurassic age overlying a Precambrian crystalline basement [*Salman and Abdula*, 1995; *Gwavava et al.*, 1992]. Together these structures represent major crustal heterogeneities, but the influence they have on rifting and strain partitioning in southern Africa is unclear.

We chose to investigate the Zinave earthquake using Interferometric Synthetic Aperture Radar (InSAR) and seismology, together with a reanalysis of InSAR for the Machaze event, to better understand the tectonics of southern Mozambique. The region is poorly instrumented and difficult to access, and so satellite geodesy provides an ideal tool to investigate faulting. In this work we investigate the spatial and temporal relationships between the 2006 Machaze and 2016 Zinave earthquakes. The temporal evolution of seismicity following the Machaze earthquake is analysed, and we conclude that the Zinave earthquake is part of an aftershock sequence.

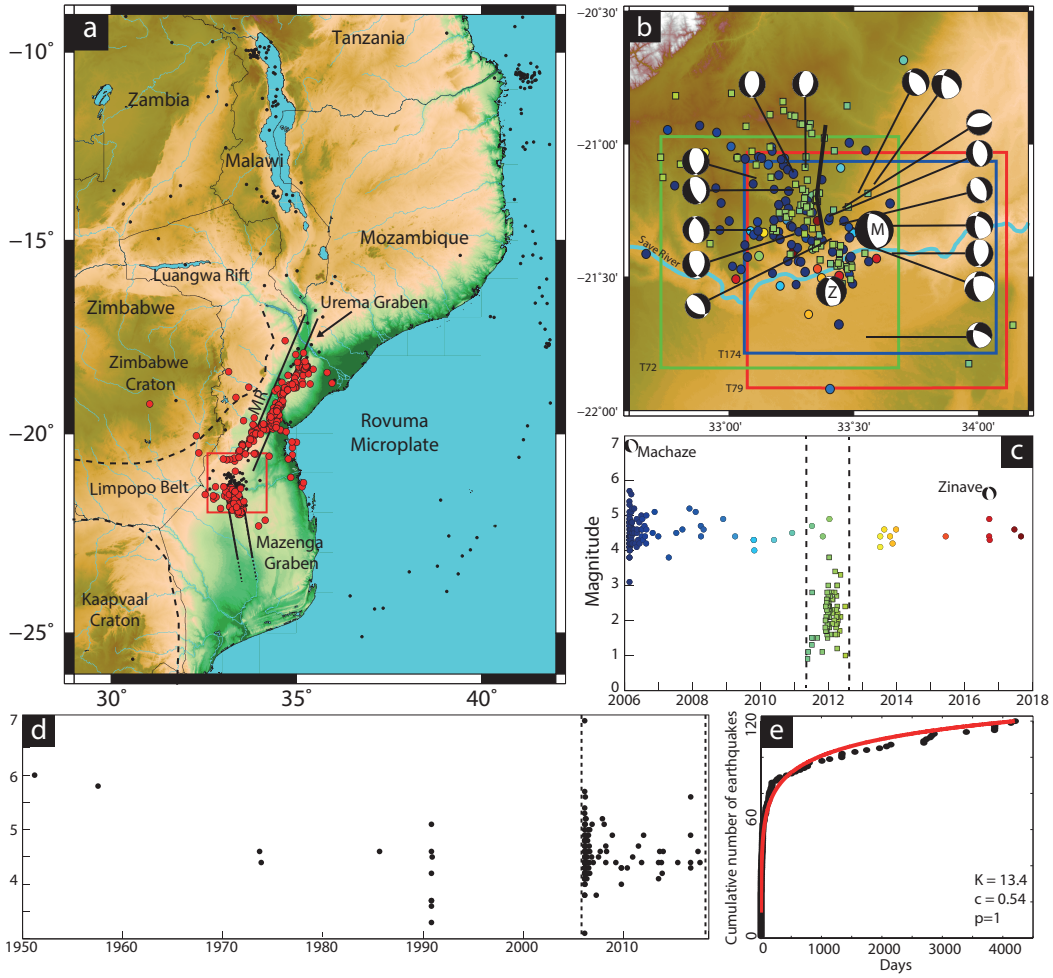

Figure 4.1: a) The southern East African Rift. The red box denotes the extent of sub-panel (b). Black circles show seismicity greater than magnitude 4.5 from the USGS catalogue, red circles represent earthquakes from the MOZART catalogue (2011 – 2013) [*Fonseca et al.*, 2014]. The approximate locations of the Kaapvaal and Zimbabwe Cratons, Limpopo Belt, Lebombo Dykes, Urema Graben, Luangwa Rift, and the Mozambique Rift (MR) are also shown [*Reeves et al.*, 2016; *Fonseca et al.*, 2014]. b) Red, green, and blue boxes show the extent of Sentinel-1 tracks T79, T72, and T174 used in this study, respectively. The USGS focal mechanisms for the Machaze (M) and Zinave (Z) earthquakes are shown, with the earthquakes that occurred since the Machaze event (coloured by time, see sub-panel (c). Circles show USGS solutions, squares are events observed by *Fonseca et al.* [2014]). The black line shows the location of the Machaze fault from *Copley et al.* [2012]. c) Magnitude-time distribution of earthquakes in the Machaze-Zinave region. The dashed lines denote the observation period of *Fonseca et al.* [2014]. d) Seismicity from 1950 – 2018 (USGS catalogue) showing a clear change in the rate of seismicity before and after 2006. The dashed region covers the same time period as on (c). e) Cumulative number of earthquakes (black circles) between the Machaze and Zinave earthquakes (USGS catalogue). The red line shows the Omori law fit, with K=13.4, c=0.54, and p=1.

We process ENVISAT interferograms to investigate the surface deformation of the Machaze event, and three overlapping tracks of Sentinel-1 data for the Zinave earthquake. We then invert the observations of surface deformation for earthquake parameters, using uniform and distributed slip models. For the Zinave earthquake, we compare the geodetic models to seismological estimates of the source parameters from an inversion of body wave waveforms. The Coulomb stress transfer following the Machaze earthquake is then calculated to investigate whether the Zinave fault was brought closer to failure following the Machaze main shock. We discuss the role that the subsurface frictional properties have in the assessment of hazard, and the style of slip that could occur in this region. We relate the occurrence of these earthquakes to fault growth, the role pre-existing structures have on controlling incipient rifting, and the evolution of the East African Rift.

4.2. Seismicity in the Mozambique Rift

The Machaze earthquake occurred on a ∼N-S striking fault that dipped unusually steeply (70° – 75°), to the west [*Attanayake and Fonseca*, 2016; *Copley et al.*, 2012; *Fenton and Bommer*, 2006]. The fault plane is thought to be a reactivated pre-existing structure within the crystalline basement, that has either been steepened or was originally strike slip [*Copley et al.*, 2012; *Yang and Chen*, 2008]. The earthquake ruptured >15 km at the surface, with up to 2 m of vertical offset [*Fenton and Bommer*, 2006]. Models based on ENVISAT interferograms shows that co-seismic slip extended down to ∼25 km depth, with diminishing amplitude between 10 km and the surface [*Copley et al.*, 2012]. This reduction of slip is interpreted to be a result of the juxtaposition of velocity weakening (crystalline basement) and velocity strengthening (sedimentary) lithologies [*Copley et al.*, 2012]. The shallow slip deficit was later partially recovered post-seismically through afterslip in the upper 10 km [*Copley et al.*, 2012]. The control of pre-existing structures and upper-crustal rheology on slip during the earthquake cycle suggests that inherited structures and lithologies play an important role in guiding tectonic rifting here, as has been observed elsewhere in the EARS [e.g., *Kolawole et al.*, 2018; *Ring*, 1994; *Versfelt and Rosendahl*, 1989].

From 1990 to 2006 there was no seismicity observed in the Machaze region, but between the Machaze event and 2018, 134 magnitude 3 or greater earthquakes were recorded (USGS catalogue) (Figure 4.1b and c). Between 2011 and 2013 there was a deployment of 30 seismometers throughout southern Mozambique [*Fonseca et al.*, 2014]. This deployment observed persistent seismicity, with 143 earthquakes greater than a magnitude 0.9 in the Machaze region, indicating that the area remained seismically active (Figure 4.1).

4.2.1. Aftershock sequences

Static and dynamic stress changes from large earthquakes cause aftershocks, which can pose a significant seismic hazard in their own right [*Stein and Liu*, 2009; *Parsons et al.*, 2008; *Wiemer et al.*, 2002]. We test whether the Zinave earthquake belongs to an aftershock sequence following the Machaze earthquake, or is an independent event. The empirical Omori law [*Omori*, 1894] states that the rate of aftershocks is inversely proportional to the time since the main shock. The modified version of this relationship (such that $p \not\equiv 1$) is given by Equation 4.1 [*Dieterich*, 1994; *Utsu*, 1961].

$$F(t) = K/(c+t)^p. \tag{4.1}$$

In the modified Omori law K and c are constants that describe the productivity, and the time-delay of the sequence (a function of catalogue completeness), respectively. The parameter p is related to the heterogeneity of the aftershock region, and can be time dependent [e.g., *Helmstetter and Shaw*, 2006; *Kisslinger and Jones*, 1991]. In our analysis we fix p to be equal to 1 for simplicity, and do not consider aftershocks of aftershocks. The Omori law fits the temporal evolution of the recorded seismicity since the Machaze earthquake well, with $K = 13.4$ and $c = 0.54$ (Figure 4.1e). This observation suggests that the Zinave earthquake is an aftershock which occurred 10.5 years after the Machaze earthquake. The high c value for the sequence indicates the seismic record is likely missing events early in the sequence, which introduces uncertainty in other model parameters, and supports our use of $p = 1$.

4.2.2. Aftershock duration in low strain rate regions

The duration of an aftershock sequence is observed to be inversely proportional to the strain rate, such that regions with low strain rates have long aftershock sequences [*Stein and Liu*, 2009]. This inverse relationship is consistent with a rate-and-state description of fault friction, where the aftershock duration (t_a) is a function of the normal stress (σ_n) and the rate of shear stressing across a fault. The rate of shear stress can be approximated using the relative velocity across a fault with a simple geometry to give Equation 4.2 [*Savage and Burford*, 1973],

$$t_a = (A\sigma_n \pi w)/(\mu v), \tag{4.2}$$

where A is a constitutive parameter [*Dieterich*, 1994], w is the fault width, μ is the rigidity, and v is the relative velocity across the fault. Using typical values of 0.01 for A, 20 km for w, 30 GPa for μ, and 15 MPa for σ_n, *Stein and Liu* [2009] determine an expected aftershock duration (in years) of $314/v$ (for v in mm/yr). In southern Mozambique, where $v \lesssim 2$ mm/yr, we may therefore expect aftershocks, and thus an elevated seismic hazard, to last up to ∼150 years [*Hodge et al.*, 2015; *Goda*, 2012]. Wider faults, a less stiff rheology, or greater normal stress across the fault would all act to increase the expected aftershock sequence duration. A 10% variation in the non-constant values in Equation 4.2, for $v = 2$ mm/yr, results in a range of aftershock durations between 115 to 210 years.

4.3. 2016 Zinave earthquake

The 22^{nd} September 2016 M_w 5.6 Zinave earthquake occurred at 20:06:11 UTC. We use observations of teleseismic body waves and the surface deformation from InSAR to investigate the fault geometry and earthquake kinematics. We invert the InSAR data for co-seismic uniform and distributed slip models.

4.3.1. Body wave inversion

We jointly inverted P and SH waveforms to obtain the strike, dip, rake, centroid depth, and source time function of the Zinave event. Seismograms recorded at epicentral distances of 30° – 80° were band-pass filtered at 15 – 100 s. These measures remove complexities due to lithospheric reverberations, interactions with the core, and short-wavelength complexity in the source process or velocity structure. We can then model the earthquake as a point source, using the MT5 program of *Zwick et al.* [1994] (based on the algorithm of *McCaffrey et al.* [1991] and *McCaffrey and Abers* [1988]). This procedure is now routine, and its application in Africa is described in detail in *Craig et al.* [2011]. P waveforms were weighted 2:1 against the SH waveforms to account for their lower amplitudes, and all seismograms were weighted according to azimuthal coverage. The velocity structure at the source was specified as a simple half-space velocity model, with Vp = 3.9 km/s and Vs = 2.2 km/s, which is based on the crustal structure used in the InSAR inversions (Section 4.3.3).

Our best-fitting model is shown in Figure 4.2. Body wave modelling indicates the earthquake occurred on an 175° striking normal fault, with a dip of 66°, rake of -69°, depth of 7 km, and moment of 9.5 x 10^{16} Nm. The seismic estimate of the strike of this earthquake is comparable to estimates of the Machaze earthquake (175° [*Yang and Chen*, 2008], 172° CMT), but the dip is ∼10° shallower. The resolution of the model is hampered by the lack of clear waveforms at stations in the Atlantic and Indian oceans, and in Antarctica. The errors in our parameters for this event are typical for this technique, and are strike ±10° dip ±5° rake ±10° and centroid depth ±4 km.

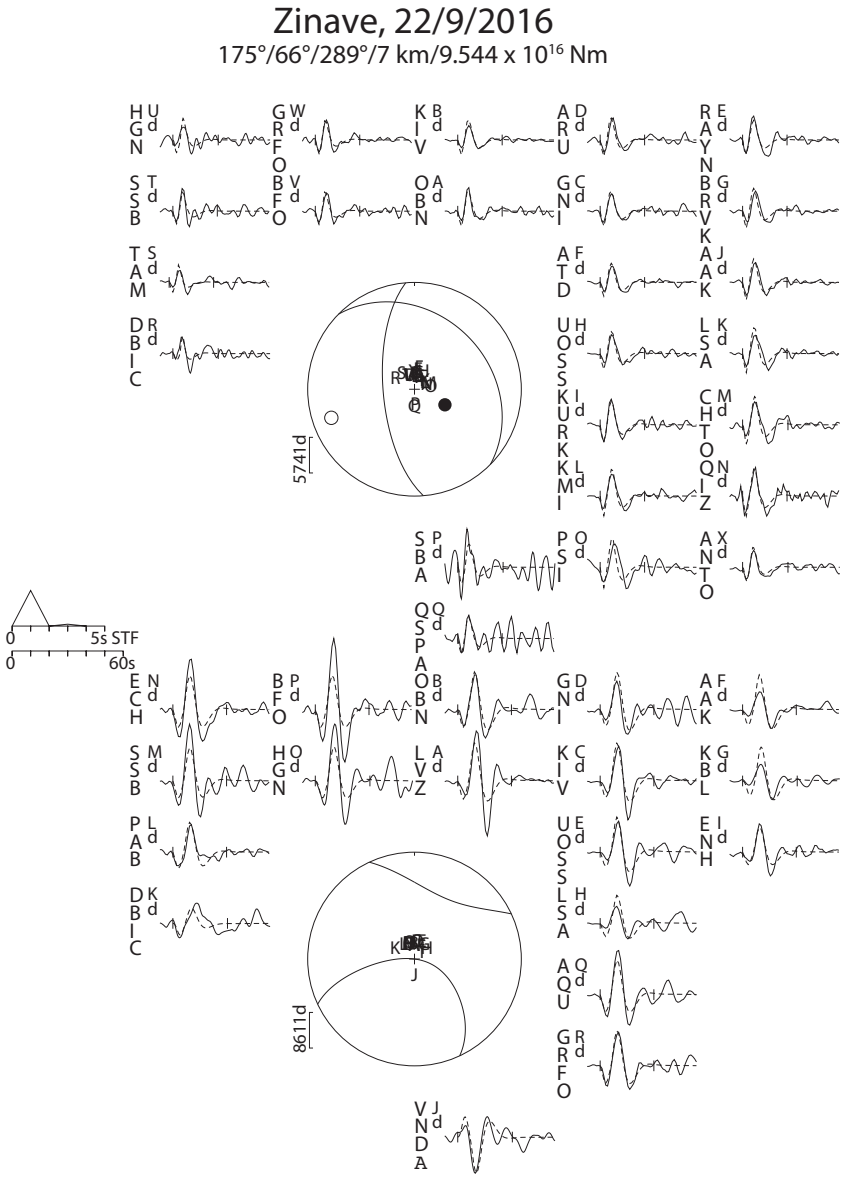

Figure 4.2: Focal mechanisms and source time function obtained from teleseismic body waveform modelling of (top) P and (bottom) SH waves from the Zinave earthquake. Mechanisms are shown as lower hemisphere projections. The best fitting source parameters are: strike 175°, dip 66°, rake -71° (289°), depth of 7 km, and moment of 9.5 x 10^{16} Nm. Seismograms are shown as solid lines next to their station code, synthetic seismograms from the model solution are shown as dashed lines. The take-off angle for each seismogram is shown labelled on the focal sphere. The source time function (STF) is shown in the centre left.

4.3.2. Sentinel-1 InSAR

To investigate the surface deformation associated with the Zinave earthquake we produced 79 Sentinel-1 interferograms, 34 of which are co-seismic, from three tracks (Table C.1). Interferograms were processed using the GAMMA software [*Werner et al.*, 2000], within the LiCSAR facility [*González et al.*, 2016]. We used the 30 m SRTM DEM [*Farr and Kobrick*, 2000] to remove topographic phase contributions, and down-sampled interferograms to a 100 m final pixel size. Each interferogram was filtered (strength 0.85) [*Goldstein and Werner*, 1998], and pixels with coherence values less than 0.8 were masked out.

In tropical regions, atmospheric water vapour can cause artefacts in interferograms, particularly in regions of high topography [e.g., *Parker et al.*, 2015; *Ebmeier et al.*, 2013; *Webley et al.*, 2004]. We see signs of turbulent atmospheric delays in some interferograms, and test using the high resolution European Centre for Medium-Range Weather Forecasts (HRES ECMWF) weather model through the GACOS facility to correct for them [*Yu et al.*, 2017a,b]. However, the model was unable to account for the observed delays, with the corrections increasing the standard deviation in our data (Figure C.1). Weather models are best suited to predicting the stratified component of atmospheric delays, often related to topography. In this region of southern Mozambique there is a maximum of ∼100 m elevation change over ∼100 km^2. As such, we do not expect topography controlled atmospheric delays to be a large source of noise. We use a pair-wise logic approach to identify atmospheric delays, and acquisitions with strong delays were removed [e.g., *Ebmeier et al.*, 2013; *Massonnet and Feigl*, 1995]. To increase the signal-to-noise ratio we stacked co-seismic interferograms from each track, ensuring each acquisition contributed equally (Table C.1, Figure C.2). Each stack was then de-ramped to remove long wavelength atmospheric, orbital, or ionospheric delays.

The Sentinel-1 interferograms show an approximately north-south trending, ∼20 km by ∼10 km region of up to ∼5 cm positive line-of-sight range change, beside a smaller region of ∼1 cm negative line-of-sight range change to the east. The boundary between these two regions is relatively sharp, and the pattern is broadly consistent with that caused by an approximately north-south striking normal fault. All Sentinel-1 interferograms were highly coherent, except for co-seismic ones in the river bed directly above the fault (Figure C.2). We suggest this loss of coherence is caused by liquefaction, a phenomenon that was extensive during the Machaze event [*López-Querol et al.*, 2007]. Chains of post-seismic interferograms for each track, covering up to 3 months after the earthquake, show no significant post-seismic deformation (Figure C.3).

The distribution of slip during an earthquake is never uniform [e.g., *Sangha et al.*, 2017; *Simons et al.*, 2011; *Reilinger et al.*, 2000]. However, the inversion for fault geometry

with variable slip is non-linear and computationally expensive. As such, we initially perform a non-linear inversion for the fault geometry, with uniform slip, and then use this fixed geometry to linearly invert for the slip on patches on the fault plane [e.g., *Bie et al.*, 2017; *Walters et al.*, 2009; *Pedersen et al.*, 2003].

4.3.3. Zinave earthquake uniform slip modelling

We use the analytical solution for slip on a rectangular dislocation in an elastic half-space [*Okada*, 1985] to model the surface displacements associated with the Zinave earthquake. We invert the observations of line-of-sight surface displacement using a Bayesian approach, incorporating the Markov chain Monte Carlo Metropolis-Hastings algorithm to explore the parameter space [*González et al.*, 2015; *Mosegaard and Tarantola*, 1995; *Hastings*, 1970], and report posterior probability density functions for each model parameter. We assume all measurement errors are Gaussian. Each interferogram stack is subsampled prior to inversion, based on the variance away from the signal, using the quad-tree approach [*Jonsson et al.*, 2002]. Initial conditions and bounds for the fault model parameters are given in Table C.2. We use a Poisson's ratio of 0.25 and shear modulus of 10 GPa for the crust.

The location of the Zinave earthquake is covered by three Sentinel-1 tracks (two ascending, tracks 72 and 174, and one descending, track 79). We perform five separate inversions using different subsets of the data to test the robustness of our solutions, and the influence of additional datasets on model parameter certainty, as each geodetic dataset has different noise and sensitivity (Table C.1, Figure 4.3). All of our inversions are consistent with a north-south trending, westward dipping normal fault (Tables 4.1 and C.3). To compare the results of each inversion we calculate the standard deviation of the 2σ confidence bounds of each model parameter, assuming the distributions are Gaussian (Table 4.2). Results of inversions using individual interferograms (from T174, T79, and T72) have the largest standard deviations, indicating they are least well constrained. The overall best constrained model is that from the inversion of InSAR data from all three tracks, with between a 38% and 79% decrease in the standard deviation of the parameter confidence bounds (Table 4.2).

The best-fit model is for a fault that is 16 km long (95% confidence: 14.8 – 16.7 km), with a dip of 59° (54° – 67°), bottom depth 7.6 km (5.6 – 8.0 km), and down-dip width of 5.1 km (1.4 – 5.7 km). All of the modelled fault parameters, 95% threshold values, and root-mean-square misfit values are given in Tables 4.1 and C.3. Overall the model is able to describe the observed surface deformation well, however there is a small residual near the southern end of the fault (Figure 4.4c, f and i). The spatial pattern of this residual is consistent between all of the tracks, and so is likely a feature of the rupture

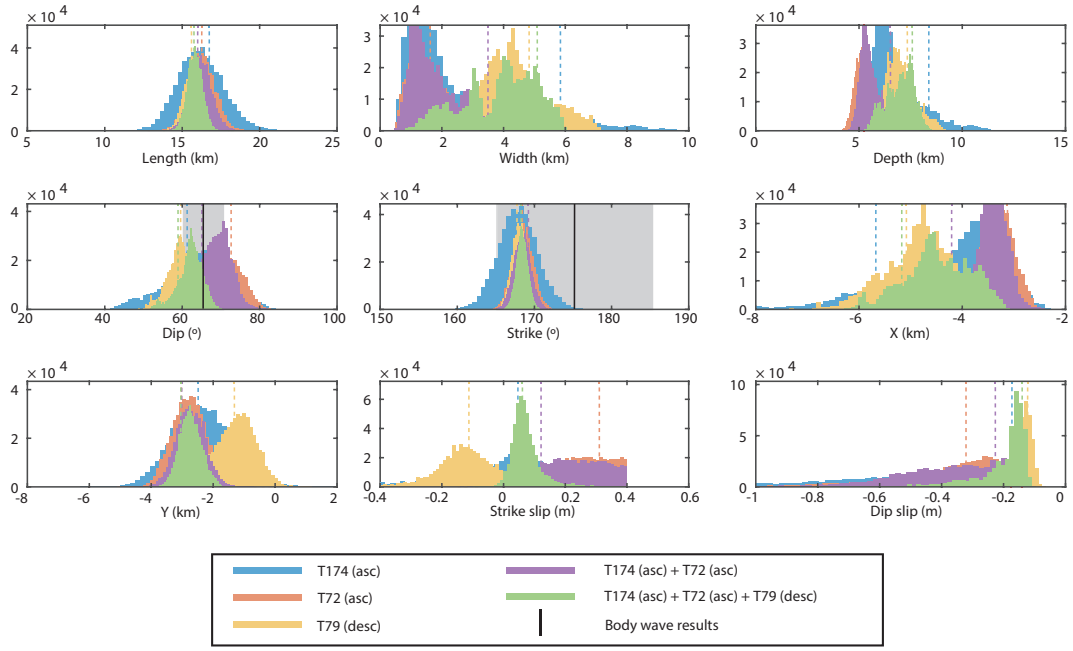

Figure 4.3: Marginal probability density functions for the fault parameters of the uniform slip distribution model of the Zinave earthquake. Vertical dashed lines show the optimal values from each inversion. Black vertical lines show the body wave inversion results for dip, and strike (Figure 4.2), with uncertainty given shown by the grey box.

that is not captured by the uniform slip model.

4.3.4. Zinave earthquake distributed slip modelling

The model with uniform slip can reproduce the first order patterns of surface deformation caused by the Zinave earthquake. However, systematic residuals suggest the slip was greater or shallower at the southern end of the fault. To test this, we refine our model by inverting for variable slip using the best combination of interferograms found in the previous section (stacks from ascending tracks 72 and 174, and descending track 79).

We use the plane defined in Section 4.3.3 (striking 168° and dipping 59°), but enlarge it to extend between the surface and a depth of 10 km, with a length of 24 km (Figure 4.5). This plane is then divided into 100 (10 by 10) smaller patches, each of which is 2.4 km horizontal by 1 km vertical in size (see Figure C.4 for comparison to model resolution). For a fixed fault geometry, the slip on each patch can be linearly related to the observations of surface deformation (Equation 4.3) [*Funning et al.*, 2005; *Wright et al.*, 2004].

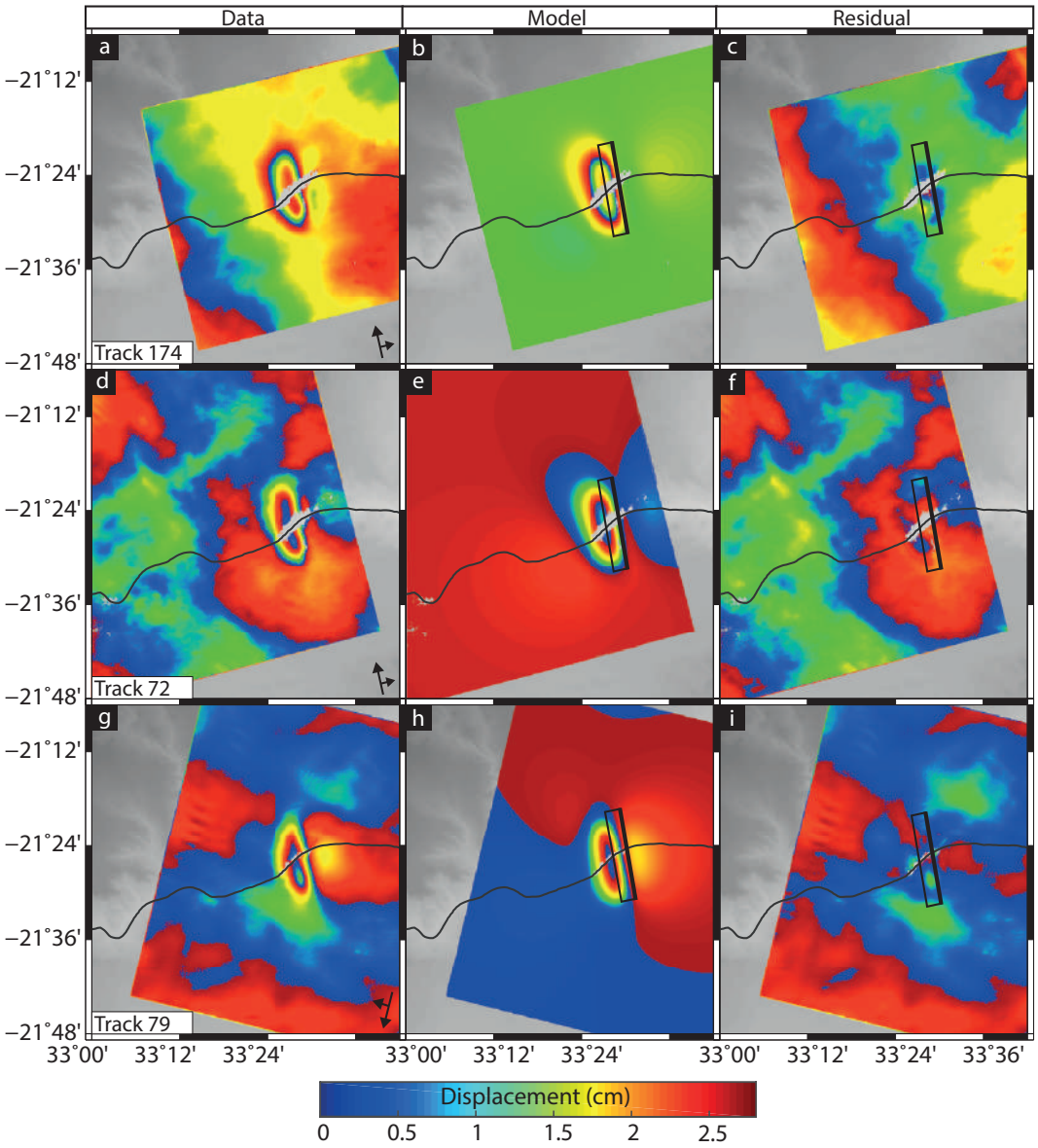

Figure 4.4: Data, model, and residual of the uniform slip inversion for the Zinave earthquake using stacks of interferograms, shown here wrapped. a–c) Track 174, d–f) track 72, h–i) track 79. The black rectangle shows the extent of the fault model, bold line represents the up dip edge.

Table 4.1: Fault parameters from the geodetic inversions, with 95% probability confidence range, and USGS focal mechanism and body wave inversion result for comparison. Fault locations (X and Y, UTM) in the geodetic inversions are for the middle of the bottom of the fault. Root-mean-square (rms) misfit is the joint rms if more than one dataset is used in the inversion.

	USGS solution		T174 + T72 + T79		Body wave
Inversion points	-		2071		-
	FP1	FP2	Optimal	95% range	Best fit
Length (m)	-	-	15800	14900 – 16800	-
Width (m)	-	-	5100	1400 – 5700	-
Depth (m)	15500	15500	7600	5600 – 8100	7000 ± 4000
Dip (°)	45.0	50	59	54 – 68	66 ± 10
Strike (°)	334	185	168	167 – 170	175 ± 10
X (UTM)	550800	550800	546600	545900 – 548400	-
Y (UTM)	7630800	7630800	7629300	762900 – 7632200	-
Strike slip (m)	-	-	0.06	0.0 – 0.20	-
Dip slip (m)	-	-0.14	-0.47 – -0.12	-	-
Rake (°)	-114.0	-68.0	-66.4	-	-71 ± 10
rms (cm)	-	-	1.0	-	-

Table 4.2: Standard deviation for the marginal posterior probability density function for each parameter. Bold font indicates the smallest standard deviation for each parameter.

	T174	T72	T79	T174 + T72	T174 + T72 + T79	Decrease in standard deviation (%)
Length (m)	1480	830	630	710	**480**	68
Width (m)	1780	**650**	1230	770	1080	39
Depth (m)	1140	**440**	770	480	610	46
Dip (°)	7.6	4.9	3.7	4.0	**3.2**	58
Strike (°)	2.5	1.3	1.0	1.1	**0.8**	70
X (m)	990	**370**	700	**370**	620	38
Y (m)	980	550	680	460	**360**	63
Strike slip (m)	0.18	0.09	0.08	0.09	**0.04**	79
Dip slip (m)	0.23	0.17	**0.06**	0.17	**0.06**	75

$$\begin{pmatrix} \mathbf{G} & X & Y & 1 \\ \kappa^2\nabla^2 & 0 & 0 & 0 \end{pmatrix} \begin{pmatrix} \mathbf{m} \\ a \\ b \\ c \end{pmatrix} = \begin{pmatrix} \mathbf{d} \\ 0 \end{pmatrix} \tag{4.3}$$

Equation 4.3 relates the displacement observations at each location (X and Y) (**d**) to the slip on each fault patch (**m**) and the Green's function (**G**) of line-of-sight displacements from 1 m of slip on each patch, using the elastic dislocation model [*Okada*, 1985]. The formulation includes ∇^2, which is the Laplacian smoothing operator to avoid sharp slip variations, and κ^2 which is a prescribed scalar smoothing factor. Equation 4.3 is solved using a non-negative least-squares algorithm [*Bro and De Jong*, 1997]. In all inversions $\kappa = 5 \times 10^5$, which was selected using a trade-off curve (Figure C.5a). A ramp (described by a and b in the x- and y-directions respectively) and an offset (c) for each interferogram stack is also solved for in the inversion.

We investigate whether the rake varies across the slip region by performing three inversions: one with variable rake (**G** is formulated such that we can solve for variable rake, i.e., non-negative slip in orthogonal components, between -45° and -135°, separately for each patch), one with the rake fixed from the geodetic uniform slip distribution model (-66°), and one with a rake fixed to the body wave inversion result (-71°, Figure C.6). We then compare the fit of the variable rake model considering the increase in model parameters using an F-test.

All three inversions show no significant difference in their root-mean-square misfit (Table C.4). However, in the variable rake model, the rake within the main slip region varies unrealistically, between -30° and -70° over ∼6 km (Figure C.7). A fixed rake model is a nested variant of the variable rake model, and as such we can perform an F-test to test whether the inclusion of variable rake is justified. The F statistic value for this test is 0.005, considerably lower than the 5% probability threshold value of 1.32. The increase in degrees of freedom for the variable rake model is therefore not statistically justified, and rejected.

The slip distribution for the Zinave earthquake using a fixed rake of -66°, and fit to the data are shown in Figure 4.5. In comparison to the uniform slip model, there is a greater area and magnitude of slip (up to 0.12 m) at the southern end of the fault compared to the north (∼0.1 m), as suggested by the residuals to the uniform slip model (Figure 4.5). The region with >2 cm of slip is ∼14 km by ∼5 km, with top and bottom boundaries at 4 km and 8 km depth respectively. For this slip distribution, the seismic moment, using a shear modulus of 32 GPa, is 1.85×10^{17} Nm. The geodetically and seismically derived values of dip, depth, and rake for this earthquake agree within error

(Figure 4.3).

The seismic moment for this event, 9.5 x 10^{16} Nm, is 47% smaller than the geodetic estimate of the moment (1.85 x 10^{17} Nm). The seismic moment of an earthquake is difficult to determine accurately with both methods, and this degree of mismatch is typical [e.g., *Weston et al.*, 2011].

4.4. 2006 Machaze earthquake

4.4.1. ENVISAT InSAR

We processed 2 ENVISAT scenes (06/06/2004 and 07/05/2006) to produce an interferogram spanning the 2006 Machaze earthquake using the ROI-PAC software [*Rosen et al.*, 2004]. These scenes were selected following *Copley et al.* [2012], but we remove topographic phase contributions using a 30 m DEM [*Farr and Kobrick*, 2000], which was not available in 2012. The interferogram was filtered with strength 0.9 [*Goldstein and Werner*, 1998]. We resample the interferogram to 90 m pixel spacing, and use the HRES ECMWF atmospheric model through the GACOS facility to correct for atmospheric delays in the interferogram [*Yu et al.*, 2017a,b]. We find the atmospheric correction reduces the standard deviation of the interferogram from 12.1 cm (90 m pixel, no correction) to 9.6 cm (90 m pixels, atmospheric correction applied).

The use of the 30 m DEM considerably extended the connected coherent region (coherence >0.1) of the ENVISAT interferogram, compared to the interferogram of *Copley et al.* [2012] which used a 90 m DEM, especially in the far-field and for some of the signal from the fault motion. However, we were still unable to unwrap within ∼8 km the fault due to poor coherence and/or high deformation rate.

4.4.2. SPOT cross-correlation

Surface deformation can be measured using the cross-correlation of optical images. To better constrain the near-field displacement field, we make use of two SPOT5 images, acquired on 3^{rd} August 2001 and 26^{th} August 2008 [*Copley et al.*, 2012]. We use the results of *Copley et al.* [2012] who cross-correlate the images using the Cosi-Corr programme [*Leprince et al.*, 2007, 2008]. Due to the non-nadir viewing geometry of the satellite, vertical displacements contribute to the apparent east-west displacement [*Copley et al.*, 2011]. For the orientation of the Machaze earthquake and SPOT satellite viewing geometry, we calculate that the vertical displacement will destructively

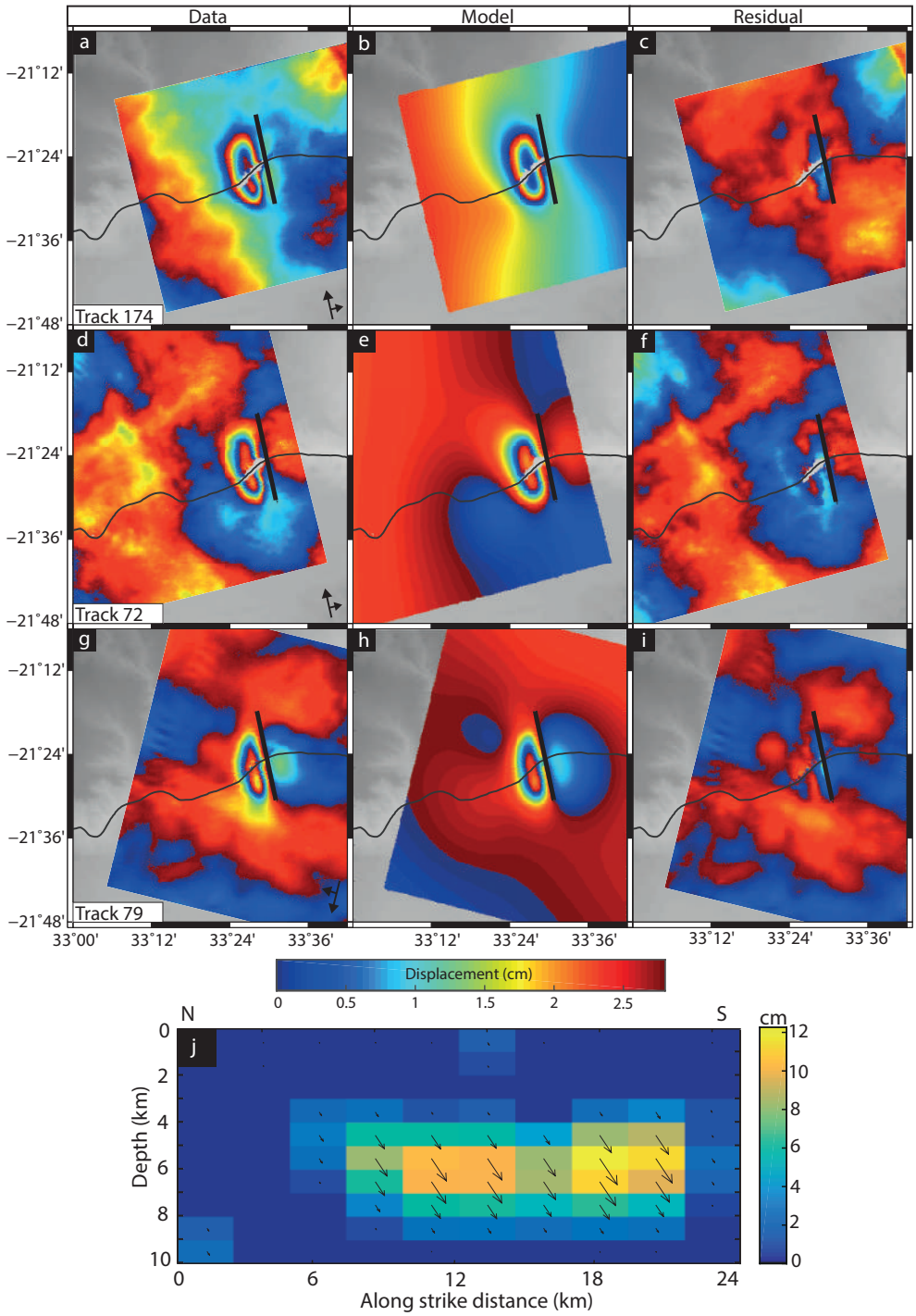

Figure 4.5: Distributed slip model for the Zinave earthquake. a–c) Data, model, and residual for track 174. d–f) Track 72 data, model, and residual. g–i) Track 79 data, model, and residual. Black lines a–i mark the top of the model, where it intersects the surface. j) Distributed slip model result for the inversion of tracks 174, 79 and 72 with rake fixed to -66°. Arrows show displacement of the east block relative to west (i.e., motion to the south is left-lateral).

interfere with the east-west component. Furthermore, the subjectivity in choice of tie-points for the cross-correlation, required because of uncertain satellite orbits, reduces the reliability of the long-wavelength displacements [*Copley et al.*, 2012, 2011]. The displacement discontinuities, however, are robust. The acquisition dates cover both co-seismic and post-seismic (30 months) periods, so the relative contribution cannot be distinguished. Nonetheless, the SPOT dataset provides crucial observations of the near-field deformation (Figure 4.6).

4.4.3. Uniform slip modelling of the Machaze earthquake using InSAR data

For the Machaze earthquake, we perform three inversions of the 06/06/2004 – 07/05/2006 ENVISAT interferogram: one with the GACOS atmospheric correction (90 m resolution) (Figure 4.6a, b and c), and two without atmospheric corrections, one full resolution (30 m pixels) (Figure C.8a–c), and one resampled to 90 m (Figure C.8d–f).

We use the same inversion methodology and crustal properties as for the Zinave earthquake. Initial conditions and inversion bounds are given in Table C.2. The results of all three of our inversions show the far-field displacements captured by the ENVISAT interferograms can be well described (2.1 – 2.4 cm rms) by a single 24 x 7 km steeply dipping (78°) fault, striking 176°, with top depth ∼7 km below the surface (Figure 4.6, 95% probability values can be found in Table 4.3). The inversion using the interferogram with corrections for atmospheric delays is our preferred model because of the noise consideration (Table 4.3). The best-fit model is a fault with 6.3 m slip, at a rake of -80°. A top depth of 7 km contrasts with observations of faulting at the surface [*Fenton and Bommer*, 2006], however this is unsurprising as the ENVISAT data used in our inversion is incoherent close to the fault trace, resulting in little sensitivity to shallow slip. As such, we repeat the inversion including the SPOT data. Our modelling results are otherwise consistent with previous seismological and geodetic estimates of the fault geometry and slip [*Copley et al.*, 2012; *Fonseca et al.*, 2014] (Table 4.3).

4.4.4. Distributed slip modelling of the Machaze earthquake, incorporating InSAR and SPOT data

Large faults are generally complex with multiple segments [e.g., *Hamling et al.*, 2016; *Fletcher et al.*, 2014]. The surface rupture following the Machaze earthquake indicates two main fault segments ruptured [*Copley et al.*, 2012; *Fenton and Bommer*, 2006]. In order to ascertain the total slip on the Machaze fault we perform a distributed slip

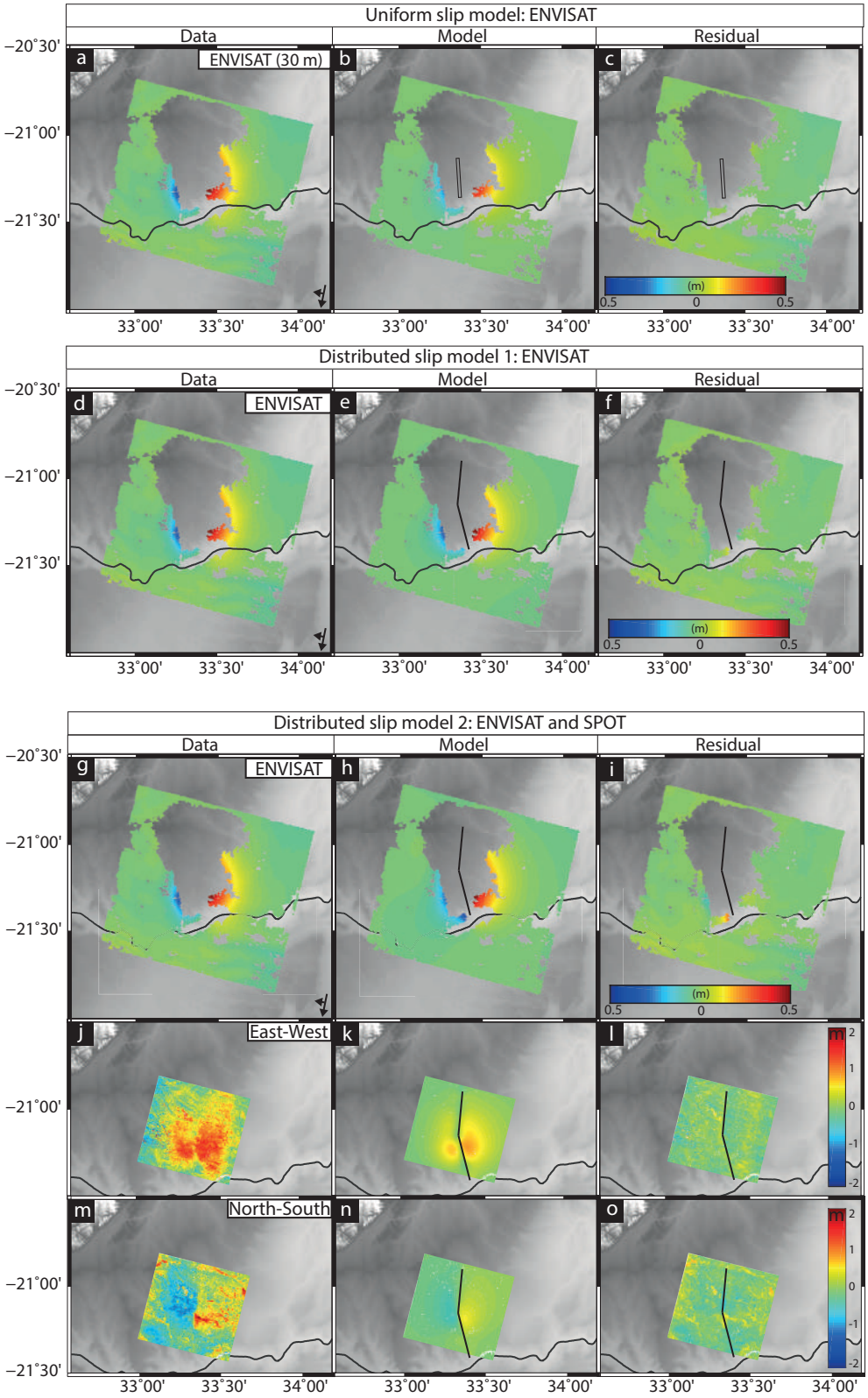

Figure 4.6: a–c) Data, model, and residual for the Machaze earthquake using the uniform slip model. Descending ENVISAT interferogram 06/06/2004 – 07/05/2006. The black rectangle on b and c shows the fault location, dipping west. d–f) Distributed slip model 1: ENVISAT data (d), model (e), residual (f). g–o) Distributed slip model 2, showing data, model, residual for the ENVISAT and SPOT offset data. Black line shows the surface trace of the fault.

Table 4.3: Model parameters and 95% probability values for the Machaze earthquake inversions, and root-mean-square (RMS) misfit between the observations and the models.

	GACOS correction		No corrections		90 m no corrections	
Inversion points	1145		1186		1053	
Standard deviation (cm)	9.6		12.6131		12.11	
	Optimal	95% range	Optimal	95% range	Optimal	95% range
Length (m)	24500	19300 – 26400	25800	23000 – 27500	27100	24800 – 28500
Width (m)	6900	6500 – 11200	25800	12200 – 18700	11000	10000 – 14700
Bottom depth (m)	13700	13400 – 17400	18400	17000 – 23500	16200	15600 – 19300
Dip (°)	78	75 – 85	76	75 – 82	75	74 – 79
Strike (°)	176	171 – 179	180	176 – 181	180	177 – 181
X (m)	-24130	-24880 – -23200	-24900	-25000 – -24000	-24800	-25000 – -24200
Y (m)	8900	5200 – 10600	7540	5700 – 8600	8100	6800 – 8900
Strike slip (m)	0.96	-0.52 – 2.96	2.37	1.90 – 2.80	2.92	2.17 – 2.98
Dip slip (m)	-5.62	-6.00 – -3.87	-3.08	-3.47 – -2.53	-3.88	-4.20 – -2.96
Rake (°)	-80	-	-52	-	-53	-
rms (m)	0.021		0.025		0.024	

model with the fault location identified by displacement discontinuities in post-seismic deformation and the SPOT data [*Copley et al.*, 2012]. We otherwise use the same method as Section 4.3.4, but with the fault divided into 3 km by 3 km patches, that extends down to 30 km, dipping at 75°. We choose to include a variable rake in all of our inversions to account for variations that might be expected between fault segments with different strikes, and between the co- and post-seismic periods. A variable rake model is also preferred by other studies of the slip during the Machaze earthquake [*Copley et al.*, 2012].

We perform two inversions, 1) using just the ENVISAT interferogram ($\kappa = 7$ x 10^5, Figure C.5b), and 2) a joint inversion using the ENVISAT interferogram and SPOT observations (which are resampled to 50 m) ($\kappa = 1.3$ x 10^6, Figure C.5c). We solve for a ramp in the ENVISAT data, and an offset in all datasets. The difference between these two models is that model 1 contains primarily far-field co-seismic deformation, but omits the near-field displacement, whilst model 2 includes the near-field observations, but also includes 30 months post-seismic deformation. Previous observations indicate that post-seismic deformation is primarily shallow afterslip on the fault [*Copley et al.*, 2012].

The slip distribution of model 1 indicates that the majority of the slip is concentrated towards the northern end of the southern fault, with some displacement on the northern segment (Figure 4.7). The displacement is primarily normal in the main rupture area, with rake values ∼-80°. In this model, however, the slip in the upper cells is small, in contrast to field observations of surface offsets of up to 2 m [*Fenton and Bommer*, 2006], probably as a result of the lack of near-field observations.

The results of the joint inversion of ENVISAT and SPOT data shows the same general pattern of slip distribution as model 1, although the slip in the uppermost cell is now 2 m (Figure 4.7, resolution shown in Figure C.9). The slip on the southern end of the northern fault has also increased by up to 1.5 m, to 4.5 m. This additional slip could be either 1) post-seismic deformation, 2) co-seismic deformation that is not detected by the ENVISAT interferogram due to its limited coherence, or 3) an artefact, as a result of the SPOT data image-processing methodology. The greatest misfit to the data are residuals in the ENVISAT observations towards the southern end of the southern fault, where the interferogram is coherent closest to the fault trace (Figure 4.6i). This may be because the SPOT data includes surface deformation caused by afterslip that is modelled, but not detected by the ENVISAT observations.

Our preferred model of the co-seismic slip distribution is that which is based upon the ENVISAT observations of the displacement with a fixed fault geometry based on the SPOT discontinuities (model 1). Uncertainties as to the geometry and timing (co-

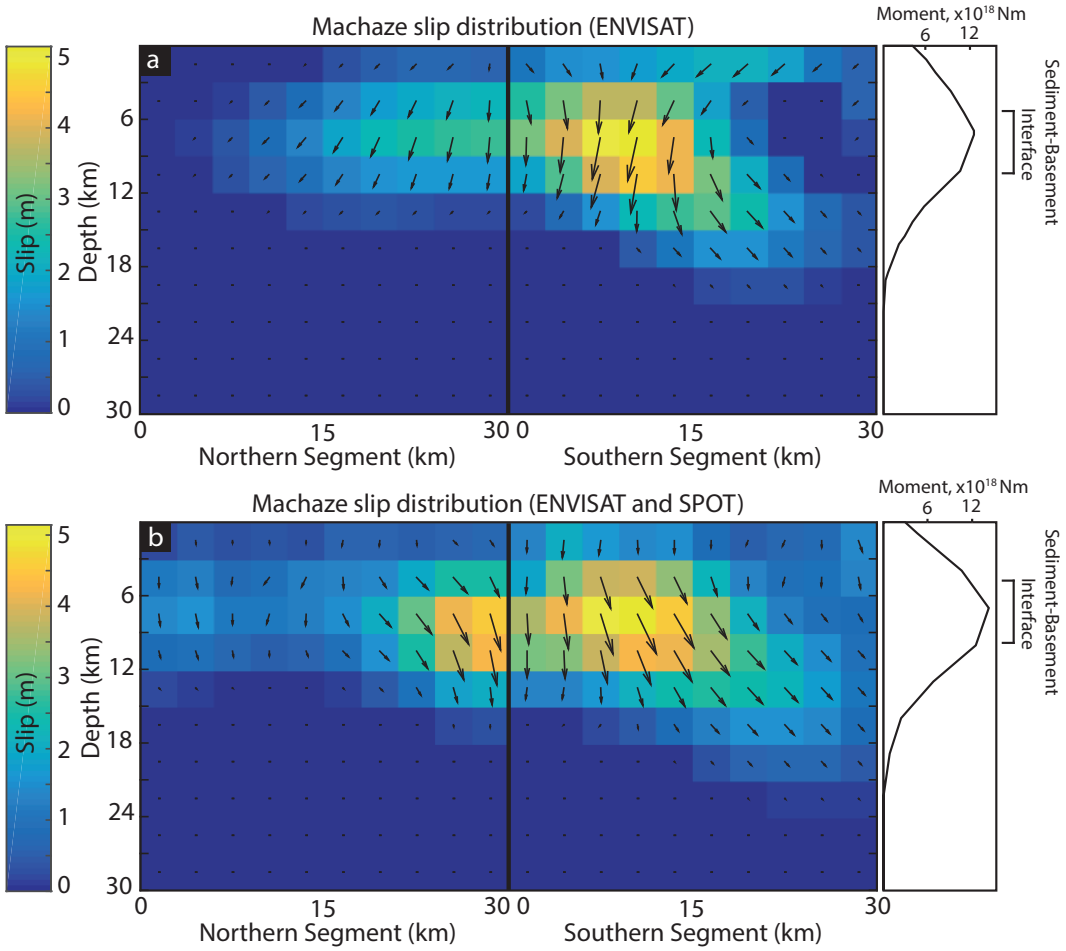

Figure 4.7: Slip distribution of model 1 (a, ENVISAT) and model 2 (b, ENVISAT and SPOT) for the Machaze earthquake. The estimated depth of the sediment-basement interface is shown. Profiles to the right of sub-panels (a) and (b) show the integrated moment release with depth.

versus post-seismic) of the displacement in the SPOT observations introduces difficulties in how to interpret the result of model 2, although they do broadly agree with model 1, and the additional shallow slip in model 2 is consistent with post-seismic deformation.

4.4.5. Comparisons to seismology

The CMT and USGS estimate the co-seismic moment of the Machaze earthquake to be 4.5 x 10^{19} Nm and 4.6 x 10^{19} Nm respectively. Using a shear modulus of 32 GPa, we calculate a seismic moment of 4.4 x 10^{19} Nm for our preferred model (model 1) and 5.3 x 10^{19} Nm for model 2. These are 5% smaller and 15% larger than the seismic estimates respectively, but within the range that may be expected given the different velocity structures and possible inclusion of post-seismic deformation in the geodetic observations [*Weston et al.*, 2011].

In both the geodetic distributed slip models, the majority of the moment release occurred at depths of less than 15 km (model 1: 95%, model 2: 94%), with a geodetic centroid of 8 km. This depth estimate is shallower than the seismological estimates of the earthquake depth of 15 ± 3 km [*Yang and Chen*, 2008], 14.8 km [*Attanayake and Fonseca*, 2016], and 13 km [*Copley et al.*, 2012]. The discrepancy is likely a result of the low depth resolution in our data due to the lack of near-field geodetic observations.

The depths of Machaze aftershocks suggest this region has a seismogenic thickness of 20 km or greater [*Craig et al.*, 2011; *Yang and Chen*, 2010]. Therefore, as the Machaze earthquake ruptured down to ∼20 km it may represent an upper bound to the size of an earthquake in this region.

4.4.6. Coulomb stress change

Earthquakes cause static stress changes in the surrounding rocks, bringing nearby regions closer to, or further from, failure. In theory, for failure to occur the co-seismic static stress change, plus any pre-existing differential stresses, must be greater than a threshold Coulomb failure criterion [*King et al.*, 1994; *Toda et al.*, 2005]. The Coulomb stress change ($\Delta\sigma_c$) is a function of the normal ($\Delta\sigma_n$) and shear stresses ($\Delta\sigma_t$) on a fault plane, and is defined as

$$\Delta\sigma_c = \Delta\sigma_t + \mu\Delta\sigma_n, \tag{4.4}$$

where μ is the coefficient of friction. In this formulation positive shear stress is in the direction of slip and positive normal stresses are unclamping. We use the *Coulomb 3.3* software package to calculate the $\Delta\sigma_c$ following the Machaze earthquake [*Lin and Stein*, 2004], using slip on a rectangular dislocation model in an elastic half-space [*Okada*, 1985]. We use $\mu = 0.4$ in our calculations, and confirm that the results shows little sensitivity within the range $\mu = 0.2 - 0.6$.

To understand whether the Machaze earthquake could have brought the Zinave fault closer to failure, we calculate both the Coulomb and normal co-seismic stress changes, and test both uniform and distributed slip models of the Machaze earthquake (Figure 4.8). We calculate the Coulomb stress change at 5 km depth, comparable to that of the peak slip on the Zinave fault, and use the results from the uniform slip model for the Zinave fault to specify receiver fault geometry (Figure 4.4, Table 4.1). Our preferred solution uses the distributed slip model based on the ENVISAT and SPOT data as it contains the most complete measure of the slip that occurred during and after

the earthquake, and will therefore give the best estimate of the overall stress change. Although the calculated stress changes close to the Machaze fault may be unreliable given the lack of near-field observations, they are relatively robust at distances comparable to the Machaze-Zinave separation (∼10 km). We find that the stress pattern does not vary greatly over the uncertainty range of the receiver fault parameters (strike: 166° – 169°, dip: 54° – 67°) given by the posterior probability density functions of our uniform slip model.

The pattern of stress change produced by the uniform and distributed slip models of the Machaze earthquake is broadly similar. For both, at 5 km depth, the stress change is asymmetric, with the largest normal and Coulomb stress changes occurring over ∼20 km to the east (< -1 MPa) and west (> 1 MPa) of the Machaze fault (Figure 4.8). Lobes of positive Coulomb stress change also extend over ∼15 km to the north and south of the fault. In all models the region of the Zinave earthquake experienced a localised ∼0.2 MPa increase in stress. This Coulomb stress change is much lower than the stress drop of the event, indicating that the fault was dominantly releasing pre-existing shear stress. Positive stress changes are more spatially heterogeneous for the distributed slip model than the uniform slip model, with positive stress changes not predicted as far away from the fault to the west.

The spatial pattern of aftershocks generally follow regions of positive stress changes [*King et al.*, 1994]. The distribution of recorded Machaze aftershocks (2006 – 2010) shows clusters in the regions of positive Coulomb stress change, including near the Zinave fault (Figure 4.8).

4.5. Discussion

4.5.1. Rheological implications

Co-seismic slip in the Machaze earthquake was largely contained within the crystalline basement, with post-seismic deformation, primarily afterslip, within the overlying sedimentary sequence. This observation led *Copley et al.* [2012] to conclude the sediments were velocity strengthening, and the basement velocity weakening. In contrast, we find slip during the Zinave earthquake occurred primarily within the sedimentary sequence.

A transition between velocity weakening and velocity strengthening rheologies can be explained by 1) laterally variable material properties, 2) temporal variations in material properties or pore pressure, or 3) stress- or time-dependent rheology. Spatial variations in frictional properties relating to lithology have been invoked to explain spatial variation

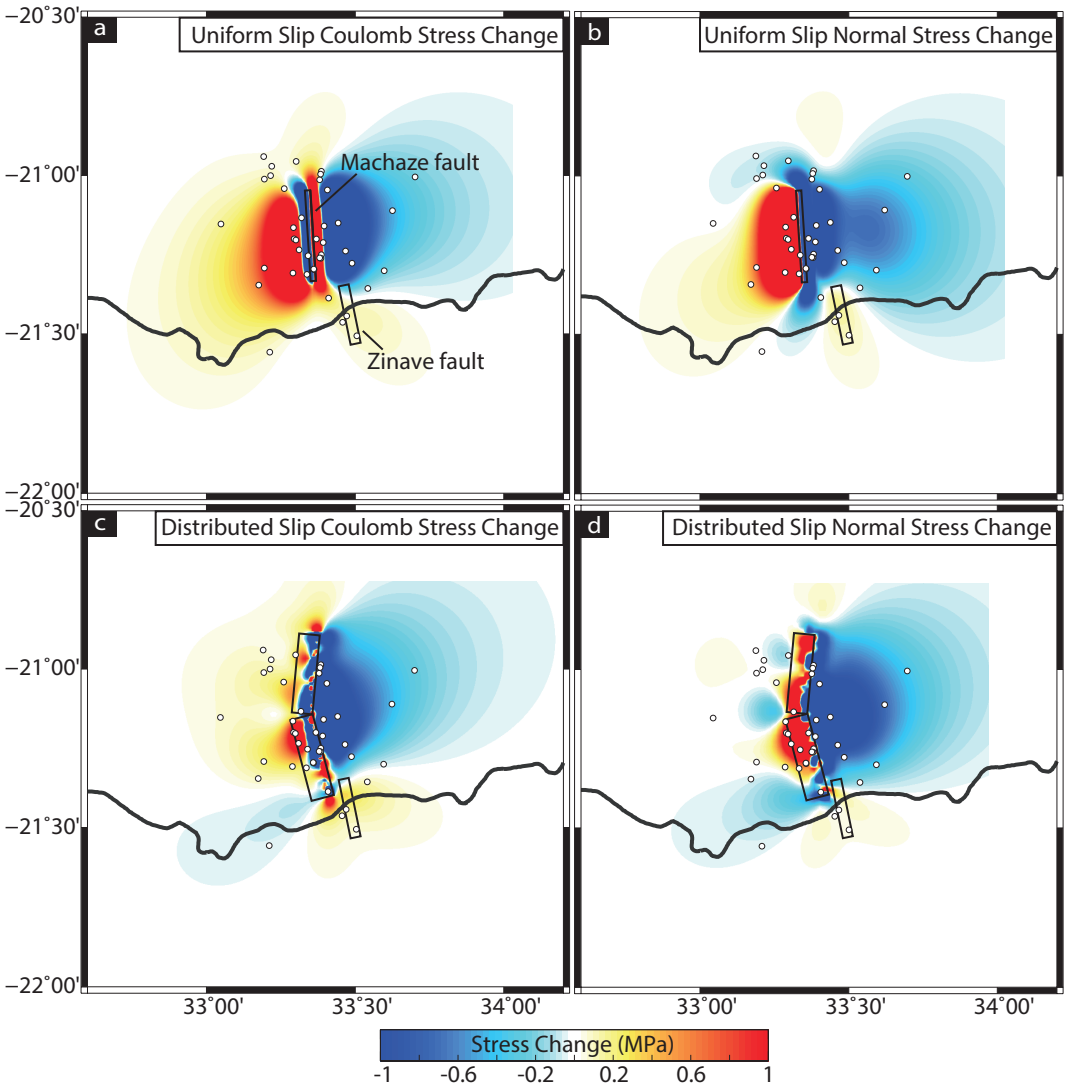

Figure 4.8: Coulomb stress change ($\Delta\sigma_c$) and normal stress change following the Machaze event, for a 5 km depth, for receiver faults with strike 168°, dip 59°, and rake -66°. a) Coulomb stress change ($\Delta\sigma_c$) as a result of the uniform slip model of the Machaze earthquake (fault between 7 – 14 km). b) Normal component of the stress change for the same earthquake as (a). c) $\Delta\sigma_c$ calculated using the distributed slip model from ENVISAT and SPOT data. d) Normal component of the $\Delta\sigma_c$ for the distributed slip model. Positive values are unclamping. The black rectangles show the vertical surface projection of the faults. White circles show the distribution of aftershocks for all depths, 2006 – 2011 from *Copley et al.* [2012]. See text for further details.

in steady-state fault stability elsewhere (e.g., 2014 South Napa earthquake [*Floyd et al.*, 2016], and the 2003 Tokachi-oki earthquake [*Miyazaki et al.*, 2004]). In the case of the Machaze–Zinave sequence there are limited geological constraints on the subsurface, but either depth variations in the sediment basement interface, or physical variations within the sedimentary deposits are plausible. Indeed, shallow aftershocks observed by [*Copley et al.*, 2012] support the presence of stick-slip regions within the sedimentary sequence. In large subduction zone earthquakes aftershocks are similarly seen to concentrate in the areas dominantly deforming by aseismic creep, and are generally thought to represent stuck asperities on a sliding fault surface [e.g., *Moreno et al.*, 2010; *Bürgmann et al.*, 2005; *Igarashi et al.*, 2003].

Alternatively, temporal changes, particularly variations in pore fluid pressure, can alter the effective friction and thus control fault strength [*Copley*, 2017; *Nur and Booker*, 1972]. This is a plausible mechanism in the Machaze region, which is a flood plain with highly seasonal rainfall, underlain by a thick sedimentary sequence of high permeability sands [*López-Querol et al.*, 2007].

A steady-state, i.e., rate-dependent, friction law assumes that afterslip occurs on stable faults in velocity strengthening regimes, and that the friction coefficient depends on the slip velocity only [e.g., *Hsu et al.*, 2006; *Perfettini and Avouac*, 2004]. Within this framework, spatial heterogeneity would be required to explain afterslip in otherwise velocity weakening zones. However, when the full rate-and-state law is considered, the distinction between velocity weakening and velocity strengthening is ambiguous [*Helmstetter and Shaw*, 2009]. When the steady-state constraint is not applied, fault behaviour is strongly influenced by post-seismic stresses, with both afterslip and earthquake nucleation possible within a homogenous medium.

4.5.2. Fault interaction and rifting

The steep dip of the Machaze earthquake fault ($\sim$75°) and nucleation within the Precambrian basement suggests that the earthquake represents a reactivation of an existing structure, rather than the formation of a new fault [*Yang and Chen*, 2008]. The exploitation of pre-existing structures is common in nascent, and mature, rift settings [*Muirhead and Kattenhorn*, 2018; *Hodge et al.*, 2018a; *Kinabo et al.*, 2008; *Laó-Dávila et al.*, 2015; *Ring*, 1994; *Versfelt and Rosendahl*, 1989]. Pre-existing structures represent weaknesses, which, even if not optimally orientated, will fail preferentially to the formation of new faults [*Scholz*, 2002]. However, in contrast, slip during the Zinave earthquake, and several aftershocks (Feb – April 2006, *Yang and Chen* [2010, 2008]), occurred within the post-Jurassic sedimentary layer on an $\sim$60° dipping plane, as predicted by Andersonian mechanics.

The Machaze-Zinave sequence raises several questions about fault growth in continental rift settings. The Zinave fault could: 1) act as a linking fault between horizontally offset basement structures [e.g., *Hodge et al.*, 2018b], and/or 2) represent the upward propagation of extension from pre-existing basement structures through un-faulted sediments.

Reactivation of pre-existing structures has implications for the determination of the stress field in extensional environments using earthquake slip vectors [*Saria et al.*, 2014; *Bird et al.*, 2006; *Delvaux and Sperner*, 2003]. If, throughout rifting, large earthquakes occur on pre-existing structures they will not fully represent the present day stress orientation. Similarly, however, slip during aftershocks may represent a combination of local stresses from the mainshock, and regional tectonics, or inter-seismic strain accumulation. *McKenzie* [1969] demonstrated that, in a triaxial stress regime, slip vectors from shallow events provide very little constraint on the orientation of the greatest principle stress.

4.6. Conclusions

The Zinave earthquake occurred on a 60° dipping normal fault, between 4 – 8 km deep. The earthquake occurred in a region of positive Coulomb stress change associated with the 2006 Machaze event, indicating it was brought closer to failure by the preceding earthquake. The depth of the Zinave earthquake suggests it is contained within sedimentary deposits, at a depth co-incident with the co-seismic slip deficit and post-seismic afterslip following the Machaze event. The occurrence of afterslip and aftershocks at the same depth suggests either spatially and/or temporally variable frictional properties, or that the fault exhibits time or stress dependent rheology.

A comparison to the modified Omori law for aftershock decay indicates that the Zinave earthquake is part of a prolonged aftershock sequence following the Machaze earthquake. Long aftershock sequences should be expected following large earthquakes in low strain regions, suggesting the seismic hazard in the least mature portions of the East African Rift is underestimated. The Machaze-Zinave sequence demonstrates that magnitude 4 – 5 earthquakes following magnitude >7 events should be expected for decades, with associated seismicity lasting for up to ∼150 years.

Chapter 5

Fault identification for buried normal faulting earthquakes: incipient rifting in the Limpopo-Shashe Belt, southern Africa

Author contributions and declaration:

J. Biggs supervised the work. P. Lundgren provided the ALOS-2 SAR data. Useful discussions were had with R.-A. Sloan. This chapter is currently under preparation for submission.

Abstract

Intra-plate earthquakes occur in regions with low strain rates. Understanding the occurrence of intra-plate earthquakes is important because of the potential hazard they pose, and the insights they can provide on the local and regional stress fields.

Here, we investigate the M_w 6.5 3^{rd} April 2017 earthquake that occurred in central Botswana, at a depth of ∼25 km. The earthquake occurred >400 km away from the nearest indication of present-day extension. Interferometric Synthetic Aperture Radar (InSAR) is an ideal tool to investigate intra-plate earthquakes, as the regions they occur in are rarely seismically instrumented. However, it is difficult to resolve the source parameters of deep earthquakes using observations of surface deformation. As such, we use complimentary ascending (Sentinel-1) and descending (ALOS-2) InSAR datasets and a Bayesian inverse methodological approach to determine posterior probability density functions for the parameters of an elastic slip dislocation model, and consider typical fault geometry relationships to determine the correct earthquake parameters. We determine that the primarily normal-faulting earthquake occurred on an north-east dipping reactivated pre-existing structure, probably in response to far-field stresses.

5.1. Introduction

The distribution and style of seismicity reflects the pattern of strain release within the crust [e.g., *Saria et al.*, 2014; *Craig et al.*, 2011; *Zoback*, 1992a]. Regions with the highest strain rates, nominally plate boundaries, have the highest rates of seismicity [*Craig et al.*, 2011; *Bilham et al.*, 2001; *Thatcher and Hanks*, 1973; *Brazangi and Isacks*, 1976], but earthquakes also occur where tectonic strain rates are low (e.g., intra-plate, volcanic, and induced seismicity settings) [*Sykes*, 1978].

Large intra-plate earthquakes, earthquakes which occur away from plate boundaries, are rare, but have been observed worldwide. Their occurrence has been related to local transient variations in fault strength or crustal stress (e.g., following deglaciation in Fennoscandia [*Craig et al.*, 2016], and erosion in New Madrid, USA [*Calais et al.*, 2010]) and far-field plate boundary stresses (e.g., Eastern North America [*Zoback*, 1992b]). Intra-plate earthquakes appear to commonly exploit pre-existing structures, for example in New Madrid [*Calais et al.*, 2010], and it has previously been suggested that some intra-plate earthquakes in North America follow the edges of cratons [*Tesauro et al.*, 2015]. Determining the cause of intra-plate earthquakes is often difficult given low deformation rates and relatively short observation periods, but is important given the different predictions each strain origin has on the evolution of the seismicity in space and with time [*Calais et al.*, 2016]. In regions with few other observations, constraints on the source parameters of intra-plate earthquakes allow us to better define the strain distribution and earthquake hazard [*Hurd and Zoback*, 2012; *Parsons et al.*, 2008; *Jain et al.*, 1994].

Southern Africa is comprised of several Archean cratons, separated by ancient collisional or extensional belts [*Begg et al.*, 2009; *Veevers and Powell*, 1994; *Thomas et al.*, 1993; *Kroner*, 1982], and has a geological history spanning 3.7 Ga [*Thomas et al.*, 1993]. The East African Rift intersects eastern southern Africa as two branches. South of Lake Tanganyika, one branch continues south through Malawi and Mozambique [*Fonseca et al.*, 2014], and the other to the SW as the Luangwa Rift into Botswana, and the Okavango Graben [*Fairhead and Girdler*, 1969; *Vail*, 1968] (Figure 5.1a,b). Some studies identify diffuse extension across the Zambia-Zimbabwe-Botswana region in response to stresses associated with the East African Rift [*Pastier et al.*, 2017], with potential localisation of strain around and between the Kaapvaal and Zimbabwe Cratons, which appear to guide rifting, in a similar way to the Tanzania Craton to the north [*Bird et al.*, 2006; *Ebinger et al.*, 1997] (Figure 5.1a).

Strain rates in central Botswana are poorly constrained due to a paucity of measurements, but are generally assumed to be low (extension <1 mm/yr) [*Stamps et al.*, 2018; *Pastier et al.*, 2017; *Saria et al.*, 2014; *Bird et al.*, 2006]. Figure 5.1a shows

the distribution of seismicity throughout southern Africa, and locations of the cratons. In general, seismicity and rifting follow the edges of the cratons (e.g., the Western and Kenyan Rifts either side of the Tanzania Craton, and the Mozambique Rift to the west of the Zimbabwe Craton), exceptions include within the Kaapvaal Craton, where seismicity is attributed to anthropogenic activity [*Richardson and Jordan*, 2002].

On 3rd April 2017 a M_w 6.5 earthquake occurred in central Botswana, near Moiyabana. The event was >450 km from the nearest region of active deformation, the ∼100 km wide Okavango Graben [*Modisi et al.*, 2000; *Fairhead and Girdler*, 1969] (Figure 5.1b), and over 800 km from the Machaze earthquake, the nearest historic magnitude >6 event (USGS catalogue). Plate motion models show the nearest plate boundary, between the Nubian and Rovuma plates, is over 800 km away [e.g., *Stamps et al.*, 2018; *Saria et al.*, 2014; *Kreemer et al.*, 2014; *Stamps et al.*, 2008]. The Okavango Graben is seismically active with north-east striking normal faulting earthquakes, and Quaternary to recent age faulting at the surface [*Mosley Bufford et al.*, 2012; *Scholz et al.*, 1976]. It is thought that this incipient rift follows a post-Karoo, pre-Cretateous failed rift zone [*Gwavava et al.*, 1992; *Scholz et al.*, 1976]. Seismicity is also observed along with the NE-SW orientated Luangwa Rift, ∼450 km north-east of the Okavango Graben (Figure 5.1a) [*Banks et al.*, 1995; *Daly et al.*, 1989].

The 2017 Moiyabana earthquake, however, occurred in a historically aseismic region, on the northern edge of the Kaapvaal Craton within the Limpopo-Shashe Belt, which formed during the collision between the Kaapvaal and Tanzania Cratons >2.5 Ga (Figure 5.1). This region has since undergone tectonothermal reworking ∼2 Ga (see *Ranganai et al.* [2002]; *Gwavava et al.* [1992] and references therein), but lack of exposure has precluded detailed field studies. Instead, information on the location and geometry of the belt has come from remote sensing techniques [e.g., *Kolawole et al.*, 2017; *Ranganai et al.*, 2002; *Gwavava et al.*, 1992; *Emenke*, 1986]. Receiver function analysis shows a relatively thick crust of 38 – 42 km [*Ebinger et al.*, 2017]. The relationship between the recent seismicity and incipient rifting in southern Africa remains an open question.

5.1.1. Difficulties in determining source parameters for buried earthquakes

Focal mechanisms calculated from seismic waves identify two nodal planes, a primary and an auxiliary. Determining which of these is the fault plane, however, requires an external dataset that may include field, aftershock, or surface deformation (e.g., Interferometric Synthetic Aperture Radar (InSAR)) observations. InSAR is a satellite based remote sensing technique, which uses the returns from two radar acquisitions to measure changes in the line-of-sight (LOS) path between the satellite and the ground. When an event ruptures the surface, phase discontinuities in InSAR data, for example, can unambiguously identify the correct plane (Figure 5.2a and b). However, the Earth acts

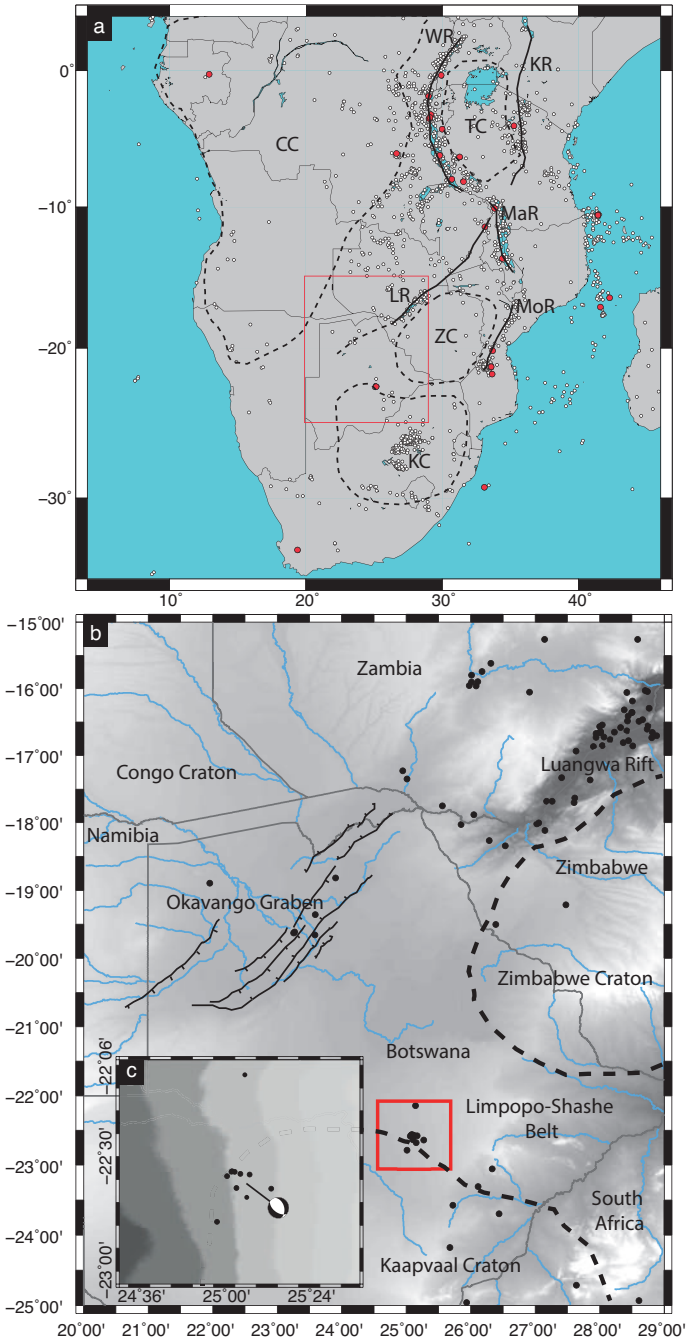

Figure 5.1: a) Distribution of seismicity, locations of cratons, and major rift branches in southern Africa. Earthquakes with magnitudes >6 are shown by red circles. Seismicity from USGS catalog 1910 – 2018. CC: Congo Craton, TC: Tanzania Craton, ZC: Zimbabwe Craton, KC: Kaapvaal Craton, WR: Western Rift, KR: Kenyan Rift, LR: Luangwa Rift, MaR: Malawi Rift, MoR: Mozambique Rift. We choose to present the cratons illustratively, given their variation with depth, spatial complexity and ill defined extents [*Craig et al.*, 2011; *Begg et al.*, 2009; *Last et al.*, 1997]. The red box denotes the extent of sub-panel (b). b) Seismicity (black circles) in the Botswana region of southern Africa. Schematic locations of the Okavango Graben, Zimbabwe, Congo, and Kaapvaal Cratons, and the Limpopo-Shashe Belt are also shown. The red box shows the extent of sub-panel (c). c) Location of the 2017 Moiyabana earthquake and aftershocks (USGS solutions). Faults in the Okavango Graben are reproduced from *Kinabo et al.* [2008].

as a short wavelength filter, and the surface deformation caused by earthquakes become increasingly smooth with increasing depth (Figures 5.2 and 5.3), making earthquake parameters harder to constrain.

We illustrate this effect by comparing the modelled surface deformation for a 19 km long normal faulting earthquake at 0 – 8 km (Figure 5.2a), 8 – 16 km (Figure 5.2c), and 16 – 24 km depths (Figure 5.2e), using the geometry of the Moiyabana earthquake according to the USGS catalogue (Table 5.1). For each depth we compare the LOS surface displacement patterns produced by an earthquake on each of the USGS nodal planes, one of which is west dipping (strike of 126°) and one east dipping (striking 343°), as seen from an ascending satellite viewing geometry. For a depth of 16 – 24 km we also show the surface deformation as seen from a descending viewing geometry.

Figure 5.2 shows that the pattern of LOS displacements from an earthquake on each nodal plane becomes increasingly similar with increasing depth. For an event at depth 0 – 8 km, the west dipping fault has three distinct lobes of deformation. The one with the greatest amplitude is associated with subsidence of the hanging wall, the second largest is associated with motion of the footwall, whilst the third is caused by uplift at the toe of the fault. In an ascending viewing geometry, the footwall displacement corresponds to a positive LOS range change, whilst uplift at the toe causes a negative LOS range change. The hanging wall and footwall lobes meet at the fault, whilst the toe lobe extends from approximately 10 to 50 km SW of the fault (Figure 5.2a). For an earthquake between 8 and 16 km the hanging wall lobe is twice as broad as it was for 0 – 8 km, and the other two lobes have a reduced amplitude. The transition between the lobes is also much smoother (Figure 5.2c). For 16 – 24 km the hanging wall lobe resembles a rounded triangle, and no sharp deformation gradients are predicted (Figure 5.2e). The footwall and toe lobes are also now comparable in magnitude (Figure 5.2d).

For the east dipping fault, we see a similar change with depth in the pattern of surface deformation. At 0 – 8 km the deformation has two main lobes, one north-east of the fault which is a combination of hanging wall subsidence and toe uplift, and another SW of the fault caused by displacement of the footwall (Figure 5.2b). In an ascending viewing geometry subsidence of the hanging wall and uplift at the toe cause positive LOS range changes, whilst footwall uplift causes negative LOS range changes. By an earthquake depth of 8 – 16 km deformation associated with the hanging wall and toe is more clearly two lobes (Figure 5.2d). The sharpest gradient in deformation is between the hanging wall and footwall lobes at the fault.

For a fault at 16 – 24 km, neither fault plane forms a single sharp deformation gradient at the surface which would help identify the fault location. The correct identification of the footwall and toe displacement relative to the hanging wall displacement is critical in

determining the location of the fault. However, the footwall lobe for the west dipping fault as seen from an ascending satellite viewing geometry is comparable in size and magnitude to the footwall lobe in the descending viewing geometry for the east dipping fault (Figures 5.2g, h, and 5.3d). This is also true for the toe lobes of the east and west dipping faults as seen from descending and ascending viewing geometries respectively (Figures 5.2g, h, and 5.3d). The combination of observations from both ascending and descending line-of-sights provides two range change components, which help mitigate this ambiguity by reducing the trade-offs when determining earthquake model parameters [*Wright et al.*, 2004].

Figure 5.3 shows the decrease in maximum range change and standard deviation across the interferogram for increasing fault depths in increments of 2 km between 0 and 22 km. Increasing the earthquake top depth results in a decrease in the amplitude of the range change, for between 8 and 16 km this decrease is ∼10 cm (46%) (Figure 5.3a). We find, for the example earthquake, that once the top depth reaches 10 km the standard deviation of the signal is comparable to the standard deviation in a typical interferogram (Figure 5.3c). For a stack of four interferograms, this depth is 16 km. The magnitude of the footwall and toe surface uplift is only significantly different for earthquakes <8 km deep (Figure 5.3d). In addition, the difference in amplitude of the surface deformation between faults 2 km separate in depth decreases with increasing depth (Figure 5.3b).

The difficulty in identifying the fault plane has been previously explored for strike slip events, such as the 2004 Al Hoceima earthquake (Morocco) [*Biggs et al.*, 2006]. In this case, models derived from the two nodal planes provided similar misfits to geodetic data, but earthquake scaling relationships [*Funning et al.*, 2005; *Scholz and Cowie*, 1990] and aftershock relocations were able to help determine the correct plane. In the 2009 Karonga normal faulting earthquake sequence, Malawi, uplift from the toe of the faults was visible in InSAR data [*Biggs et al.*, 2010a]. In this case, surface offsets were diagnostic in determining the fault plane, aided by ascending and descending InSAR observations.

We observe a similar ambiguity between nodal planes for buried normal faulting earthquakes. To determine the fault plane we utilise ascending and descending InSAR observations, model probabilities, and scaling relationships. Fault plane ambiguity for deep earthquakes is a particular problem in regions with a large seismogenic thickness, such as southern Africa.

5.1.2. Seismology and previous work

Moment tensors for the M_w 6.5 2017 Moiyabana earthquake from the USGS and CMT catalogue indicates the normal faulting earthquake occurred on a NNW-SSE striking fault, and that the event was relatively deep (23.5 km (USGS), 30 km (CMT)) (Table 5.1). Nine aftershocks, with magnitudes 4.0 – 5.0, were recorded within the first 12

Table 5.1: Optimal and 95% confidence bounds for the parameters of the Okada model for the Moiyabana earthquake. Depth is to the bottom of the fault plane. Figure 5.4 shows the data, model, and residuals for the oblique slip, dip slip, and west dipping models. RMS is data-model root-mean-square residual misfit, NP is nodal plane, LB is lower bound and UB is upper bound. Seismic moment values for models from this work are calculated using a shear modulus of 32 GPa. The preferred model of *Kolawole et al.* [2017] is also presented, with values given here as in the paper (fault location, length, and earthquake moment are not reported). The results of *Albano et al.* [2017] are also shown, although it should be noted that it is not stated in the original work where on the fault the depth corresponds to.

	Oblique slip model			Dip slip model			West dipping model			USGS		CMT		*Kolawole et al.* [2017]	*Albano et al.* [2017]		
Parameter	Optimal	LB	UB	Optimal	LB	UB	Optimal	LB	UB	NP1	NP2	NP1	NP2	Preferred	Optimal	LB	UB
X (Lat)	25.2	25.1	25.2	25.2	25.1	25.2	24.1	22.5	24.4	25.2		25.2		-	25.12	-7 (km)	12.9 (km)
Y (Long)	-22.7	-22.7	-22.65	-22.62	-22.63	-22.61	-24.03	-26.20	-23.95	-22.64		-22.54		-	-22.63	-14.7 (km)	5.5 (km)
Depth (km)	24.0	20.1	25.2	26.3	22.2	29.1	21.4	20.1	22.9	23.5		30		24	25	21.4	34.6
Length (km)	19.0	14.9	22.4	18.9	12.0	22.7	19.3	14.7	22.6	-		-		-	21	2.3	28.9
Width (km)	8.0	2.1	9.6	11.5	2.1	17.9	1.7	1.8	6.6	-	-	-		3.75	3.6	1.6	17.1
Strike (°)	300	297	302	301	298	304	122	122	122	343	126	332	126	NW-SE	304	278	324.5
Dip (°)	56	54	59	56	53	60	31	30	34	44	53	41	51	53	65	44.6	82.2
Dip slip (m)	-0.84	-3.44	-0.65	-0.65	-4.22	-0.36	-4.17	-3.97	-0.99	-		-		-1.59	-1.85	-4.87	-0.45
Strike slip (m)	-0.17	-1.15	0.04	-	-	-	0.44	0.08	0.42	-		-		-0.85	-1.77	-4.6	3.9
Rake (°)	-78	-89	-62	-90	-	-	-96	-102	-92	-62	-114	-70	-107	-114	-136	-	-
Joint RMS (cm)		1.50			1.53			1.53		-		-		-		-	
Slip-to-length ratio		5×10^{-5}			3×10^{-5}			2×10^{-4}		-		-		-		1.2×10^{-4}	
Moment (Nm)		4.2×10^{18}			4.5×10^{18}			4.1×10^{18}		6.1×10^{18}		7.0×10^{18}		-		6.14×10^{18}	

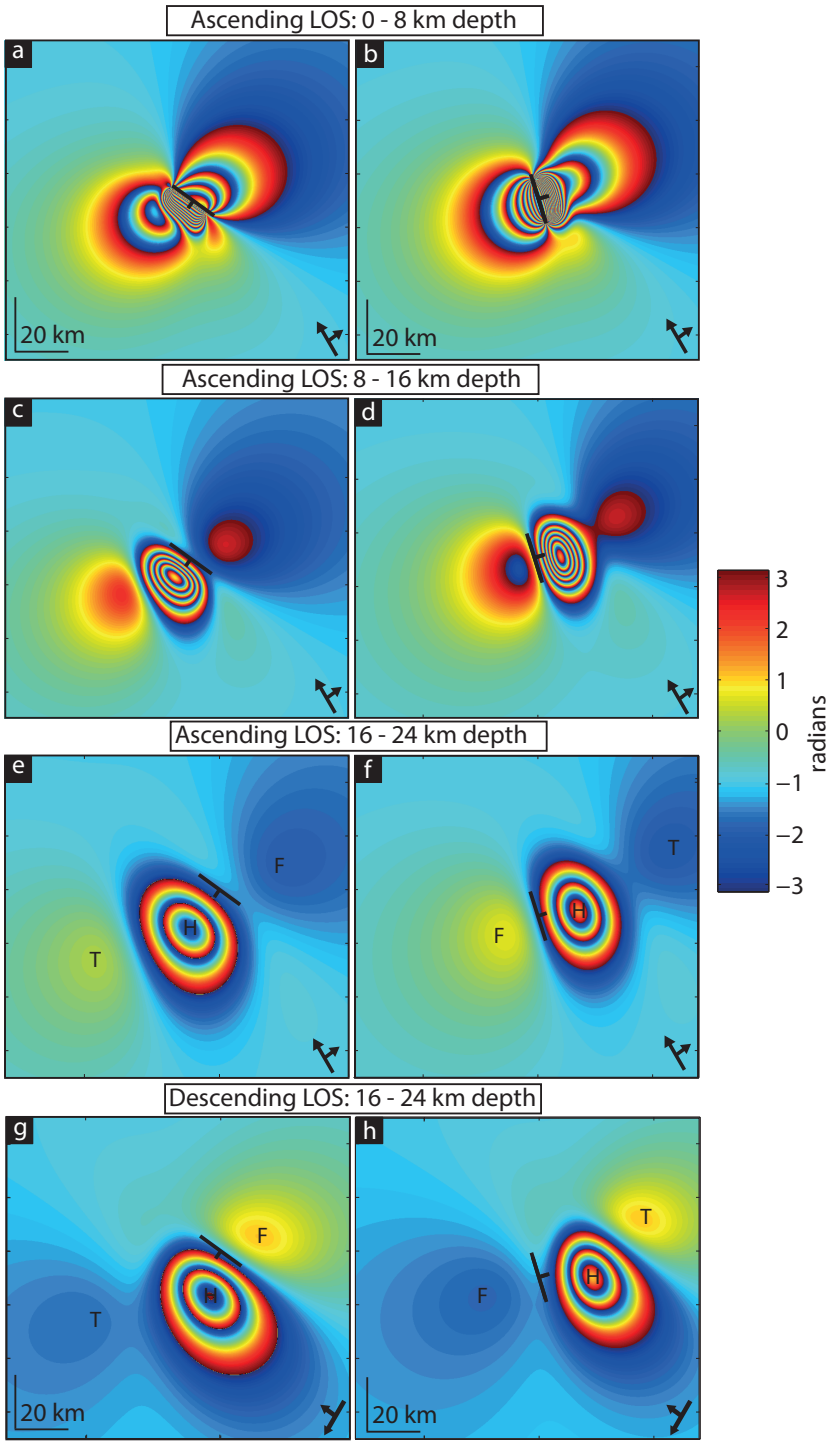

Figure 5.2: a) Forward model of USGS nodal plane with strike 126° (west dipping), rake -114°, and dip 53° for an earthquake between 8 km depth and the surface, as seen from an ascending satellite viewing geometry (incidence angle 42°, heading 346°). b) Forward model of USGS nodal plane with strike 343°(east dipping), rake -62°, and dip 44° for a fault between 8 km depth and the surface. c) 126° striking fault between 8 – 16 km depth. d) 343° striking fault between 8 – 16 km depth. e) 126° striking fault between 16 – 24 km depth. f) 343° striking fault between 16 – 24 km depth. g–h) Same as (e–f) but for a descending viewing geometry (incidence angle 47°, heading -165°). Black line shows the modelled fault, with tick showing direction of dip. H, F, and T denote the hanging wall, footwall, and toe lobes respectively.

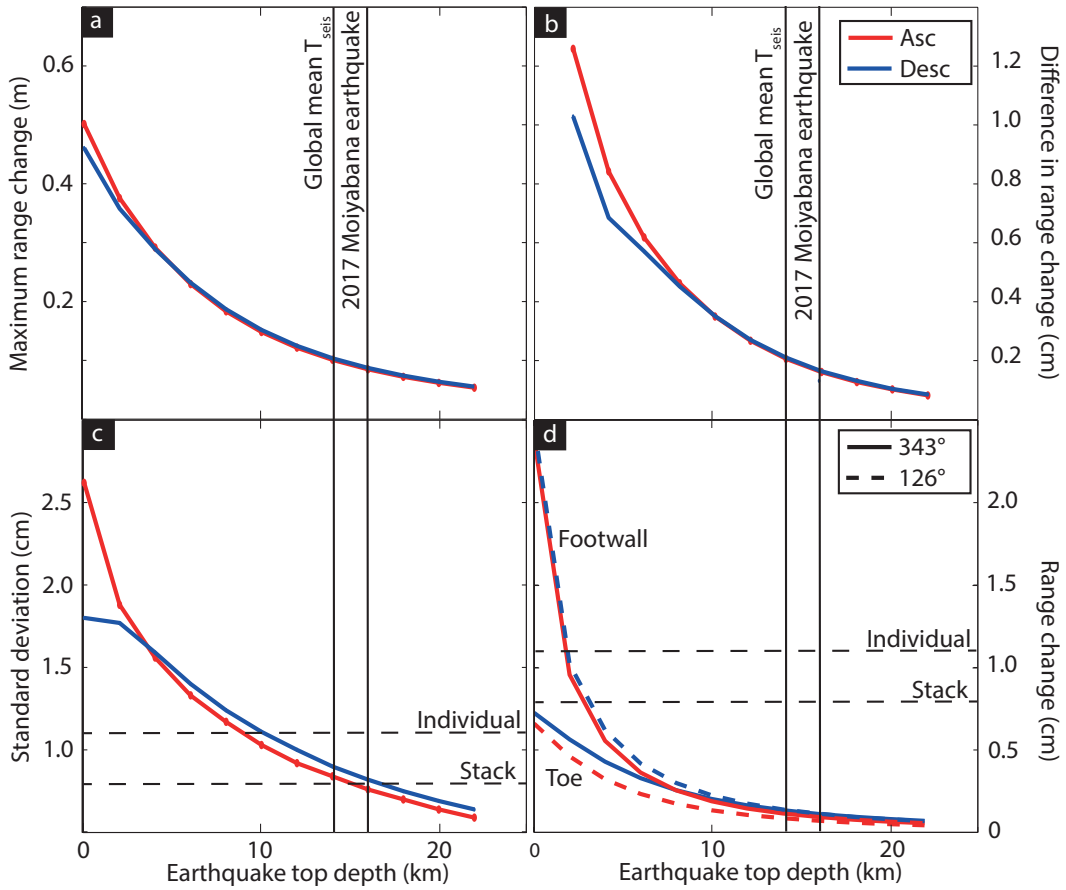

Figure 5.3: a) Maximum range change against earthquake top depth for ascending and descending satellite viewing geometries, calculated using the 343° striking (east dipping) earthquake model. The global mean estimate of the seismogenic thickness [*Wright et al.*, 2013] and top depth of the 2017 Moiyabana earthquake are shown for comparison. b) Reduction in maximum range change with increasing top depth. c) Standard deviation of the modelled range change. Dashed lines show the mean standard deviation for individual Sentinel-1 interferograms, and the interferogram stack, used in Chapter 5. d) Maximum range change associated with the footwall and fault toe for both a 343° and 126° striking faults, as seen from either ascending or descending viewing geometries.

months following the earthquake, all of which were within 20 km of the main shock (Figure 5.1c).

InSAR has previously been used to investigate the Moiyabana earthquake [*Kolawole et al.*, 2017; *Albano et al.*, 2017], but both studies use a single Sentinel-1 interferogram (30/03/2017 – 11/04/2017) and assume a north-east dipping fault plane. Models of earthquakes using individual interferograms are highly sensitive to the noise and satellite viewing geometry [*Biggs et al.*, 2007; *Wright et al.*, 2004]. For example, the fault model of *Albano et al.* [2017] has a 3 km down-dip width, 21 km length, and 2.5 m of slip, resulting in an unrealistic slip-to-length ratio of 1.2 x 10^{-4}, much greater than the expected range of 1 x 10^{-5} to 7.5 x 10^{-5} [*Leonard*, 2010; *Wells and Coppersmith*, 1994].

We analyse InSAR observations of this earthquake using a robust and exhaustive data analysis methodology to accurately determine the earthquake source parameters, and thus provide informative constraints on the local tectonics.

5.2. InSAR processing and observations

We use use data from the Sentinel-1 and ALOS-2 satellites, processed using the GAMMA software package [*Werner et al.*, 2000], to investigate the surface deformation caused by the Moiyabana earthquake.

We processed two descending ALOS-2 radar scenes to produce one interferogram (Table 5.2), and seven Sentinel-1 scenes to produce seven interferograms, six of which span the earthquake (Table 5.2). Topographic phase delays were corrected using the SRTM 30 m digital elevation model (DEM) [*Farr and Kobrick*, 2000] and all interferograms were filtered using a non-linear spectral filter with strength 0.4 [*Goldstein and Werner*, 1998], and unwrapped using the Minimum Cost Flow SNAPHU algorithm [*Chen and Zebker*, 2001].

Atmospheric artefacts can be a considerable source of noise in InSAR data [e.g., *Li et al.*, 2009; *Elliott et al.*, 2008], and we test a range of mitigating techniques including using external datasets and weather models, and a statistical approach (stacking) [e.g., *Yu et al.*, 2017a; *Bekaert et al.*, 2015; *Doin et al.*, 2009; *Elliott et al.*, 2008; *Wright et al.*, 2001]. The GACOS corrections of *Yu et al.* [2017a,b] model the atmospheric delay using a DEM, observations of the precipitable water vapour from ECMWF (European Centre for Medium Range Weather Forecasts) [*Jolivet et al.*, 2011; *Dee et al.*, 2011], and GPS observations, if available. This region of Botswana has very low relief, and a comparison between the ALOS-2 observations and the predicted atmospheric delays from GACOS suggest the observed atmospheric noise patterns are not captured by the model, and are thus likely be due to either be turbulent effects, or a change in atmospheric

conditions between ECMWF data and SAR acquisitions (∼3 hours) (Figure D.1). We find the GACOS atmospheric correction reduces the standard deviation of the ALOS-2 interferogram by only ∼0.1 cm, and thus choose not to apply the correction. We instead remove a linear ramp from all interferograms to account for long wavelength atmospheric delays and/or residual orbital errors.

To increase the signal-to-noise ratio, we stack the four most coherent Sentinel-1 interferograms that span the earthquake, such that the stack contains three pre- and three post-seismic acquisitions [*Biggs et al.*, 2007; *Emardson et al.*, 2003; *Wright et al.*, 2001] (Table 5.2). For a stack of N independent interferograms, stacking will increase the signal-to-noise ratio by a factor of $\sqrt{N}$, for situations where the signal in each interferogram is the same, and the remaining phase changes, e.g., atmospheric noise, are uncorrelated between acquisitions [*Biggs et al.*, 2007]. The mean standard deviation away from the co-seismic signal of individual Sentinel-1 interferograms in here is 1.2 cm (Table 5.2), whilst the standard deviation of the stack is 0.6 cm (Figure 5.3c). The standard deviation of the ALOS-2 interferogram is 2.1 cm, but no additional interferograms are available for stacking.

Both the co-seismic ALOS-2 and Sentinel-1 interferograms show a ∼50 by 30 km region of positive range change of up to 6 cm, elongated NW-SE, corresponding to hanging wall subsidence (Figure 5.4). Neither the individual interferograms nor the stack show a region of range change associated with possible footwall uplift, as predicted by our forward models, that is clearly distinct from atmospheric artefacts (Figure 5.2).

5.3. Fault plane modelling

We used the analytical Okada rectangular dislocation model [*Okada*, 1985] and a Bayesian inversion approach, incorporating Markov chain Monte Carlo algorithms, to investigate source parameters for the Moiyabana earthquake. We report marginal posterior probability density functions for each parameter to allow us to explore the non-uniqueness of the model, and calculate earthquake scaling relations [*Bagnardi and Hooper*, 2018; *González et al.*, 2015; *Hooper et al.*, 2013; *Mosegaard and Tarantola*, 1995; *Scholz and Cowie*, 1990]. We subsample interferograms using the quadtree approach, based on the data variance [*Jonsson et al.*, 2002], and assume measurement errors for each interferogram are independent and Gaussian. We performed 1 x 10^6 iterations, using flat prior probabilities between fixed bounds.

To ensure a full exploration of the parameter space we invert 1) each interferogram independently, 2) the Sentinel-1 stack, and 3) both the ALOS-2 interferogram and Sentinel-1 stack jointly. We vary the initial starting conditions to isolate both nodal planes, and test both purely normal and oblique fault displacements.

Table 5.2: Summary of datasets used in Chapter 5, and interferograms included in the stack. Line-of-sight (LOS) vector convention is east (E), north (N), up (U).

Satellite	Mode	Wavelength (cm)	Orbit	Number of scenes	Interferograms	LOS vector [E N U]	Stack
Sentinel-1	TOPS	5.6 (C-band)	Ascending	7	06/03/2017 – 11/04/2017	[-0.65 -0.17 0.74]	N
					18/03/2017 – 11/04/2017		Y
					18/03/2017 – 23/04/2017		Y
					25/03/2017 – 06/04/2017		Y
					30/03/2017 – 11/04/2017		Y
					30/03/2017 – 23/04/2017		N
					11/04/2017 – 17/05/2017		N
ALOS-2	ScanSAR	23.6 (L-band)	Descending	2	1	[0.71 -0.18 0.68]	
					02/04/2017 – 14/05/2017		-

Initially, we invert one Sentinel-1 interferogram (30/03/2017 – 23/04/2017), for the parameters of a model with pure dip slip motion, and find two distinct peaks in the posterior probability density function for the strike: one at ∼120° (west dipping) and ∼300° (east dipping) (Figure 5.5e, blue distribution). These correspond to the two nodal planes identified by seismology, and demonstrate the non-uniqueness discussed in Section 5.1.1 associated with using a single interferogram [*Wright et al.*, 2004]. We then perform a joint inversion of the ascending Sentinel-1 stack and descending ALOS-2 interferogram (Figure 5.5, orange and yellow distributions), keeping the strike as a free parameter (0° – 360°), but varying the initial conditions such that one inversion (orange) starts at 120°, and one at 300° (yellow). Both of the inversions converge on a strike of ∼300°, demonstrating that combining ascending and descending datasets helps discriminate between nodal planes for deep earthquakes (Table 5.1). We perform another inversion of both datasets, including both dip and strike slip displacement as free parameters (Figure 5.5, purple distribution), which also converges on a strike of 297° – 302° (95% confidence bounds), with a rake of -78° (-62° – -89°, 95% confidence bounds) (Table 5.1). This is consistent with the USGS and CMT solutions which have rakes of -62° and -70° respectively.

The fit of the oblique slip model is indistinguishable from that with only dip slip displacement (Table 5.1), with root-mean-square misfit values of 1.50 cm and 1.53 cm respectively (Figure 5.4). To test whether the addition of strike slip displacement in our model is statistically justified, we calculate the Akaike Information Criterion (AIC) values for the models [*Akaike*, 1974]. AIC considers the trade-off between the complexity of a particular model (number of model parameters, k), and its goodness of fit (model likelihood, l), as given by Equation 5.1, where the model with the smallest AIC value is the better model. We choose to use AIC in model selection as it utilises the probabilities calculated in the inversion methodology.

$$AIC = 2k - 2\ln(l). \tag{5.1}$$

We calculate the AIC values for the oblique and pure normal models to be 5.5 and 4.2 respectively. The relative likelihood of the oblique slip model to be the better model is 0.52 [*Burnham and Anderson*, 2003]. This indicates that, from the InSAR data alone, the inclusion of strike slip displacement is not statistically justified. However, as the seismological observations indicate some non-normal slip, our preferred model is that which includes oblique slip.

For comparison, we repeat the inversion again with initial conditions based on the west dipping model (the strike, ∼120° is allowed to vary ±5°, Figure 5.4) (Table 5.1). The west dipping model produces a comparable misfit (1.53 cm) to the east dipping models

(1.50 and 1.53 cm), and the spatial pattern of the residuals are not greatly different (Figure 5.4). However, the model is less realistic: requiring ∼4 m dip slip displacement, on a fault that is only 1.7 km wide down dip by 19 km, and dipping at 31°. These values contradict the seismological observations, and expected slip-to-length ratio (yielding 2 x 10^{-4} versus 1 x 10^{-5} to 7.5 x 10^{-5} [*Leonard*, 2010; *Wells and Coppersmith*, 1994]). By comparison, the slip-to-length ratios of the oblique and dip slip models are 5 x 10^{-5} and 3 x 10^{-5} respectively, which lie within the global range.

The preferred model, based on descending ALOS-2 and ascending Sentinel-1 interferograms and assuming some oblique slip, has a length of 19 km (95% probability confidence range: 15 – 22 km), width of 8 km (2 – 10 km), strike and dip of 300° (297° – 302°) and 56° (54° – 59°), and rake of -78° (-62° – -89°) (Table 5.1). The earthquake model also has a realistic slip-to-length ratio of 5 x 10^{-5}. The seismic moment of this model of the earthquake, using a shear modulus of 32 GPa, is 4.2 x 10^{18} Nm (95% confidence bounds: 3.9 – 4.5 x 10^{18} Nm), comparable to, but slightly lower than, the USGS and CMT estimates of 6.1 x 10^{18} Nm and 7.0 x 10^{18} Nm.

Figure 5.4 shows the data, model, and residual of all of the joint inversion models. A notable residual is located to the north-west of the fault plane in the ALOS-2 data. Given no such residual is present in the Sentinel-1 interferogram this is unlikely to be an un-modelled feature of the co-seismic displacement. Instead, we consider whether the residual is 1) post-seismic deformation, or 2) turbulent atmospheric noise. The ALOS-2 interferogram we use is 21 days longer than the Sentinel-1 data, and thus could contain 21 days of post-seismic deformation that the Sentinel-1 interferograms do not. To investigate any deformation between 03/04/2017 and 14/05/2017 we process the 11/04/2017 – 17/05/2017 Sentinel-1 interferogram (Figure D.2). It shows no clear signal in the area corresponding to the ALOS-2 residuals, suggesting the residual is not caused by post-seismic deformation. Instead, we conclude the residuals to the ALOS-2 data are caused by turbulent atmospheric delays.

5.4. Discussion

The Moiyabana earthquake provides a rare constraint on the present day stress field in Botswana [*Scholz et al.*, 1976]. We have demonstrated that the 2017 M_w 6.5 Moiyabana earthquake occurred on an ∼19 x 8 km north-east dipping (56°) fault, with bottom depth of ∼24 km (20 – 25 km) (Table 5.1). The location and orientation of the fault agrees with independently mapped structures from aeromagnetic surveys of the region (Figure D.3) [*Kolawole et al.*, 2017; *Ranganai et al.*, 2002] and with a north-west striking gravity anomaly, aligned with the Precambrian fabric that underlies the more

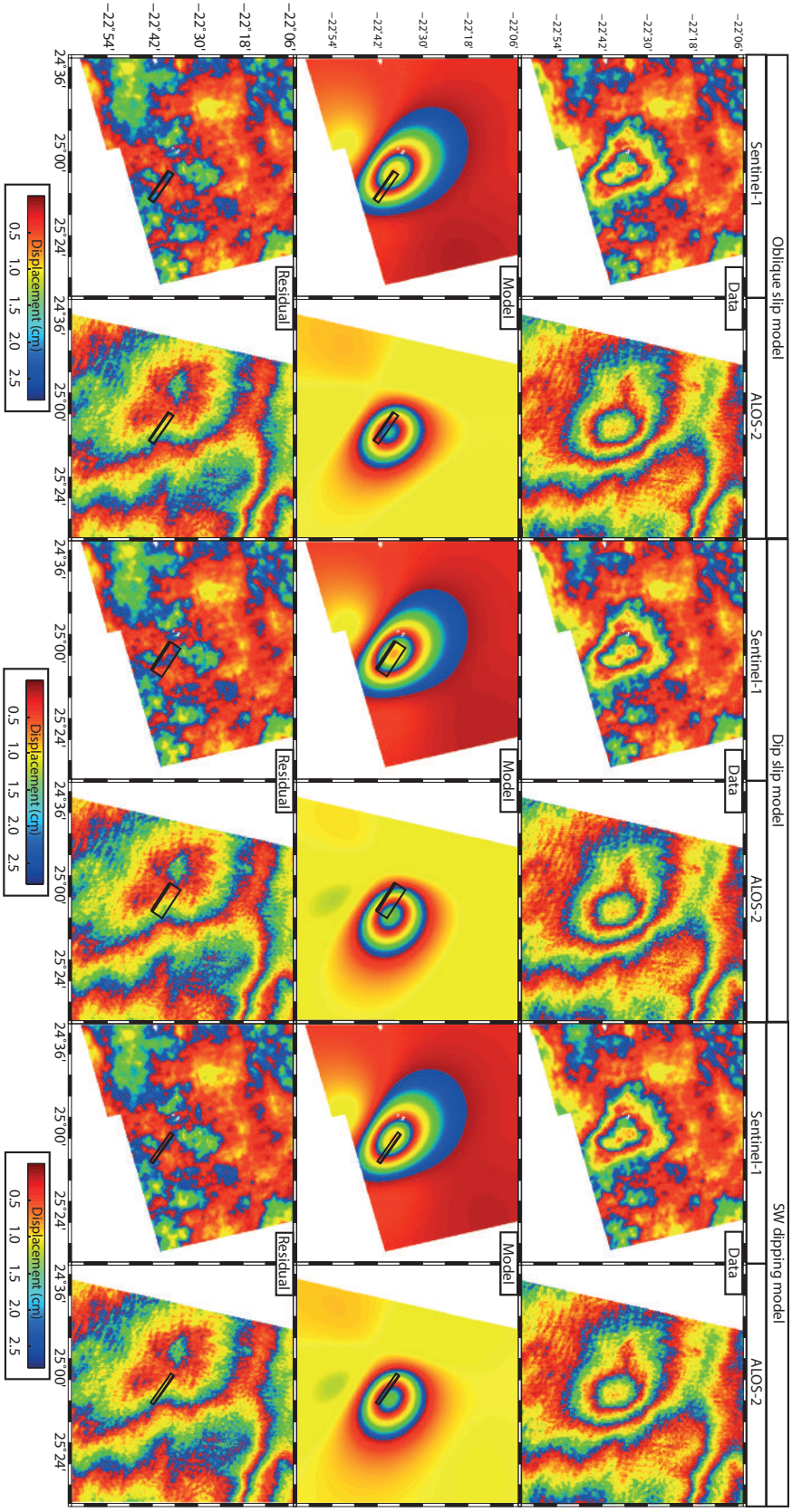

Figure 5.4: Data, model, and residual plots for oblique slip, dip slip, and SW dipping models of the Moiyabana earthquake. The bold line represents the up-dip fault edge.

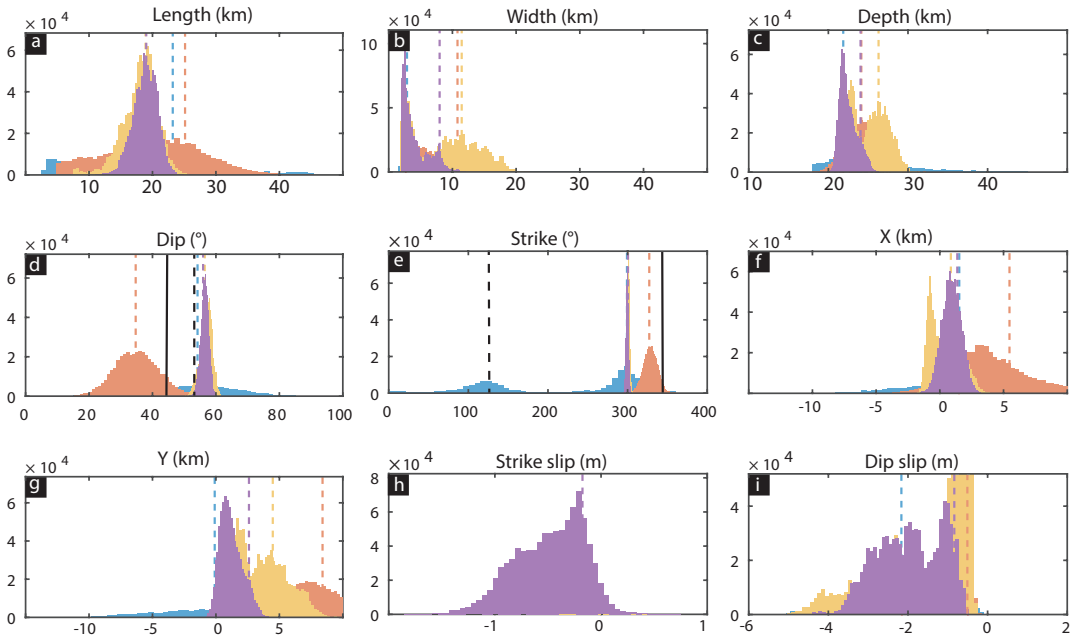

Figure 5.5: Marginal probability density functions for the model parameters of each inversion: Sentinel-1 interferogram only (blue), Sentinel-1 and ALOS-2 interferograms with 120° strike (west dipping) initial condition (orange), Sentinel-1 and ALOS-2 interferograms with 300° strike (east dipping) initial condition (yellow), and Sentinel-1 and ALOS-2 with dip slip and strike slip displacements (purple). Dashed and complete black lines indicate the USGS estimates for dip, and strike. X and Y are given relative to 25.147° E, -22.658° N.

recent (Karoo) dyking sequences [*Le Gall et al.*, 2002] between two Neoarchean thrust faults [*Ranganai et al.*, 2002]. The presence and orientation of a Precambrian fabric is further highlighted by shear wave splitting observations [*Silver et al.*, 2001], wherein fast polarisation directions in the mantle systematically reflect geological structures, for example the Limpopo-Shashe Belt, and not the present day plate motions (Figure D.3). The coincidence of gravity and magnetic anomalies with the location of the fault model suggests faulting occurred on a reactivated pre-existing structure. This is consistent with models of early rift development which show that faulting occurs preferentially on pre-existing faults, if suitably orientated, rather than through the formation of new fractures [e.g., *Hodge et al.*, 2018a; *Kolawole et al.*, 2018; *Korme et al.*, 2004; *Modisi*, 2000; *Scholz and Contreras*, 1998; *Holdsworth et al.*, 1997; *Birt et al.*, 1997; *Sibson*, 1990].

In addition to subsurface heterogeneities providing planes of weakness, strain partitioning can occur around rigid bodies [*Koptev et al.*, 2015; *Tesauro et al.*, 2015; *Craig et al.*, 2011; *Le Gall et al.*, 2008]. The Moiyabana earthquake occurred in the Archean collision zone between the Kaapvaal and Zimbabwe Cratons [*Roering et al.*, 1992]. These cratons are cold, hard, and rigid, with tensile strengths much greater than the forces that are available [*Kendall and Lithgow-Bertelloni*, 2016; *Buck*, 2006; *Lenardic et al.*, 2000]. They will therefore perturb the strain field, possibly locally focussing the strain across the Limpopo-Shashe Belt region, promoting failure.

The NE-SW extension direction indicated by the Moiyabana earthquake demonstrates a change in the stress orientation from the NW-SE extension that occurs in the Okavango [*Modisi*, 2000; *Scholz et al.*, 1976]. This is consistent with the thin shell finite element models for stress distribution, based on geological indicators and incorporating lateral density variations, of *Bird et al.* [2006], which shows strain localisation around the cratons. Alternative sources of stress may include local perturbations associated with lithospheric compensation and flexure [e.g., *Ergin and Aktar*, 2018; *Craig et al.*, 2016; *Hampel and Hetzel*, 2006; *Bungum et al.*, 2005]. However, the region has been relatively stable since $\sim$2 Ga, and thus the required loading/unloading processes are absent. As such, we conclude far-field stresses are responsible for this earthquake.

The modelled and observed role of local heterogeneities in southern Africa suggests that further faulting, and any subsequent rifting, will follow the boundaries of cratons, as is also observed around the Tanzania Craton [*Craig et al.*, 2011; *Ebinger et al.*, 1997]. The role locally weaker and stronger regions of the lithosphere have in influencing the stress field should therefore be considered in models of rifting, and in seismic hazard assessments. Ultimately, this earthquake indicates extensional stresses associated with the East African Rift continue south-east of the Okavango region.

The Moiyabana earthquake occurred relatively deep (16 – 24 km), compared to global

assessments of seismogenic thicknesses [*Wright et al.*, 2013]. However, earthquakes rupturing depths >20 km are not uncommon in eastern and southern Africa [e.g., *Craig et al.*, 2011; *Yang and Chen*, 2010; *Jackson and Blenkinsop*, 1993]. Deep earthquakes in Malawi have been interpreted to be a result of rupture of thick, cold lithosphere [*Foster and Jackson*, 1998; *Nyblade and Langston*, 1995; *Jackson and Blenkinsop*, 1993], and the depth of the Botswana earthquake suggests seismogenic thicknesses are also large here. The collision between the Kaapvaal and Zimbabwe Cratons provides a plausible mechanism for thickening of the crust ∼2.5 Ga, that has resulted in the thick, cold, and therefore strong, lithosphere of Botswana today [*Ebinger et al.*, 2017; *Nguuri et al.*, 2001].

Future assessments of seismic hazard in southern Africa will need to consider the spatial extent of large seismogenic thicknesses and low strain rates to properly quantify the hazard associated with large, if infrequent, earthquakes [*England and Jackson*, 2011; *Stein and Liu*, 2009; *Scholz et al.*, 1986].

5.5. Conclusions

Here, we demonstrate that the 3^{rd} April 2017 M_w 6.5 Moiyabana normal faulting earthquake occurred on a buried north-east dipping fault plane. Fault identification for buried normal faulting earthquakes can be difficult from observation of surface deformation, and we here demonstrate the advantage of stacking interferograms, incorporating observations from multiple satellite line-of-sights, and using a probabilistic inversion scheme.

Independent magnetic and gravity surveys identify Precambrian structures with the same trend as our preferred model of the Moiyabana earthquake. The event likely represents the reactivation of one of these structures, possibly in response to far-field extensional stresses associated with rifting in East Africa. We emphasise the role inherited weaknesses (Precambrian faults) and rigid blocks (the Kaapvaal and Tanzania Cratons) may have had in influencing the strain field within which this earthquake occurred.

Chapter 6

Concluding Remarks

6.1. Summary and implications

Crustal heterogeneities can represent zones of relative weakness or strength, and thus play a major role in continental rifting. In this thesis I have explored the contribution of heterogeneities in facilitating and guiding rifting as it develops, with specific consideration to fault reactivation and fluid migration. Here, I summarise these findings, and discuss the implications of the work. The influence of pre-existing structures throughout rifting is illustrated schematically in Figure 6.1.

At mature continental rifts the emplacement of magma plays an important role in accommodating extension. In Chapter 2 I explore how a pre-rift rift-oblique fault structure has influenced magma emplacement at the Corbetti caldera, Ethiopia. I show that a crustal scale feature that cross-cuts the caldera has influenced magma storage over hundreds of thousands of years, magma transportation over tens of thousands of years, and hydrothermal circulation over annual timescales using geophysical (InSAR and seismology) and geomorphological (caldera shape and vent distribution) datasets. This work fits with a growing body of literature on how influential fault structures are on magmatism in rifts: from the location of magma reservoirs and eruptive centres [e.g., *Corti et al.*, 2018; *Robertson et al.*, 2016], to the composition of erupted products [e.g., *Hutchison et al.*, 2018]. The work also has implications on our understanding of the relationship between tectonics and caldera formation [e.g., *Saxby et al.*, 2016; *Holohan et al.*, 2008; *Girard and Vries*, 2005].

Corbetti is one of several active magmatic centres within the East African Rift today (Figure 1.4). In Chapter 3 I document inflation of the caldera at vertical rates of $\sim$7 cm/yr, that has been ongoing since mid-2009. I find a Mogi model at 6.6 km depth with a volume change of $\sim$0.01 km^3/yr is the most statically justified fit to InSAR and GPS observations of the surface displacement. The source is coincident with a conductive anomaly, and is located on the pre-existing structure I identified in Chapter 2. This, as well as the depth, duration, and rate of deformation, evidence for brittle failure around the source, and modelled density (*Biggs et al.*, In Review) indicates that the source is magmatic. The deformation at Corbetti therefore provides an observation of the mechanism and timescales of upper crustal magma reservoir growth in a rift caldera setting. The rate of volume change at Corbetti is greater than the long-term eruption rate, indicating the assembly of magma reservoirs occurs in pulses of above average magma flux.

Dyking is often considered the most important mechanism for magma transport in rift settings [e.g., *Sigmundsson et al.*, 2014; *Wright et al.*, 2006]. However, the cumulative volume change we have observed at Corbetti so far is comparable to that of several recent dyking events in less mature sections of the rift [*Pallister et al.*, 2010; *Calais et al.*,

2008], suggesting reservoir growth can represent a volumetrically significant component of magma transport in the crust. The inferences of magma reservoir geometry, size, and depth at Corbetti contribute to our growing understanding of magma reservoir properties elsewhere in the rift [e.g., *Biggs et al.*, 2016; *Field et al.*, 2012; *Wauthier et al.*, 2012; *Biggs et al.*, 2011, 2009b], and helps us to understand how they may change throughout rifting [*Biggs et al.*, 2013; *Field et al.*, 2012].

Corbetti has evidence for lava flows and VEI 4 – 5 eruptions during the Holocene [*Fontijn et al.*, 2018], is ∼10 km from two major population centres, and yet has no permanent or real-time monitoring. As such, observations of a prolonged, elevated magma flux into the caldera has significant implications in determining the potential hazard at Corbetti, and other comparable systems in the EARS. Almost all of the EARS volcanoes lack permanent monitoring, with the result of large uncertainties in the hazard posed by volcanoes throughout East Africa.

In contrast to Ethiopia, extension rates in southern Mozambique are low (∼2 mm/yr [*Saria et al.*, 2014]). Nonetheless, the Mozambique Rift is seismically active, and provides a locality to observe purely amagmatic rifting. I analyse InSAR observations of the 2006 M_w 7.0 Machaze and 2016 M_w 5.6 Zinave earthquakes (Chapter 4). I find, in agreement with other studies, that the Machaze fault dip is steep (∼75°), and was likely a reactivation of a pre-existing structure in the basement. The Zinave fault, on the other hand, occurred between 4 – 8 km deep, in what is believed to be post-Jurassic sediments where pre-existing structures may not be expected. A temporal analysis of the intervening seismicity shows a good fit with the Omori law, indicating the Zinave earthquake is part of a >10 year aftershock sequence following the Machaze earthquake. Indeed, the Machaze-Zinave sequence provides an example of elevated seismicity, and thus hazard, which in low strain settings should be expected for potentially decades. The Coulomb stress change on the 2016 fault plane from the 2006 event shows that the prior earthquake increased the stress on the fault, promoting failure. The triggering of earthquakes from static stress changes is not new, but this observation shows how slip on pre-existing structures can influence the formation of newer, shallower, faults in an incipient rift setting.

Central Botswana is a region where strain rates are poorly constrained, and it is unclear precisely whether or where rifting is occurring. However, in 2017 a M_w 6.5 normal faulting earthquake demonstrated that the region is, at least locally, subject to extensional stresses. In Chapter 5 I used ascending and descending InSAR observations, a Bayesian inversion approach, and empirical earthquake scaling laws to ascertain the Botswana earthquake occurred on a north-east dipping fault between 16 and 24 km depth. The location of this earthquake is significant: >400 km from the nearest surface expression of rifting, and in the collision zone between two thick, rigid Archean cratons.

We hypothesise that this earthquake occurred on a pre-existing structure, identified through a comparison with aeromagnetic data, as a result of far-field stresses being focussed around the cratons. The Botswana earthquake therefore demonstrates how large scale crustal heterogeneities are able to partition strain in a pre- to incipient-rift environment.

6.2. Outlook

This thesis investigates magmatic and amagmatic rifting, and the influence of pre-existing structures. However, this thesis only provides an incremental step towards fully understanding continental rifting. The EARS is a constantly evolving feature, and, with time, subsequent continuous and discrete rifting episodes will occur, facilitating further insights.

Volcanoes, a clear indicator of magmatic rifting, are inherently complex systems, and a range of behaviours and styles are observed along the EARS. InSAR is an invaluable tool to investigate processes at active systems, but for a holistic understanding a multidisciplinary approach will be necessary [*Till et al.*, 2018], through combining different geophysical techniques with field observations, geochemistry, and modelling approaches [e.g., *Pritchard et al.*, 2018]. The RiftVolc project, which focusses on the Main Ethiopian Rift, is an example of interdisciplinary collaboration with the explicit intent of understanding the past behaviour, present-day activity, and future hazard of MER volcanoes.

Insofar, RiftVolc collaborators have begun to quantify the location, occurrence, and geochemistry of previous eruptions of Corbetti, Aluto, O'a, Bora-Baricha, Boset-Bericha, Tullu Moye, Gedemsa, Kone, and Fentale [*Siegburg et al.*, 2018; *Fontijn et al.*, 2018; *Hutchison et al.*, 2018], and build a picture present-day activity (*Temtime et al.* [2018], Chapter 3). Geodetic, seismic, and remote sensing techniques have been applied to understand the geothermal reservoirs at volcanoes within the MER. This has included their internal seasonal pressure variations [*Birhanu et al.*, 2018], circulation pathways [*Nowacki et al.*, 2018; *Lloyd et al.*, 2018; *Braddock et al.*, 2017], the identification, temperature, and temporal evolution of fumarolic behaviour [*Braddock et al.*, 2017], and CO_2 degassing [*Hunt et al.*, 2017]. The seismic hazard within the MER has also been investigated, with particular focus on the M_w 4.3 January 2016 Hawassa earthquake [*Wilks et al.*, 2017b]. These studies together demonstrate that the MER is volcanically and seismically active, and could potentially host a devastating volcanic eruption.

Many geodetic studies have highlighted the present-day restlessness of East African volcanoes [e.g., *Biggs et al.*, 2011, 2009b], and recent and historical magmatic events have demonstrated their ongoing hazard [*Goitom et al.*, 2015]. Correctly quantifying

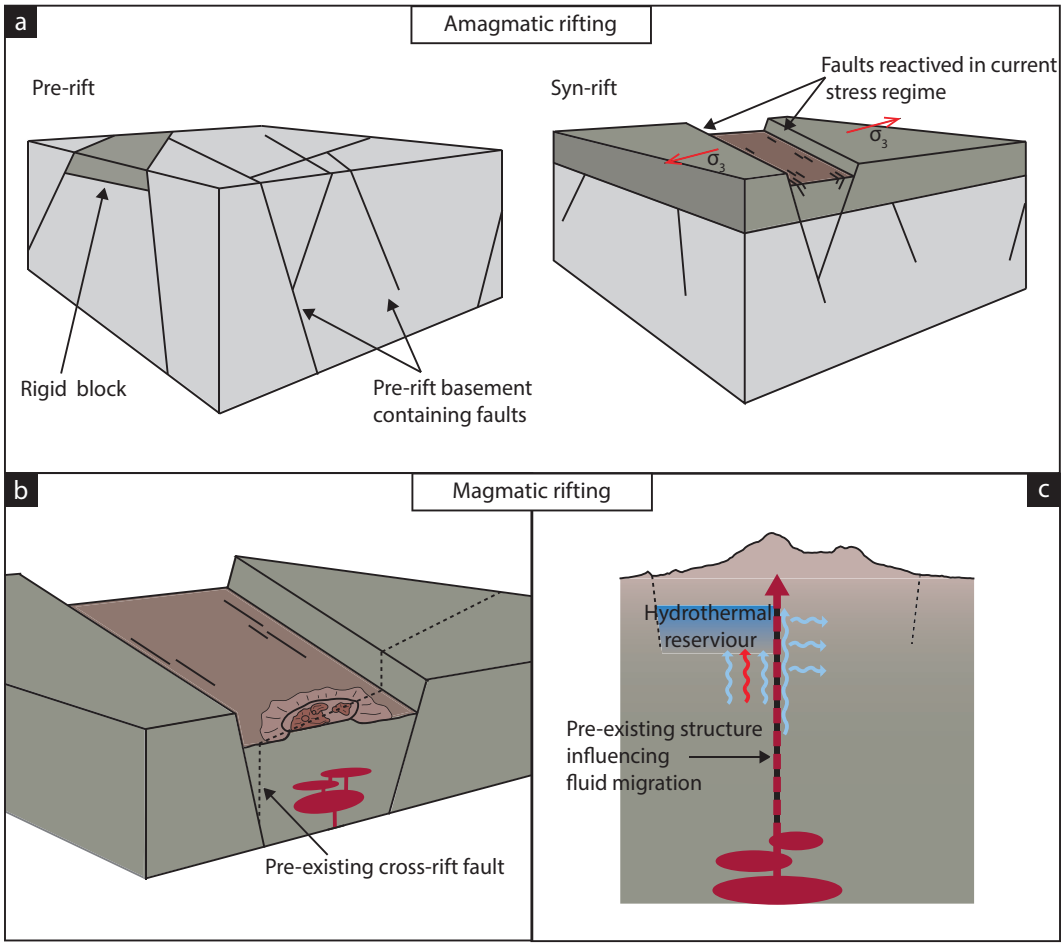

Figure 6.1: a) Crustal structure, pre-rift, is heterogeneous, containing faults and contrasting lithologies. As rifting initiates, faults oriented such that failure occurs via frictional processes will be reactivated before the formation of new faults (Chapters 4 and 5). This can have the effect of guiding where rifting occurs. Slip on these faults can result in the formation of new faults. b) Magma has an increasingly important role in accommodating extension as rifting develops (Chapter 3). Faults which cross-cut the rift can guide magma migration, influencing the location of surface volcanism. c) Cross-rift structures can also guide the circulation of hydrothermal fluids, acting as permeable pathways or barriers to flow (Chapter 2).

hazard is especially important as populations grow and infrastructure develops. As such, volcano monitoring should be a priority. The use of InSAR for this is an objective of the COMET Volcano Deformation Database, which will use data from the Sentinel-1 satellite constellation to produce interferograms of most of the world's Holocene volcanoes in near-real time. This will not only characterise the behaviour of currently active systems, but also create baseline measurements [*Ebmeier et al.*, 2018].

Regular and frequent SAR acquisitions over the world's highly straining regions, including the EARS, is important. These regions are where most of the worlds earthquakes will occur, and thus having the data available (freely and publicly in many cases, e.g., Sentinel-1) will allow rapid and high quality observations of events soon after they occur. These observations can then be used to direct fieldwork, or for scientific investigation in their own right.

InSAR can also be used to observe the long wavelength deformation associated with plate boundaries [e.g., *Pagli et al.*, 2014; *Walters et al.*, 2014]. High resolution, spatially extensive maps of crustal velocity fields fields allow us to determine where strain is distributed. In Afar, three contrasting styles of rifting have been observed using InSAR: localised transient post-dyking deformation, distributed spreading over several overlapping segments, and localised inter-dyking deformation [*Pagli et al.*, 2014]. Extending observations of the velocity field into the MER would 1) provide additional constraints on the relative displacement of the Wonji Fault Belt, the border faults, and at the magmatic centres, 2) identify regions of extension rates elevated above the long-term average (e.g., by magma migration), and 3) identify possible relationships between spreading rate and lithological properties (e.g., crustal thickness, presence of heterogeneities, available melt). Quantifying the strain distribution throughout the MER is also important given the direct relationship between strain accumulation and seismic hazard. The MER is also well suited to make these observations: there is good InSAR coverage (from several ascending and descending Sentinel-1 SAR images) and numerous continuous and campaign GPS sites, the extension is oriented favourably (∼east-west) for satellite InSAR observations, and recent developments in weather models should help reduce noise [*Yu et al.*, 2017a,b].

The EARS is not the only example of rifting on Earth. In this thesis I discuss the influence that rift-parallel and rift-perpendicular pre-existing structures have in crustal extension. Similar to the EARS, rifting in Iceland, part of the Mid-Atlantic Ridge system, occurs above an upwelling mantle plume [*Bijwaard and Spakman*, 1999; *Schilling*, 1991, 1973]. Although in contrast, the Icelandic crust is younger, has fewer inherited fault structures, and no cratons. By looking at Iceland we can therefore ask how, in comparison to the EARS, does magma transportation and strain partitioning occur in the relative absence of crustal heterogeneities, and what is the difference in strain

partitioning between regions of differing crustal thicknesses, heat flows, and extension rates?

Transtensional rifting in the Taupo Volcanic Zone (TVZ), New Zealand, is driven by back-arc spreading associated with the subduction of the Pacific plate. The TVZ has a central region of silicic calderas, with andesite-dacite stratovolcanoes along strike to the north and south [*Wilson et al.*, 1995]. Faults from the underlying Mesozoic basement are thought to control magma migration [*Cole et al.*, 2010], promote hydrothermal fluid circulation [*Rowland and Sibson*, 2004], and be reactivated during caldera faulting [*Seebeck et al.*, 2010]. TVZ extension rates are comparable to the MER (6 – 8 mm/yr [*Villamor and Berryman*, 2001; *Darby and Meertens*, 1995]), and its spatial scale is similar (∼50 – 60 km wide), but the TVZ rhyolite production rates (mean eruption rate of 9 x 10^{-3} km^3/yr over the last 1.6 Ma) and heat flow (700 mW/m^3) are higher [*Wilson et al.*, 1995; *Bibby et al.*, 1995]. The TVZ is therefore a setting where we can test the ubiquitousness of the influence of pre-existing structures: does a high heat and melt flux reduce or increase the interrelationship between inherited structures and melt transportation? Do inherited structures partition strain in the TVZ in the same was as in the EARS, and what impact do they have on the localisation of rifting, and the migration and geochemical evolution of the melt?

The success in this thesis of using InSAR to investigate magmatic and amagmatic rifting demonstrates the relevance of InSAR to study future rifting processes in the EARS, and at other rift systems. As the current and future dedicated InSAR satellites continuously acquire more data from across the world, we will increasingly be able to investigate smaller magnitude, longer duration signals in noisier environments, and better understand the causative processes.

Appendices

Appendix A

Additional Material for Chapter 2

A.1. Interferogram theory and post-processing

A.1.1. Interferogram de-ramping

Interferograms from all sensors in Chapter 2 were individually de-ramped to remove phase contributions from orbital, ionospheric and long wavelength atmospheric delays where necessary [e.g., *Biggs et al.*, 2007], (Figure A.2). This de-ramping is done by inverting for the constants a, b, c, d and e that describe a polynomial of the equation,

$$\begin{bmatrix} 1 & x_1 & y_1 & x_1^2 & y_1^2 & x_1y_1 \\ 1 & x_2 & y_2 & x_2^2 & y_2^2 & x_2y_2 \\ 1 & x_3 & y_3 & x_3^2 & y_3^2 & x_3y_3 \\ \vdots & \vdots & \vdots & \vdots & \vdots & \vdots \\ 1 & x_n & y_n & x_n^2 & y_n^2 & x_ny_n \end{bmatrix} \begin{bmatrix} a \\ b \\ c \\ d \\ e \end{bmatrix} = \begin{bmatrix} z_1 \\ z_2 \\ z_3 \\ \vdots \\ z_n \end{bmatrix}$$

where x and y represent a pixel's location, n is the number of pixels, and z is the phase at each pixel. The polynomial ramp is then reconstructed using these constants and removed from the corresponding interferogram. This method, however, will also remove any signals that can also be described by a polynomial, limiting the maximum size of ground deformation we can investigate to less than the length scale of the interferograms: ∼50 km east-west, and ∼30 km north-south.

A.1.2. Displacement components

For each pixel in a single interferogram the local east-west (e), north-south (n) and up (u) displacement components can be calculated from the satellite's heading (H, clockwise from north) and incidence angle at the ground surface (i, between line-of-sight and vertical) through:

$$\begin{pmatrix} p_e \\ p_n \\ p_u \end{pmatrix} = \begin{pmatrix} -\cos(H).\sin(i) \\ \sin(H).\sin(i) \\ \cos(i) \end{pmatrix}.$$

For points which are observed by a satellite with ascending (a) and descending (d) viewing geometries, $\hat{\mathbf{p}}$ becomes the 2 x 3 matrix

$$\mathbf{P} = \begin{pmatrix} \hat{p}_a \\ \hat{p}_d \end{pmatrix} = \begin{pmatrix} p_{ea} & p_{na} & p_{ua} \\ p_{ad} & p_{nd} & p_{ud} \end{pmatrix},$$

and $\mathbf{r}$ becomes the 3 x 2 matrix

$$\mathbf{R} = \begin{pmatrix} \mathbf{r}_{ea} & \mathbf{r}_{ed} \\ \mathbf{r}_{na} & \mathbf{r}_{nd} \\ \mathbf{r}_{ua} & \mathbf{r}_{ud} \end{pmatrix}.$$

Through the equation $\mathbf{R} = \mathbf{P}\mathbf{u}$, $\mathbf{u}$, the displacement in e, n and u, can inverted for in a weighted least squares sense,

$$\mathbf{u} = [\mathbf{P}^T \Sigma_R^{-1} \mathbf{P}]^{-1} \mathbf{P}^T \Sigma_R^{-1} \mathbf{R}, \tag{A.1}$$

where Σ_R is the covariance matrix of errors in the observed range changes.

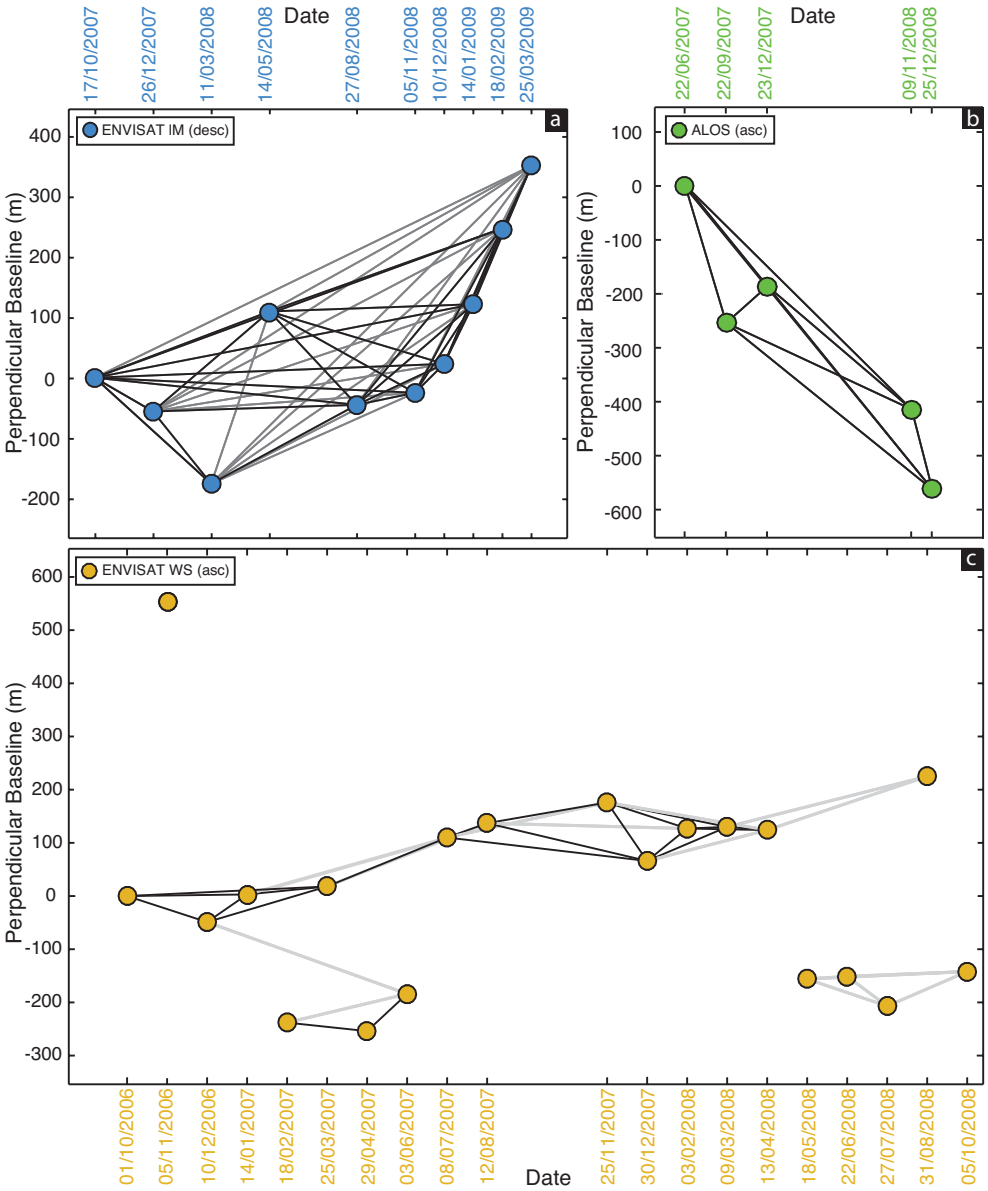

Figure A.1: Temporal-perpendicular baseline plots for ENVISAT IM (a), ALOS (b) and ENVISAT WS (c) data used in Chapter 2. The lines between dates represent the interferograms produced in Chapter 2. Black lines show interferograms that informed analysis, grey lines represent interferograms whose coherence was inadequate or were not used.

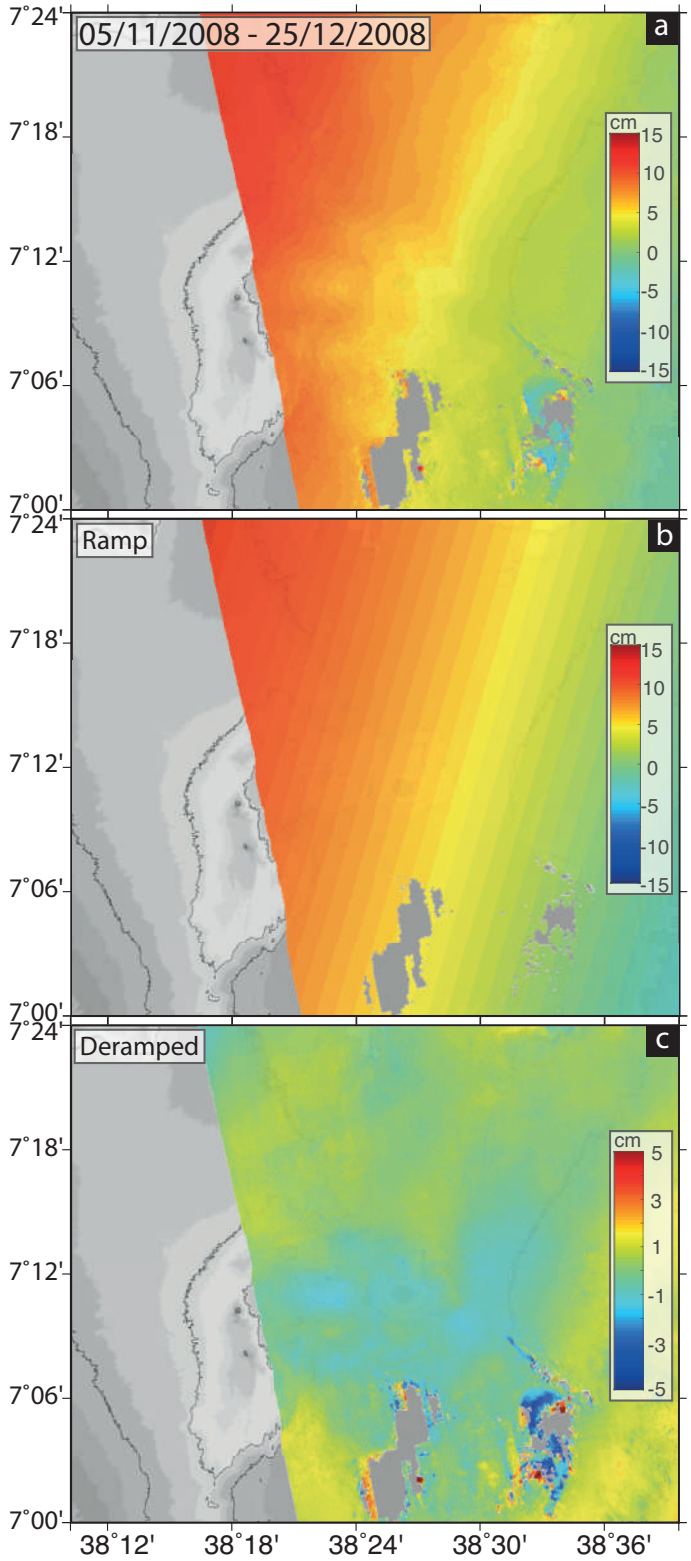

Figure A.2: Illustration of the effect of removing a ramp from one the interferograms. a) Initial interferogram, b) the calculated ramp, c) the residual between the two (de-ramped interferogram). Note the change in colour scale.

Table A.1: Summary of InSAR data used in Chapter 2.

ENVISAT IM Track 321			ENVISAT WS Track 386			ALOS Track 605		
Start date	End date	Perpendicular baseline (m)	Start date	End date	Perpendicular baseline (m)	Start date	End date	Perpendicular baseline (m)
17/10/2007	26/12/2007	-56	01/10/2006	10/12/2006	-60	22/06/2007	22/09/2007	-255
17/10/2007	05/03/2008	-176	01/10/2006	14/01/2007	-7	22/06/2007	23/12/2007	-186
17/10/2007	14/05/2008	110	01/10/2006	25/03/2007	11	22/06/2007	09/11/2008	-415
17/10/2007	27/08/2008	-47	10/12/2006	14/01/2007	52	22/06/2007	25/12/2008	-564
17/10/2007	05/11/2008	-26	10/12/2006	25/03/2007	72	22/09/2007	23/12/2007	68
17/10/2007	10/12/2008	27	14/01/2007	25/03/2007	19	22/09/2007	09/11/2008	-161
17/10/2007	14/01/2009	127	25/03/2007	08/07/2007	122	22/09/2007	25/12/2008	-310
26/12/2007	05/03/2008	-121	08/07/2007	12/08/2007	5	23/12/2007	09/11/2008	-229
26/12/2007	14/05/2008	165	08/07/2007	25/11/2007	47	09/11/2008	25/12/2008	-158
26/12/2007	27/08/2008	7	08/07/2007	30/12/2007	-62	23/12/2007	25/12/2008	-378
05/03/2008	10/12/2008	202	12/08/2007	25/11/2007	42	-	-	-
14/05/2008	27/08/2008	-157	12/08/2007	30/12/2007	-67	-	-	-
14/05/2008	05/11/2008	-136	25/11/2007	30/12/2007	-109	-	-	-
14/05/2008	10/12/2008	-84	25/11/2007	03/02/2008	-47	-	-	-
14/05/2008	14/01/2009	17	25/11/2007	09/03/2008	-57	-	-	-
14/05/2008	18/02/2009	143	30/12/2007	03/02/2008	62	-	-	-
27/08/2008	05/11/2008	21	30/12/2007	09/03/2008	52	-	-	-
27/08/2008	10/12/2008	74	30/12/2007	13/04/2008	46	-	-	-
27/08/2008	14/01/2009	174	03/02/2008	13/04/2008	15	-	-	-
05/11/2008	10/12/2008	53	09/03/2008	13/04/2008	6	-	-	-
05/11/2008	14/01/2009	153	-	-	-	-	-	-
05/11/2008	18/02/2009	279	-	-	-	-	-	-
10/12/2008	14/01/2009	99	-	-	-	-	-	-
10/12/2008	18/02/2009	226	-	-	-	-	-	-
10/12/2008	25/03/2009	331	-	-	-	-	-	-
14/01/2009	18/02/2009	126	-	-	-	-	-	-
14/01/2009	25/03/2009	231	-	-	-	-	-	-
18/02/2009	25/03/2009	105	-	-	-	-	-	-

Appendix B

Additional Material for Chapter 3

Introduction

This appendix includes additional information on InSAR sensor and processing parameters, observations, model results, and goodness of fit. We also discuss whether the inclusion of a second shallow source is able to increase the fit of our geodetic Bayesian modelling.

B.1. Multiple deformation sources at Corbetti

To test whether the residuals in the north of the caldera in 2014 – 2015 could be explained by a known source, we investigate deformation of a shallow hydrothermal system located in the southern half of the caldera (Figure 3.5) (*Lloyd et al.* [2018], Chapter 2). Individual interferograms show no clear indication of activity of this source in 2010, or 2015 – 2017. However, during 2014 – 2015 there are residuals between the combined source model and the CSK interferograms (Figure 3.5). These residuals are located in the north of the caldera, but to confirm that this location is robust (e.g., not a function of the interferogram offset included in the inversion), we test the inclusion of a second shallow source, using the Okada model. We impose constraints on the shallow source based on *Lloyd et al.* [2018]: located in the south of the caldera, with strike 090° – 105°, and on the deeper source based on the combined and 2014 – 2015 inversions. We also test imposing a reference level, rather than as a free parameter.

We find that the shallow source in the offset and no offset inversions has an opening of 2 and 1 cm respectively, and does not describe the residuals. The AIC values for the inclusion of a second source (16.5 and 12.5 for with and without an offset respectively) are also higher than for the one source model. These results indicate that the inclusion of deformation of a second shallow source in the south of the caldera at this time is neither necessary or justified, but does not rule out the possibility that some deformation was occurring.

B.2. Source variation with time

We consider residuals from the linear volume change (2012 – 2017) to test for source variation with time. A clear increase in root-mean-square (rms) residual can be seen during 2014 – 2015 in the ascending and descending CSK data. A second increase in the rms residual can be seen in 2016 – 2017 for ascending Sentinel-1 interferograms. To take into account the interferogram noise, we consider the residual between the rms model residual and the standard deviation of the interferogram (Figure B.7b). The increase in rms residual 2014 – 2015 is still apparent, suggesting that there is signal within the interferogram that is not captured by our model. In contrast, during 2015 – 2016, by

considering the standard deviation, we can see that the increase in rms residual for the Sentinel-1 interferograms was due to low signal-to-noise ratios in short timespan interferograms.

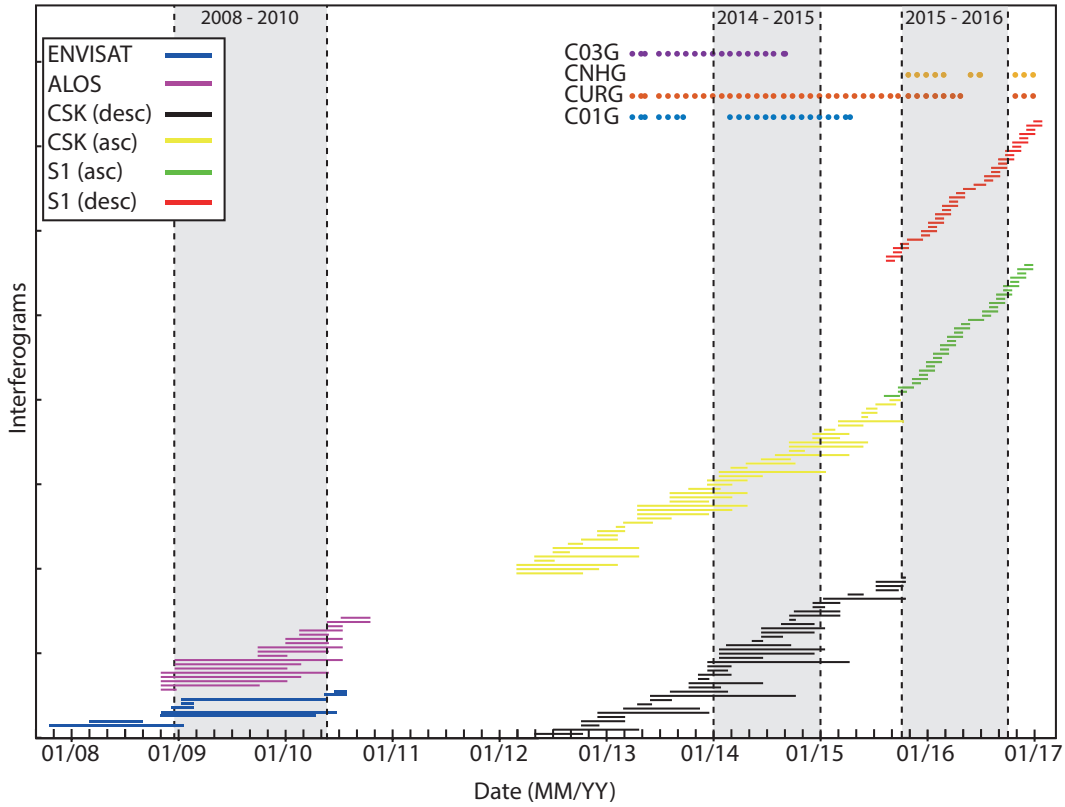

Figure B.1: Temporal coverage of geodetic data used in Chapter 2. CSK: Cosmo-SkyMed, S1: Sentinel-1. Each horizontal line represents an interferogram. Each circle represents a monthly GPS solution. The colour scheme for each dataset is continued throughout. The grey regions correspond to the time periods used in the source inversions in Section 3.5.1.

Table B.1: Summary of the sensor and important sensor parameters used in Chapter 3. Incidence and heading angles are the mean for each scene.

Satellite	Mode	Observation period	Wavelength (cm)	Orbit	Number of scenes	Heading angle (°)	Look angle (°)
ALOS-1	Fine Beam	December 2007 – September 2010	23.6 (L-band)	Ascending	9	-12	38
ENVISAT	Image Mode (IM)	October 2007 – July 2010	5.6 (C-band)	Descending	9	-167	22
Cosmo-SkyMed	StripMap	March 2012 – November 2015	3.1 (X-band)	Ascending	35	-11	37
Cosmo-SkyMed	StripMap	March 2012 – November 2015	3.1 (X-band)	Descending	32	-169	40
Sentinel-1	TOPS	August 2015 – December 2016	5.6 (C-band)	Ascending	20	-11	41
Sentinel-1	TOPS	August 2015 – January 2017	5.6 (C-band)	Descending	21	-169	55

Table B.2: Chapter 3 InSAR processing parameters. [1]Goldstein and Werner non-linear spectral filter [*Goldstein and Werner*, 1998], [2]SNAPHU Minimum Cost Flow (MCF) [*Chen and Zebker*, 2001]

Sensor	ALOS	ENVISAT	CSK		Sentinel-1	
Time coverage (mm/yy)	12/07 – 09/10	10/07 – 07/10	03/12 – 11/15		08/15 – 01/17	
Orbit direction	asc	desc	asc	desc	asc	desc
Number of scenes	9	9	35	32	20	21
Number of interferograms	25	45	159	131	32	34
Max perpendicular baseline (m)	500	800	500		150	
Max temporal baseline (days)	730	600	500		50	
Final pixel size (m)	120	120	See text		100	
Filter strength[1]	0.4[1]	0.8[1]			0.85[1]	
Unwrapping method	Snaphu MCF[2]	Snaphu MCF[2]	Snaphu MCF[2]		Snaphu MCF[2]	
Coherence threshold	0.1	0.1	0.6		0.7	

Table B.3: Summary of InSAR and GPS data at CURG and C01G. For each InSAR dataset the maximum displacements, and the line-of-sight displacements at CURG and C01G are shown. Displacement vector is east, north, and up.

	3-component displacement vector	Dates	Maximum	C01G cm/yr	CURG
ALOS (asc)	(0.37 -0.08 0.93)	27/09/2009 – 30/09/2010	4.0 ± 1.2	1.0 ± 0.03	2.90 ±0.02
C01G	(0 0 1)	31/03/2013 – 15/04/2015	-	6.6 ± 1.2	-
LOS (S1 asc)	(-0.64 -0.13 0.75)	31/03/2013 – 15/04/2015	-	4.3 ± 1.9	-
LOS (S1 desc)	(0.80 -0.16 0.57)	31/03/2013 – 15/04/2015	-	4.6 ± 1.9	-
CURG	(0 0 1)	31/03/2013 – 31/12/2016	-	-	3.9 ± 0.7
LOS (S1 asc)	(-0.64 -0.13 0.75)	31/03/2013 – 31/12/2016	-	-	4.1 ± 1.1
LOS (S1 desc)	(0.80 -0.16 0.57)	31/03/2013 – 31/12/2016	-	-	1.7 ± 1.1
Sentinel-1 (asc)	(-0.64 -0.13 0.75)	12/08/2015 – 28/12/2016	4.0 ± 1.0	2.6 ± 1.0	3.1 ± 1.0
Sentinel-1 (desc)	(0.80 -0.16 0.57)	19/08/2015 – 11/12/2016	3.8 ± 0.4	2.9 ± 0.4	2.1 ± 0.4

Table B.4: Input data and inversion parameters for each inversion.

Data	LOS/site	Timespan (DD/MM/YYYY)	Model	Number of inversions	Subsampled data points
ALOS	asc	09/11/2008 – 30/06/2010	MOGI	5.0E+05	929
ENVISAT	desc	06/11/2008 – 24/06/2010			633
ALOS	asc	09/11/2008 – 30/06/2010	OKADA	5.0E+05	929
ENVISAT	desc	06/11/2008 – 24/06/2010			633
CSK	asc	24/01/2014 – 19/01/2015			800
CSK	desc	25/01/2014 – 11/12/2014			675
	C01G		MOGI	5.0E+05	1
GPS	C03G	28/02/2014 – 31/08/2014			3
	CURG				3
CSK	asc	24/01/2014 – 19/01/2015			800
CSK	desc	25/01/2014 – 11/12/2014			675
	C01G		OKADA	5.0E+05	3
GPS	C03G	28/02/2014 – 31/08/2014			3
	CURG				3
S1	asc	29/09/2015 – 17/10/2016			689
S1	desc	06/10/2015 – 30/09/2016	MOGI	5.0E+05	486
GPS	CURG	26/09/2015 – 31/10/2016			3
	CNHG	31/10/2015 – 31/10/2016			3
S1	asc	29/09/2015 – 17/10/2016			689
S1	desc	06/10/2015 – 30/09/2016	OKADA	5.0E+05	486
GPS	CURG	26/09/2015 – 31/10/2016			3
	CNHG	31/10/2015 – 31/10/2016			3
ALOS	asc	09/11/2008 – 30/06/2010			929
ENVISAT	desc	06/11/2008 – 24/06/2010			633
CSK	asc	24/01/2014 – 19/01/2015			800
CSK	desc	25/01/2014 – 11/12/2014			675
S1	asc	29/09/2015 – 17/10/2016	MOGI	5.0E+05	689
S1	desc	06/10/2015 – 30/09/2016			486
	C01G	31/03/2013 – 15/04/2015			3
GPS	C03G	31/03/2013 – 05/09/2014			3
	CNHG	31/10/2015 – 31/12/2016			3
	CURG	23/03/2013 – 31/12/2016			3
ALOS	asc	09/11/2008 – 30/06/2010			929
ENVISAT	desc	06/11/2008 – 24/06/2010			633
CSK	asc	24/01/2014 – 19/01/2015			800
CSK	desc	25/01/2014 – 11/12/2014			675
S1	asc	29/09/2015 – 17/10/2016	OKADA	5.0E+05	689
S1	desc	06/10/2015 – 30/09/2016			486
	C01G	31/03/2013 – 15/04/2015			3
GPS	C03G	31/03/2013 – 05/09/2014			3
	CNHG	31/10/2015 – 31/12/2016			3
	CURG	23/03/2013 – 31/12/2016			3

Table B.5: Initial starting values and range for Okada and Mogi model parameters. X and Y are distance from the centre of the caldera. Z is depth below the surface, dV/yr is the rate of volume change.

	Mogi model			Okada model		
	Initial	Lower	Upper	Initial	Lower	Upper
X (km)	0	-10	10	4	-10	10
Y (km)	0	-10	10	0	-10	10
Depth (km)	3	0.1	15	6	2	15
dV/yr (m^3/yr)	1e6	0	1e9	-	-	-
Length (km)	-	-	-	10	2	20
Width (km)	-	-	-	10	2	20
Strike (°)	-	-	-	100	0	360
Opening/yr (m/yr)	-	-	-	1	0	3

Table B.6: Optimal model parameters for the Mogi and Okada models of the uplift at Corbetti. X and Y are the distances to the east and north from the centre of the caldera. Z is depth below the surface, dV/yr is the rate of volume change, L and W are the Okada length and width. op/yr is the opening of the Okada model per year.

Time period	2008 – 2010	2008 – 2010	2014 – 2015	2014 – 2015	2015 – 2016	2015 – 2016	Combined	Combined
Dataset	ALOS + ENVI	ALOS + ENVI	CSK + GPS	CSK + GPS	S1 + GPS	S1 + GPS	Combined	Combined
Model	MOGI	OKADA	MOGI	OKADA	MOGI	OKADA	MOGI	OKADA
X (m)	1.91E+03	-6.40E+03	2.52E+03	4.71E+03	1.82E+03	-1.54E+03	2.05E+03	-2.73E+03
Y (m)	-2.35E+02	2.50E+03	8.82E+02	-8.88E+02	-5.57E+02	4.20E+03	-3.10E+01	-2.52E+03
Z (m)	5.98E+03	6.19E+03	7.61E+03	6.75E+03	6.91E+03	6.93E+03	6.58E+03	6.82E+03
dV/yr (m^3/yr)	4.99E+06	4.61E+06	2.42E+07	1.80E+07	1.26E+07	1.24E+07	9.14E+06	8.42E+06
L (m)		6.74E+03		7.93E+03		1.06E+04		9.98E+03
W (m)		9.88E+03		1.25E+04		9.53E+03		6.54E+03
Strike (°)		202		19		277		110
op/yr (m/yr)		0.07		0.19		0.12		0.13

Table B.7: Table of root-mean-square (rms) residuals for each dataset for each model, with Akaike Information Criterion values (AIC), and relative likelihood (L), compared to the model with the lowest AIC value.

	RMS residuals (cm)	
	MOGI	OKADA
ALOS	0.56	0.56
ENVISAT	0.85	0.83
AIC	-4.6	-3.8
L	-	0.67
CSK (asc)	0.92	0.66
CSK (desc)	1.05	0.77
GPS (mean)	1.2	1.4
AIC	-4.1	-0.6
L	-	0.17
S1 (asc)	0.79	0.86
S1 (desc)	1.70	1.84
GPS (mean)	1.01	1.47
AIC	-4.0	-1.96
L	-	0.36
ALOS	0.6	0.6
ENVISAT	1.3	1.4
CSK (asc)	2.1	1.9
CSK (desc)	1.9	1.9
S1 (asc)	1.1	1.2
S1 (desc)	1.3	1.2
GPS (mean)	0.7	0.7
AIC	2.5	3.2
L	-	0.70

Table B.8: Locations and time of deployment and decommissioning for the seismic stations used in Chapter 2.

Station	Latitude	Longitude	Deployment	Decommission
C01E	7.22327	38.38505	13/01/2012	01/02/2014
C02E	7.14882	38.43224	14/01/2012	31/01/2014
C03E	7.19804	38.48441	14/01/2012	03/06/2014
C04E	7.21787	38.47640	03/06/2013	31/01/2014
C05E	7.25978	38.30228	25/01/2013	01/02/2014
C06E	7.13389	38.37214	25/02/2013	02/02/2014
C07E	7.26028	38.44400	23/09/2013	01/02/2014

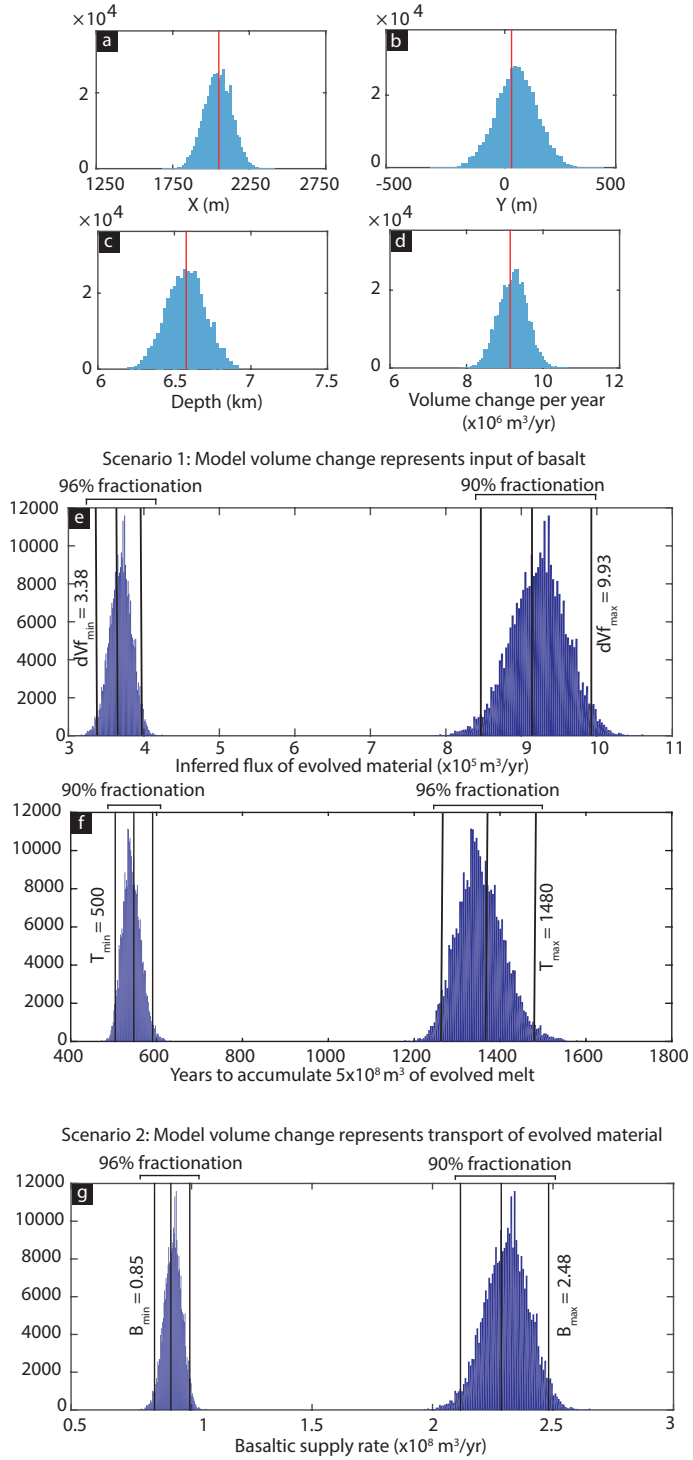

Figure B.2: a–d) Marginal posterior probability density functions for Mogi model (combined inversion) X and Y location, depth, and rate of volume change. e) Inferred flux of evolved material (scenario 1) for 90% and 96% fractionation given the probability density function for rate of volume change in (d). Vertical lines show 2.5%, optimal, and 97.5% confidence internals for each fractionation factor. f) Probability density functions for the time taken to accumulate 5 x 10^8 m^3 of evolved melt given the fluxes derived in (e). g) Probability density functions for inferred basaltic supply rate, for 90% and 96% fractionation, given (d) represents transport of evolved material (scenario 2).

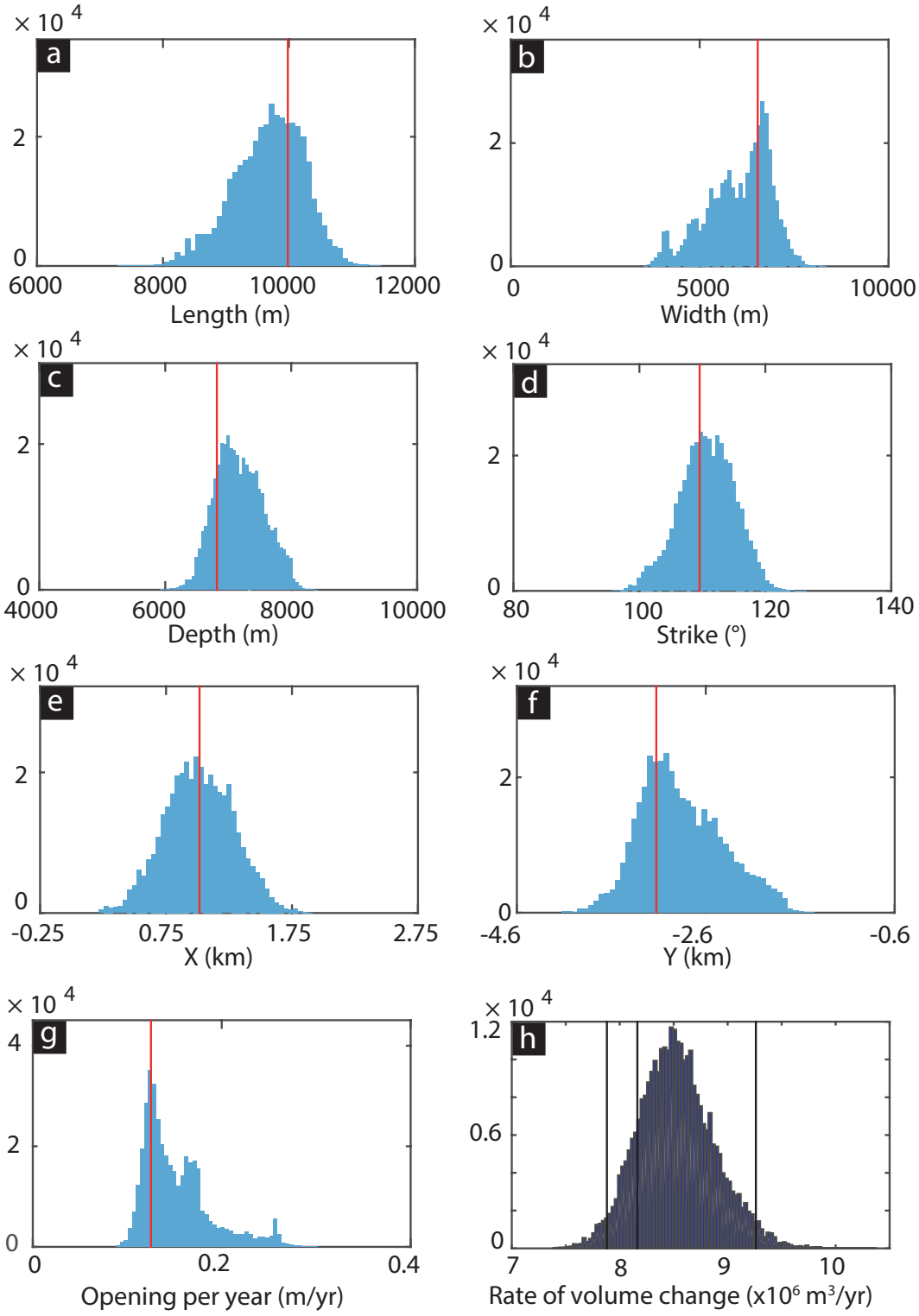

Figure B.3: a–g) Marginal posterior probability density functions for the model parameters of the Okada model (combined inversion). X and Y give the location of the edge of the model. Red vertical lines show the optimal values. h) Probability density function for the rate of volume change of the Okada model. Black vertical lines show the optimal values and 95% thresholds.

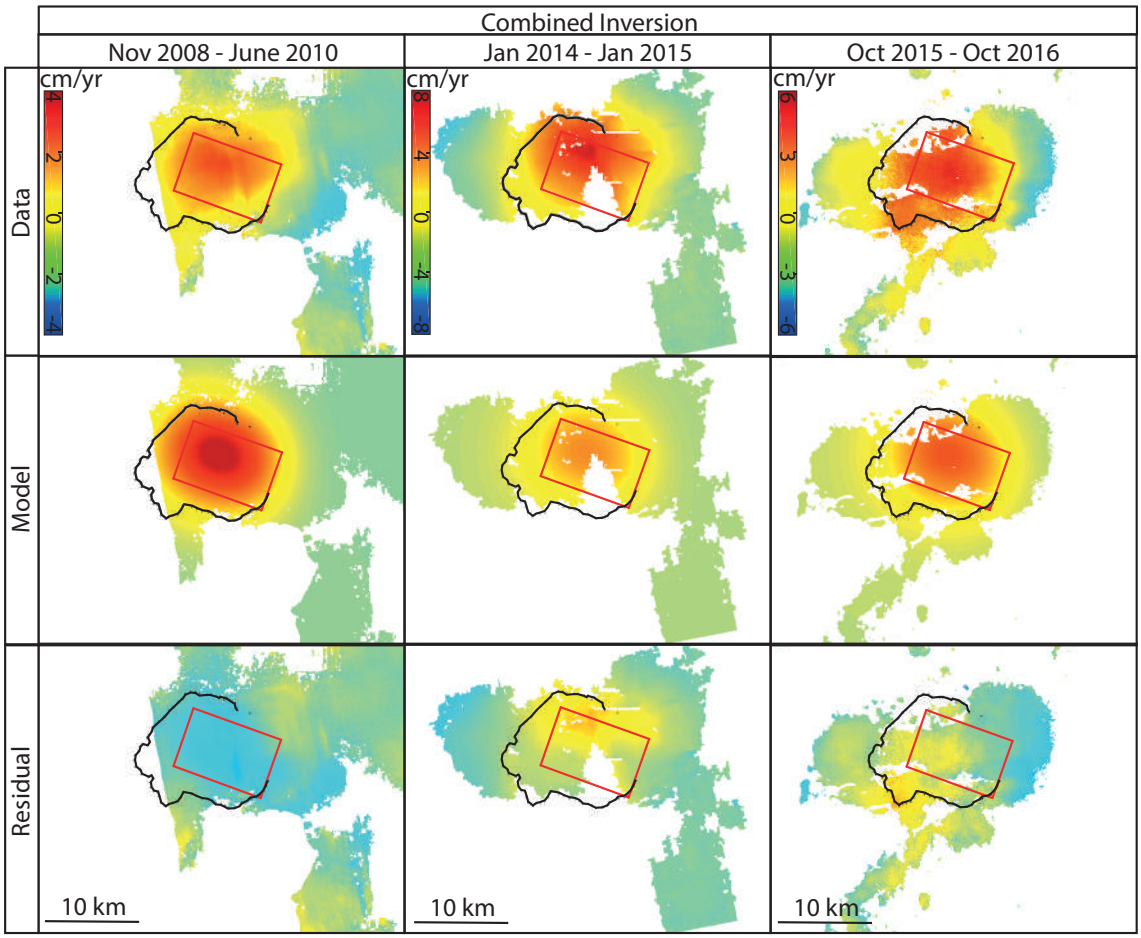

Figure B.4: Okada model data-model-residual plots for an interferogram from each time period used in the combined inversion. The caldera outline is shown on each subplot. The red rectangle denotes the surface projection of the Okada model.

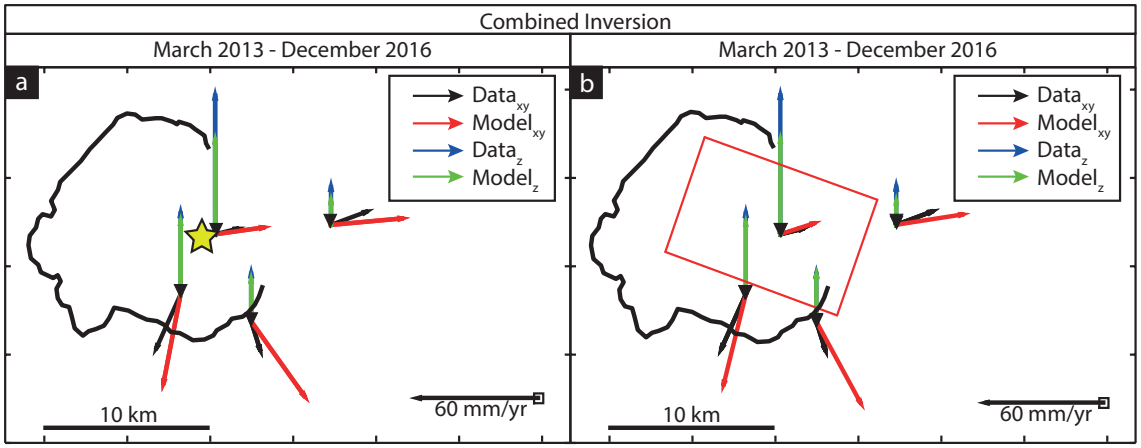

Figure B.5: a) GPS observations, and Mogi model results from the combined inversion. The yellow star denotes the location of the Mogi source at the surface. b) GPS observations, and Okada model results from the combined inversion. The red rectangle denotes the location of the Okada model at the surface. The caldera outline is shown on each subplot.

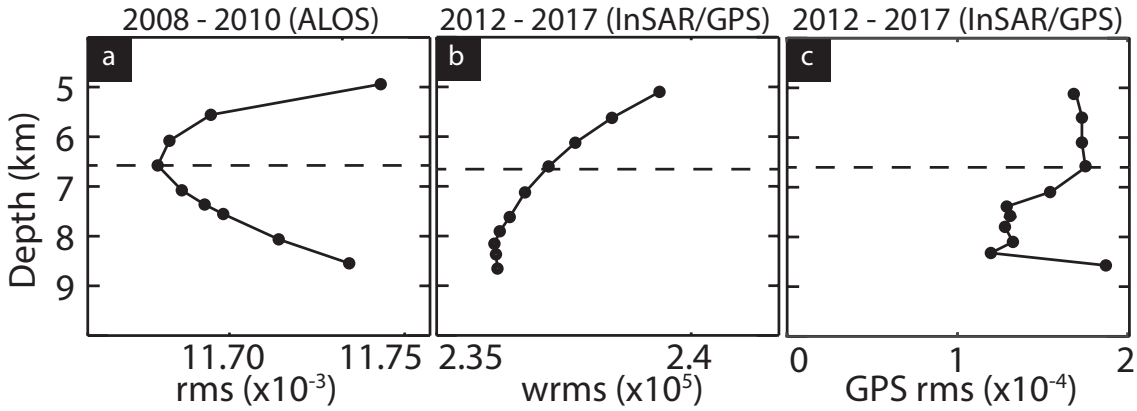

Figure B.6: Depth against root-mean-square (rms) misfit for a) ALOS data (2008 – 2010), with minimum at 6.6 km (dashed line), b) InSAR and GPS data (weighted rms (wrms)) for 2012 – 2017, c) GPS data only throughout 2012 – 2017, for the same inversion as (b).

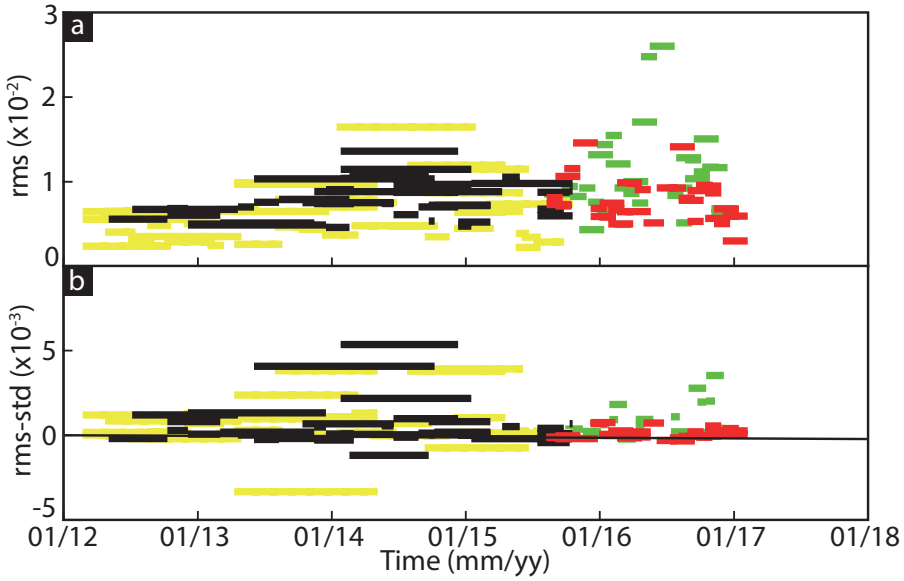

Figure B.7: a) Root-mean-square (rms) misfit misfit between each interferogram and modelled displacement. Interferogram duration shown by the length of bar. b) rms misfit for each interferogram minus the standard deviation of the interferogram.

Appendix C

Additional Material for Chapter 4

Introduction

This appendix contains further information on the data used in Chapter 4, the modelling methodology, and alternative inversion results.

C.0.1. Distributed slip model resolution

The resolution matrix for the distributed slip model, **R**, is dependent on the smoothed Green's function, where $\mathbf{G}_s$ is $[\mathbf{G}\kappa^2\nabla^2]^T$ [*Funning et al.*, 2005]. The resolution matrix is given by

$$\mathbf{R} = \left(\mathbf{G}_s^T\mathbf{G}_s\right)^{-1}\mathbf{G}^T\mathbf{G}. \tag{C.1}$$

The diagonal values of **R** represent the model resolution. We define the horizontal and vertical resolution length scales for each patch as the distance in each direction over which the values are greater than $1/e$ of the maximum value of the resolution matrix [*Biggs et al.*, 2006; *Funning et al.*, 2005]. For perfectly resolved models **R** will be an identity matrix. The distributed slip model for the Zinave earthquake has 7.5 km and 5 km horizontal and vertical resolutions in the peak slip region respectively (Figure C.4). The inversion for the slip distribution of the Machaze earthquake using ENVISAT data (model 1) has a more variable resolution, but is ∼14 km in the horizontal and vertical in the peak slip region (Figure C.8).

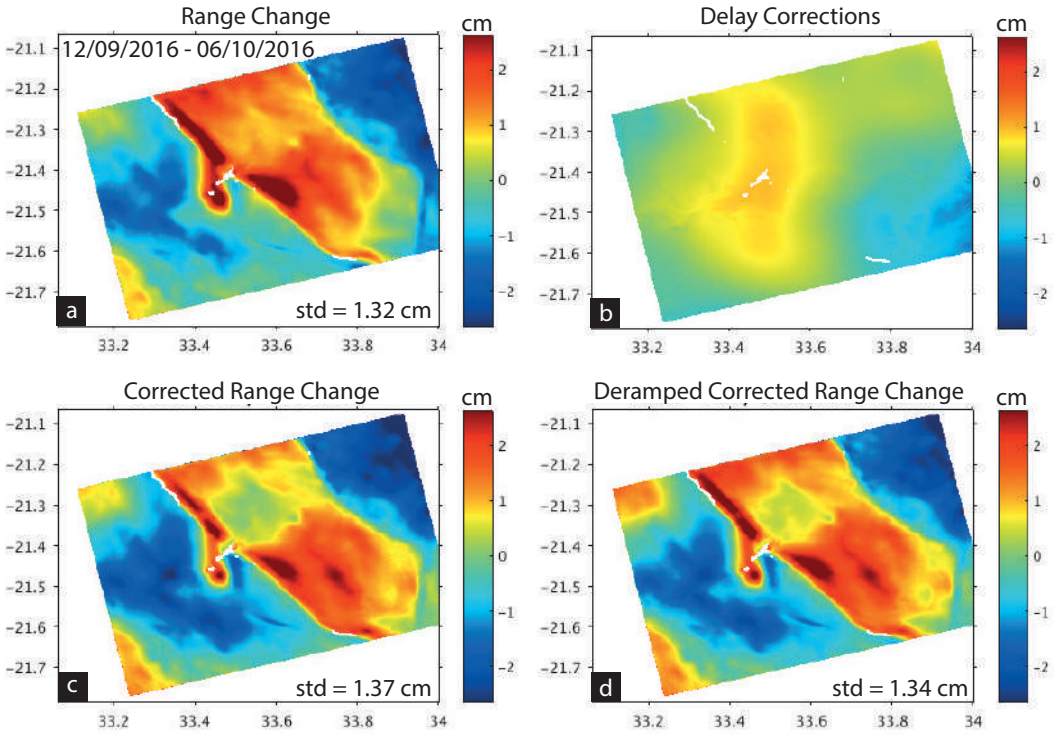

Figure C.1: Atmospheric corrections for Zinave co-seismic interferogram 12/09/2016 – 06/10/2016 (track 174). a) Observations, b) delay correction, c) corrected observations, d) de-ramped corrected observations. Standard deviations (std) for (a), (b), and (d) are shown.

Table C.1: Summary of Sentinel-1 InSAR data used in Chapter 4. Line-of-sight vector is given as east, north, up.

Satellite	Track	Pass direction	Line-of-sight vector (E, N, U)	Number of interferograms	Co-seismic interferograms	Stacked
Sentinel-1	79	Desc	0.5446 -0.1334 0.8280	19	7	4
						13/08/2017 – 06/10/2017
						13/08/2017 – 30/10/2017
						06/09/2017 – 06/10/2017
						06/09/2017 – 30/10/2017
	174	Asc	-0.5251 -0.1262 0.8416	35	14	6
						23/07/2017 – 29/09/2017
						23/07/2017 – 11/10/2017
						12/08/2017 – 11/10/2017
						12/08/2017 – 04/11/2017
						17/09/2017 – 29/09/2017
						17/09/2017 – 04/11/2017
	72	Asc	-0.6848 -0.1755 0.7073	25	13	6
						19/08/2017 – 24/09/2017
						19/08/2017 – 18/10/2017
						31/08/2017 – 18/10/2017
						31/08/2017 – 30/10/2017
						12/09/2017 – 24/09/2017
						12/09/2017 – 30/10/2017

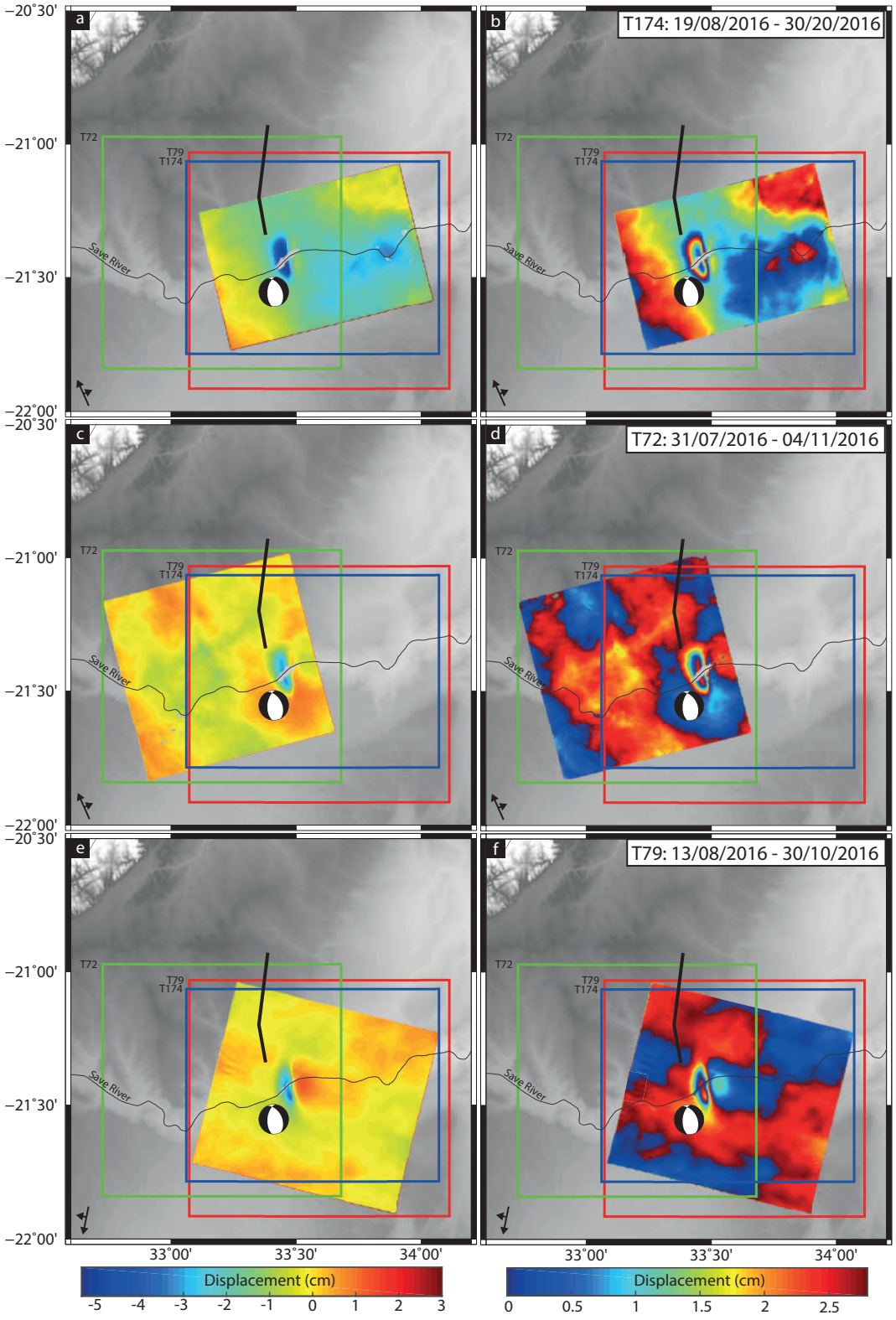

Figure C.2: Unwrapped (left) and wrapped (right) stacked Sentinel-1 interferograms of the Zinave earthquake from tracks T174 (top), T72 (middle), and T79 (bottom). Black line shows the location of the Machaze earthquake fault from *Copley et al.* [2012].

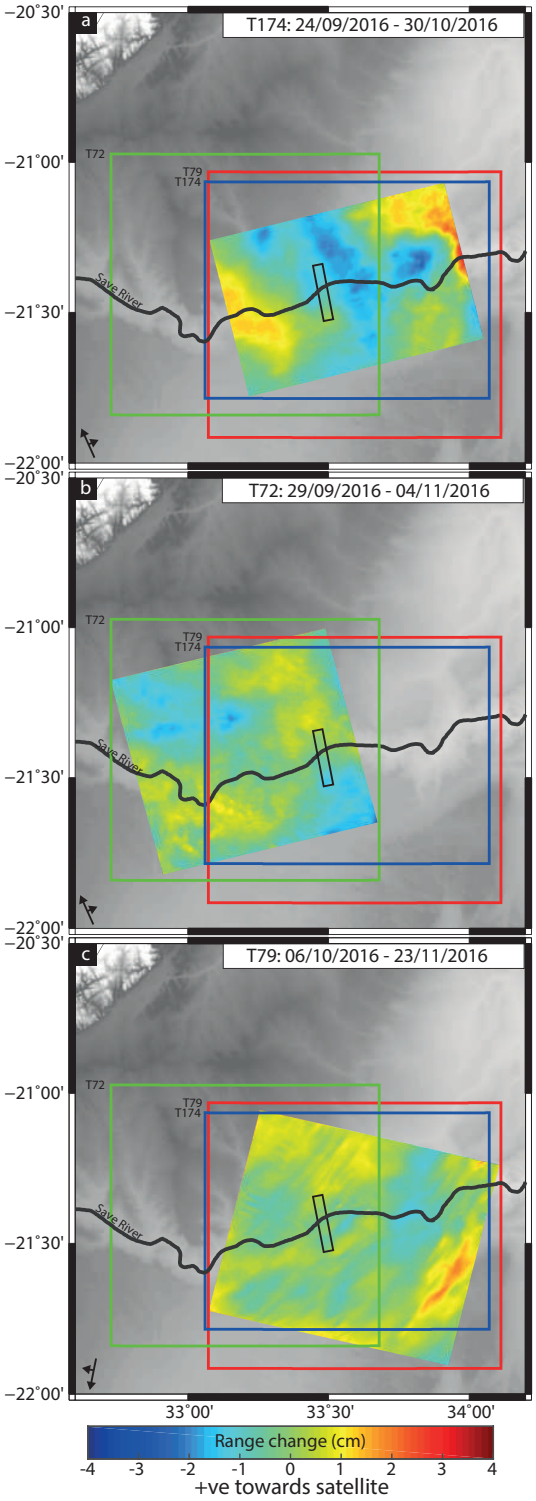

Figure C.3: Observations of the post-seismic range change following the Zinave earthquake for a) track 174: 24/09/2016 – 30/10/2016, b) track 72: 29/09/2016 – 04/11/2016, c) track 79 06/10/2016 – 23/11/2016, showing no deformation.

Table C.2: Initial conditions and inversion bounds for each parameter for the uniform slip distribution inversion of the Zinave and Machaze earthquakes.

Uniform slip bounds		Zinave	Machaze
Length (km)	Lower	8	5
	Initial	15	60
	Upper	25	100
Width (km)	Lower	0.5	1
	Initial	4	15
	Upper	10	35
Depth (km)	Lower	0.5	0.2
	Initial	6	10
	Upper	15	40
Dip (°)	Lower	-85	0.01
	Initial	70	70
	Upper	85	89.9
Strike (°)	Lower	Variable	140
	Initial	(see text)	196
	Upper		280
X (km)	Lower	-8	-25
	Initial	0	0
	Upper	8	25
Y (km)	Lower	-8	-25
	Initial	0	0
	Upper	8	25
Strike slip (m)	Lower	-0.4	-3
	Initial	0	0
	Upper	0.4	5
Dip slip (m)	Lower	-1	-6
	Initial	0	0
	Upper	0	10

Table C.3: Fault parameters from the geodetic inversions, with 95% confidence, and USGS focal mechanism for comparison. Fault locations (X and Y, UTM) in the geodetic inversions are for the middle of the bottom of the fault. Root-mean-square (rms) misfit is the joint rms if more than one dataset is used in the inversion.

	USGS solution		T174		T72		T79		T174 + T72		T174 + T72 + T79	
Inversion points	-		695		743		633		1438		2071	
	FP1	FP2	Optimal	95% range	Optimal	95% range	Optimal	95% range	Optimal	95% range	Optimal	95% range
Length (m)	-	-	16700	13500 – 19300	16300	14600 – 17900	15600	14600 - 17000	16000	14800 – 17600	15800	14900 – 16800
Width (m)	-	-	5800	700 – 7400	1600	700 – 3300	4800	1600 - 6700	35000	700 – 3500	5100	1400 – 5700
Depth (m)	15500	15500	8400	5100 – 9800	5200	4500 - 6300	7300	5600 - 8700	6500	4800 – 6600	7600	5600 – 8100
Dip (°)	45	50	61	47 – 79	72	59 – 78	60	52 – 67	65	60 – 76	59	54 – 68
Strike (°)	334	185	168	163 – 173	169	166 – 171	168	166 – 170	169	166 – 171	168	167 – 170
X (m)	550800	550800	546100	545000 – 549000	548700	547600 – 549100	546700	545600 – 548300	547600	547400 – 548900	546600	545900 – 548400
Y (m)	7630800	7630800	7629900	7628200 – 7632200	7629400	7628600 – 7630700	7631000	7629700 – 7632300	7629400	7628800 – 7630600	7629300	762900 – 7632200
Strike slip (m)	-	-	0.05	-0.33 – 0.37	0.31	0.08 – 0.39	-0.11	-0.32 – 0.00	0.12	0.07 – 0.39	0.06	0.0 – 0.20
Dip slip (m)	-	-	-0.14	-0.93 – -0.12	-0.32	-0.83 – -0.17	-0.12	-0.35 – -0.09	-0.17	-0.77 – -0.17	-0.14	-0.47 – -0.12
Rake (°)	-114	-68	-72	-	-46	-	47	-	-55	-	-66	-
rms (cm)	-		0.8		0.5		0.5		1.0		1.0	

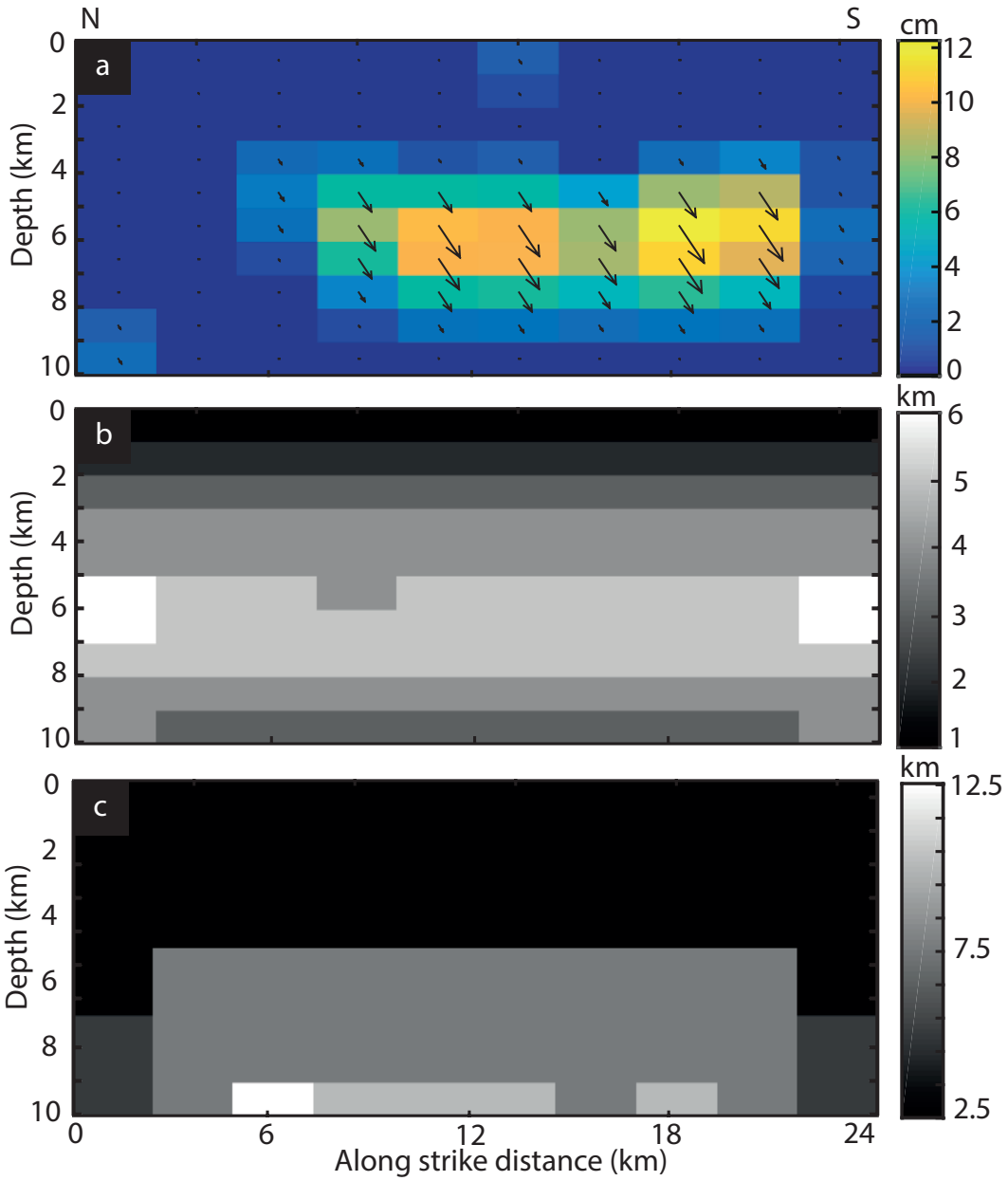

Figure C.4: a) Slip distribution for the Zinave earthquake, with rake fixed at -66°. b) Length scale of vertical resolution. c) Length scale of horizontal resolution. Each cell is 1 km horizontally by 2.4 km vertically.

Table C.4: Root-mean-square (rms) residuals for the variable rake, uniform slip rake (-66°), and body wave slip rake (-71°), with associated F-statistic values.

rms (cm)	Variable rake	Uniform slip rake	Body wave rake
Joint	0.44	0.44	0.44
Track 174	0.47	0.47	0.47
Track 79	0.43	0.43	0.43
Track 72	0.43	0.43	0.43
F-statistic	-	0.0045	0.0045

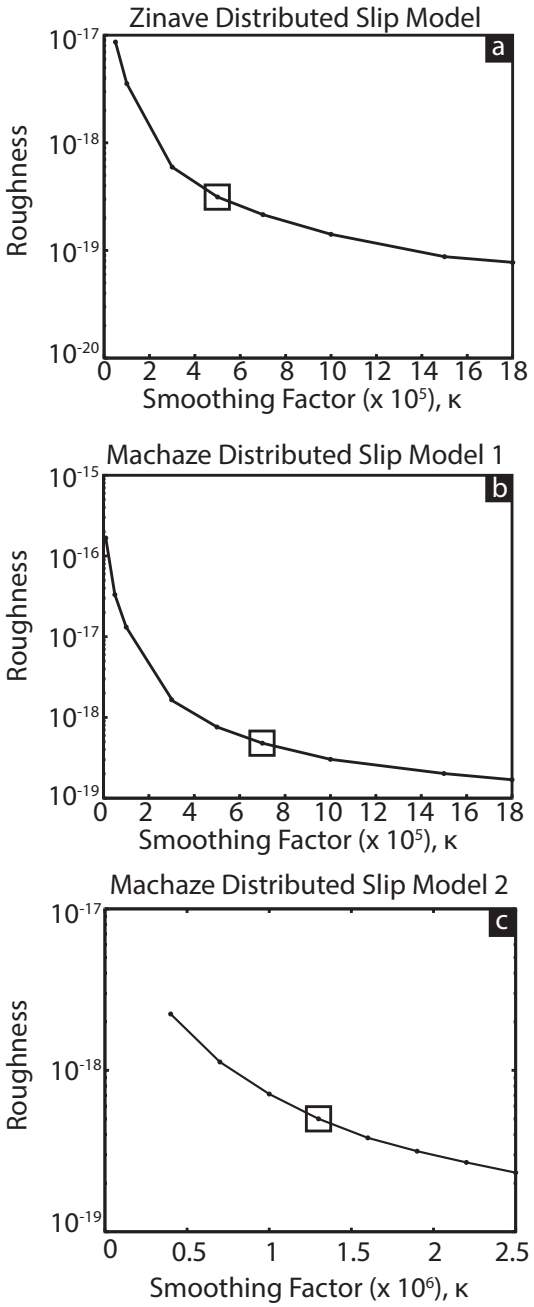

Figure C.5: Smoothing factor versus model roughness for a) Zinave distributed slip model, b) Machaze model 1 (ENVISAT), c) Machaze model 2 (ENVISAT and SPOT). The chosen smoothing factor value is shown by a black box in each subplot.

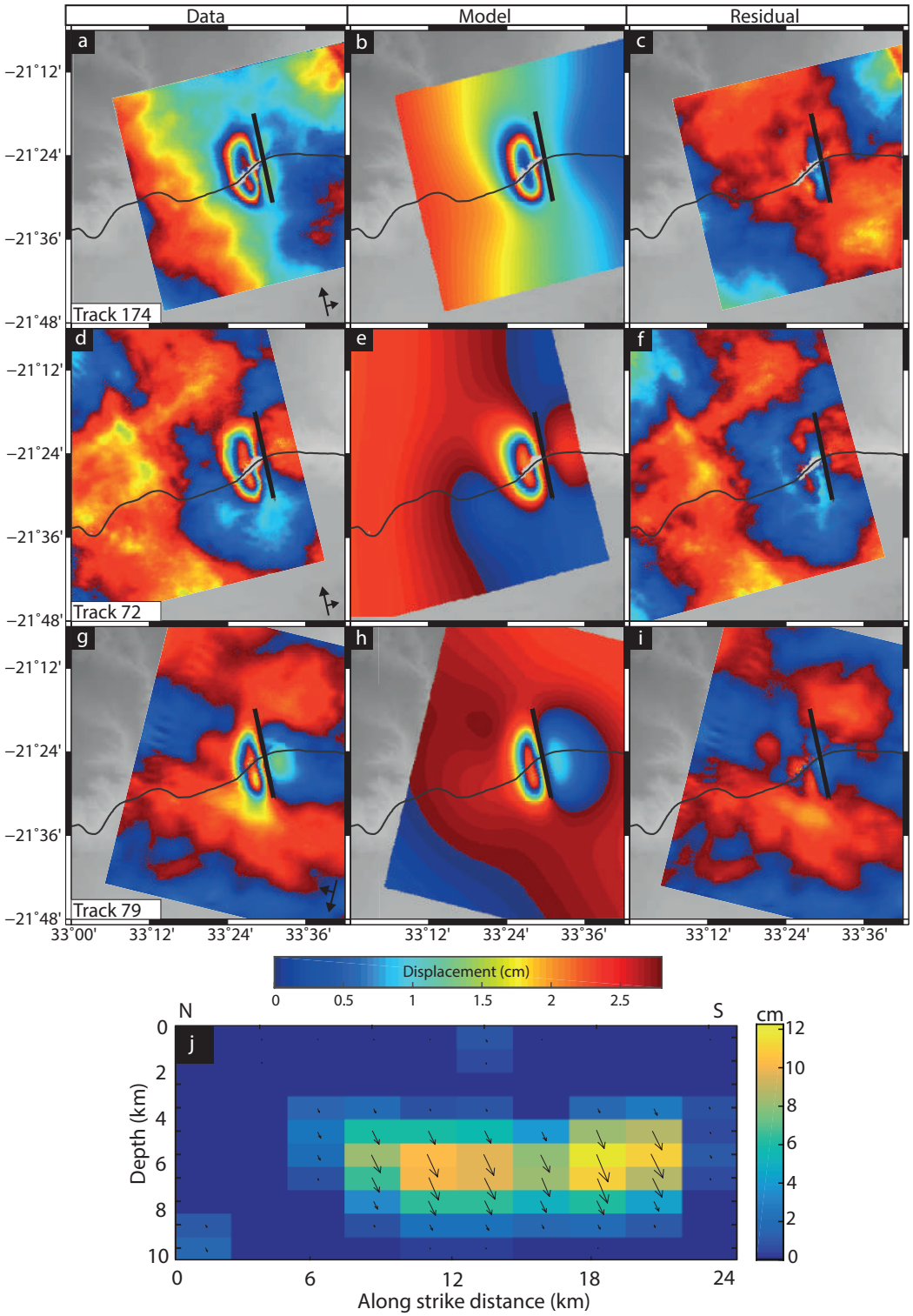

Figure C.6: Fixed rake (-71°) model for the Zinave earthquake. a–c) Data, model, and residual to the distributed slip model for track 174. d–f) Track 72 data, model, and residual. g–i) Track 79 data, model, and residual. Black lines though (a–i) mark the top of the distributed slip model, where it intersects the surface. j) Distributed slip model result for the inversion of tracks 174, 79, and 72 with rake fixed to -71°. Arrows show displacement of the east block relative to west (i.e., motion to the south is left-lateral).

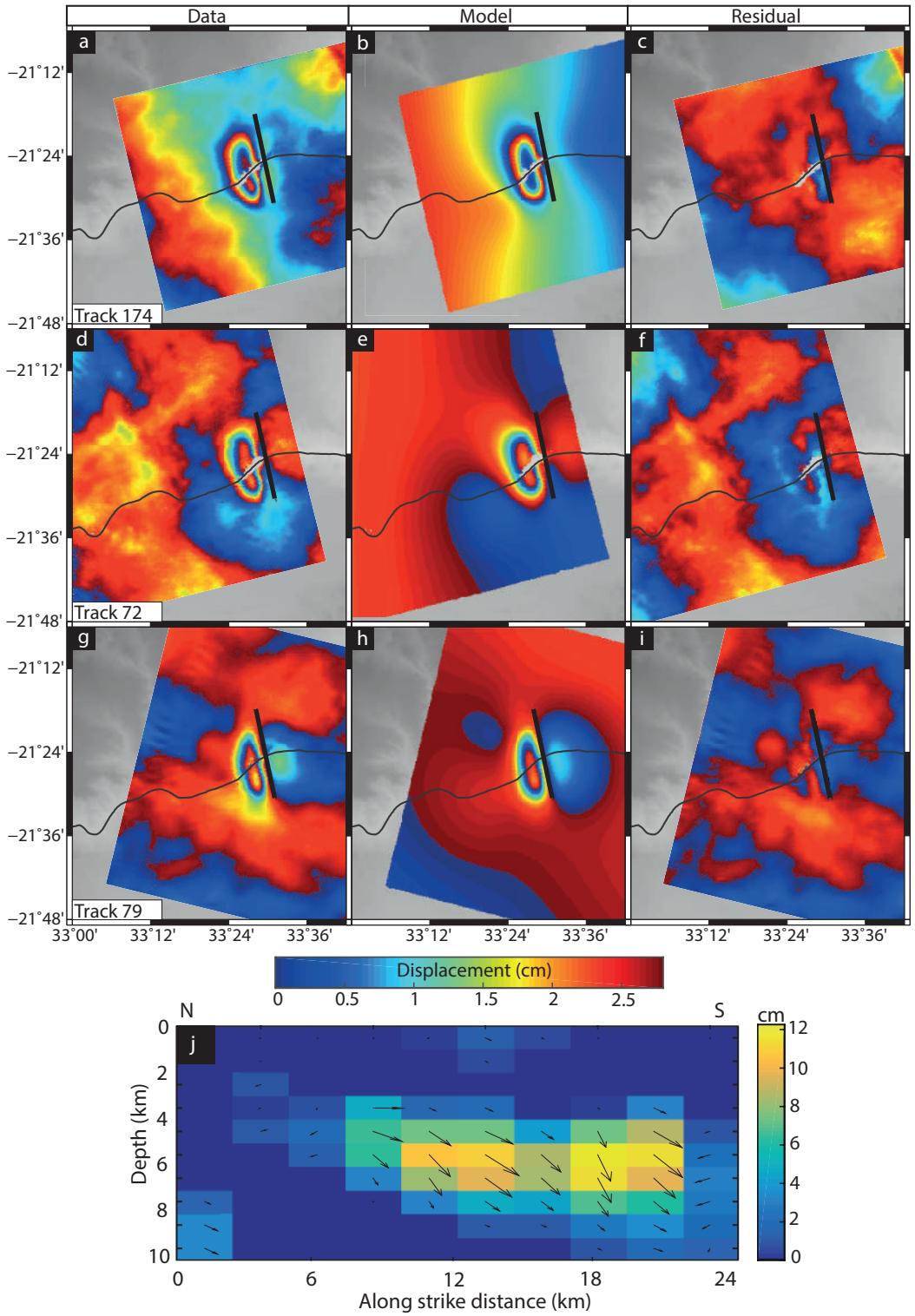

Figure C.7: Variable rake model for the Zinave earthquake. a–c) Data, model, and residual to the distributed slip model for track 174. d–f) Track 72 data, model, and residual. g–i) Track 79 data, model, and residual. Black lines though a–i mark the top of the distributed slip model, where it intersects the surface. j) Distributed slip model result for the inversion of tracks 174, 79 and 72 with variable rake. Arrows show displacement of the east block relative to west (i.e., motion to the south is left-lateral).

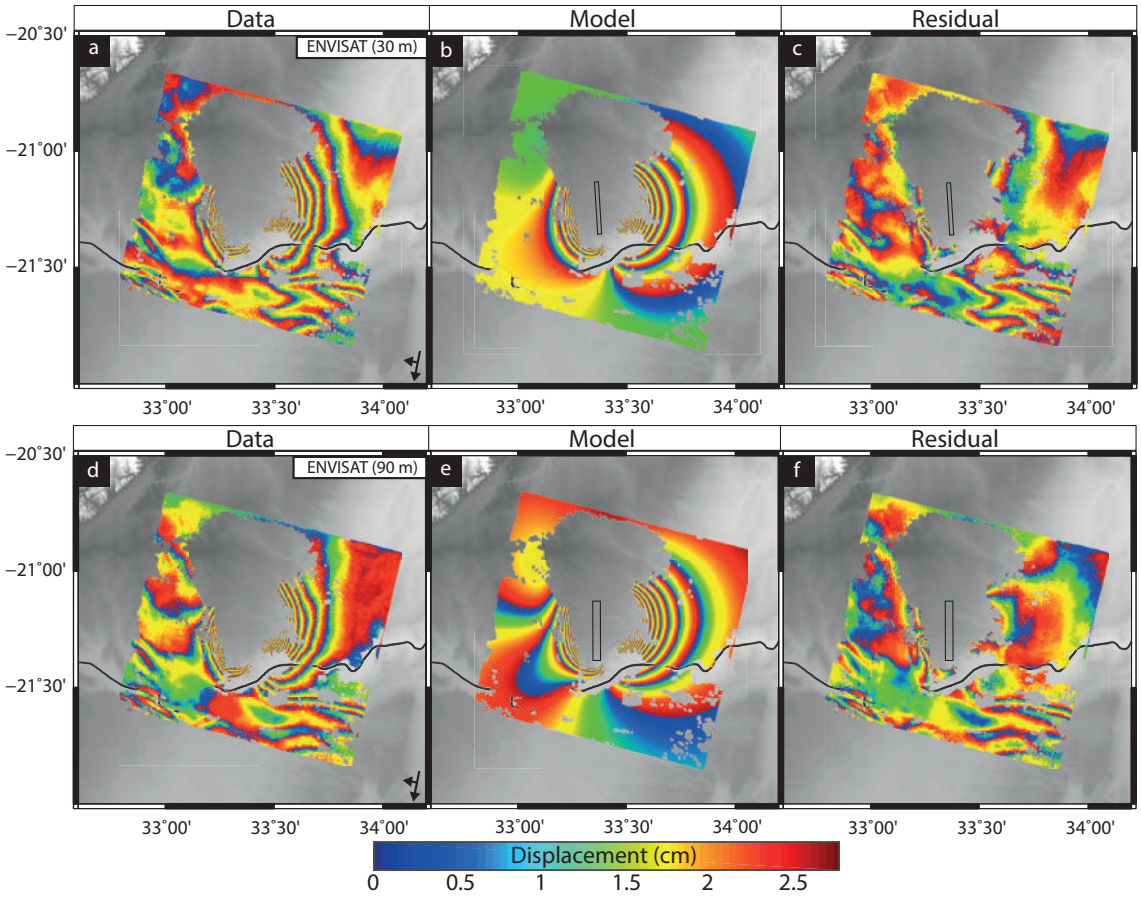

Figure C.8: a) Data, b) model, and c) residual for the uniform slip model of the Machaze earthquake, using ENVISAT data at 30 m resolution. d) Data, e) model, and f) residual for the uniform slip model of the Machaze earthquake, using ENVISAT data resampled to 90 m. Root-mean-square misfit values can be found in Tables 4.1 and C.3.

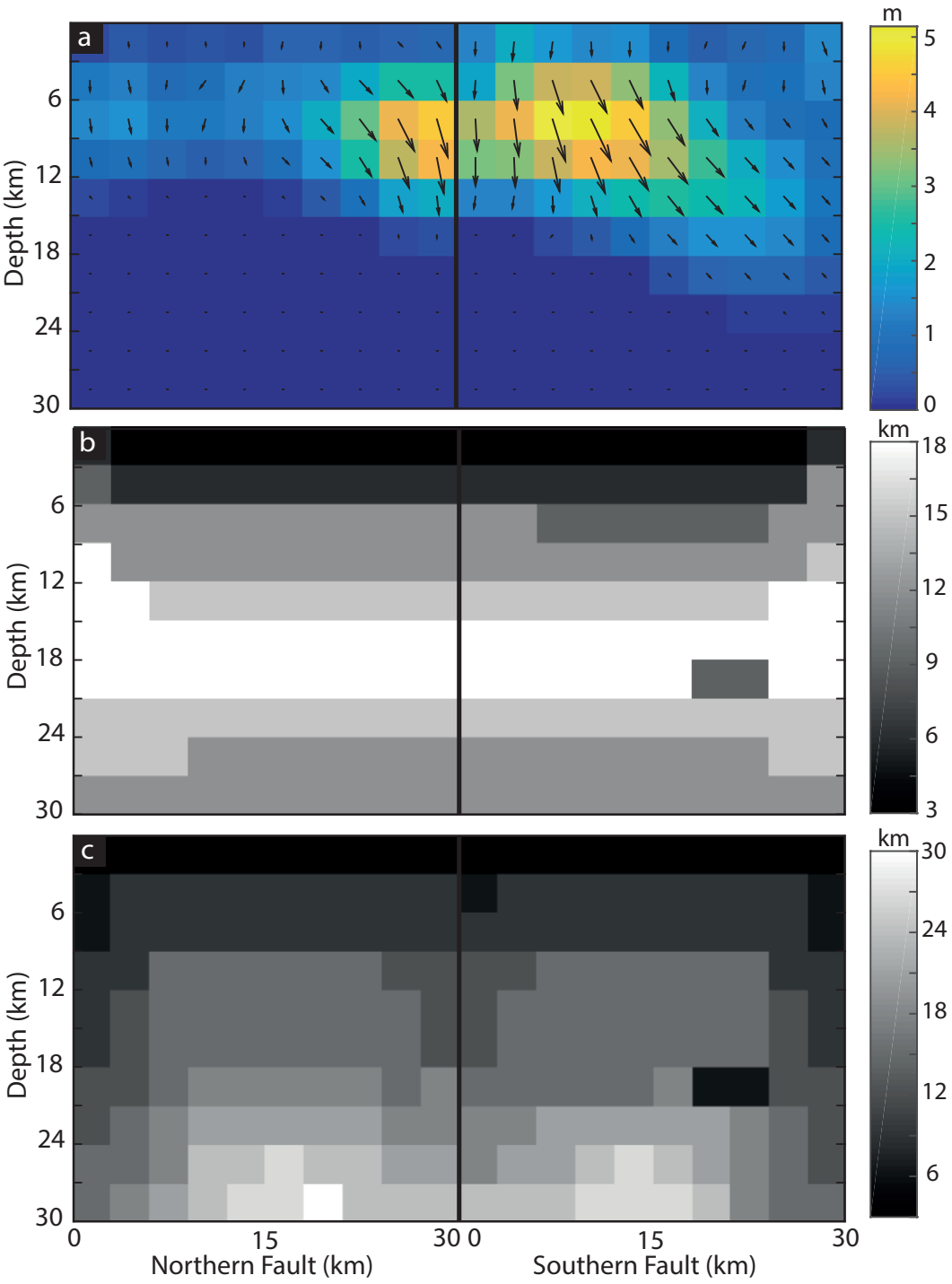

Figure C.9: a) Slip distribution for the Machaze earthquake using ENVISAT and SPOT data. b) Length scale of vertical resolution. c) Length scale of horizontal resolution. Each cell is 3 km horizontally by 3 km vertically.

Appendix D

Additional Material for Chapter 5

Introduction

This appendix contains further examples of the atmospheric corrections and post-seismic interferograms discussed in Chapter 5.

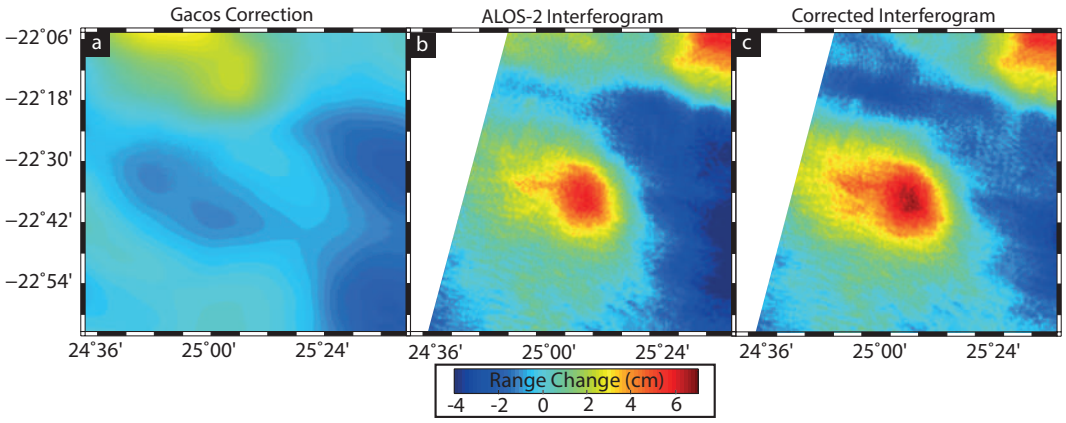

Figure D.1: a) GACOS atmospheric correction for ALOS-2 02/04/2017 – 14/05/2017 interferogram. b) ALOS-2 02/04/2017 – 14/05/2017 interferogram with standard deviation 2.1 cm. c) GACOS correction applied to ALOS-2 interferogram with standard deviation 2.0 cm.

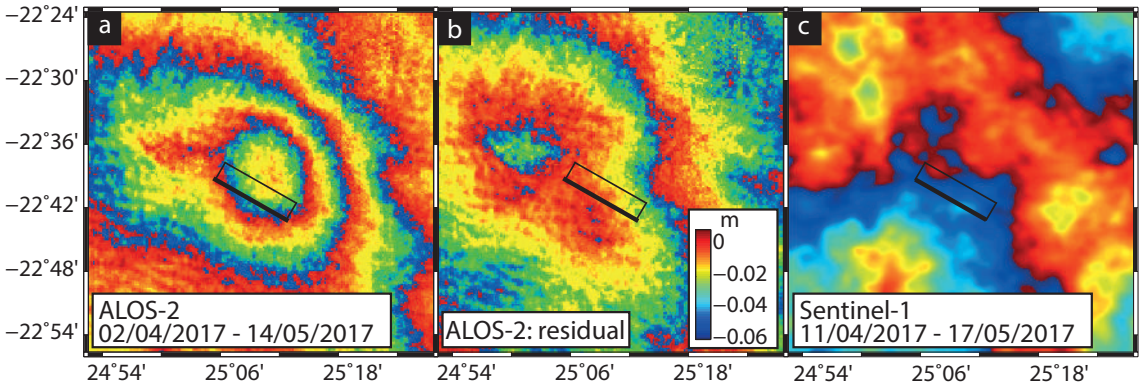

Figure D.2: a) ALOS-2 co-seismic interferogram (02/04/2017 – 14/05/2017), b) residual between model 1 and (a). c) Post-seismic Sentinel-1 interferogram (11/04/2017 – 17/05/2017) showing no post-seismic deformation. The earthquake occurred on 03/04/2017.

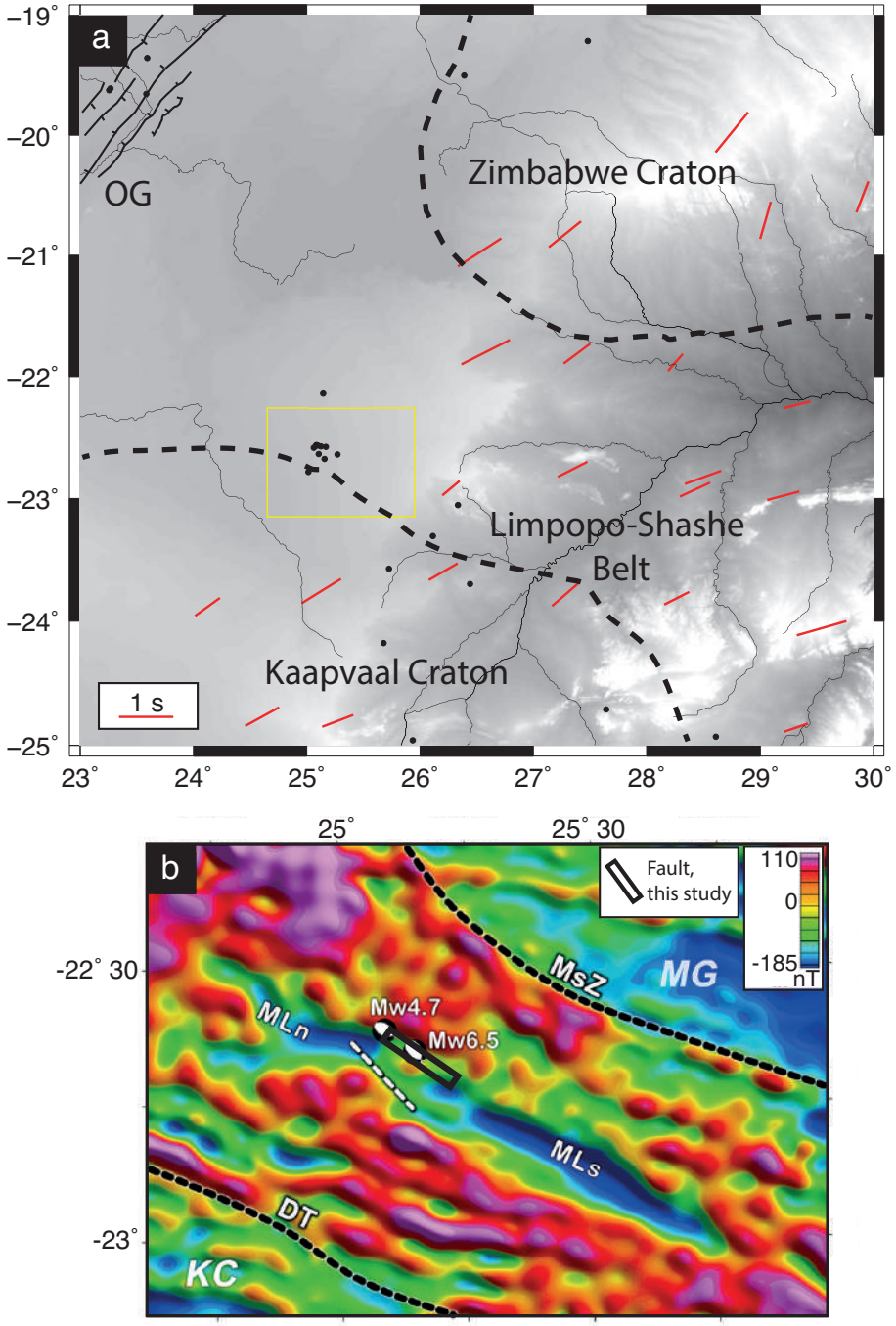

Figure D.3: a) Shear wave splitting observations (red bars) from *Silver et al.* [2001] showing a north-east to east rotation of the fast wave polarisation direction associated with the Limpopo-Shashe Belt. The orientation and length of the red bars show the fast polarisation direction and splitting delay times respectively. The yellow box denotes the extent of sub-panel (b). OG: Okavango Graben. Earthquakes are shown by filled black circles. b) Low-pass filtered aeromagnetic data presented by *Kolawole et al.* [2017], indicating magnetic anomaly striking NW-SE. Dashed white line shows the fault determined by *Kolawole et al.* [2017] from InSAR observations. Black rectangle shows the fault from this study. MLn and MLs refer to the Moiyabana Lineament north and south. Other abbreviations correspond to features referred to in *Kolawole et al.* [2017].

References

Abebe, B., V. Acocella, T. Korme, and D. Ayalew (2007), Quaternary faulting and volcanism in the Main Ethiopian Rift, *Journal of African Earth Sciences*, *48*(2-3), 115–124.

Acocella, V. (2007), Understanding caldera structure and development: An overview of analogue models compared to natural calderas, *Earth-Science Reviews*, *85*(3-4), 125–160.

Acocella, V. (2014), Structural control on magmatism along divergent and convergent plate boundaries: Overview, model, problems, *Earth Science Reviews*, *136*, 226–288.

Acocella, V., T. Korme, F. Salvini, and R. Funiciello (2002), Elliptic calderas in the Ethiopian Rift: control of pre-existing structures, *Journal of Volcanology and Geothermal Research*, *119*(1-4), 189–203.

Acocella, V., T. Korme, and F. Salvini (2003), Formation of normal faults along the axial zone of the Ethiopian Rift, *Journal of Structural Geology*, *25*(4), 503–513.

Agostini, A., G. Corti, A. Zeoli, and G. Mulugeta (2009), Evolution, pattern, and partitioning of deformation during oblique continental rifting: Inferences from lithospheric-scale centrifuge models, *Geochemistry, Geophysics, Geosystems*, *10*(11).

Agostini, A., M. Bonini, G. Corti, F. Sani, and F. Mazzarini (2011), Fault architecture in the Main Ethiopian Rift and comparison with experimental models: Implications for rift evolution and Nubia Somalia kinematics, *Earth and Planetary Science Letters*, *301*(3-4), 479–492.

Akaike, H. (1974), A new look at the statistical model identification, *IEEE Transactions on Automatic Control*, *19*(6), 716–723.

Albano, M., M. Polcari, C. Bignami, M. Moro, M. Saroli, and S. Stramondo (2017), Did Anthropogenic Activities Trigger the 3 April 2017 Mw 6.5 Botswana Earthquake?, *Remote Sensing*, *9*(12), 1028.

Ali, S. T., N. C. Davatzes, K. L. Feigl, H. F. Wang, W. Foxall, R. J. Mellors, and J. Akerley (2015), Deformation at Brady Hot Springs geothermal field measured by time series analysis of InSAR data, *Proceedings of the Fourtieth Workshop on Geothermal Reservoir Engineering*, pp. 1–5.

Altamimi, Z., P. Rebischung, L. Métivier, and X. Collilieux (2016), ITRF2014: A new release of the International Terrestrial Reference Frame modeling nonlinear station motions, *Journal of Geophysical Research: Solid Earth*, *121*(8), 6109–6131.

Amelung, F., S. Jonsson, H. Zebker, and P. Segall (2000), Widespread uplift and 'trapdoor' faulting on Galapagos volcanoes observed with radar interferometry, *Nature*, *407*(6807), 993–996.

Annen, C. (2009), From plutons to magma chambers: Thermal constraints on the accumulation of eruptible silicic magma in the upper crust, *Earth and Planetary Science Letters*, *284*, 409–416.

Arnold, D. W., J. Biggs, K. Anderson, S. Vallejo Vargas, G. Wadge, S. K. Ebmeier, M. F. Naranjo, and P. Mothes (2017), Decaying Lava Extrusion Rate at El Reventador Volcano, Ecuador, Measured Using High-Resolution Satellite Radar, *Journal of Geophysical Research: Solid Earth*, *122*(12), 9966–9988.

Asfaw, L. M. (1982), Development of earthquake-induced fissures in the Main Ethiopian Rift, *Nature*, *297*, 393–395.

Attanayake, J., and J. F. Fonseca (2016), The intraplate Mw 7 Machaze earthquake in Mozambique: Improved point source model, stress drop, and geodynamic implications, *Journal of African Earth Sciences*, *117*, 252–262.

Backus, G., and F. Gilbert (1970), Uniqueness in the Inversion of Inaccurate Gross Earth Data, *Philosophical Transactions of the Royal Society A: Mathematical, Physical and Engineering Sciences*, *266*(1173), 123–192.

Bagnardi, M., and A. Hooper (2018), Inversion of surface deformation data for rapid estimates of source parameters and uncertainties: a Bayesian approach, *Geochemistry Geophysics Geosystems*, *In Press*.

Bagnardi, M., F. Amelung, and M. P. Poland (2013), A new model for the growth of basaltic shields based on deformation of Fernandina volcano, Galápagos Islands, *Earth and Planetary Science Letters*, *377-378*, 358–366.

Bai, W. M., C. Vigny, Y. Ricard, and C. Froidevoix (1992), On the origin of deviatoric stresses in the lithosphere, *Journal of Geophysical Research*, *97*(B8), 11,729–11,737.

Baker, J., M. Thirlwall, and M. Menzies (1996), SrNdPb isotopic and trace element evidence for crustal contamination of plume-derived flood basalts: Oligocene flood volcanism in western Yemen, *Geochimica et Cosmochimica Acta*, *60*(14), 2559–2581.

Banks, N. L., K. A. Bardwell, and S. Musiwa (1995), Karoo Rift basins of the Luangwa Valley, Zambia, *Geological Society, London, Special Publications*, *80*(1), 285–295.

Bastow, I. D., G. W. Stuart, J.-M. Kendall, and C. J. Ebinger (2005), Upper-mantle seismic structure in a region of incipient continental breakup: northern Ethiopian rift, *Geophys. J. Int.*, pp. 479–493.

Bastow, I. D., S. Pilidou, J. M. Kendall, and G. W. Stuart (2010), Melt-induced seismic anisotropy and magma assisted rifting in Ethiopia: Evidence from surface waves, *Geochemistry, Geophysics, Geosystems*, *11*(6).

Battaglia, M., C. Troise, F. Obrizzo, F. Pingue, and G. De Natale (2006), Evidence for fluid migration as the source of deformation at Campi Flegrei caldera (Italy), *Geophysical Research Letters*, *33*(1).

Becerril, L., A. Cappello, I. Galindo, M. Neri, and C. Del Negro (2013), Spatial probability distribution of future volcanic eruptions at El Hierro Island (Canary Islands, Spain), *Journal of Volcanology and Geothermal Research*, *257*, 21–30.

Begg, G., W. Griffin, L. Natapov, S. Y. O'Reilly, S. Grand, C. O'Neill, J. Hronsky, Y. P. Djomani, C. Swain, T. Deen, and P. Bowden (2009), The lithospheric architecture of Africa: Seismic tomography, mantle petrology, and tectonic evolution, *Geosphere*, *5*(1), 23–50.

Bekaert, D. P., A. Hooper, and T. J. Wright (2015), A spatially variable power law tropospheric correction technique for InSAR data, *Journal of Geophysical Research: Solid Earth*, *120*(2), 1345–1356.

Berardino, P., G. Fornaro, R. Lanari, S. Member, E. Sansosti, and S. Member (2002), A New Algorithm for Surface Deformation Monitoring Based on Small Baseline Differential SAR Interferograms, *IEEE Transactions on geoscience and remote sensing*, *40*(11), 2375–2383.

Beutel, E., J. van Wijk, C. Ebinger, D. Keir, and A. Agostini (2010), Formation and stability of magmatic segments in the Main Ethiopian and Afar rifts, *Earth and Planetary Science Letters*, *293*(3-4), 225–235.

Bialas, R. W., W. R. Buck, and R. Qin (2010), How much magma is required to rift a continent?, *Earth and Planetary Science Letters*, *292*(1-2), 68–78.

Bibby, H. M., T. G. Caldwell, F. J. Davey, and T. H. Webb (1995), Geophysical evidence on the structure of the Taupo Volcanic Zone and its hydrothermal circulation, *Journal of Volcanology and Geothermal Research*, *68*(1-3), 29–58.

Bie, L., P. J. González, and A. Rietbrock (2017), Slip distribution of the 2015 Lefkada earthquake and its implications for fault segmentation, *Geophysical Journal International Geophys. J. Int*, *210*, 420–427.

Biggs, J., and M. E. Pritchard (2017), Global volcano monitoring: What does it mean when volcanoes deform?, *Elements*, *13*(1), 17–22.

Biggs, J., J. Gottsmann, R. Lloyd, Y. Birhanu, and E. Lewi (), The assembly of upper crustal magma reservoirs during continental rifting, *Nature Geoscience*.

Biggs, J., E. Bergman, B. Emmerson, G. J. Funning, J. Jackson, B. Parsons, and T. J. Wright (2006), Fault identification for buried strike-slip earthquakes using InSAR: The 1994 and 2004 Al Hoceima, Morocco earthquakes, *Geophysical Journal International*, *166*(3), 1347–1362.

Biggs, J., T. Wright, Z. Lu, and B. Parsons (2007), Multi-interferogram method for measuring interseismic deformation: Denali Fault, Alaska, *Geophysical Journal International*, *170*(3), 1165–1179.

Biggs, J., F. Amelung, N. Gourmelen, T. H. Dixon, and S.-W. Kim (2009a), InSAR observations of 2007 Tanzania rifting episode reveal mixed fault and dyke extension in an immature continental rift, *Geophysical Journal International*, *179*(1), 549–558.

Biggs, J., E. Y. Anthony, and C. J. Ebinger (2009b), Multiple inflation and deflation events at Kenyan volcanoes, East African Rift, *Geology*, *37*, 979–982.

Biggs, J., E. Nissen, T. Craig, J. Jackson, and D. P. Robinson (2010a), Breaking up the hanging wall of a rift-border fault: The 2009 Karonga earthquakes, Malawi, *Geophysical Research Letters*, *37*(11).

Biggs, J., Z. Lu, T. Fournier, and J. T. Freymueller (2010b), Magma flux at Okmok Volcano, Alaska, from a joint inversion of continuous GPS, campaign GPS, and interferometric synthetic aperture radar, *Journal of Geophysical Research*, *115*(B12), B12,401.

Biggs, J., I. D. Bastow, D. Keir, and E. Lewi (2011), Pulses of deformation reveal frequently recurring shallow magmatic activity beneath the Main Ethiopian Rift, *Geochemistry, Geophysics, Geosystems*, *12*(9).

Biggs, J., M. Chivers, and M. C. Hutchinson (2013), Surface deformation and stress interactions during the 2007-2010 sequence of earthquake, dyke intrusion and eruption in northern Tanzania, *Geophysical Journal International*, *195*(1), 16–26.

Biggs, J., S. K. Ebmeier, W. P. Aspinall, Z. Lu, M. E. Pritchard, R. S. J. Sparks, and T. a. Mather (2014), Global link between deformation and volcanic eruption quantified by satellite imagery., *Nature communications*, *5*, 3471.

Biggs, J., E. Robertson, and K. Cashman (2016), The lateral extent of volcanic interactions during unrest and eruption, *Nature Geoscience*, *9*(4), 308–311.

Bignami, C., S. Corradini, L. Merucci, M. De Michele, D. Raucoules, G. De Astis, S. Stramondo, and J. Piedra (2014), Multisensor satellite monitoring of the 2011 Puyehue-cordon caulle eruption, *IEEE Journal of Selected Topics in Applied Earth Observations and Remote Sensing*, *7*(7), 2786–2796.

Bijwaard, H., and W. Spakman (1999), Tomographic evidence for a narrow whole mantle plume below Iceland, *Earth and Planetary Science Letters*, *166*(3-4), 121–126.

Bilham, R., R. Bendick, K. Larson, P. Mohr, J. Braun, S. Tesfaye, and L. Asfaw (1999), Secular and tidal strain across the Main Ethiopian Rift, *Geophysical Research Letters*, *26*(18), 2789–2792.

Bilham, R., V. K. Gaur, and P. Molnar (2001), Earthquakes: Himalayan seismic hazard, *Science*, *293*(5534), 1442–1444.

Bird, P., Z. Ben-Avraham, G. Schubert, M. Andreoli, and G. Viola (2006), Patterns of stress and strain rate in southern Africa, *Journal of Geophysical Research: Solid Earth*, *111*(8), B08,402.

Birhanu, Y., and R. Bendick (2015), Monsoonal loading in Ethiopia and Eritrea from vertical GPS displacement time series, *Journal of Geophysical Research: Solid Earth*, *120*(10), 7231–7238.

Birhanu, Y., R. Bendick, S. Fisseha, E. Lewi, M. Floyd, R. King, and R. Reilinger (2016), GPS constraints on broad scale extension in the Ethiopian Highlands and Main Ethiopian Rift, *Geophysical Research Letters*, *43*(13), 6844–6851.

Birhanu, Y., M. Wilks, J. Biggs, J. M. Kendall, A. Ayele, and E. Lewi (2018), Seasonal patterns of seismicity and deformation at the Alutu geothermal reservoir, Ethiopia, induced by hydrological loading.

Birt, C., P. Maguire, M. Khan, H. Thybo, G. Keller, and J. Patel (1997), The influence of pre-existing structures on the evolution of the southern Kenya Rift Valley - evidence from seismic and gravity studies, *Tectonophysics*, *278*(1-4), 211–242.

Boccaletti, M., M. Bonini, R. Mazzuoli, B. Abebe, L. Piccardi, and L. Tortorici (1998), Quatemary oblique extensional tectonics in the Ethiopian Rift (Horn of Africa), *Tectonophysics*, *287*, 97–116.

Bonafede, M. (1991), Hot fluid migration: an efficient source of ground deformation: application to the 1982 - 1985 crisis at Campi Flegrei-Italy, *Journal of Volcanology and Geothermal Research*, *48*(1), 187–198.

Bonafede, M., and C. Ferrari (2009), Analytical models of deformation and residual gravity changes due to a Mogi source in a viscoelastic medium, *Tectonophysics*, *471*(1-2), 4–13.

Bonini, M., G. Corti, F. Innocenti, P. Manetti, F. Mazzarini, T. Abebe, and Z. Pecskay

(2005), Evolution of the Main Ethiopian Rift in the frame of Afar and Kenya rifts propagation, *Tectonics*, *24*.

Bower, S. M., and A. W. Woods (1998), On the influence of magma chambers in controlling the evolution of explosive volcanic eruptions, *Journal of Volcanology and Geothermal Research*, *86*(1-4), 67–78.

Braddock, M., J. Biggs, I. M. Watson, W. Hutchison, D. M. Pyle, and T. A. Mather (2017), Satellite observations of fumarole activity at Aluto volcano, Ethiopia: Implications for geothermal monitoring and volcanic hazard, *Journal of Volcanology and Geothermal Research*, *341*, 70–83.

Brazangi, M., and B. Isacks (1976), Spatial distribution of earthquaktes and subduction of the Nasca plate beneath South America, *Geology*, *4*(1971), 686–692.

Bro, R., and S. De Jong (1997), A fast non-negativity-constrained least squares algorithm, *Journal of Chemometrics*, *11*, 393–401.

Brunetti, C., N. Linde, and J. A. Vrugt (2017), Bayesian model selection in hydrogeophysics: Application to conceptual subsurface models of the South Oyster Bacterial Transport Site, Virginia, USA, *Advances in Water Resources*, *102*, 127–141.

Buck, W. R. (1991), Modes of continental lithospheric extension, *Journal of Geophysical Research: Solid Earth*, *96*(B12), 20,161–20,178.

Buck, W. R. (2006), The role of magma in the development of the Afro-Arabian Rift System, *Geological Society, London, Special Publications*, *259*(1), 43–54.

Bungum, H., C. Lindholm, and J. I. Faleide (2005), Postglacial seismicity offshore mid-Norway with emphasis on spatio-temporal-magnitudal variations, *Marine and Petroleum Geology*, *22*(1-2 SPEC. ISS.), 137–148.

Bürgmann, R., P. A. Rosen, and E. J. Fielding (2000), Synthetic Aperture Radar Interferometry to Measure Earth's Surface Topography and Its Deformation, *Annual Review of Earth and Planetary Sciences*, *28*(1), 169–209.

Bürgmann, R., M. G. Kogan, G. M. Steblov, G. Hilley, V. E. Levin, and E. Apel (2005), Interseismic coupling and asperity distribution along the Kamchatka subduction zone, *Journal of Geophysical Research: Solid Earth*, *110*(7), 1–17.

Burnham, K. P., and D. Anderson (2003), *Model Selection and Multimodel Inference*, 488 pp., Springer Science & Business Media.

Calais, E., N. D'Oreye, J. Albaric, A. Deschamps, D. Delvaux, J. Déverchère, C. Ebinger, R. W. Ferdinand, F. Kervyn, A. S. Macheyeki, A. Oyen, J. Perrot, E. Saria, B. Smets, D. S. Stamps, and C. Wauthier (2008), Strain accommodation by slow slip and dyking in a youthful continental rift, East Africa., *Nature*, *456*(7223), 783–7.

Calais, E., A. M. Freed, R. Van Arsdale, and S. Stein (2010), Triggering of New Madrid seismicity by late-Pleistocene erosion, *Nature*, *466*(7306), 608–611.

Calais, E., T. Camelbeeck, S. Stein, M. Liu, and T. J. Craig (2016), A new paradigm for large earthquakes in stable continental plate interiors, *Geophysical Research Letters*, *43*(20), 10,621–10,637.

Cardona, C., A. Tassara, F. Gil-Cruz, L. Lara, S. Morales, P. Kohler, and L. Franco (2018), Crustal seismicity associated to rapid surface uplift at Laguna del Maule Volcanic Complex, Southern Volcanic Zone of the Andes, *Journal of Volcanology and Geothermal Research*, *353*, 83–94.

Casey, M., C. Ebinger, D. Keir, R. Gloaguen, and F. Mohamed (2006), Strain accommodation in transitional rifts: extension by magma intrusion and faulting in Ethiopian rift magmatic segments, (2003), 143–163.

Cashman, K. V., and R. Sparks (2013), How volcanoes work: A 25 year perspective, *Bulletin of the Geological Society of America*, *125*(5-6), 664–690.

Chaussard, E., and F. Amelung (2014), Regional controls on magma ascent and storage in volcanic arcs, *Geochemistry, Geophysics, Geosystems*, *15*, 1407–1418.

Chen, C. W., and H. A. Zebker (2001), Two-dimensional phase unwrapping with use of statistical models for cost functions in nonlinear optimization, *Journal of the Optical Society of America. A*, *18*(2), 338.

Chorowicz, J. (2005), The East African rift system, *Journal of African Earth Sciences*, *43*(1-3), 379–410.

Chu, D., and R. G. Gordon (1999), Evidence for motion between Nubia and Somalia along the Southwest Indian ridge, *Nature*, *398*(6722), 64–67.

Coco, A., J. Gottsmann, F. Whitaker, A. Rust, G. Currenti, A. Jasim, and S. Bunney (2016), Numerical models for ground deformation and gravity changes during volcanic unrest: simulating the hydrothermal system dynamics of a restless caldera, *Solid Earth*, *7*, 557–577.

Cole, J., D. Milner, and K. Spinks (2005), Calderas and caldera structures: a review, *Earth-Science Reviews*, *69*(1-2), 1–26.

Cole, J., K. Spinks, C. Deering, I. Nairn, and G. Leonard (2010), Volcanic and structural evolution of the Okataina Volcanic Centre; dominantly silicic volcanism associated with the Taupo Rift, New Zealand, *Journal of Volcanology and Geothermal Research*, *190*(1), 123–135.

Connor, C., R. Sparks, R. Mason, C. Bonadonna, and S. Young (2003), Exploring links between physical and probabilistic models of volcanic eruptions: The Soufrière Hills Volcano, Montserrat, *Geophysical Research Letters*, *30*(13), 1997–2000.

Copley, A. (2017), The strength of earthquake-generating faults, *Journal of the Geological Society*, *175*, 2017–037.

Copley, A., J.-P. Avouac, J. Hollingsworth, and S. Leprince (2011), The 2001 Mw 7.6 Bhuj earthquake, low fault friction, and the crustal support of plate driving forces in India, *Journal of Geophysical Research*, *116*(B8), B08,405.

Copley, A., J. Hollingsworth, and E. Bergman (2012), Constraints on fault and lithosphere rheology from the coseismic slip and postseismic afterslip of the 2006 Mw7.0 Mozambique earthquake, *Journal of Geophysical Research: Solid Earth*, *117*(3), 1–16.

Cornwell, D., G. Mackenzie, R. England, P. Maguire, L. Asfaw, and B. Oluma (2006), Northern Main Ethiopian Rift crustal structure from new high-precision gravity data, *Geological Society, London, Special Publications*, *259*(1), 307–321.

Corti, G. (2009), Continental rift evolution: From rift initiation to incipient break-up in the Main Ethiopian Rift, East Africa, *Earth-Science Reviews*, *96*(1-2), 1–53.

Corti, G., F. Sani, S. Agostini, M. Philippon, D. Sokoutis, and E. Willingshofer (2018), Off-axis volcano-tectonic activity during continental rifting: Insights from the transversal Goba-Bonga lineament, Main Ethiopian Rift (East Africa), *Tectonophysics*, *728-729*, 75–91.

Craig, T. J., J. A. Jackson, K. Priestley, and D. Mckenzie (2011), Earthquake distribution patterns in Africa: Their relationship to variations in lithospheric and geological structure, and their rheological implications, *Geophysical Journal International*, *185*(1), 403–434.

Craig, T. J., E. Calais, L. Fleitout, L. Bollinger, and O. Scotti (2016), Evidence for the release of long-term tectonic strain stored in continental interiors through intraplate earthquakes, *Geophysical Research Letters*, *43*(13), 6826–6836.

Daly, E., D. Keir, C. J. Ebinger, G. W. Stuart, I. D. Bastow, and A. Ayele (2008), Crustal tomographic imaging of a transitional continental rift: The Ethiopian rift, *Geophysical Journal International*, *172*(3), 1033–1048.

Daly, M. C., J. Chorowicz, and J. D. Fairhead (1989), Rift basin evolution in Africa: the influence of reactivated steep basement shear zones, *Geological Society, London, Special Publications*, *44*(1), 309–334.

Daniels, K., I. Bastow, D. Keir, R. Sparks, and T. Menand (2014), Thermal models of dyke intrusion during development of continent-ocean transition, *Earth and Planetary Science Letters*, *385*, 145–153.

Darby, D. J., and C. M. Meertens (1995), Terrestrial and GPS measurements of deformation across the Taupo back arc and Hikurangi forearc regions in New Zealand, *Journal of Geophysical Research: Solid Earth*, *100*(B5), 8221–8232.

De Zan, F., and A. M. Guarnieri (2006), TOPSAR: Terrain observation by progressive scans, *IEEE Transactions on Geoscience and Remote Sensing*, *44*(9), 2352–2360.

Dee, D. P., S. M. Uppala, A. J. Simmons, P. Berrisford, P. Poli, S. Kobayashi, U. Andrae, M. A. Balmaseda, G. Balsamo, P. Bauer, P. Bechtold, A. C. Beljaars, L. van de Berg, J. Bidlot, N. Bormann, C. Delsol, R. Dragani, M. Fuentes, A. J. Geer, L. Haimberger, S. B. Healy, H. Hersbach, E. V. Hólm, L. Isaksen, P. Kållberg, M. Köhler, M. Matricardi, A. P. Mcnally, B. M. Monge-Sanz, J. J. Morcrette, B. K. Park, C. Peubey, P. de Rosnay, C. Tavolato, J. N. Thépaut, and F. Vitart (2011), The ERA-Interim reanalysis: Configuration and performance of the data assimilation system, *Quarterly Journal of the Royal Meteorological Society*, *137*(656), 553–597.

Degruyter, W., C. Huber, O. Bachmann, K. M. Cooper, and A. J. Kent (2016), Magma reservoir response to transient recharge events: The case of Santorini volcano (Greece), *Geology*, *44*(1), 23–26.

Delvaux, D., and B. Sperner (2003), New aspects of tectonic stress inversion with reference to the TENSOR program, *Geological Society, London, Special Publications*, *212*(1), 75–100.

Di Paola, G. (1971), Geology of the Corbetti Caldera Area (Main Ethiopian Rift Valley), *Bulletin of Volcanology*, *35*(497).

Didana, Y. L., S. Thiel, and G. Heinson (2014), Magnetotelluric imaging of upper crustal partial melt at Tendaho graben in Afar, Ethiopia, *Geophysical Research Letters*, *41*(9), 3089–3095.

Dieterich, J. (1994), A constitutive law for rate of earthquake production and its application to earthquake clustering, *Journal of Geophysical Research: Solid Earth*, *99*(B2), 2601–2618.

Dietterich, H. R., M. P. Poland, D. A. Schmidt, K. V. Cashman, D. R. Sherrod, and A. T. Espinosa (2012), Tracking lava flow emplacement on the east rift zone of

Kilauea, Hawaii, with synthetic aperture radar coherence, *Geochemistry, Geophysics, Geosystems*, *13*(5).

Doin, M. P., C. Lasserre, G. Peltzer, O. Cavalié, and C. Doubre (2009), Corrections of stratified tropospheric delays in SAR interferometry: Validation with global atmospheric models, *Journal of Applied Geophysics*, *69*(1), 35–50.

D'Oreye, N., J. Fernandez, P. Gonzalez, F. Kervyn, C. Wauthier, C. Frischknecht, E. Calais, S. Heleno, V. Cayol, A. Oyen, and P. Marinkovic (2008), Systematic InSAR monitoring of African active volcanic zones: What we have learned in three years, or an harvest beyond our expectations, in *2008 Second Workshop on Use of Remote Sensing Techniques for Monitoring Volcanoes and Seismogenic Areas*, pp. 1–6, IEEE.

D'Oreye, N., P. J. González, A. Shuler, A. Oth, L. Bagalwa, G. Ekström, D. Kavotha, F. Kervyn, C. Lucas, F. Lukaya, E. Osodundu, C. Wauthier, and J. Fernández (2011), Source parameters of the 2008 Bukavu-Cyangugu earthquake estimated from InSAR and teleseismic data, *Geophysical Journal International*, *184*(2), 934–948.

Doubre, C., and G. Peltzer (2007), Fluid-controlled faulting process in the Asal Rift, Djibouti, from 8 yr of radar interferometry observations, *Geology*, *35*(1), 69.

Dragoni, M., and C. Magnanensi (1989), Displacement and stress produced by a pressurized, spherical magma chamber, surrounded by a viscoelastic shell, *Physics of the Earth and Planetary Interiors*, *56*(3-4), 316–328.

Dugda, M. T., A. A. Nyblade, J. Julia, C. A. Langston, C. J. Ammon, and S. Simiyu (2005), Crustal structure in Ethiopia and Kenya from receiver function analysis: Implications for rift development in eastern Africa, *Journal of Geophysical Research: Solid Earth*, *110*(1), 1–15.

Dunbar, J. A., and D. S. Sawyer (1988), Continental rifting at pre-existing lithospheric weaknesses, *Nature*, *333*(6172), 450–452.

Dunbar, J. A., and D. S. Sawyer (1989), How preexisting weaknesses control the style of continental breakup, *Journal of Geophysical Research*, *94*(B6), 7278.

Dzurisin, D., M. Lisowski, and C. W. Wicks (2009), Continuing inflation at Three Sisters volcanic center, central Oregon Cascade Range, USA, from GPS, leveling, and InSAR observations, *Bulletin of Volcanology*, *71*(10), 1091–1110.

Ebinger, C. (2005), Continental break-up: The East African perspective, *Astronomy and Geophysics*, *46*(2), 2.16–2.21.

Ebinger, C., and M. Casey (2001), Continental breakup in magmatic provinces: An Ethiopian example, *Geology*, *29*(6), 527.

Ebinger, C., B. Rosendahl, and D. Reynolds (1987), Tectonic model of the Malawi rift, Africa, *Tectonophysics*, *141*(1-3), 215–235.

Ebinger, C., Y. P. Djomani, E. Mbede, A. Foster, and J. B. Dawson (1997), Rifting Archaean lithosphere: the Eyasi-Manyara-Natron rifts, East Africa, *Journal of the Geological Society*, *154*(6), 947–960.

Ebinger, C. J. (1989), Tectonic development of the western branch of the East African rift system, *Geological Society of America Bulletin*, *101*(July), 885–903.

Ebinger, C. J., and N. H. Sleep (1998), Cenozoic magmatism throughout east Africa resulting from impact of a single plume, *Nature*, *395*, 788–791.

Ebinger, C. J., A. L. Deino, R. E. Drake, and A. L. Tesha (1989), Chronology of volcanism and rift basin propagation: Rungwe Volcanic Province, East Africa, *Journal of Geophysical Research: Solid Earth*, *94*(B11), 15,785–15,803.

Ebinger, C. J., G. D. Karner, and J. K. Weissel (1991), Mechanical strength of extended continental lithosphere: Constraints from the Western Rift System, East Africa, *Tectonics*, *10*(6), 1239–1256.

Ebinger, C. J., D. Keir, A. Ayele, E. Calais, T. J. Wright, M. Belachew, J. O. S. Hammond, E. Campbell, and W. R. Buck (2008), Capturing magma intrusion and faulting processes during continental rupture: seismicity of the Dabbahu (Afar) rift, *Geophys. J. Int*, *174*, 1138–1152.

Ebinger, C. J., D. Keir, I. D. Bastow, K. Whaler, J. O. S. Hammond, A. Ayele, M. S. Miller, C. Tiberi, and S. Hautot (2017), Crustal structure of active deformation zones in Africa: Implications for global crustal processes, *Tectonics*, pp. 1–35.

Ebmeier, S. K., J. Biggs, T. A. Mather, J. R. Elliott, G. Wadge, and F. Amelung (2012), Measuring large topographic change with InSAR: Lava thicknesses, extrusion rate and subsidence rate at Santiaguito volcano, Guatemala, *Earth and Planetary Science Letters*, *335-336*, 216–225.

Ebmeier, S. K., J. Biggs, T. A. Mather, and F. Amelung (2013), Applicability of InSAR to tropical volcanoes: insights from Central America, *Geological Society, London, Special Publications*, *380*(1), 15–37.

Ebmeier, S. K., B. J. Andrews, M. C. Araya, D. W. Arnold, J. Biggs, C. Cooper, E. Cottrell, M. Furtney, J. Hickey, J. Jay, R. Lloyd, A. L. Parker, M. E. Pritchard, E. Robertson, E. Venzke, and J. L. Williamson (2018), Synthesis of global satellite observations of magmatic and volcanic deformation: implications for volcano monitoring & the lateral extent of magmatic domains, *Journal of Applied Volcanology*, *7*(1), 1–26.

Elliott, J. R., J. Biggs, B. Parsons, and T. J. Wright (2008), InSAR slip rate determination on the Altyn Tagh Fault, northern Tibet, in the presence of topographically correlated atmospheric delays, *Geophysical Research Letters*, *35*(12).

Elliott, J. R., R. J. Walters, and T. J. Wright (2016), The role of space-based observation in understanding and responding to active tectonics and earthquakes, *Nature Communications*, *7*(13844).

Emardson, T. R., M. Simons, and F. H. Webb (2003), Neutral atmospheric delay in interferometric synthetic aperture radar applications: Statistical description and mitigation, *Journal of Geophysical Research: Solid Earth*, *108*(B5), 2231.

Emenke, E. A. (1986), Gravity signature of the limpopo-Kaapvaal fossil plate boundary in southern africa, *Tectonophysics*, *128*(1-2), 127–137.

England, P., and J. Jackson (2011), Uncharted seismic risk, *Nature Geoscience*, *4*(6), 348–349.

Ergin, M., and M. Aktar (2018), Lower crustal seismic activity in the Adana Basin (Eastern Mediterranean): Possible connection to gravitational flexure, *Tectonophysics*, *730*, 1–10.

Fagereng, Å. (2013), Fault segmentation, deep rift earthquakes and crustal rheology: Insights from the 2009 Karonga sequence and seismicity in the Rukwa-Malawi rift zone, *Tectonophysics*, *601*, 216–225.

Fairhead, J., and N. Henderson (1977), The Seismicity of Southern-Africa and Incipient Rifting, *Tectonophysics*, *41*(4), T19–T26.

Fairhead, J. D., and R. W. Girdler (1969), How far does the rift system extend through Africa?, *Nature*, *221*(5185), 1018–1020.

Farr, T., and M. Kobrick (2000), Shuttle Radar Topography Mission Produces a Wealth of Data, *Eos, Transactions American Geophysical Union*, *81*(48), 581–583.

Fenton, C. H., and J. J. Bommer (2006), The Mw 7 Machaze, Mozambique, earthquake of 23 February 2006, *Seismological Research Letters*, *77*(4), 426–439.

Fialko, Y. (2006), Interseismic strain accumulation and the earthquake potential on the southern San Andreas fault system, *Nature*, *441*(7096), 968–971.

Field, L., J. Blundy, R. A. Brooker, T. Wright, and G. Yirgu (2012), Magma storage conditions beneath Dabbahu Volcano (Ethiopia) constrained by petrology, seismicity and satellite geodesy, *Bulletin of Volcanology*, *74*(5), 981–1004.

Finnegan, N. J., M. E. Pritchard, R. B. Lohman, and P. R. Lundgren (2008), Constraints on surface deformation in the Seattle, WA, urban corridor from satellite radar interferometry time-series analysis, *Geophys. J. Int.*, *174*(1), 29–41.

Fletcher, J. M., O. J. Teran, T. K. Rockwell, M. E. Oskin, K. W. Hudnut, K. J. Mueller, R. M. Spelz, S. O. Akciz, E. Masana, G. Faneros, E. J. Fielding, S. Leprince, A. E. Morelan, J. Stock, D. K. Lynch, A. J. Elliott, P. Gold, J. Liu-Zeng, A. González-Ortega, A. Hinojosa-Corona, and J. González-García (2014), Assembly of a large earthquake from a complex fault system: Surface rupture kinematics of the 4 April 2010 El Mayor Cucapah (Mexico) Mw 7.2 earthquake, *Geosphere*, *10*(4), 797–827.

Floyd, M. A., R. J. Walters, J. R. Elliott, G. J. Funning, J. L. Svarc, J. R. Murray, A. J. Hooper, Y. Larsen, P. Marinkovic, R. Bürgmann, I. A. Johanson, and T. J. Wright (2016), Spatial variations in fault friction related to lithology from rupture and afterslip of the 2014 South Napa, California, earthquake, *Geophysical Research Letters*, *43*(13), 6808–6816.

Folch, A., and J. Gottsmann (2006), Faults and ground uplift at active calderas, *Geological Society, London, Special Publications*, *269*(1), 109–120.

Fonseca, J. F. B. D., J. Chamussa, A. Domingues, G. Helffrich, E. Antunes, G. van Aswegen, L. V. Pinto, S. Custodio, and V. J. Manhica (2014), MOZART: A Seismological Investigation of the East African Rift in Central Mozambique, *Seismological Research Letters*, *85*(1), 108–116.

Fontijn, K., G. G. Ernst, M. A. Elburg, D. Williamson, E. Abdallah, S. Kwelwa, E. Mbede, and P. Jacobs (2010a), Holocene explosive eruptions in the Rungwe Volcanic Province, Tanzania, *Journal of Volcanology and Geothermal Research*, *196*(1-2), 91–110.

Fontijn, K., D. Delvaux, G. G. J. Ernst, M. Kervyn, E. Mbede, and P. Jacobs (2010b), Tectonic control over active volcanism at a range of scales: Case of the Rungwe Volcanic Province, SW Tanzania; and hazard implications, *Journal of African Earth Sciences*, *58*(5), 764–777.

Fontijn, K., D. Williamson, E. Mbede, and G. G. Ernst (2012), The Rungwe Volcanic Province, Tanzania - A volcanological review, *Journal of African Earth Sciences*, *63*, 12–31.

Fontijn, K., K. McNamara, A. Zafu Tadesse, D. M. Pyle, F. Dessalegn, W. Hutchison, T. A. Mather, and G. Yirgu (2018), Contrasting styles of post-caldera volcanism along the Main Ethiopian Rift: Implications for contemporary volcanic hazards, *Journal of Volcanology and Geothermal Research*.

Foster, A. N., and J. A. Jackson (1998), Source parameters of large African earthquakes:implications for crustal rheology and regional kinematics, *Geophysical Journal International*, *134*(2), 422–448.

Funning, G. J., and A. Garcia (2017), A systematic study of earthquake detectability using Sentinel-1 Interferometric Wide-Swath data, (April 2016).

Funning, G. J., B. Parsons, T. J. Wright, J. A. Jackson, and E. J. Fielding (2005), Surface displacements and source parameters of the 2003 Bam (Iran) earthquake from Envisat advanced synthetic aperture radar imagery, *Journal of Geophysical Research B: Solid Earth*, *110*(9), 1–23.

Furman, T. (1995), Melting of metasomatized subcontinental lithosphere: undersaturated mafic lavas from Rungwe, Tanzania, *Contributions to Mineral Petrolology*, *122*(1-2), 97–115.

Furman, T., J. Bryce, T. Rooney, B. Hanan, G. Yirgu, and D. Ayalew (2006), Heads and tails: 30 million years of the Afar plume, *Geological Society, London, Special Publications*, *259*(1), 95–119.

Gaffney, E. S., B. Damjanac, and G. A. Valentine (2007), Localization of volcanic activity: 2. Effects of pre-existing structure, *Earth and Planetary Science Letters*, *263*(3-4), 323–338.

Gallacher, R. J., D. Keir, N. Harmon, G. Stuart, S. Leroy, J. O. Hammond, J. M. Kendall, A. Ayele, B. Goitom, G. Ogubazghi, and A. Ahmed (2016), The initiation of segmented buoyancy-driven melting during continental breakup, *Nature Communications*, *7*, 13,110.

Garnero, E. J., and A. K. McNamara (2008), Structure and Dynamics of Earth's Lower Mantle, *Science*, *320*(May), 626–628.

Garnero, E. J., A. K. McNamara, and S. H. Shim (2016), Continent-sized anomalous zones with low seismic velocity at the base of Earth's mantle, *Nature Geoscience*, *9*(7), 481–489.

Girard, G., and B. V. W. D. Vries (2005), The Managua Graben and Las Sierras-Masaya volcanic complex (Nicaragua); pull-apart localization by an intrusive complex: results from analogue modeling, *144*, 37–57.

Gislason, G., H. Eysteinsson, V. Hardardottir, and G. Bjornsson (2012), Reykjavik Geothermal: Corbetti Geothermal Prospect, *Tech. rep.*

Gíslason, G., H. Eysteinsson, G. Bjornsson, and V. Hardardottir (2015), Results of Surface Exploration in the Corbetti Geothermal Area, Ethiopia, in *Paper presented at World Geothermal Congress, Melbourne, Australia, 19-25 April 2015*, April.

Gleeson, M. L., M. J. Stock, D. M. Pyle, T. A. Mather, W. Hutchison, G. Yirgu, and J. Wade (2017), Constraining magma storage conditions at a restless volcano in the Main Ethiopian Rift using phase equilibria models, *Journal of Volcanology and Geothermal Research*, *337*, 44–61.

Global Volcanism Program (2013), Volcanoes of the World.

Goda, K. (2012), Nonlinear response potential of Mainshock-Aftershock sequences from Japanese earthquakes, *Bulletin of the Seismological Society of America*, *102*(5), 2139–2156.

Goitom, B., C. Oppenheimer, J. O. Hammond, R. Grandin, T. Barnie, A. Donovan, G. Ogubazghi, E. Yohannes, G. Kibrom, J.-M. Kendall, S. A. Carn, D. Fee, C. Sealing, D. Keir, A. Ayele, J. Blundy, J. Hamlyn, T. Wright, and S. Berhe (2015), First recorded eruption of Nabro volcano, Eritrea, 2011, *Bulletin of Volcanology*, *77*(10), 85.

Goldstein, M. R., and L. C. Werner (1998), Radar interferogram filtering for geophysical applications, *Geophysical Research Letters*, *25*(21), 4035–4038.

González, P., R. Walters, E. Hatton, K. Spaans, A. McDougall, A. Hooper, and T. Wright (2016), LiCSAR: Tools for automated generation of Sentinel-1 frame interferograms, *AGU Fall Meeting*.

González, P. J., M. Bagnardi, A. J. Hooper, Y. Larsen, P. Marinkovic, S. V. Samsonov, and T. J. Wright (2015), The 2014-2015 eruption of Fogo volcano: Geodetic modeling of Sentinel-1 TOPS interferometry, *Geophysical Research Letters*, *42*(21), 9239–9246.

Gottsmann, J., and H. Odbert (2014), The effects of thermomechanical heterogeneities in island arc crust on time-dependent preeruptive stresses and the failure of an andesitic reservoir, *Journal of Geophysical Research: Solid Earth*, *119*(6), 4626–4639.

Grandin, R., A. Socquet, R. Binet, Y. Klinger, E. Jacques, J. B. De Chabalier, G. C. King, C. Lasserre, S. Tait, P. Tapponnier, A. Delorme, and P. Pinzuti (2009), September 2005 Manda hararo-dabbahu rifting event, Afar (Ethiopia): Constraints provided by geodetic data, *Journal of Geophysical Research: Solid Earth*, *114*(8), B08,404.

Greenfield, T., and R. S. White (2015), Building icelandic igneous crust by repeated melt injections, *Journal of Geophysical Research B: Solid Earth*, *120*(11), 7771–7788.

Gregg, P. M., S. L. De Silva, E. B. Grosfils, and J. P. Parmigiani (2012), Catastrophic caldera-forming eruptions: Thermomechanics and implications for eruption triggering and maximum caldera dimensions on Earth, *Journal of Volcanology and Geothermal Research*, *241-242*, 1–12.

Gudmundsson, A. (1990), Emplacement of dikes, sills and crustal magma chambers at divergent plate boundaries, *Tectonophysics*, *176*(3-4), 257–275.

Gudmundsson, A. (2011), Deflection of dykes into sills at discontinuities and magma-chamber formation, *Tectonophysics*, *500*(1-4), 50–64.

Gudmundsson, A. (2012), Magma chambers: Formation, local stresses, excess pressures, and compartments, *Journal of Volcanology and Geothermal Research*, *237-238*, 19–41.

Gudmundsson, A., and K. Nilsen (2006), Ring-faults in composite volcanoes: structures, models and stress fields associated with their formation, *Geological Society, London, Special Publications*, *269*, 83–108.

Gwavava, O., C. Swain, F. Podmore, and J. Fairhead (1992), Evidence of crustal thinning beneath the Limpopo Belt and Lebombo monocline of southern Africa based on regional gravity studies and implications for the reconstruction of Gondwana, *Tectonophysics*, *212*(1-2), 1–20.

Hamling, I. J., A. Ayele, L. Bennati Laura, E. Calais, C. J. Ebinger, D. Keir, E. Lewi, T. J. Wright, and G. Yirgu (2009), Geodetic observations of the ongoing

Dabbahu rifting episode: New dyke intrusions in 2006 and 2007, *Geophysical Journal International*, *178*(2), 989–1003.

Hamling, I. J., T. J. Wright, E. Calais, L. Bennati, and E. Lewi (2010), Stress transfer between thirteen successive dyke intrusions in Ethiopia Stress transfer from a large earthquake may trigger subsequent earthquakes in nearby regions, *Nature Geoscience*, *3*.

Hamling, I. J., C. A. Williams, and S. Hreinsdóttir (2016), Depressurization of a hydrothermal system following the August and November 2012 Te Maari eruptions of Tongariro, New Zealand, *Geophysical Research Letters*, *43*(1), 168–175.

Hamling, I. J., S. Hreinsdóttir, K. Clark, J. Elliott, C. Liang, E. Fielding, N. Litchfield, P. Villamor, L. Wallace, T. J. Wright, E. D'Anastasio, S. Bannister, D. Burbidge, P. Denys, P. Gentle, J. Howarth, C. Mueller, N. Palmer, C. Pearson, W. Power, P. Barnes, D. J. Barrell, R. Van Dissen, R. Langridge, T. Little, A. Nicol, J. Pettinga, J. Rowland, and M. Stirling (2017), Complex multifault rupture during the 2016 Mw 7.8 Kaikoura earthquake, New Zealand, *Science*, *356*(6334).

Hammond, J. O., J. M. Kendall, G. W. Stuart, D. Keir, C. Ebinger, A. Ayele, and M. Belachew (2011), The nature of the crust beneath the Afar triple junction: Evidence from receiver functions, *Geochemistry, Geophysics, Geosystems*, *12*(12).

Hampel, A., and R. Hetzel (2006), Response of normal faults to glacial - interglacial fluctuations of ice and water masses on Earth's surface, *Journal of Geophysical Research*, *111*.

Hastings, W. (1970), Monte Carlo sampling methods using Markov chains and their applications, *Biometrika*, *57*(1), 97–109.

Heise, W., T. G. Caldwell, H. M. Bibby, and S. L. Bennie (2010), Three-dimensional electrical resistivity image of magma beneath an active continental rift, Taupo Volcanic Zone, New Zealand, *Geophysical Research Letters*, *37*(10).

Helmstetter, A., and B. E. Shaw (2006), Relation between stress heterogeneity and aftershock rate in the rate-and-state model, *Journal of Geophysical Research*, *111*(B7).

Helmstetter, A., and B. E. Shaw (2009), Afterslip and aftershocks in the rate-and-state friction law, *J. Geophys. Res*, *114*.

Henderson, S. T., and M. E. Pritchard (2017), Time-dependent deformation of Uturuncu volcano, Bolivia, constrained by GPS and InSAR measurements and implications for source models, *Geosphere*, *13*(6), 1834–1854.

Hendrie, D., N. Kusznir, C. Morley, and C. Ebinger (1994), Cenozoic extension in northern Kenya: a quantitative model of rift basin development in the Turkana region, *Tectonophysics*, *236*(1-4), 409–438.

Herring, T., B. King, and S. McClusky (2010), Introduction to GAMIT/GLOBK Reference manual Global Kalman filter VLBI and GPS analysis program. Release 10.3. EAPS.

Hickey, J., J. Gottsmann, and R. Del Potro (2013), The large-scale surface uplift in the Altiplano-Puna region of Bolivia: A parametric study of source characteristics and crustal rheology using finite element analysis, *Geochemistry, Geophysics, Geosystems*, *14*(3), 540–555.

Hickey, J., J. Gottsmann, H. Nakamichi, and M. Iguchi (2016), Thermomechanical

controls on magma supply and volcanic deformation: application to Aira caldera, Japan., *Scientific reports*, *6*, 32,691.

Hodge, M., J. Biggs, K. Goda, and W. Aspinall (2015), Assessing infrequent large earthquakes using geomorphology and geodesy: the Malawi Rift, *Natural Hazards*, *76*(3), 1781–1806.

Hodge, M., J. Biggs, A. Fagereng, and H. Mdala (2018a), Controls on early-rift geometry: new perspectives from the Bilila-Mtakataka fault, Malawi, *Geophysical Research Letters*.

Hodge, M., Fagereng, and J. Biggs (2018b), The Role of Coseismic Coulomb Stress Changes in Shaping the Hard Link Between Normal Fault Segments, *Journal of Geophysical Research: Solid Earth*, *123*(1), 797–814.

Hodgson, I., F. Illsley-Kemp, R. J. Gallacher, D. Keir, C. J. Ebinger, and K. Mtelela (2017), Crustal Structure at a Young Continental Rift: A Receiver Function Study From the Tanganyika Rift, *Tectonics*, *36*(12), 2806–2822.

Holdsworth, R. E., C. A. Butler, and A. M. Roberts (1997), The recognition of reactivation during continental deformation, *Journal of the Geological Society*, *154*(2), 73–78.

Holohan, E. P., V. R. Troll, T. R. Walter, S. M, S. Mcdonnell, and Z. K. Shipton (2005), Elliptical calderas in active tectonic settings: an experimental approach, *Journal of Volcanology and Geothermal Research*, *144*, 119–136.

Holohan, E. P., B. Van Wyk de Vries, and V. R. Troll (2008), Analogue models of caldera collapse in strike-slip tectonic regimes, *Bulletin of Volcanology*, *70*(7), 773–796.

Hooper, A., H. Zebker, P. Segall, and B. Kampes (2004), A new method for measuring deformation on volcanoes and other natural terrains using InSAR persistent scatterers, *Geophysical Research Letters*, *31*(23), 1–5.

Hooper, A., J. Pietrzak, W. Simons, H. Cui, R. Riva, M. Naeije, A. Terwisscha van Scheltinga, E. Schrama, G. Stelling, and A. Socquet (2013), Importance of horizontal seafloor motion on tsunami height for the 2011 Mw=9.0 Tohoku-Oki earthquake, *Earth and Planetary Science Letters*, *361*, 469–479.

Hsu, Y.-J., M. Simons, J.-P. Avouac, J. Galetzka, Kerry Sieh, M. Chlieh, D. Natawidjaja, L. Prawirodirdjo, and Y. Bock (2006), Frictional Afterslip Following the 2005 Nias-Simeulue Earthquake, Sumatra, *Science*, *312*(5782), 1918–1921.

Hunt, J. A., A. Zafu, T. A. Mather, D. M. Pyle, and P. H. Barry (2017), Spatially Variable CO2 Degassing in the Main Ethiopian Rift: Implications for Magma Storage, Volatile Transport, and Rift-Related Emissions, *Geochemistry, Geophysics, Geosystems*, *18*(10), 3714–3737.

Hurd, O., and M. D. Zoback (2012), Regional Stress Orientations and Slip Compatibility of Earthquake Focal Planes in the New Madrid Seismic Zone, *Seismological Research Letters*, *83*(4), 672–679.

Hutchison, W., T. a. Mather, D. M. Pyle, J. Biggs, and G. Yirgu (2015a), Structural controls on fluid pathways in an active rift system: A case study of the Aluto volcanic complex, *Geosphere*, (3), 1–21.

Hutchison, W., D. M. Pyle, T. A. Mather, G. Yirgu, J. Biggs, B. E. Cohen, D. Barfod, and E. Lewi (2015b), The eruptive history and magmatic evolution of Aluto volcano:

new insights into silicic peralkaline volcanism in the Ethiopian rift, *Journal of Volcanology and Geothermal Research*, pp. 1–82.

Hutchison, W., R. Fusillo, D. M. Pyle, T. A. Mather, J. D. Blundy, J. Biggs, G. Yirgu, B. E. Cohen, R. A. Brooker, D. N. Barfod, and A. T. Calvert (2016), A pulse of mid-Pleistocene rift volcanism in Ethiopia at the dawn of modern humans, *Nature Communications*, *7*, 13,192.

Hutchison, W., T. A. Mather, D. M. Pyle, A. J. Boyce, M. L. Gleeson, G. Yirgu, J. D. Blundy, D. J. Ferguson, C. Vye-Brown, I. L. Millar, K. W. Sims, and A. A. Finch (2018), The evolution of magma during continental rifting: New constraints from the isotopic and trace element signatures of silicic magmas from Ethiopian volcanoes, *Earth and Planetary Science Letters*, *489*, 203–218.

Igarashi, T., T. Matsuzawa, and A. Hasegawa (2003), Repeating earthquakes and interplate aseismic slip in the northeastern Japan subduction zone, *Journal of Geophysical Research: Solid Earth*, *108*(B5).

Ingleby, T., and T. J. Wright (2017), Omori-like decay of postseismic velocities following continental earthquakes, *Geophysical Research Letters*, *44*(7), 3119–3130.

Jackson, J., and T. Blenkinsop (1993), THE Malaŵi Earthquake of March 10, 1989: DEep faulting within the East African Rift System, *Tectonics*, *12*(5), 1131–1139.

Jackson, J., and T. Blenkinsop (1997), The Bilila-Mtakataka fault in Malawi: an active, 100-km long, normal fault segment in thick seismogenic crust, *Tectonics*, *16*(1), 137–150.

Jain, S. K., C. V. R. Murty, and N. Chandak (1994), The September 29, 1993, M6. 4 Killari, Maharashtra Earthquake in Central India, *EERI Special earthquake report, EERI Newsletter*, *28*(1), 8.

Jay, J., M. Welch, M. Pritchard, P. b. Mares, M. c. Mnich, A. Melkonian, F. Aguilera, J. Naranjo, M. Sunagua, and J. Clavero (2013), Volcanic hotspots of the central and southern andes as seen from space by ASTER and MODVOLC between the years 2000 and 2010, *Geological Society Special Publication*, *380*(1), 161–185.

Jeffreys, H. (1935), Some Tests of Significance, Treated by the Theory of Probability, *Mathematical Proceedings of the Cambridge Philosophical Society*, *31*(02), 203.

Jellinek, A. M., and D. J. DePaolo (2003), A model for the origin of large silicic magma chambers: Precursors of caldera-forming eruptions, *Bulletin of Volcanology*, *65*(5), 363–381.

Jolivet, R., R. Grandin, C. Lasserre, M. P. Doin, and G. Peltzer (2011), Systematic InSAR tropospheric phase delay corrections from global meteorological reanalysis data, *Geophysical Research Letters*, *38*(17).

Jonsson, S., H. Zebker, P. Segall, and F. Amelung (2002), Fault Slip Distribution of the 1999 Mw 7.1 Hector Mine, California, Earthquake, Estimated from Satellite Radar and GPS Measurements, *Bulletin of the Seismological Society of America*, *92*(4), 1377–1389.

Jourdan, F., G. Féraud, H. Bertrand, M. K. Watkeys, A. B. Kampunzu, and B. Le Gall (2006), Basement control on dyke distribution in Large Igneous Provinces: Case study of the Karoo triple junction, *Earth and Planetary Science Letters*, *241*(1-2), 307–322.

Karakas, O., and J. Dufek (2015), Melt evolution and residence in extending crust:

Thermal modeling of the crust and crustal magmas, *Earth and Planetary Science Letters*, *425*, 131–144.

Karakas, O., W. Degruyter, O. Bachmann, and J. Dufek (2017), Lifetime and size of shallow magma bodies controlled by crustal-scale magmatism, *Nature Geoscience*, *10*(6), 446–450.

Kass, R. E., and A. E. Raftery (2008), Bayes Factors, *Journal of the American Statistical Association*, *90*(430), 773–795.

Keir, D., J. M. Kendall, C. J. Ebinger, and G. W. Stuart (2005), Variations in late syn-rift melt alignment inferred from shear-wave splitting in crustal earthquakes beneath the Ethiopian rift, *Geophysical Research Letters*, *32*(23), 1–4.

Keir, D., C. J. Ebinger, G. W. Stuart, E. Daly, and A. Ayele (2006), Strain accommodation by magmatism and faulting as rifting proceeds to breakup: Seismicity of the northern Ethiopian rift, *Journal of Geophysical Research*, *111*(B5).

Keir, D., I. D. Bastow, K. a. Whaler, E. Daly, D. G. Cornwell, and S. Hautot (2009), Lower crustal earthquakes near the Ethiopian rift induced by magmatic processes, *Geochemistry, Geophysics, Geosystems*, *10*(6).

Keir, D., C. Pagli, I. D. Bastow, and A. Ayele (2011), The magma-assisted removal of Arabia in Afar: Evidence from dike injection in the Ethiopian rift captured using InSAR and seismicity, *Tectonics*, *30*.

Kendall, J.-M., and C. Lithgow-Bertelloni (2016), Why is Africa rifting?, *Geological Society, London, Special Publications*, *420*, SP420.17.

Kendall, J.-M., G. W. Stuart, C. J. Ebinger, I. D. Bastow, and D. Keir (2005), Magma-assisted rifting in Ethiopia., *Nature*, *433*(7022), 146–8.

Kendall, J.-M., S. Pilidou, D. Keir, I. Bastow, G. Stuart, and A. Ayele (2006), Mantle upwellings, melt migration and the rifting of Africa: insights from seismic anisotropy, *Geological Society, London, Special Publications*, *259*(1), 55–72.

Keranen, K., and S. Klemperer (2008), Discontinuous and diachronous evolution of the Main Ethiopian Rift: Implications for development of continental rifts, *Earth and Planetary Science Letters*, *265*(1-2), 96–111.

Keranen, K., S. Klemperer, and R. Gloaguen (2004), Three-dimensional seismic imaging of a protoridge axis in the Main Ethiopian rift, *Geology*, *32*(11), 949.

Kinabo, B. D., E. A. Atekwana, J. P. Hogan, M. P. Modisi, D. D. Wheaton, and A. B. Kampunzu (2007), Early structural development of the Okavango rift zone, NW Botswana, *Journal of African Earth Sciences*, *48*(2-3), 125–136.

Kinabo, B. D., J. P. Hogan, E. A. Atekwana, M. G. Abdelsalam, and M. P. Modisi (2008), Fault growth and propagation during incipient continental rifting: Insight from a combined aeromagnetic and Shuttle Radar Topography Mission digital elevation model investigation of the Okavango Rift Zone, northwest Botswana, *Tectonics*, *27*(3).

King, G. C. P., R. S. Stein, and J. Lin (1994), Static stress changes and the triggering of earthquakes, *International Journal of Rock Mechanics and Mining Sciences & Geomechanics Abstracts*, *32*(2), A50–A51.

Kisslinger, C., and L. M. Jones (1991), Properties of aftershock sequences in southern California, *Journal of Geophysical Research*, *96*(B7), 11,947.

Kolawole, F., E. A. Atekwana, S. Malloy, D. S. Stamps, R. Grandin, M. G. Abdelsalam, K. Leseane, and E. M. Shemang (2017), Aeromagnetic, gravity, and Differential Interferometric Synthetic Aperture Radar analyses reveal the causative fault of the 3 April 2017 M w 6.5 Moiyabana, Botswana, earthquake, *Geophysical Research Letters*, *44*(17), 8837–8846.

Kolawole, F., E. A. Atekwana, D. A. Laó-Dávila, M. G. Abdelsalam, P. R. Chindandali, J. Salima, and L. Kalindekafe (2018), Active deformation of Malawi Rift's North Basin hinge zone modulated by reactivation of pre-existing Precambrian shear zone fabric, *Tectonics*.

Koptev, A., E. Calais, E. Burov, S. Leroy, and T. Gerya (2015), Dual continental rift systems generated by plume-lithosphere interaction, *Nature Geoscience*, *8*(5), 388–392.

Korme, T., J. Chorowicz, B. Collet, and F. F. Bonavia (1997), Volcanic vents rooted on extension fractures and their geodynamic implications in the Ethiopian Rift, *Journal of Volcanology and Geothermal Research*, *79*(3-4), 205–222.

Korme, T., V. Acocella, and B. Abebe (2004), The Role of Pre-existing Structures in the Origin, Propagation and Architecture of Faults in the Main Ethiopian Rift, *Gondwana Research*, *7*(2), 467–479.

Kreemer, C., G. Blewitt, and E. C. Klein (2014), A geodetic plate motion and Global Strain Rate Model, *Geochemistry, Geophysics, Geosystems*, *15*(10), 3849–3889.

KRISP Working Party (1991), Large-scale variation in lithospheric structure along and across the Kenya rift, *Nature*, *354*(6350), 223–227.

Kroner, A. (1982), Rb/Sr geochronology and tectonic evolution of the Pan-African Damara Belt of Namibia, southwestern Africa., *American Journal of Science*, *282*(9), 1471–1507.

Lanari, R., P. Lundgren, M. Manzo, and F. Casu (2004), Satellite radar interferometry time series analysis of surface deformation for Los Angeles, California, *Geophysical Research Letters*, *31*(12), 2–6.

Laó-Dávila, D. A., H. S. Al-Salmi, M. G. Abdelsalam, and E. A. Atekwana (2015), Hierarchical segmentation of the Malawi Rift: The influence of inherited lithospheric heterogeneity and kinematics in the evolution of continental rifts, *Tectonics*, *34*(12), 2399–2417.

Last, R. J., A. A. Nyblade, C. A. Langston, and T. J. Owens (1997), functions and Rayleigh wave phase velocities, *Journal of Geophysical Research: Solid Earth*, *102*(B11), 469–483.

Le Corvec, N., K. B. Spörli, J. Rowland, and J. Lindsay (2013), Spatial distribution and alignments of volcanic centers: Clues to the formation of monogenetic volcanic fields, *Earth-Science Reviews*, *124*, 96–114.

Le Gall, B., G. Tshoso, F. Jourdan, G. Féraud, H. Bertrand, J. J. Tiercelin, A. B. Kampunzu, and M. P. Modisi (2002), 40Ar/39Ar geochronology and structural data from the giant Okavango and related mafic dyke swarms, Karoo Igneous province, Northern Botswana, *Earth and Planetary Science Letters*, *202*(3-4), 595–606.

Le Gall, B., P. Nonnotte, J. Rolet, M. Benoit, H. Guillou, M. Mousseau-Nonnotte, J. Albaric, and J. Deverchère (2008), Rift propagation at craton margin. Distribution of faulting and volcanism in the North Tanzanian Divergence (East Africa) during

Neogene times, *Tectonophysics*, *448*(1-4), 1–19.

Le Mével, H., K. L. Feigl, L. Cõrdova, C. DeMets, and P. Lundgren (2015), Evolution of unrest at Laguna del Maule volcanic field (Chile) from InSAR and GPS measurements, 2003 to 2014, *Geophysical Research Letters*, *42*(16), 6590–6598.

Lenardic, A., L. Moresi, and H. Mühlhaus (2000), The role of mobile belts for the longevity of deep cratonic lithosphere: The crumple zone model, *Geophysical Research Letters*, *27*(8), 1235–1238.

Leonard, M. (2010), Earthquake fault scaling: Self-consistent relating of rupture length, width, average displacement, and moment release, *Bulletin of the Seismological Society of America*, *100*(5 A), 1971–1988.

Leprince, S., J. Avouac, and F. Ayoub (2007), Ortho-rectification, coregistration, and subpixel correlation of optical satellite and aerial images, *IEEE Trans. Geosci. Remote Sens.*, *45*(1529-1558).

Leprince, S., P. Musé, and J. P. Avouac (2008), In-flight CCD distortion calibration for pushbroom satellites based on subpixel correlation, *IEEE Transactions on Geoscience and Remote Sensing*, *46*(9), 2675–2683.

Li, Z., E. Fielding, and P. Cross (2009), Integration of InSAR Time-Series Analysis and Water-Vapor Correction for Mapping Postseismic Motion After the 2003 Bam (Iran) Earthquake, *IEEE Transactions on Geoscience and Remote Sensing*, *47*(9), 3220–3230.

Lin, J., and R. S. Stein (2004), Stress triggering in thrust and subduction earthquakes and stress interaction between the southern San Andreas and nearby thrust and strike-slip faults, *Journal of Geophysical Research: Solid Earth*, *109*(B2).

Lipman, P., J. Moore, and D. Swanson (1981), 1981 bulging of the north flank before the May 18 eruption: geodetic data, *US Geol. Surv. Prof. Pap.*, *1250*, 143–156.

Lipman, P. W. (1997), Subsidence of ash-flow calderas: relation to caldera size and magma-chamber geometry, *Bulletin of Volcanology*, *59*(3), 198–218.

Lloyd, R., J. Biggs, M. Wilks, A. Nowacki, J. Michael Kendall, A. Ayele, E. Lewi, and H. Eysteinsson (2018), Evidence for cross rift structural controls on deformation and seismicity at a continental rift caldera, *Earth and Planetary Science Letters*, *487*(C), 190–200.

Lomax, A., J. Virieux, P. Volant, and C. Berge-Thierry (2000), Probabilistic Earthquake Location in 3D and Layered Models, in *Advances in Seismic Event Location*, chap. 18, pp. 101–134, Springer Netherlands, Dordrecht.

López-Querol, S., M. R. Coop, J. J. Bommer, C. Fenton, and W. W. Sim (2007), Back-analysis of liquefaction in the 2006 Mozambique earthquake, *Georisk: Assessment and Management of Risk for Engineered Systems and Geohazards*, *1*(2), 89–101.

Lu, Z., J. A. Power, V. S. McConnell, C. Wicks, and D. Dzurisin (2002), Preeruptive inflation and surface interferometric coherence characteristics revealed by satellite radar interferometry at Makushin Volcano, Alaska: 1993-2000, *Journal of Geophysical Research: Solid Earth*, *107*(B11).

Lu, Z., D. Dzurisin, J. Biggs, C. Wicks, and S. McNutt (2010), Ground surface deformation patterns, magma supply, and magma storage at Okmok volcano, Alaska, from InSAR analysis: 1. Intereruption deformation, 19970-2008, *Journal of*

Geophysical Research: Solid Earth, *115*(5).

Maccaferri, F., E. Rivalta, D. Keir, and V. Acocella (2014), Off-rift volcanism in rift zones determined by crustal unloading, *Nature Geoscience*, *7*(4), 297–300.

Maccaferri, F., V. Acocella, and E. Rivalta (2015), How the differential load induced by normal fault scarps controls the distribution of monogenic volcanism, *Geophysical Research Letters*, *42*(18), 7507–7512.

Mackenzie, G. D., H. Thybo, and P. K. H. Maguire (2005), Crustal velocity structure across the Main Ethiopian Rift: results from two-dimensional wide-angle seismic modelling, *Geophysical Journal International*, *162*(3), 994–1006.

Maguire, P., G. Keller, S. Klemperer, G. Mackenzie, K. Keranen, S. Harder, B. O'Reilly, H. Thybo, L. Asfaw, M. Khan, and M. Amha (2006), Crustal structure of the northern Main Ethiopian Rift from the EAGLE controlled-source survey; a snapshot of incipient lithospheric break-up, *Geological Society, London, Special Publications*, *259*(1), 269–292.

Marti, J., and A. Gudmundsson (2000), The Las Cañadas caldera (Tenerife, Canary Islands): an overlapping collapse caldera generated by magma-chamber migration, *Journal of Volcanology and Geothermal Research*, *103*(1), 161–173.

Martin - Jones, C. M., C. S. Lane, N. J. G Pearce, V. C. Smith, H. F. Lamb, F. Schaebitz, M. C. Brown, U. Frank, and A. Asrat (2017), Recurrent explosive eruptions from a high - risk Main Ethiopian Rift volcano throughout the Holocene, *Geology*, *45*(12), 1127–1130.

Maslin, M. A., C. M. Brierley, A. M. Milner, S. Shultz, M. H. Trauth, and K. E. Wilson (2014), East african climate pulses and early human evolution, *Quaternary Science Reviews*, *101*, 1–17.

Massonnet, D., and K. L. Feigl (1995), Discrimination of geophysical phenomena in satellite radar interferograms, *Geophysical Research Letters*, *22*(12), 1537–1540.

Massonnet, D., and K. L. Feigl (1998), Radar Interferometry and its Application to Changes in the Earth's Surface, *Reviews of Geophysics*, *4*(36), 441–500.

Massonnet, D., M. Rossi, C. Carmona, F. Adragna, G. Peltzer, K. Feigl, and T. Rabaute (1993), The displacement field of the Landers earthquake mapped by radar interferometry, *Nature*, *364*(6433), 138–142.

Massonnet, D., P. Briole, and A. Arnaud (1995), Deflation of Mount Etna monitored by spaceborne radar interferometry, *Nature*, *375*(6532), 567–570.

Masterlark, T. (2007), Magma intrusion and deformation predictions: Sensitivities to the Mogi assumptions, *Journal of Geophysical Research: Solid Earth*, *112*(6), B06,419.

Mazzarini, F., G. Corti, P. Manetti, and F. Innocenti (2004), Strain rate and bimodal volcanism in the continental rift: Debre Zeyt volcanic field, northern MER, Ethiopia, *Journal of African Earth Sciences*, *39*(3), 415–420.

Mazzarini, F., T. O. Rooney, and I. Isola (2013), The intimate relationship between strain and magmatism: A numerical treatment of clustered monogenetic fields in the Main Ethiopian Rift, *Tectonics*, *32*(1), 49–64.

McCaffrey, R., and G. Abers (1988), SYN3: a program for inversion of teleseismic waveforms on microcomputers, Air Force Geophysics Laboratory Technical Report AFGL-TR-0099, Technical report, Hanscom Air Force Base, MA., *Tech. rep.*

McCaffrey, R., P. Zwick, and G. Abers (1991), SYN4 program, *IASPEI Software Library*, *3*, 81–166.

McConnell, R. B. (1972), Geological Development of the Rift System of Eastern Africa, *Geological Society of America Bulletin*, *83*(9), 2549–2572.

McKenzie, D. (1969), The relation between fault plane solution for earthquakes.

Mckenzie, D., and M. J. Bickle (1988), The volume and composition of melt generated by extension of the lithosphere, *Journal of Petrology*, *29*(3), 625–679.

McTigue, D. F. (1987), Elastic stress and deformation near a finite spherical magma body: Resolution of the point source paradox, *Journal of Geophysical Research*, *92*(B12), 12,931.

Menand, T., C. Annen, and M. d. S. Blanquat (2015), Rates of magma transfer in the crust: Insights into magma reservoir recharge and pluton growth, *Geology*, *43*(3), 199–202.

Milani, E. J., and I. Davison (1988), Basement control and transfer tectonics in the Recôncavo-Tucano-Jatobá rift, Northeast Brazil, *Tectonophysics*, *154*(1-2), 41–70.

Miller, C. A., H. Le Mével, G. Currenti, G. Williams-Jones, and B. Tikoff (2017), Microgravity changes at the Laguna del Maule volcanic field: Magma-induced stress changes facilitate mass addition, *Journal of Geophysical Research: Solid Earth*, *122*(4), 3179–3196.

Miyazaki, S., P. Segall, J. Fukuda, and T. Kato (2004), Space time distribution of afterslip following the 2003 Tokachi-oki earthquake: Implications for variations in fault zone frictional properties, *Geophysical Research Letters*, *31*(6).

Modisi, M., E. Atekwana, A. Kampunzu, and T. Ngwisanyi (2000), Rift kinematics during the incipient stages of continental extension: Evidence from the nascent Okavango rift basin, northwest Botswana, *Geology*, *28*(10), 939.

Modisi, M. P. (2000), Fault system at the southeastern boundary of the Okavango Rift, Botswana, *Pergamon Journal of African Earth Sciences*, *30*(3), 569–578.

Mogi, K. (1958), Relations between the eruptions of various volcanoes and the deformations of the ground surfaces around them, *Bulletin of the Earthquake Research Institute*, *36*, 99–134.

Mohr, P., and C. Wood (1976), Volcano spacings and lithospheric attenuation in the Eastern Rift of Africa, *Earth and Planetary Science Letters*, *33*(1), 126–144.

Mohr, P. A. (1967), Major Volcano-Tectonic Lineament in the Ethiopian Rift System, *Nature*, pp. 664–665.

Mohr, P. A. (1968), Transcurrent Faulting in the Ethiopian Rift, *Nature*, *218*, 938–940.

Moreno, M., M. Rosenau, and O. Oncken (2010), 2010 Maule earthquake slip correlates with pre-seismic locking of Andean subduction zone, *Nature*, *467*(7312), 198–202.

Morley, C. K., W. A. Wescott, D. M. Stone, R. M. Harper, S. T. Wigger, and F. M. Karanja (1992), Tectonic evolution of the northern Kenyan Rift, *Journal of the Geological Society*, *149*(3), 333–348.

Mosegaard, K., and A. Tarantola (1995), Monte Carlo sampling of solutions to inverse problems, *Journal of Geophysical Research: Solid Earth*, *100*(B7), 12,431–12,447.

Mosley Bufford, K., E. A. Atekwana, M. G. Abdelsalam, E. Shemang, E. A. Atekwana, K. Mickus, M. Moidaki, M. P. Modisi, and L. Molwalefhe (2012), Geometry and faults tectonic activity of the Okavango Rift Zone, Botswana: Evidence from magnetotelluric and electrical resistivity tomography imaging, *Journal of African Earth Sciences*, *65*, 61–71.

Muirhead, J. D., and S. A. Kattenhorn (2018), Activation of preexisting transverse structures in an evolving magmatic rift in East Africa, *Journal of Structural Geology*, *106*, 1–18.

Muirhead, J. D., S. A. Kattenhorn, and N. Le Corvec (2015), Varying styles of magmatic strain accommodation across the East African Rift, *Geochemistry, Geophysics, Geosystems*, *16*(8), 2775–2795.

Muluneh, A. A., M. Cuffaro, and C. Doglioni (2014), Tectonophysics Left-lateral transtension along the Ethiopian Rift and constrains on the mantle-reference plate motions, *Tectonophysics*, *632*, 21–31.

Neave, D. A., G. Fabbro, R. A. Herd, C. M. Petrone, and M. Edmonds (2012), Melting, differentiation and degassing at the pantelleria volcano, Italy, *Journal of Petrology*, *53*(3), 637–663.

Newman, A. V., T. H. Dixon, G. I. Ofoegbu, and J. E. Dixon (2001), Geodetic and seismic constraints on recent activity at Long Valley Caldera, California: Evidence for viscoelastic rheology, *Journal of Volcanology and Geothermal Research*, *105*(3), 183–206.

Nguuri, T. K., J. Gore, D. E. James, S. J. Webb, C. Wright, T. G. Zengeni, O. Gwavava, and J. A. Snoke (2001), Crustal structure beneath southern Africa and its implications for the formation and evolution of the Kaapvaal and Zimbabwe cratons, *Geophysical Research Letters*, *28*(13), 2501–2504.

Nicol, A., J. J. Walsh, P. Villamor, H. Seebeck, and K. R. Berryman (2010), Normal fault interactions, paleoearthquakes and growth in an active rift, *Journal of Structural Geology*, *32*(8), 1101–1113.

Nobile, A., C. Pagli, D. Keir, T. J. Wright, A. Ayele, J. Ruch, and V. Acocella (2012), Dike-fault interaction during the 2004 Dallol intrusion at the northern edge of the Erta Ale Ridge (Afar, Ethiopia), *Geophysical Research Letters*, *39*(19).

Nostro, C., L. Chiaraluce, M. Cocco, D. Baumont, and O. Scotti (2005), Coulomb stress changes caused by repeated normal faulting earthquakes during the 1997 Umbria-Marche (central Italy) seismic sequence, *Journal of Geophysical Research: Solid Earth*, *110*(5), 1–19.

Nowacki, A., M. Wilks, J. M. Kendall, J. Biggs, and A. Ayele (2018), Characterising hydrothermal fluid pathways beneath Aluto volcano, Main Ethiopian Rift, using shear wave splitting, *Journal of Volcanology and Geothermal Research*.

Nur, A., and J. Booker (1972), Aftershocks caused by pore fluid flow?, *Science*, *175*(4024), 885–887.

Nyblade, A. A., and C. A. Langston (1995), East-African Earthquakes Below 20-Km Depth and Their Implications for Crustal Structure, *Geophysical Journal International*, *121*(1), 49–62.

Okada, Y. (1985), Surface deformation due to shear and tensile faults in a half-space, *International Journal of Rock Mechanics and Mining Sciences Geomechanics*

Abstracts, *75*(4), 1135–1154.

Omori, F. (1894), On after-shocks of earthquakes, *J. Coll. Sci. Imp. Univ. Tokyo*, *7*, 111–200.

Pagli, C., T. J. Wright, C. J. Ebinger, S.-H. Yun, J. R. Cann, T. Barnie, and A. Ayele (2012), Shallow axial magma chamber at the slow-spreading Erta Ale Ridge, *Nature Geoscience*, *5*(4), 284–288.

Pagli, C., H. Wang, T. J. Wright, E. Calais, and E. Lewi (2014), Current plate boundary deformation of the Afar rift from a 3-D velcoity field inversion of InSAR and GPS, *Journal of Geophysical Research: Solid Earth*, *119*(11), 8562–8575.

Pallister, J. S., W. A. McCausland, S. Jónsson, Z. Lu, H. M. Zahran, S. El Hadidy, A. Aburukbah, I. C. Stewart, P. R. Lundgren, R. A. White, and M. R. Moufti (2010), Broad accommodation of rift-related extension recorded by dyke intrusion in Saudi Arabia, *Nature Geoscience*, *3*(10), 705–712.

Park, J. W., N. Gourmelen, A. Shepherd, S. W. Kim, D. G. Vaughan, and D. J. Wingham (2013), Sustained retreat of the Pine Island Glacier, *Geophysical Research Letters*, *40*(10), 2137–2142.

Parker, A. L., J. Biggs, R. J. Walters, S. K. Ebmeier, T. J. Wright, N. A. Teanby, and Z. Lu (2015), Systematic assessment of atmospheric uncertainties for InSAR data at volcanic arcs using large-scale atmospheric models: Application to the Cascade volcanoes, United States, *Remote Sensing of Environment*, *170*, 102–114.

Parks, M. M., J. D. Moore, X. Papanikolaou, J. Biggs, T. A. Mather, D. M. Pyle, C. Raptakis, D. Paradissis, A. Hooper, B. Parsons, and P. Nomikou (2015), From quiescence to unrest: 20 years of satellite geodetic measurements at Santorini volcano, Greece, *Journal of Geophysical Research: Solid Earth*, *120*(2), 1309–1328.

Parsons, T., C. Ji, and E. Kirby (2008), Stress changes from the 2008 Wenchuan earthquake and increased hazard in the Sichuan basin, *Nature*, *454*(7203), 509–510.

Pastier, A. M., O. Dauteuil, M. Murray-Hudson, F. Moreau, A. Walpersdorf, and K. Makati (2017), Is the Okavango Delta the terminus of the East African Rift System? Towards a new geodynamic model: Geodetic study and geophysical review, *Tectonophysics*, *712-713*, 469–481.

Peccerillo, A. (2003), Relationships between Mafic and Peralkaline Silicic Magmatism in Continental Rift Settings: a Petrological, Geochemical and Isotopic Study of the Gedemsa Volcano, Central Ethiopian Rift, *Journal of Petrology*, *44*(11), 2003–2032.

Peccerillo, A., C. Donati, A. Santo, A. Orlando, G. Yirgu, and D. Ayalew (2007), Petrogenesis of silicic peralkaline rocks in the Ethiopian rift: Geochemical evidence and volcanological implications, *Journal of African Earth Sciences*, *48*(2-3), 161–173.

Pedersen, R., and F. Sigmundsson (2004), InSAR based sill model links spatially offset areas of deformation and seismicity for the 1994 unrest episode at Eyjafjallajökull volcano, Iceland, *Geophysical Research Letters*, *31*(14), L14,610.

Pedersen, R., S. Jónsson, T. Árnadóttir, F. Sigmundsson, and K. L. Feigl (2003), Fault slip distribution of two June 2000 MW6.5 earthquakes in South Iceland estimated from joint inversion of InSAR and GPS measurements, *Earth and Planetary Science Letters*, *213*(3-4), 487–502.

Perfettini, H., and J.-P. Avouac (2004), Postseismic relaxation driven by brittle creep:

A possible mechanism to reconcile geodetic measurements and the decay rate of aftershocks, application to the Chi-Chi earthquake, Taiwan, *Journal of Geophysical Research: Solid Earth*, *109*(B2).

Philippon, M., G. Corti, F. Sani, M. Bonini, M. L. Balestrieri, P. Molin, E. Willingshofer, D. Sokoutis, and S. Cloetingh (2014), Evolution, distribution, and characteristics of rifting in southern Ethiopia, *Tectonics*, *33*(4), 485–508.

Pinel, V., and C. Jaupart (2003), Magma chamber behavior beneath a volcanic edifice, *Journal of Geophysical Research*, *108*(B2), 1–17.

Pizzi, A., M. Coltorti, B. Abebe, L. Disperati, G. Sacchi, and R. Salvini (2006), The Wonji fault belt (Main Ethiopian Rift): structural and geomorphological constraints and GPS monitoring, *Geological Society, London, Special Publications*, *259*(1), 191–207.

Pouclet, A., H. Bellon, and K. Bram (2016), The Cenozoic volcanism in the Kivu rift: Assessment of the tectonic setting, geochemistry, and geochronology of the volcanic activity in the South-Kivu and Virunga regions, *Journal of African Earth Sciences*, *121*, 219–246.

Pritchard, M., S. de Silva, G. Michelfelder, G. Zandt, S. McNutt, J. Gottsmann, M. West, J. Blundy, D. Christensen, N. Finnegan, E. Minaya, R. Sparks, M. Sunagua, M. Unsworth, C. Alvizuri, M. Comeau, R. del Potro, D. Díaz, M. Diez, A. Farrell, S. Henderson, J. Jay, T. Lopez, D. Legrand, J. Naranjo, H. McFarlin, D. Muir, J. Perkins, Z. Spica, A. Wilder, and K. Ward (2018), Synthesis: PLUTONS: Investigating the relationship between pluton growth and volcanism in the Central Andes, *Geosphere*.

Pritchard, M. E., and M. Simons (2004), An InSAR-based survey of volcanic deformation in the southern Andes, *Geophysical Research Letters*, *31*(15).

Prodehl, C., J. Ritter, J. Mechie, G. Keller, M. Khan, B. Jacob, K. Fuchs, I. Nyambok, J. Obel, and D. Riaroh (1997), The KRISP 94 lithospheric investigation of southern Kenya - the experiments and their main results, *Tectonophysics*, *278*(1-4), 121–147.

Raftery, A. E., M. A. Newton, J. M. Satagopan, and P. N. Krivitsky (2007), Estimating the Integrated Likelihood via Posterior Simulation Using the Harmonic Mean Identity, *Bayesian Statistics*, (8), 1–45.

Ranganai, R. T., A. B. Kampunzu, E. A. Atekwana, B. K. Paya, J. G. King, D. I. Koosimile, and E. H. Stettler (2002), Gravity evidence for a larger Limpopo Belt in southern Africa and geodynamic implications, *Geophysical Journal International*, *149*(3), F9–F14.

Rapprich, I. V. (2013), Hawassa Subsheet - Explanatory Notes, *Tech. rep.*

Rapprich, V., V. Žáček, K. Verner, V. Erban, T. Goslar, Y. Bekele, F. Legesa, T. Hroch, and P. Hejtmánková (2016), Wendo Koshe Pumice: The latest Holocene silicic explosive eruption product of the Corbetti Volcanic System (Southern Ethiopia), *Journal of Volcanology and Geothermal Research*, *310*, 159–171.

Reeves, C. V., J. P. Teasdale, and E. S. Mahanjane (2016), Insight into the Eastern Margin of Africa from a new tectonic model of the Indian Ocean, *Geological Society, London, Special Publications*, *431*(1), 299–322.

Reid, F. H. (1910), The California Earthquake of April 18, 1906, *Report of the State Earthquake Investigation Commission*, *2*, 16–18.

Reilinger, R. E., S. Ergintav, R. Bürgmann, P. Segall, E. H. Hearn, S. McClusky, H. Woith, and J. Zschau (2000), Time-Dependent Distibuted Afterslip on and Deep below the Izmit Earthquake Rupture, *Bulletin of the Seismological Society of America*, *92*(1), 126–137.

Richardson, E., and T. H. Jordan (2002), Seismicity in deep gold mines of South Africa: Implications for tectonic earthquakes, *Bulletin of the Seismological Society of America*, *92*(5), 1766–1782.

Ring, U. (1994), The influence of preexisting structure on the evolution of the Cenozoic Malawi rift (East African rift system), *13*(2), 313–326.

Robertson, E. (2015), Magma storage and transport at Kenyan Rift Volcanoes: a remote sensing perspective, Ph.D. thesis, University of Bristol.

Robertson, E. A. M., J. Biggs, K. V. Cashman, M. Floyd, and C. Vye-Brown (2016), Influence of regional tectonics and pre-existing structures on the formation of elliptical calderas in the Kenyan Rift, *Geological Society, London, Special Publications*, *420*, SP420–12.

Roering, C., D. D. van Reenen, C. A. Smit, J. M. Barton, J. H. de Beer, M. J. de Wit, E. H. Stettler, J. F. van Schalkwyk, G. Stevens, and S. Pretorius (1992), Tectonic model for the evolution of the Limpopo Belt, *Precambrian Research*, *55*(1-4), 539–552.

Rogers, N., R. Macdonald, J. Fitton, R. George, M. Smith, and B. Barreiro (2000), Two mantle plumes beneath the East African rift system: Sr, Nd and Pb isotope evidence from Kenya Rift basalts, *Earth and Planetary Science Letters*, *176*(3-4), 387–400.

Roman, A., and C. Jaupart (2014), The impact of a volcanic edifice on intrusive and eruptive activity, *Earth and Planetary Science Letters*, *408*, 1–8.

Rooney, T. O. (2017), The Cenozoic magmatism of East-Africa: Part I - Flood basalts and pulsed magmatism, *Lithosphere*, *286-287*, 264–301.

Rosen, P. A., S. Hensley, G. Peltzer, and M. Simons (2004), Updated repeat orbit interferometry package released, *Eos, Transactions American Geophysical Union*, *85*(5), 47–47.

Rosen, P. A., E. M. Gurrola, G. Franco Sacco, and H. A. Zebker (2012), The InSAR Scientific Computing Environment, *Proceedings of the 9th European Conference on Synthetic Aperture Radar*, pp. 730–733.

Rosendahl, B. R., E. Kilembe, and K. Kaczmarick (1992), Comparison of the Tanganyika, Malawi, Rukwa and Turkana Rift zones from analyses of seismic reflection data, *Tectonophysics*, *213*(1-2), 235–256.

Rowland, J. V., and R. H. Sibson (2004), Structural controls on hydrothermal flow in a segmented rift system, Taupo Volcanic Zone, New Zealand, *Geofluids*, *4*(4), 259–283.

Salman, G., and I. Abdula (1995), Development of the Mozambique and Ruvuma sedimentary basins, offshore Mozambique, *Sedimentary Geology*, *96*, 7–41.

Samrock, F., A. Kuvshinov, J. Bakker, A. Jackson, and S. Fisseha (2015), 3-D analysis and interpretation of magnetotelluric data from the Aluto-Langano geothermal field, Ethiopia, *Geophysical Journal International*, *202*(3), 1923–1948.

Sangha, S., G. Peltzer, A. Zhang, L. Meng, C. Liang, P. Lundgren, and E. Fielding (2017), Fault geometry of 2015, Mw7.2 Murghab, Tajikistan earthquake controls

rupture propagation: Insights from InSAR and seismological data, *Earth and Planetary Science Letters*, *462*, 132–141.

Saria, E., E. Calais, D. S. Stamps, D. Delvaux, and C. J. H. Hartnady (2014), Present-day kinematics of the East African Rift, *Journal of Geophysical Research: Solid Earth*, *119*(4), 3584–3600.

Saunders, S. (2001), The shallow plumbing system of Rabaul caldera: a partially intruded ring fault?, *Bulletin of Volcanology*, *63*(6), 406–420.

Savage, J. C., and R. O. Burford (1973), Geodetic determination of relative plate motion in central California, *Journal of Geophysical Research*, *78*(5), 832–845.

Saxby, J., J. Gottsmann, K. Cashman, and E. Gutie (2016), Magma storage in a strike-slip caldera, *Nature communications*, *7*, 1–10.

Schilling, J. G. (1973), Iceland mantle plume: Geochemical study of Reykjanes Ridge, *Nature*, *242*(5400), 565–571.

Schilling, J.-G. (1991), Fluxes and excess temperatures of mantle plumes inferred from their interaction with migrating mid-ocean ridges, *Nature*, *352*(6334), 397–403.

Scholz, C. (2002), *The Mechanics of Earthquakes and Faulting*, 2nd ed., Cambridge University Press, Cambridge.

Scholz, C. H., and J. C. Contreras (1998), Mechanics of continental rift architecture, *Geology*, *26*(11), 967.

Scholz, C. H., and P. Cowie (1990), Determination of total strain from faulting using slip measurements, *Nature*, *346*(6287), 837.

Scholz, C. H., T. A. Koczynski, and D. G. Hutchins (1976), Evidence for Incipient Rifting in Southern Africa, *Geophysical Journal of the Royal Astronomical Society*, *44*(1), 135–144.

Scholz, C. H., C. Aviles, and S. Wesnousky (1986), Scaling differences between large intraplate and interplate earthquakes, *Bulletin of the Seismological Society of America*, *76*(1), 65–70.

Scholz, C. H., N. H. Dawers, J.-Z. Yu, M. H. Anders, and P. A. Cowie (1993), Fault growth and fault scaling laws: Preliminary results, *Journal of Geophysical Research: Solid Earth*, *98*(B12), 21,951–21,961.

Schöpa, A., and C. Annen (2013), The effects of magma flux variations on the formation and lifetime of large silicic magma chambers, *Journal of Geophysical Research: Solid Earth*, *118*(3), 926–942.

Seebeck, H., a. Nicol, T. Stern, H. Bibby, and V. Stagpoole (2010), Fault controls on the geometry and location of the Okataina Caldera, Taupo Volcanic Zone, New Zealand, *Journal of Volcanology and Geothermal Research*, *190*(1-2), 136–151.

Segall, P. (2005), *Earthquake and Volcano deformation*, 517 pp., Princeton University Press.

Sengör, A., O. Tüysüz, C. İmren, M. Sakinç, H. Eyidogan, N. Görür, X. Le Pichon, and C. Rangin (2005), The North Anatolian Fault: a new look, *Annual Review of Earth and Planetary Sciences*, *33*(1), 37–112.

Sibson, R. H. (1990), Rupture nucleation on unfavorably oriented faults, *Bulletin of the Seismological Society of America*, *80*(6), 1580–1604.

Siebert, L., T. Simkin, and P. Kimberly (2010), *Volcanoes of the World*, third edit ed., 568 pp pp., University of California Press, Berkeley.

Siegburg, M., T. M. Gernon, J. M. Bull, D. Keir, D. N. Barfod, R. N. Taylor, B. Abebe, and A. Ayele (2018), Geological evolution of the Boset-Bericha Volcanic Complex, Main Ethiopian Rift: 40Ar/39Ar evidence for episodic Pleistocene to Holocene volcanism, *Journal of Volcanology and Geothermal Research*, *351*, 115–133.

Sigmundsson, F., A. Hooper, S. Hreinsdóttir, K. S. Vogfjörd, B. G. Ófeigsson, E. R. Heimisson, S. Dumont, M. Parks, K. Spaans, G. B. Gudmundsson, V. Drouin, T. Árnadóttir, K. Jónsdóttir, M. T. Gudmundsson, T. Högnadóttir, H. M. Fridriksdóttir, M. Hensch, P. Einarsson, E. Magnússon, S. Samsonov, B. Brandsdóttir, R. S. White, T. Ágústsdóttir, T. Greenfield, R. G. Green, Á. R. Hjartardóttir, R. Pedersen, R. A. Bennett, H. Geirsson, P. C. la Femina, H. Björnsson, F. Pálsson, E. Sturkell, C. J. Bean, M. Möllhoff, A. K. Braiden, and E. P. Eibl (2014), Segmented lateral dyke growth in a rifting event at Bárdarbunga volcanic system, Iceland, *Nature*, *517*(7533), 191–195.

Silver, P. G., S. Gao, K. H. Liu, and K. S. Group (2001), Mantle deformation beneath southern Africa, *Geophysical re*, *28*(13), 2493–2496.

Simiyu, S. M. (2010), Status of Geothermal Exploration in Kenya and Future Plans for Its Development, *Proceedings World Geothermal Congress 2010*.

Simons, M., S. E. Minson, A. Sladen, F. Ortega, J. Jiang, S. E. Owen, L. Meng, J. P. Ampuero, S. Wei, R. Chu, D. V. Helmberger, H. Kanamori, E. Hetland, A. W. Moore, and F. H. Webb (2011), The 2011 magnitude 9.0 Tohoku-Oki earthquake: Mosaicking the megathrust from seconds to centuries, *Science*, *332*(6036), 1421–1425.

Smets, B., D. Delvaux, K. A. Ross, S. Poppe, M. Kervyn, N. D'Oreye, and F. Kervyn (2016), The role of inherited crustal structures and magmatism in the development of rift segments: Insights from the Kivu basin, western branch of the East African Rift, *Tectonophysics*, *683*, 62–76.

Specht, T. D., and B. R. Rosendahl (1989), Architecture of the Lake Malawi Rift, East Africa, *Journal of African Earth Sciences*, *8*, 355–382.

Stamps, D. S., E. Calais, E. Saria, C. Hartnady, J.-M. Nocquet, C. J. Ebinger, and R. M. Fernandes (2008), A kinematic model for the East African Rift, *Geophysical Research Letters*, *35*(5).

Stamps, D. S., E. Saria, and C. Kreemer (2018), A Geodetic Strain Rate Model for the East African Rift System, *Scientific Reports*, *8*(1), 732.

Stein, R. S., G. C. P. King, and J. Lin (1994), Stress Triggering of the 1994 M = 6.7 Northridge, California, Earthquake by Its Predecessors, *Science*, *265*(5177), 1432–1435.

Stein, S., and M. Liu (2009), Long aftershock sequences within continents and implications for earthquake hazard assessment, *Nature*, *462*(7269), 87–89.

Steinbruch, F. (2010), Geology and geomorphology of the Urema Graben with emphasis on the evolution of Lake Urema, *Journal of African Earth Sciences*, *58*(2), 272–284.

Suess, E. (1891), Die Bruche des ostlichen Afrika: Denkschriften der Kaiserlichsche, *Akademie der Wissenschaften zu Wien (Mathematik-Naturwis- senschaften)*, *58*, 555–584.

Sykes, L. R. (1978), Intraplate seismicity, reactivation of preexisting zones of weakness, alkaline magmatism, and other tectonism postdating continental fragmentation, *Reviews of Geophysics*, *16*(4), 621–688.

Szpak, Z. L., W. Chojnacki, and A. van den Hengel (2014), Guaranteed Ellipse Fitting with a Confidence Region and an Uncertainty Measure for Centre, Axes, and Orientation, *Journal of Mathematical Imaging and Vision*, *52*(2), 173–199.

Taisne, B., and S. Tait (2011), Effect of solidification on a propagating dike, *Journal of Geophysical Research*, *116*(B1).

Tarantola, A. (2005), *Inverse problem theory and methods for model parameter estimation*, 342 pp., Society for Industrial and Applied Mathematics.

Tarasewicz, J., B. Brandsdóttir, R. S. White, M. Hensch, and B. Thorbjarnardóttir (2012), Using microearthquakes to track repeated magma intrusions beneath the Eyjafjallajkull stratovolcano, Iceland, *Journal of Geophysical Research: Solid Earth*, *117*(2), 1–13.

Temtime, T., J. Biggs, E. Lewi, I. Hamling, T. Wright, and A. Ayele (2018), Spatial and temporal patterns of deformation at the Tendaho geothermal prospect, Ethiopia, *Journal of Volcanology and Geothermal Research*, *357*, 56–67.

Tesauro, M., M. K. Kaban, and W. D. Mooney (2015), Variations of the lithospheric strength and elastic thickness in North America, *Geochemistry, Geophysics, Geosystems*, *16*(7), 2197–2220.

Thatcher, W., and T. C. Hanks (1973), Source parameters of southern California earthquakes, *Journal of Geophysical Research*, *78*(35), 8547–8576.

Thomas, R. J., M. W. Von Veh, and S. Mccourt (1993), The tectonic evolution of southern Africa: an overview, *Journal of African Earth Sciences*, *16*(12), 5–24.

Till, C. B., M. Pritchard, C. A. Miller, K. K. Brugman, and J. Ryan-Davis (2018), Super-volcanic investigations, *Nature Geoscience*, *11*(4), 227–229.

Toda, S., R. S. Stein, K. Richards-Dinger, and S. B. Bozkurt (2005), Forecasting the evolution of seismicity in southern California: Animations built on earthquake stress transfer, *Journal of Geophysical Research B: Solid Earth*, *110*(5), 1–17.

Toombs, A., and G. Wadge (2012), Co-eruptive and inter-eruptive surface deformation measured by satellite radar interferometry at Nyamuragira volcano, D.R. Congo, 1996 to 2010, *Journal of Volcanology and Geothermal Research*, *245-246*, 98–122.

Turcotte, L., and H. Emerman (1983), Mechanism of active and passive Rifting, *Tectonophysics*, *94*(1-4), 39–50.

Tuttle, M. P., E. S. Schweig, J. D. Sims, R. H. Lafferty, L. W. Wolf, and M. L. Haynes (2002), The Earthquake Potential of the New Madrid Seismic Zone, *Bulletin of the Seismological Society of America*, *92*(6), 2080–2089.

Utsu, T. (1961), A statistical study on the occurence of aftershocks, *Geophys. Mag.*, *30*, 512–605.

Vail, R. J. (1968), The southern extension of the East African Rift System and related igneous activity, *Geologische Rundschau*, *10*(1), 161–168.

Vauchez, A., G. Barruol, and A. Tommasi (1997), Why do continents break-up parallel to ancient orogenic belts?, *Terra Nova*, *9*(2), 62–66.

Veevers, J., and C. Powell (1994), *Permian-Triassic Pangean basins and foldbelts along the Panthalassan margin of Gondwanaland*, 368 pp., Geological Society of America.

Verdon, J. P., D. A. Angus, J. Michael Kendall, and S. A. Hall (2008), The effect of microstructure and nonlinear stress on anisotropic seismic velocities, *Geophysics*, *73*(4), D41–D51.

Verdon, J. P., J.-M. Kendall, and A. Wüstefeld (2009), Imaging fractures and sedimentary fabrics using shear wave splitting measurements made on passive seismic data, *Geophysical Journal International*, *179*(2), 1245–1254.

Versfelt, J., and B. Rosendahl (1989), Relationships between pre-rift structure and rift architecture in Lakes Tanganyika and Malawi, East Africa, *Nature*, *337*(6205), 354–357.

Vigny, C., P. Huchon, J. C. Ruegg, K. Khanbari, and L. M. Asfaw (2006), Confirmation of Arabia plate slow motion by new GPS data in Yemen, *Journal of Geophysical Research: Solid Earth*, *111*(2).

Villamor, P., and K. Berryman (2001), A late quaternary extension rate in the Taupo Volcanic Zone, New Zealand, derived from fault slip data, *New Zealand Journal of Geology and Geophysics*, *44*(2), 243–269.

Voight, B., A. T. Linde, I. S. Sacks, G. S. Mattioli, R. S. Sparks, D. Elsworth, D. Hidayat, P. E. Malin, E. Shalev, C. Widiwijayanti, S. R. Young, V. Bass, A. Clarke, P. Dunkley, W. Johnston, N. McWhorter, J. Neuberg, and P. Williams (2006), Unprecedented pressure increase in deep magma reservoir triggered by lava-dome collapse, *Geophysical Research Letters*, *33*(3).

Wadge, G., P. W. Webley, I. N. James, R. Bingley, A. Dodson, S. Waugh, T. Veneboer, G. Puglisi, M. Mattia, D. Baker, S. C. Edwards, S. J. Edwards, and P. J. Clarke (2002), Atmospheric models, GPS and InSAR measurements of the tropospheric water vapour field over Mount Etna, *Geophysical Research Letters*, *29*(19).

Wadge, G., P. Cole, A. Stinton, J.-C. Komorowski, R. Stewart, A. Toombs, and Y. Legendre (2011), Rapid topographic change measured by high-resolution satellite radar at Soufriere Hills Volcano, Montserrat, 2008–2010, *Journal of Volcanology and Geothermal Research*, *199*(1-2), 142–152.

Wadge, G., J. Biggs, R. Lloyd, and J.-M. Kendall (2016), Historical volcanism and the state of stress in the East African Rift System, *Frontiers in Earth Science*, *4*(86).

Walsh, J., A. Nicol, and C. Childs (2002), An alternative model for the growth of faults, *Journal of Structural Geology*, *24*(11), 1669–1675.

Walter, T., and V. Troll (2001), Formation of caldera periphery faults: an experimental study, *Bulletin of Volcanology*, (63), 191–203.

Walter, T. R., and M. Motagh (2014), Deflation and inflation of a large magma body beneath Uturuncu volcano, Bolivia? Insights from InSAR data, surface lineaments and stress modelling, *Geophysical Journal International*, *198*(1), 462–473.

Walters, R. J., J. R. Elliott, N. D'Agostino, P. C. England, I. Hunstad, J. A. Jackson, B. Parsons, R. J. Phillips, and G. Roberts Edinburgh (2009), The 2009 L'Aquila earthquake (central Italy): A source mechanism and implications for seismic hazard, *Geophysical Research Letters*, *36*(17).

Walters, R. J., R. J. Holley, B. Parsons, and T. J. Wright (2011), Interseismic strain

accumulation across the North Anatolian Fault from Envisat InSAR measurements, *Geophysical Research Letters*, *38*(5).

Walters, R. J., B. Parsons, and T. J. Wright (2014), Constraining crustal velocity fields with InSAR for Eastern Turkey: Limits to the block-like behavior of eastern Anatolia, *Journal of Geophysical Research: Solid Earth*, *119*(6), 5215–5234.

Wauthier, C., V. Cayol, F. Kervyn, and N. D'Oreye (2012), Magma sources involved in the 2002 Nyiragongo eruption, as inferred from an InSAR analysis, *Journal of Geophysical Research*, *117*(B5).

Wauthier, C., V. Cayol, M. Poland, F. Kervyn, N. D'Oreye, A. Hooper, S. Samsonov, K. Tiampo, and B. Smets (2013), Nyamulagira's magma plumbing system inferred from 15 years of InSAR, *Geological Society, London, Special Publications*, *380*(1), 39–65.

Webley, P., G. Wadge, and I. James (2004), Determining radio wave delay by non-hydrostatic atmospheric modelling of water vapour over mountains, *Physics and Chemistry of the Earth, Parts A/B/C*, *29*(2-3), 139–148.

Wedmore, L. N. J., J. P. Faure Walker, G. P. Roberts, P. R. Sammonds, K. J. W. McCaffrey, and P. A. Cowie (2017), A 667 year record of coseismic and interseismic Coulomb stress changes in central Italy reveals the role of fault interaction in controlling irregular earthquake recurrence intervals, *Journal of Geophysical Research: Solid Earth*, *122*(7), 5691–5711.

Wells, D. L., and K. J. Coppersmith (1994), New Empirical Relationships among Magnitude, Rupture Length, Rupture Width, Rupture Area, and Surface Displacement, *Bulletin of the Seismological Society of America*, *84*(4), 974–1002.

Werner, C., U. Wegmüller, T. Strozzi, and A. Wiesmann (2000), GAMMA SAR and Interferometric Processing Software.

Weston, J., A. M. G. Ferreira, and G. J. Funning (2011), Global compilation of interferometric synthetic aperture radar earthquake source models: 1. Comparisons with seismic catalogs, *Journal of Geophysical Research*, *116*(B8), B08,408.

Whaler, K., and S. Hautot (2006), The electrical resistivity structure of the crust beneath the northern Main Ethiopian Rift, *Geological Society, London, Special Publications*, *259*, 293–305.

Whitmarsh, R. B., G. Manatschal, and T. A. Minshull (2001), Evolution of magma-poor continental margins from rifting to seafloor spreading, *Nature*, *413*(6852), 150–154.

Wicks, C. W. (2002), Magmatic activity beneath the quiescent Three Sisters volcanic center, central Oregon Cascade Range, USA, *Geophysical Research Letters*, *29*(7), 2–5.

Wiemer, S., M. Gerstenberger, and E. Hauksson (2002), Mine Earthquake: Implications for Aftershock Hazard, *Bulletin of the Seismological Society of America*, *92*(4), 1227–1240.

Wilks, M. (2016), A Seismological Investigation into Tectonic, Magmatic and Hydrothermal Processes at Aluto and Corbetti, Two Restless Volcanoes in the Main Ethiopian Rift, Phd., Univeristy of Bristol.

Wilks, M., J.-M. Kendall, A. Nowacki, J. Biggs, J. Wookey, Y. Birhanu, A. Ayele, and T. Bedada (2017a), Seismicity associated with magmatism, faulting and hydrothermal circulation at Aluto Volcano, Main Ethiopian Rift, *Journal of Volcanology and*

Geothermal Research, *340*, 52–67.

Wilks, M., A. Ayele, J. M. Kendall, and J. Wookey (2017b), The 24th January 2016 Hawassa earthquake: Implications for seismic hazard in the Main Ethiopian Rift, *Journal of African Earth Sciences*, *125*, 118–125.

Wilson, C. J. N., B. F. Houghton, M. O. Mcwilliams, M. A. Lanphere, S. D. Weaver, and R. M. Briggs (1995), Volcanic and structural evolution of Taupo Volcanic Zone, New Zealand: a review, *Journal of Volcanology and Geothermal ResearchJournal of Volcanology and Geothermal Research*, *68*(68), 1–28.

Woldegabriel, G., J. L. Aronson, and R. C. Walter (1990), Geology, geochronology, and rift basin development in the central sector of the Main Ethiopian Rift, *Geological Society of America Bulletin*, *12*(4), 439–458.

Wood, D. A., H. J. Zal, C. A. Scholz, C. J. Ebinger, and I. Nizere (2017), Evolution of the Kivu Rift, East Africa: interplay among tectonics, sedimentation and magmatism, *Basin Research*, *29*, 175–188.

Wright, T., B. Parsons, and E. Fielding (2001), Measurement of interseismic strain accumulation across the North Anatolian Fault by satellite radar interferometry, *Geophysical Research Letters*, *28*(10), 2117–2120.

Wright, T. J., B. E. Parsons, and Z. Lu (2004), Toward mapping surface deformation in three dimensions using InSAR, *Geophysical Research Letters*, *31*, 1–5.

Wright, T. J., C. Ebinger, J. Biggs, A. Ayele, G. Yirgu, D. Keir, and A. Stork (2006), Magma-maintained rift segmentation at continental rupture in the 2005 Afar dyking episode, *Nature*, *442*(7100), 291–294.

Wright, T. J., J. R. Elliott, H. Wang, and I. Ryder (2013), Earthquake cycle deformation and the Moho: Implications for the rheology of continental lithosphere, *Tectonophysics*, *609*, 504–523.

Wuestefeld, A., O. Al-Harrasi, J. P. Verdon, J. Wookey, and J. M. Kendall (2010), A strategy for automated analysis of passive microseismic data to image seismic anisotropy and fracture characteristics, *Geophysical Prospecting*, *58*(5), 755–773.

Xu, W., and S. Jónsson (2014), The 2007–8 volcanic eruption on Jebel at Tair island (Red Sea) observed by satellite radar and optical images, *Bulletin of Volcanology*, *76*(2), 795.

Xu, W., E. Rivalta, and X. Li (2017), Magmatic architecture within a rift segment: Articulate axial magma storage at Erta Ale volcano, Ethiopia, *Earth and Planetary Science Letters*, *476*, 79–86.

Yang, X.-M., P. M. Davis, and J. H. Dieterich (1988), Deformation from inflation of a dipping finite prolate spheroid in an elastic half-space as a model for volcanic stressing, *Journal of Geophysical Research*, *93*(B5), 4249–4257.

Yang, Z., and W. P. Chen (2008), Mozambique earthquake sequence of 2006: High-angle normal faulting in southern Africa, *Journal of Geophysical Research: Solid Earth*, *113*(12).

Yang, Z., and W. P. Chen (2010), Earthquakes along the East African Rift System: A multiscale, system-wide perspective, *Journal of Geophysical Research: Solid Earth*, *115*(12).

Yu, C., N. T. Penna, and Z. Li (2017a), Generation of real-time mode high-resolution

water vapor fields from GPS observations, *Journal of Geophysical Research*, *122*(3), 2008–2025.

Yu, C., Z. Li, and N. T. Penna (2017b), Interferometric synthetic aperture radar atmospheric correction using a GPS-based iterative tropospheric decomposition model, *Remote Sensing of Environment*, *204*, 109–121.

Žáček, V., V. Rapprich, K. Verner, T. Hroch, D. Tarekegu, K. Dereje, L. Firdawok, B. Habtamu, and D. Čížek (2014), Shashemene Geological Map. 1:50,000.

Zebker, H. A., P. A. Rosen, and S. Hensley (1997), Atmospheric effectsin interferometric synthetic aperture radar surface deformation and topographic maps, *102*, 7547–7563.

Zoback, M. L. (1992a), First- and second-order patterns of stress in the lithosphere: The World Stress Map Project, *Journal of Geophysical Research*, *97*(B8), 11,703.

Zoback, M. L. (1992b), Stress field constraints on intraplate seismicity in eastern North America, *Journal of Geophysical Research*, *97*(B8), 11,761–11,782.

Zwick, P., R. McCaffrey, and G. Abers (1994), MT5 program, IASPEI Software Library, 4.